

Universiteit
Leiden
The Netherlands

Gaining control of lipid-based nanomedicine by understanding the nano-bio interface

Pattipeiluhu, R.

Citation
Pattipeiluhu, R. (2021, December 9). *Gaining control of lipid-based nanomedicine by understanding the nano-bio interface*. Retrieved from https://hdl.handle.net/1887/3245795

Version:	Publisher's Version
License:	Licence agreement concerning inclusion of doctoral thesis in the Institutional Repository of the University of Leiden
Downloaded from:	https://hdl.handle.net/1887/3245795

Note: To cite this publication please use the final published version (if applicable).

Gaining control of lipid-based nanomedicine by understanding the nano-bio interface

Proefschrift

ter verkrijging van de
graad van doctor aan de Universiteit Leiden,
op gezag van rector magnificus prof.dr.ir. H. Bijl,
volgens besluit van het college voor promoties
te verdedigen op donderdag 9 December 2021
klokke 13.45 uur

door

Roy Pattipeiluhu
Geboren op 3 oktober 1991
te Rotterdam, Nederland

Promotiecomissie

Promotor

Prof. dr. Alexander Kros	Leiden University

Co-promotor

Dr. Thomas H. Sharp	Leiden University Medical Centre

Overige commissieleden

Prof. dr. Hermen S. Overkleeft (voorzitter)	Leiden University
Prof. dr. Joke A. Bouwstra (secretaris)	Leiden University
Prof. dr. Matthias Barz	Leiden University
Prof. dr. Nico A.J.M. Sommerdijk	Radboud University Medical Center
Dr. Roy van der Meel	Eindhoven University of Technology

“We bewonderen de chaos omdat we zo graag orde willen scheppen”

- M.C. Escher

Table of contents

Chapter 1 7
Introduction

Chapter 2 33
Unbiased Identification of the Liposome Protein Corona Using Photoaffinity Based Chemoproteomics

Chapter 3 53
Anionic Lipid Nanoparticles Preferentially Deliver mRNA to the Hepatic Reticuloendothelial System

Chapter 4 79
Site Selective Binding of Apolipoprotein E in the Protein Corona of Anionic Liposomes

Chapter 5 97
Paracrystalline Inverted Lipid Phases Encapsulating siRNA Enhance Lipid Nanoparticle Mediated Transfection

Chapter 6 121
Summary and Outlook

Appendix 1 129
Supplementary Information to Chapter 2

Appendix 1 179
Supplementary Information to Chapter 3

Appendix 1 201
Supplementary Information to Chapter 4

Appendix 1 215
Supplementary Information to Chapter 5

Nederlandse samenvatting 237

Curriculum Vitae 243

List of Publications 245

Chapter 1

Introduction

1.1 The concept and design of nanomedicine

In 1900, Paul Ehrlich conceived the scientific concept of the "magic bullet". The idea postulated a therapeutic agent that, like the bullet of a gun, could hit diseased cells without harming healthy cells.[1] Traditionally, antibiotics are often defined as magic bullets, laying the foundation for pharmaceutical research.[2] In modern medicine, the principal concept of a magic bullet has transcended from an ideal binary response and the paradigm continues by the development of 'personalized and tailored drugs' that precisely target the specific molecular defects of a patient.[3] For example, gene therapy in which exclusively the defective gene is repaired is considered as a modern day approach for the development of a magic bullet.

The application of nanotechnology to the field of medicine is considered as one of the technologies that can realize the concept of the "magic bullet". Nanotechnology is a field of research that focuses on engineering functional systems at the molecular scale, typically defined in the range of 1 to 100 nm, in which its lower limit is defined by the size of the individual molecules. These functional systems are commonly achieved through the "bottom-up" assembly of molecular components through chemical principles. In medicinal approaches, the understanding and control over the self-assembly of these molecular components with therapeutics agents allows for the fabrication of nanosized materials (nanoparticles) that can be applied for therapies, defined as nanomedicines.

Nanomedicine spans a variety of medical applications such as therapeutics, diagnostics, imaging and tissue engineering.[4,5] Out of these different nanomedical applications, nanoparticle based drug delivery is one of the most extensively explored.[6] The key principles of nanoparticle-based drug delivery is to obtain one or more benefits over the administered drug alone.[7] Firstly, the strategy allows for the delivery of sensitive cargo that would otherwise be degraded by the body before reaching its target. Secondly, nanoparticles can alter the biodistribution compared to administration of the free drug, allowing the drug to reach novel targets. Thirdly, the nanoparticles can serve as a platform for slow release of the desired therapeutic, prolonging the bioavailability of the drug. Finally, nanoparticles can facilitate the intracellular delivery of cargo that is not capable of passing endogenous barriers by itself.

While nanoparticles are formally defined as particles in the 1–100 nm size range, nanomedicine for drug delivery purposes are typically defined within the 10–450 nm range. Over the past decades, intensive research has yielded a large variety of nanoparticle types (**Figure 1a**). These nanoparticles are typically fabricated from the bottom-up using either

synthetic organic (*e.g.*, polymers, proteins), bio-derived organic (*e.g.*, lipids, proteins) or inorganic materials (*e.g.*, iron oxide, silica). In addition, hybrid nanoparticles that contain a variety of these materials are also extensively investigated.[8] Furthermore, there is an increasing interest in nanoparticles derived from biological systems, such as a weakened viruses or virus-like particles, as well as biomimetic or bio-derived nanoparticles such as engineered extracellular vesicles, lipoprotein mimics and exosomes.[9]

The choice for a certain nanoparticle type depends on the desired purpose. For example, organic nanoparticles are often employed for drug delivery purposes due to their high flexibility in cargo encapsulation and fabrication from non-toxic components. However, inorganic nanoparticles can offer exclusive magnetic, electrical and optical properties for isolation and imaging purposes.[10] These nanoparticles can function as carriers for a variety of cargos, such as DNA/RNA and small molecules (**Figure 1b**). The successful encapsulation of these cargos is dependent on the nanoparticle type and the physicochemical characteristics of its component. Another common strategy that is often employed in nanoparticle design is the chemical conjugation of different (bio)molecules or (bio)polymers to the nanoparticle surface (**Figure 1c**). This can be employed for the stabilisation of the nanoparticle and its encapsulated cargo, or for targeting/shielding strategies in order to manipulate the nanoparticle behaviour *in vivo*.

However, although these principles of nanomedicine design are stated as straightforward, simple and ideal, there are multiple layers of complexity involved with nanomedicine design and application. A successful strategy depends on the proper therapeutic target, the ability to fabricate a fitting nanoparticle carrier and its performance in biological systems.

1.2 Lipid based nanomedicine

Out of the different nanoparticle types, lipid-based nanoparticles were among the first to be investigated and are the most extensively pursued for drug delivery purposes. In addition, the majority of clinically approved nanocarriers for drug delivery belong to the class of lipid-based nanoparticles.[11] They are either completely, or mostly, made from lipid molecules. Lipids are a group of organic biomolecules and one of the most abundant cellular metabolites. The lipids used for nanoparticle fabrication are typically amphiphilic small molecules, possessing both a hydrophobic and hydrophilic region (**Figure 2a**). In nature, these amphiphilic lipids are crucial for the assembly of cellular membranes, in which phospholipids organize themselves into bilayers with a spatiotemporal pattern containing various other lipids. This self-assembly process of amphipathic lipids is a chemical property that enables cells to segregate their internal constituents from the

external environment. The first type of lipid-based nanomedicine, liposomes, relied on this process of vesicle self-assembly. These vesicles, formed from mainly phospholipids, were discovered in the early 1960s and initially used as model systems for cellular membranes.[12] This gave researchers an unique tool to study multiple cellular mechanisms, such as diffusion across membranes.[13,14] It was not until the early 1970s that liposomes were pursued as possible carriers for therapeutically relevant agents.[15–17]

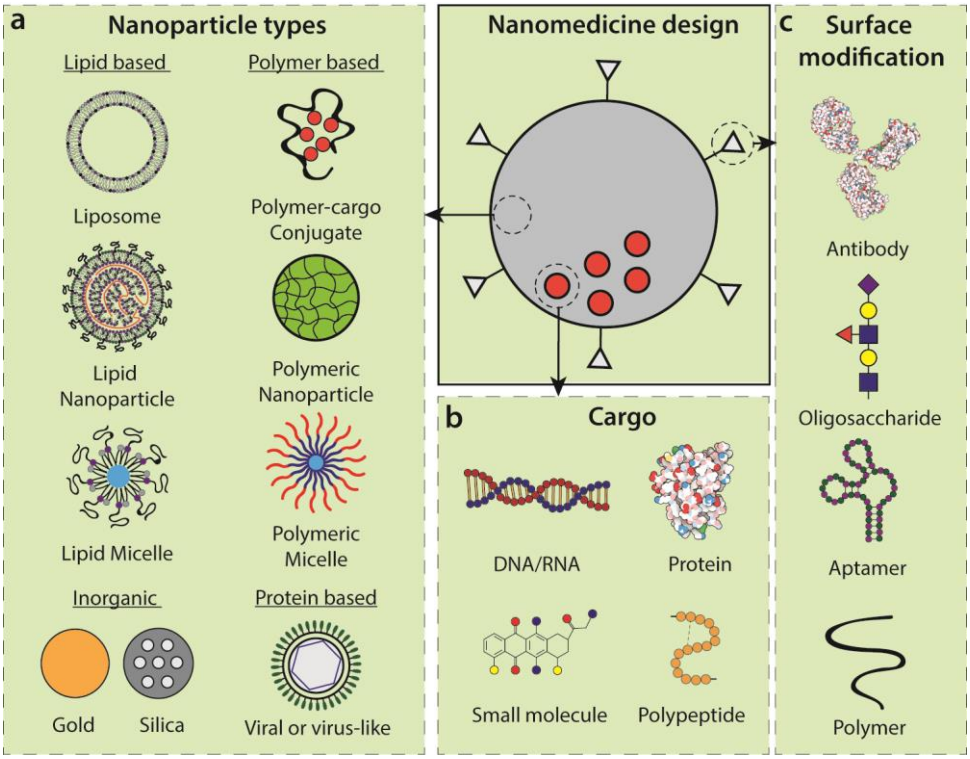


Figure 1. Schematic representation nanomedicine design. (a) Commonly used nanoparticle variants for drug delivery purposes **(b)** encapsulated cargos and **(c)** types of surface modifications.

Lipid-based nanomedicine such as liposomes possess several benefits that are still valid to this date. Firstly, due to the biological nature of lipids, the components of lipid-based nanomedicine are often non-toxic and biodegradable. Secondly, the assembly of lipid-based nanomedicine is controllable at the nanometre scale. Finally, the wide variety of lipid molecules gives rise to a plethora of formulations with varying lipid compositions. Identification of lipid species has shown that there are over 40,000 unique known lipid structures that can be classified by structural similarity to 8 different categories.[18,19] Out of

these categories, phospholipids, sterol lipids and sphingolipids are currently most common for the fabrication of lipid-based nanoparticles (**Figure 2b**).[20]

The versatility of lipid molecules also allows for a variety of physicochemical properties of lipid-based nanoparticles (**Figure 2c**). The saturation of alkyl chains in the lipid backbone can modulate the stiffness of lipid mixtures, whereas the preferred geometry of lipid molecules can determine the morphology and size of the nanoparticles. Furthermore, the surface charge of lipid-based nanoparticles depends on the formal charge and organization of the lipids in their composition. There has been a large improvement in understanding the influence of lipid properties (*e.g.*, charge, geometry) on self-assembly, as well as development of production (*e.g.*, thin-film hydration, microfluidics) and characterization techniques (*e.g.*, light scattering, electron microscopy).[21,22] This allows for the fabrication of different variants of lipid-based nanoparticles beyond liposomes, such as (filled) lipid nanoparticles (LNPs), lipid micelles and lipid emulsions (**Figure 1a**). Finally, the chemical structure of lipid molecules can be altered through chemical conjugation or bottom-up synthesis of these molecules, allowing for the fabrication of novel lipids and the fabrication of hybrids of lipids with other biomolecules (*e.g.*, glycans, peptides).

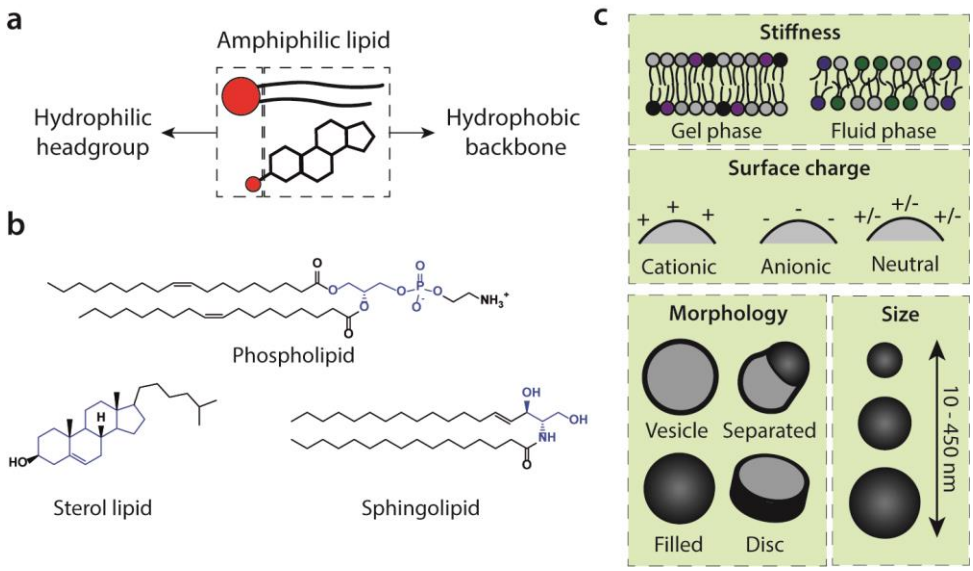


Figure 2. Building blocks and characteristics of lipid-based nanomedicine. (**a**) Schematic representation of common amphiphilic lipids used for the self-assembly of lipid-based nanoparticles. Amphiphilicity is caused by the presence of both a hydrophobic and hydrophilic domain within the same molecule. (**b**) Common lipid groups used for the self-assembly of lipid-based nanoparticles.

Important structural characteristics are displayed in blue: Phospholipids contain a phosphorylated glycerol group; Sterol lipids contain a fused four-ring core structure with varying substituents; Sphingolipids contain a sphingoid base backbone which is substituted to fatty acid amides. (**c**) Lipid-based nanomedicine can vary in multiple physicochemical properties, depending on the choice of lipids. These include, but are not limited to, a difference in morphology, stiffness, surface charge and size.

1.3 Ionizable Lipid Nanoparticles (LNPs) for RNA Therapeutics

Out of the various lipid-based nanomedicines available, the use of the ionizable lipid nanoparticles (LNPs) for RNA therapeutics resembles the current state-of-the-art for lipid-based nanomedicine.[23] In 2018, Onpattro® was the first LNP based RNA interference (RNAi) therapeutic that was accepted in the clinical for the treatment of hereditary transthyretin-mediated amyloidosis, effective through the silencing of transthyretin production in liver hepatocytes after intravenous administration.[24] Furthermore, the onset of the 2020 pandemic due to SARS-CoV-2 has greatly accelerated the development and transition of multiple LNP based messenger RNA (mRNA) prophylactic vaccines into the clinic.[25–28] All together, these successes highlight the bright future of using LNPs for multiple RNA-based therapeutics.

1.3.1 Self-assembly of LNPs

LNPs are self-assembled from multiple lipid components, relying on the electrostatic complexation for the entrapment and protection of fragile RNA molecules using ionizable lipids (ILs) (**Figure 3a,b**). These ILs represent the second generation of lipids used for gene therapy.[29] Initially, permanently cationic lipids were utilized to electrostatically complex negatively charged RNA or DNA molecules, forming so-called lipoplexes.[30] These generated permanently cationic nanoparticles which, due to their surface properties, displayed a limited biodistribution and poor bioavailability, in combination with toxic side effects.[31] ILs circumvent these limitations with tertiary amines, which are predominantly cationic at an acidic pH, while regaining a neutral formal charge at a physiological pH. A combination of ILs and other lipids are mixed with RNA molecules at an acidic pH,[32,33] leading to the spontaneous electrostatic complexation of the RNA by the cationic ILs and nanoprecipitation with the other lipids into intermediate LNPs containing RNA (**Figure 3c**).[34–36] Afterwards, the lipid solvent and acidic buffer are replaced for a physiologically-friendly buffer (PBS, pH = 7.4), which leads to the formation of stable LNPs. Furthermore, any ILs on the surface of the LNP will regain a formal neutral charge at this pH, leading to a zwitterionic neutral surface charge. Throughout this process, the additional lipids used next to ILs serve a variety of purposes. Structural lipids, such as cholesterol, allow for the

formation of a hydrophobic core structure along with the IL-RNA complexes.[37,38] Since the LNPs are assembled in aqueous solution, the helper (phospho)lipids and polyethylene glycol (PEG) conjugated lipids are predominately enriched on the surface of LNPs,[39] and are essential for the colloidal stability of the particles through the formation of a monolayer or bilayer between the hydrophobic core of the LNPs and the aqueous solution. Nevertheless, although solid core structure LNPs are reported most frequently, variation in lipid type, composition and cargo type can lead to the formation of polymorphic or phase separated LNPs.[40–42] For example, the large differences in length and structural organization of siRNA vs. mRNA can significantly impact the complexation state with ionizable lipids.[42] In a similar fashion, there is an increasing number of ILs with diverse chemical structures, such as branched variants and lipidoids.[43–47] The combination of these ILs with the other helper lipids can significantly impact the formation of lipid superstructures and successful RNA encapsulation.

Combining different helper- and PEG-lipids can affect the formation of LNP surface properties.[48,49] The virtually endless variation in possibilities add to the complexity of predicting LNP structures, as well as evaluating their impact on performance in biological systems. Further in-depth biophysical characterization and coupling to efficiency might allow for the elucidation of important structure-activity relationships that will allow for the design of more potent LNPs in the future.

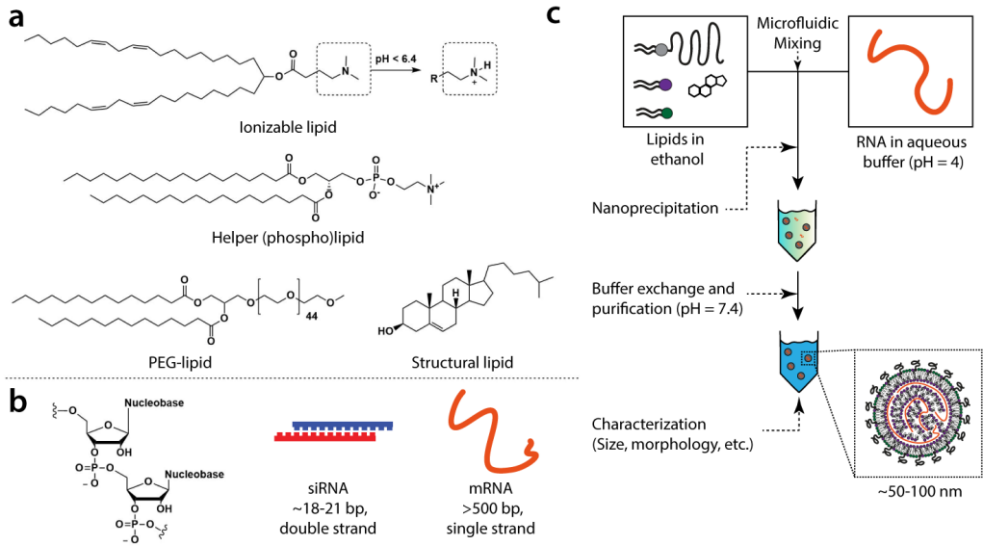


Figure 3. The concept and fabrication of ionizable lipid nanoparticles. (**a**) Examples of lipid components commonly used for LNPs. IL = DLin-MC3-DMA, helper lipid = DSPC, PEG-lipid = DMG-PEG2000, structural lipid = cholesterol. (**b**) Structure of commonly used RNA molecules in LNP fabrication. (**c**) The fabrication process of LNPs.

1.3.2 The intracellular mechanism of LNPs

The use of ILs for the assembly of LNPs serves an additional, and crucial, second purpose. Upon administration, LNPs are typically taken up by cells through a form of endocytosis, which can be facilitated through a receptor-mediated interaction. Upon cellular uptake, the LNPs will end up in endosomal vesicles which are designed for the processing and degradation of foreign compounds by endogenous enzymes.[50] In addition, the pH of the endosomal vesicles is decreased in order to facilitate the degradation processes. Due to the ionizable properties of the LNPs, this leads to protonation of the IL and consequently a cationic surface charge. Since the surface charge of endosomal membranes is typically anionic, this promotes a direct electrostatic interaction between the LNP and the endosomal membrane (**Figure 4**). In this process, destabilization of the LNP as well as the endosomal membrane allows for the de-complexation of the LNPs and consequently for the escape of RNA molecules into the cytosol and further processing by the endogenous machinery.[51] To this end, the formation of non-lamellar and de-stabilizing LNP-membrane intermediates are known to facilitate a more efficient release of RNA molecules into the cytosol.[52,53] However, to date, the absolute efficiency of RNA escape from the LNPs into

the cytosol is estimated to be in the range of ~2%.[54,55] Although sufficient for certain purposes, improvement of this endosomal escape efficiency will pave the way for the delivery of more complex and larger RNA constructs, for example for genome editing. In addition, increased potency will benefit the therapeutic window of LNP-RNA based drugs and decrease costs of production.

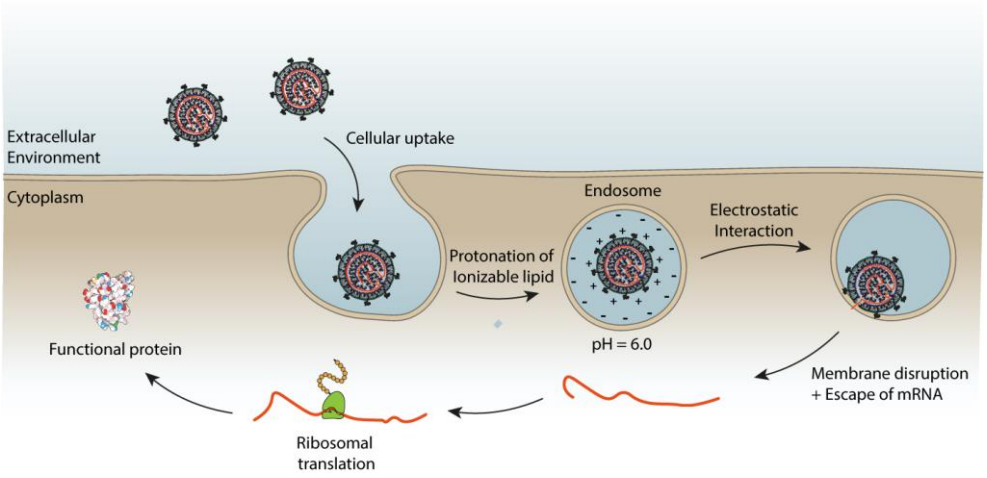


Figure 4. The intracellular mechanism of LNPs containing RNA. Uptake of LNPs is typically mediated through a form of endocytosis. Herein, acidification in the endosome leads to protonation of the ionizable lipids in LNPs and induces an electrostatic interaction between the LNP and endosomal membrane. This interaction leads to membrane disruption and escape of RNA molecules into the cytosol, where they can exhibit their biological effect.

1.4 Clearance of nanomedicine

Although the field of nanomedicine has produced some very promising avenues of therapeutic application, for example by drug delivery to liver hepatocytes or local administration, extra-hepatic drug delivery remains troublesome. Consequently, the body's response to foreign material is one of the most challenging barriers to overcome. For the relevance to this thesis, the focus will be on the clearance of nanoparticles after intravenous administration. However, the mechanisms explained here also affect locally administered nanomedicines as they often reach the bloodstream by, for example, lymphatic drainage.[56–58]

There are three major organs that dominate the clearance of injected nanoparticles: the liver, the spleen and the kidneys (**Figure 5**). The majority of the nanoparticles (30-99%) are

cleared through the liver (hepatic clearance).[59–61] More specifically, early reports established the preferentially accumulation of liposomes in the reticuloendothelial system (RES).[62,63] The RES is the combination of macrophages and specialized cell types, such as scavenger endothelial cells, that are responsible for the clearance of foreign and colloidal material from the blood.[64,65] Within the liver, hepatocytes, liver sinusoidal endothelial cells (LSECS) and Kupffer cells (KCs) orchestrate the uptake and clearance of nanoparticles (**Figure 5**). KCs are known to phagocytose bacteria, viruses and (large) nanoparticles in order to remove them from the bloodstream.[65,66] LSECs are specialized scavenger endothelial cells (SECs) responsible for clearing the blood of colloidal waste, viruses and oxidized macromolecules (*e.g.* oxLDL).[67–69] There are multiple classes of scavenger receptors on their cell surface that perform this function.[68,70] Hepatocytes are not specialized to scavenge the blood of harmfull materials and therefore have a lower endocytic capability and express few scavenger receptors. Instead, they are mostly involved in metabolic processes such as lipid and protein synthesis. Furthermore, in order for nanoparticles to reach the hepatocytes, they have to diffuse through fenestrations of LSECs (<100 nm) and transverse the Space of Disse.[61] Therefore, in general, hepatocyte uptake by nanomedicines is only observed at higher doses, when the scavenger receptors are saturated.

In the case of lipid-based systems, hepatocytes play a more profound role in uptake and clearance than for other nanomedicines.[71,72] One of the key functions of hepatocytes is the uptake of lipids from systemic circulation. Endogenous (dietary) fats are transported by lipoproteins (*e.g.*, HDL, LDL, chylomicrons) and taken up by specific lipoprotein receptors (*e.g.*, LDL-receptor family) expressed on hepatocytes. It is known that some lipid-based nanomedicines are taken up and processed by LDL-receptors in similar ways.[72,73] Further downstream, the final fate of the nanoparticle components is typically determined by the material. For example, lipid-based nanoparticles are generally dissociated intracellularly followed by metabolization and biliary secretion of their components via the gall bladder, ending up in the feces.[59] In contrast, inorganic nanoparticles are typically retained in the cells for longer periods prior to biliary secretion.[74]

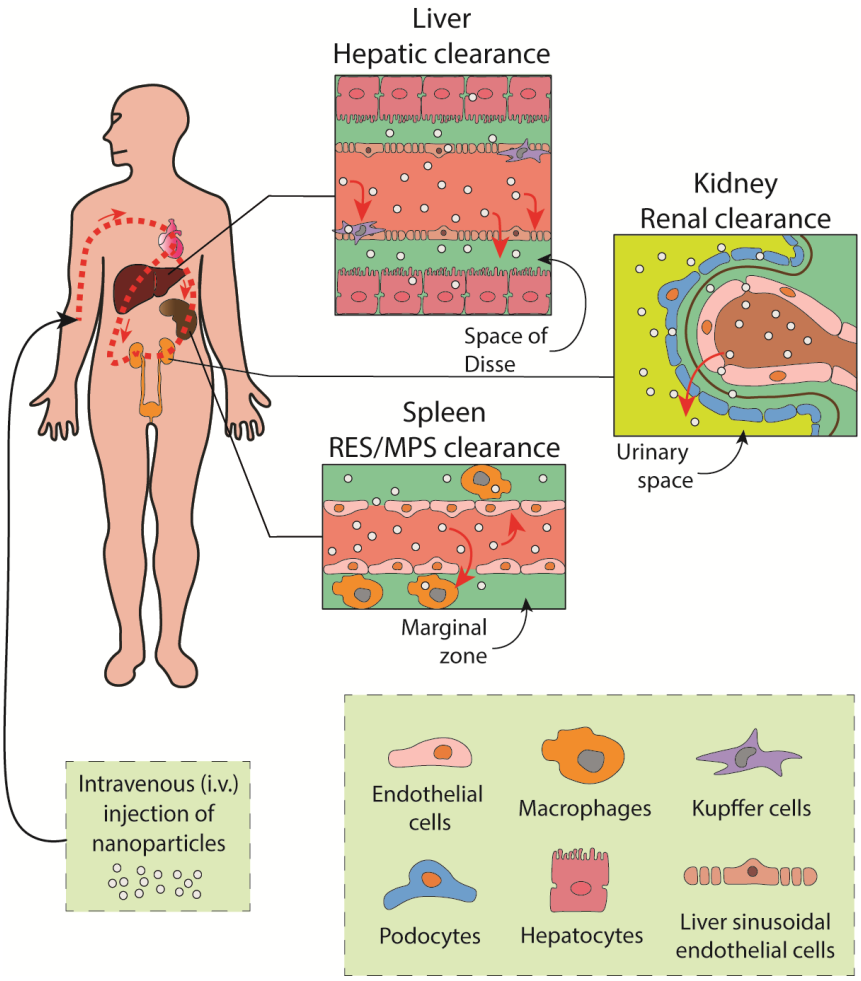


Figure 5. Major organs responsible for nanoparticle clearance upon intravenous (*i.v.*) administration. Nanoparticles in the bloodstream encounter multiple organs during circulation, where the liver, spleen and kidneys are able to remove these particles depending on a variety of nanoparticle characteristics such as size, charge and material. Clearance by the reticuloendothelial system (RES) is most predominant in the liver and spleen, where macrophages, Kupffer cells, macrophages and (liver sinusoidal) endothelial cells remove nanoparticles using a variety of scavenging receptors. Diffusion of nanoparticles through the fenestrations of LSECs in the liver and gaps of ECs in the spleen are largely depend on their size. Renal clearance through the spleen is typically observed for small (<10 nm) nanoparticles, or for metabolised components of nanoparticle reagents and cargo.

Another important organ in the sequestration and clearance of nanoparticles *in vivo* is the spleen.[75] The spleen is responsible for a variety of processes, such as the synthesis of antibodies, production of lymphocytes, sequestration of pathogens, and the regulation of red blood cells and platelets. Similar to the liver, the spleen contains RES cells that are able to scavenge and degrade foreign materials in the blood (**Figure 5**). Splenic macrophages reside in the splenic red pulp and the marginal zone and are the primary regulators of scavenging nanoparticles from the blood sinusoids in the spleen. A process called splenic filtration determines whether nanoparticles will be taken up by macrophages in the marginal zone or in the red pulp.[61] It is typically believed that size is one of the large determinants of this process, although other nanoparticle characteristics such as charge and type of material have been found to be equally important.[76] Furthermore, the spleen has been shown to play a crucial role in the accelerated clearance of lipid-based nanoparticles upon repeated injections.[77,78] Especially in the case of PEGylated or immuno-liposomes, the spleen was found to generate IgM monoclonal antibodies that facilitated the clearance of repeated injections of these nanoparticles by the liver.[79] These results indicate that the spleen is an important regulator of nanoparticle clearance, both by direct and indirect processes.

The last major organ responsible for clearance of IV injected is the kidneys. The kidneys are unique compared to the liver and spleen, by the fact that clearance is not predominantly regulated by RES cells. Instead, the kidney is responsible for the renal clearance of compounds and macromolecules from the blood into the urine. This happens through a process called glomerular filtration, in which the kidneys filter excess fluid and waste products out of the blood. This process is highly dependent on a small size of the waste product and is therefore typically observed only for small (<10 nm) nanoparticles (**Figure 5**).[80,81] Since lipid-based nanoparticles are generally bigger than 10 nm, clearance or retention of these particles by the kidneys is only observed in negligible amounts.[76,81] However, the processing of lipid-based nanoparticles by other organs often leads to the excretion of its metabolites into the blood and clearance by the kidneys, which can lead to the determination of these products in the urine.[82,83] Therefore, although kidneys are not always responsible for the direct clearance of lipid-based nanoparticles, they can give important information about the pharmacokinetics and pharmacodynamics of the encapsulated drug and the lipid components.

1.5 Challenges at the nano-bio interface

The current limitations regarding nanoparticle clearance have hampered nanomedicine development for decades and therefore have been at the core of many research topics. More recently, effort is directed to understanding and exploiting the more specific molecular interactions that underpin these mechanisms, often referred to as the "bio-nano" interface.[80,84–86] This topic aims at the understanding the interaction of endogenous molecules and structures (*e.g.*, proteins, membranes, etc.) with the introduced nanomedicines.

1.5.1 The protein corona of nanoparticles

The adsorption of proteins to a nanoparticle surface is of great importance for the biodistribution and clearance of nanoparticles *in vivo*, and has been studied since the 1990s.[87–89] Nowadays, protein adsorption to nanoparticles is better known as the formation of a "protein corona".[85,90] When introduced into a biological system, nanoparticles encounter a complex mixture of cells, endogenous nanoparticles, proteins and small molecules. For example, human blood can be divided into three phases: the erythrocytes (red blood cells), the buffy coat (white blood cells and platelets) and plasma (**Figure 6a**). The latter contains a large collection and diversity of blood proteins. Therefore, upon administration, the "synthetic identity" of the nanoparticle can change and adapt a "biological identity" (**Figure 6b**). To some extent, it is the protein corona and not the underlying synthetic surface of a nanoparticle, which the body "sees" and interacts with.[91]

The composition and extent of the protein corona is dependent on the "synthetic identity" of a nanoparticle. Physicochemical properties of nanoparticles such as size, surface charge and chemical composition can affect the adsorption of proteins (**Figure 6c**).[92,93] Over the past decade, enormous efforts have focused on the generation of protein corona profiles for a myriad of nanoparticle types.[85,90,94–96] However, identification of reliable profiles and important protein-nanoparticle interactions has been challenging due to limitations and drawbacks in separation techniques of protein coronas from biological media.[97–100]

Derived from studies that have explored the affinity and kinetics of protein binding to nanoparticles, the protein corona is often divided in the "hard" and "soft" corona.[92,101] Here, the "hard" corona is considered as the first layer of tightly binding proteins that are directly adsorbed to the nanoparticle surface. The "soft" corona is considered as a group of proteins that interact with the underlying "hard" corona or with low-affinity binding. The general presence and influence of the "soft" corona still originates from heavy speculation and its

presence can be debated on the basis of limitations in protein corona characterisation techniques.[97,98]

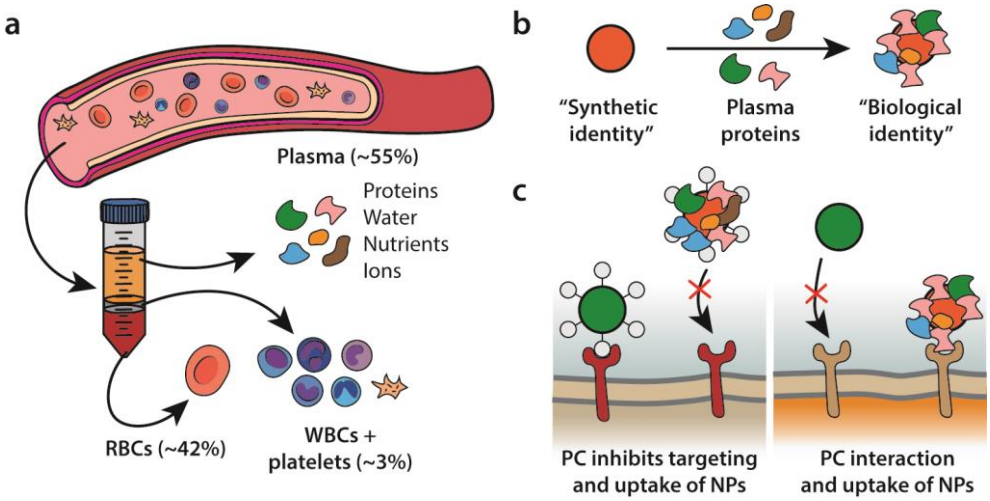


Figure 6. The formation of a nanoparticle protein corona. (a) Blood can be divided into three parts: RBCs, WBCs with platelets and plasma. **(b)** Exposure of nanoparticles to plasma proteins leads to the formation of a biological identity. **(c)** The protein corona can influence the behaviour of design nanoparticles by interfering with targeting strategies or by leading to uptake by undesired cell surface receptors. **Abbreviations used:** RBCs = Red Blood Cells, WBCs = White Blood Cells, PC = protein corona, NP = nanoparticle

Besides nanoparticle characteristics, the biological medium can also impact the formation and composition of the protein corona. Since the majority of nanoparticles are administered intravenously, plasma or serum are generally the most investigated biological fluids. Working with whole blood in *in vitro* conditions is problematic due to aggregation without supplementation with anticoagulants. Other biological fluids, such as cerebrospinal fluid or intramuscular fluid, are not yet widely investigated for protein corona formation. However, these fluids are interesting for elucidating the protein corona formation for local administration routes of nanomedicine.[102,103]

The general presence a protein corona is known to influence the behaviour of nanoparticles in various ways. One of the most profound effects is the possibility of inhibiting targeting strategies (**Figure 6c**). For example, it was found that nanoparticles functionalised with transferrin ligands had a significantly reduced uptake with the desired transferrin receptor in the presence of plasma proteins.[104] Similar effects have been reported for other functional ligands such as antibodies, aptamers and click-chemistry handles.[105–107]

Therefore, protein corona formation is often stated as one of the reasons for the limited translation of targeting strategies (**Figure 6**). The protein corona is also known facilitate bodily clearance of nanoparticles (**Figure 6c**),[108,109] in particular by enhancing phagocytic uptake by macrophages.[110–113] Studying specific (classes of) proteins is considered as the next crucial step for mechanistic understanding of the protein corona. Recent efforts have elucidated the influence of apolipoprotein E,[109,114] clusterins[115] and complement components[116] on the behaviour of nanoparticles *in vitro* and *in vivo*. Further exploration of these avenues will allow for the development of rational strategies in manipulating nanoparticle behaviour.

1.5.2 Receptor mediated uptake and endosomal processing

Crucial for the eventual cellular uptake of nanomedicine from the bloodstream is the interaction between nanoparticles, or their protein corona, with cell-surface receptors. Scavenger receptors (SRs) are a group of cell surface receptors that play a crucial role in maintaining homeostasis and immunity, for example by facilitating the clearance of harmful, degraded or foreign material.[117] Throughout the body, SRs are predominantly expressed on macrophages and scavenging endothelial cells (SECs).[67,118–120] SRs are separated into 10 families (classes A-J) according to sequence and further classified based on the variations of the sequence.[121,122] Out of these, several SRs have shown to be involved in the cellular uptake of nanoparticles (**Figure 7a**). A portion of these receptors (MARCO, SR-A1 and SR-B1), are known to facilitate the internalization of a large variety of nanoparticle types in macrophages, without apparent specificity.[72,123–126] However, stabilin receptors expressed on KCs and LSECs are found to take up a large variety of anionic nanoparticles, in which the preference for *stab1* or *stab2* is dependent on nanoparticle size.[127,128] For lipid-based nanomedicine specifically, various lipoprotein receptors (LDLr and LRP1) are known to facilitate uptake (**Figure 7a**).[72,73,129] In these cases, the presence of apolipoprotein E (apoE) in the nanoparticle protein corona is required for efficient uptake. Identification and understanding of the behaviour of SRs in nanoparticle clearance and uptake is important for the safe and efficient development of nanomedicine.[130] This knowledge can provide new strategies for avoiding or inhibiting rapid clearance by undesired cell types, or by the targeting of specific cell types through these receptors.[131,132]

In all cases, nanoparticles are trapped within membrane vesicles (endosomes, phagosomes, pinosomes) that mature into lysosomes and where the particles are exposed to a variety of degradation proteins (*e.g.*, nucleases, proteases) that aim to process the internalized components (**Figure 7b**). In addition to lysosomal degradation, transcytosis and endocytic

recycling have also been found to limit the intracellular delivery of the nanomedicine cargo (**Figure 7c,d**).[55,133]

The crucial step for delivery of the nanomedicine cargo is the escape from these vesicular bodies before degradation or exocytosis can occur.[134] Therefore, research has focused on generating nanoparticle variants that can promote endosomal escape, for example through the introduction of membrane destabilization or fusogenic properties.[135,136] Nevertheless, efficient endosomal escape remains among one of the most challenging hurdles in nanomedicine delivery. Further understanding of the molecular details of intracellular processes and to what extent nanoparticle properties influence endosomal escape of their cargo can yield new strategies to improve endosomal escape and provide more efficient nanomedicines.

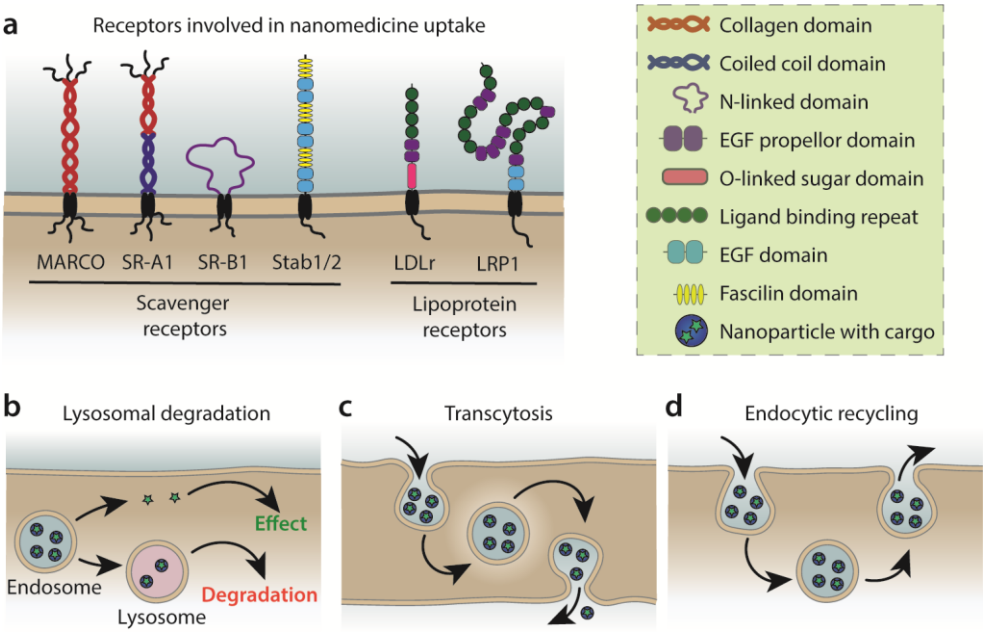


Figure 7. Cellular receptors and mechanisms involved in uptake of lipid-based nanomedicine. (**a**) Common examples of scavenger receptors involved in nanoparticle uptake (**b-d**) Intracellular mechanisms known to limit delivery of NP cargo: lysosomal degradation, transcytosis and endocytic recycling. **Abbreviations:** MARCO = macrophage receptor with collagenous structure, Stab = stabilin receptor, SR = scavenger receptor, LDLr = low-density lipoprotein receptor, LRP1 = Low density lipoprotein-related protein 1, NP = nanoparticle.

1.5.3 Translation from *in vitro* to *in vivo*

Another important parameter are the complicated steps in crossing the *in vitro – in vivo* gap.[86] For example, after the fabrication of nanoparticles, they are typically subject to physiochemical analyses such as size determination, morphology, drug encapsulation, etc. However, the introduction of these nanoparticles into a biological system might change those common parameters. Another layer of complexity is that this type of biological system will significantly determine their effect. For example, nanoparticles are commonly tested in cell culture systems for their toxicity, uptake and efficacy, but typically display different behaviour in *in vivo* systems.[137] For example, due to the presence of scavenger receptors and differences in plasma protein composition.[104] Further translation beyond mice can be limited by genetic differences, non-representative disease models and the changes caused by the use of immunodeficient animals.[138–140]

Therefore, more representative animal models are currently being developed and limitations of animal models are highlighted and accounted for to further the translation of nanomedicines.[141,142] Nevertheless, animal models can be expensive, laborious and require certain expertise and ethics approval, and are not readily available for all researchers. Therefore, simpler and alternative biological systems are investigated for the proper translation of nanomedicine strategies. Whereas cell culture is suitable for the study of intracellular processes such as endosomal escape, they do not provide complex multi- and intercellular processes. Consequently, the use of organoids or other 3D cell culture systems can prove to be useful.[143] Furthermore, the use of embryonic zebrafish embryos has been shown useful for the investigation of nanoparticles *in vivo* as a preclinical model.[127,144–146] These embryos have a relatively low cost of maintenance, small size (0.7 mm – 4 mm), rapid development and an external fertilization that allows for genetic manipulations. Furthermore, their optical transparency enables fluorescent imaging of nanoparticles biodistributions *in vivo* in real-time.[147] These advantages are beneficial for the mechanistic evaluation of nanoparticle behaviour *in vivo* at a molecular level. Drawbacks for translation to murine and human models are its non-mammalian nature, development specific processes, lack of adaptive immunity and not fully developed organs. Nevertheless, zebrafish embryos have proven as good predictors of nanoparticle interactions with the RES cells and their receptors (*e.g.* stabilins) in the translation to mammalian models.[127,145] The implementation and combination of different (animal) models for assessing nanoparticle behaviour can help with the productive translation of new nanomedicines in the coming decades.

1.6 Aim and outline

This thesis focuses on the investigation of and exploitation of fundamental knowledge of lipid-based nanomedicine at the interface with biological systems. An ensemble of chemical, biophysical and biological tools are employed to study the effects of nanoparticle structure, protein corona, nanoparticle-receptor interactions and the intracellular processing of lipid-based nanoparticles.

Chapter 2 describes an alternative method for the protein corona determination of liposomes. Here, photoaffinity based chemoproteomics is used to remove the bias of current methods towards large and abundant proteins and allows for the validation of protein binding in simple mixtures of proteins. In turn, it reveals a more rational protein corona profile for liposomes, dominated by apolipoproteins and less complex than previously thought.

Chapter 3 describes the exploitation of the fundamental understanding of nanoparticle-receptor interactions in order to design LNPs that can preferentially deliver mRNA to the reticuloendothelial system through a stabilin receptor mediated interaction. Here, embryonic zebrafish are used to evaluate and validate the designed LNPs before translation validation in mice.

Chapter 4 describes an in-depth molecular view of key protein-nanoparticle interactions. Here, protein adsorption to anionic and zwitterionic lipid-based nanoparticles is studied using the photoaffinity based method described in Chapter 2. This work expands the method towards the use for lipid nanoparticles encapsulating RNA, as well as underlines the apolipoprotein-dominated but yet simple protein corona profiles generated on a collection of liposomal formulations. Specifically, it is shown that apolipoprotein E binds anionic liposomes through its surface exposed heparin binding site. In contrast, the binding to zwitterionic liposomes and lipid nanoparticles is either absent or occurs through in a non-heparin competitive manner.

Chapter 5 describes the programmable induction of paracrystalline inverse hexagonal lipid phases encapsulating siRNA in the core of lipid nanoparticles. Using a combination of cryogenic electron microscopy, tomography and small-angle X-ray scattering, these structures are characterized and the effects of temperature, RNA content and lipid composition are studied. Furthermore, it is shown that the presence of these paracrystalline phases enhances the intracellular silencing efficiency through a preferred one-step deliver mechanism.

Chapter 6 summarizes the key findings of this thesis and poses important further avenues for the understanding of nanomedicine at the bio-nano interface, such as the (un)importance of the protein corona and the general flow of fundamental nanomedicine research.

1.7 References

1. Schwartz, R. S. Paul Ehrlich's Magic Bullets. *N. Engl. J. Med.* **350**, 1079–1080 (2004).
2. Blair, J. Making magic bullets. *Nat. Microbiol.* **2**, 17110 (2017).
3. Strebhardt, K. & Ullrich, A. Paul Ehrlich's magic bullet concept: 100 years of progress. *Nat. Rev. Cancer* **8**, 473–480 (2008).
4. Pelaz, B. *et al.* Diverse Applications of Nanomedicine. *ACS Nano* **11**, 2313–2381 (2017).
5. Shi, J., Votruba, A. R., Farokhzad, O. C. & Langer, R. Nanotechnology in Drug Delivery and Tissue Engineering: From Discovery to Applications. *Nano Lett.* **10**, 3223–3230 (2010).
6. Chariou, P. L., Ortega-Rivera, O. A. & Steinmetz, N. F. Nanocarriers for the Delivery of Medical, Veterinary, and Agricultural Active Ingredients. *ACS Nano* **14**, 2678–2701 (2020).
7. Soares, S., Sousa, J., Pais, A. & Vitorino, C. Nanomedicine: Principles, Properties, and Regulatory Issues. *Front. Chem.* **6**, 360 (2018).
8. Sailor, M. J. & Park, J.-H. Hybrid nanoparticles for detection and treatment of cancer. *Adv. Mater.* **24**, 3779–3802 (2012).
9. Yoo, J.-W., Irvine, D. J., Discher, D. E. & Mitragotri, S. Bio-inspired, bioengineered and biomimetic drug delivery carriers. *Nat. Rev. Drug Discov.* **10**, 521–535 (2011).
10. Giner-Casares, J. J., Henriksen-Lacey, M., Coronado-Puchau, M. & Liz-Marzán, L. M. Inorganic nanoparticles for biomedicine: where materials scientists meet medical research. *Mater. Today* **19**, 19–28 (2016).
11. Jang, H. L., Zhang, Y. S. & Khademhosseini, A. Boosting clinical translation of nanomedicine. *Nanomedicine* **11**, 1495–1497 (2016).
12. Bangham, A. D. & Horne, R. W. Negative staining of phospholipids and their structural modification by surface-active agents as observed in the electron microscope. *J. Mol. Biol.* **8**, 660-IN10 (1964).
13. Bangham, A. D., Standish, M. M. & Watkins, J. C. Diffusion of univalent ions across the lamellae of swollen phospholipids. *J. Mol. Biol.* **13**, 238-IN27 (1965).
14. Bangham, A.D.; Hill, M.W.; Miller, N. G. Preparation and use of liposomes as models of biological membranes. in *Methods in Membrane Biology* 1–68 (1974). doi:10.1007/978-1-4615-7422-4
15. Gregoriadis, G. & Ryman, B. E. Fate of protein-containing liposomes injected into rats. An approach to the treatment of storage diseases. *Eur. J. Biochem.* **24**, 485–491 (1972).
16. Gregoriadis, G., Leathwood, P. D. & Ryman, B. E. Enzyme entrapment in liposomes. *FEBS Lett.* **14**, 95–99 (1971).
17. Gregoriadis, G. & Ryman, B. E. Lysosomal localization of enzyme-containing liposomes injected into rats. *Biochem. J.* **128**, 142P-143P (1972).
18. Sud, M. *et al.* LMSD: LIPID MAPS structure database. *Nucleic Acids Res.* **35**, D527-32 (2007).
19. Fahy, E. *et al.* Update of the LIPID MAPS comprehensive classification system for lipids. *J. Lipid Res.* 9–14 (2009).
20. Rajabi, M. & Mousa, S. A. Lipid Nanoparticles and their Application in Nanomedicine. *Curr. Pharm. Biotechnol.* **17**, 662–672 (2016).

21. Shah, R., Eldridge, D., Palombo, E., Harding, I. *Lipid Nanoparticles: Production, Characterization and Stability*. (Springer International Publishing, 2015). doi:10.1007/978-3-319-10711-0
22. Patil, Y. P. & Jadhav, S. Novel methods for liposome preparation. *Chem. Phys. Lipids* **177**, 8–18 (2014).
23. Samaridou, E., Heyes, J. & Lutwyche, P. Lipid nanoparticles for nucleic acid delivery: Current perspectives. *Adv. Drug Deliv. Rev.* **154–155**, 37–63 (2020).
24. Akinc, A. *et al.* The Onpattro story and the clinical translation of nanomedicines containing nucleic acid-based drugs. *Nat. Nanotechnol.* **14**, 1084–1087 (2019).
25. Zhang, N.-N. *et al.* A Thermostable mRNA Vaccine against COVID-19. *Cell* **182**, 1271–1283 (2020).
26. Jackson, L. A. *et al.* An mRNA Vaccine against SARS-CoV-2 — Preliminary Report. *N. Engl. J. Med.* **383**, 1920–1931 (2020).
27. Lu, J. *et al.* A COVID-19 mRNA vaccine encoding SARS-CoV-2 virus-like particles induces a strong antiviral-like immune response in mice. *Cell Res.* **30**, 936–939 (2020).
28. McKay, P. F. *et al.* Self-amplifying RNA SARS-CoV-2 lipid nanoparticle vaccine candidate induces high neutralizing antibody titers in mice. *Nat. Commun.* **11**, 3523 (2020).
29. Rietwyk, S. & Peer, D. Next-Generation Lipids in RNA Interference Therapeutics. **11**, 7572–7586 (2017).
30. Tros de Ilarduya, C., Sun, Y. & Düzgüneş, N. Gene delivery by lipoplexes and polyplexes. *Eur. J. Pharm. Sci. Off. J. Eur. Fed. Pharm. Sci.* **40**, 159–170 (2010).
31. Zhang, J.-S., Liu, F. & Huang, L. Implications of pharmacokinetic behavior of lipoplex for its inflammatory toxicity. *Adv. Drug Deliv. Rev.* **57**, 689–698 (2005).
32. Evers, M. J. W. *et al.* State-of-the-Art Design and Rapid-Mixing Production Techniques of Lipid Nanoparticles for Nucleic Acid Delivery. *Small methods* **1700375**, 1–20 (2018).
33. Leung, A. K. K., Tam, Y. Y. C., Chen, S., Hafez, I. M. & Cullis, P. R. Microfluidic Mixing: A General Method for Encapsulating Macromolecules in Lipid Nanoparticle Systems. *J. Phys. Chem. B* **119**, 8698–8706 (2015).
34. Kulkarni, J. A. *et al.* Spontaneous, solvent-free entrapment of siRNA within lipid nanoparticles. *Nanoscale* **12**, 23959–23966 (2020).
35. Kulkarni, J. A. *et al.* On The Formation and Morphology of Lipid Nanoparticles Containing Ionizable Cationic Lipids and siRNA. *ACS Nano* **12**, 4787–4795 (2018).
36. Kulkarni, J. A. *et al.* Fusion-dependent formation of lipid nanoparticles containing macromolecular payloads. *Nanoscale* **11**, 9023–9031 (2019).
37. Leung, A. K. K. *et al.* Lipid nanoparticles containing siRNA synthesized by microfluidic mixing exhibit an electron-dense nanostructured core. *J. Phys. Chem. C* **116**, 18440–18450 (2012).
38. Evers, M. J. W. *et al.* State-of-the-Art Design and Rapid-Mixing Production Techniques of Lipid Nanoparticles for Nucleic Acid Delivery. *Small Methods* **2**, 1700375 (2018).
39. Arteta, M. Y. *et al.* Successful reprogramming of cellular protein production through mRNA delivered by functionalized lipid nanoparticles. *Proc. Natl. Acad. Sci. U. S. A.* **115**, E3351–E3360 (2018).
40. Eygeris, Y., Patel, S., Jozic, A. & Sahay, G. Deconvoluting Lipid Nanoparticle Structure for Messenger RNA Delivery. *Nano Lett.* **20**, 4543–4549 (2020).
41. Patel, S. *et al.* Naturally-occurring cholesterol analogues in lipid nanoparticles induce polymorphic shape and enhance intracellular delivery of mRNA. *Nat. Commun.* **11**, 983 (2020).

42. Brader, M. L. *et al.* Encapsulation state of messenger RNA inside lipid nanoparticles. *Biophys. J.* (2021). doi:https://doi.org/10.1016/j.bpj.2021.03.012
43. Whitehead, K. A. *et al.* Degradable lipid nanoparticles with predictable in vivo siRNA delivery activity. *Nat. Commun.* **5**, 1–10 (2014).
44. Love, K. T. *et al.* Lipopeptide nanoparticles for potent and selective siRNA delivery in rodents and nonhuman primates. *Proc. Natl. Acad. Sci.* **111**, 5753–5753 (2014).
45. Love, K. T. *et al.* Lipid-like materials for low-dose, in vivo gene silencing. *Proc. Natl. Acad. Sci.* **107**, 9915–9915 (2010).
46. Chen, D. *et al.* Rapid Discovery of Potent siRNA-Lipid-Nanoparticles Enabled by Controlled Microfluidic Formulation Rapid Discovery of Potent siRNA-Lipid-Nanoparticles Enabled by Controlled Microfluidic Formulation. **4**, 1–5 (2012).
47. Jayaraman, M. *et al.* Maximizing the potency of siRNA lipid nanoparticles for hepatic gene silencing in vivo. *Angew. Chemie - Int. Ed.* **51**, 8529–8533 (2012).
48. Kulkarni, J. A., Witzigmann, D., Leung, J., Tam, Y. Y. C. & Cullis, P. R. On the role of helper lipids in lipid nanoparticle formulations of siRNA. *Nanoscale* **11**, 21733–21739 (2019).
49. Cheng, X. & Lee, R. J. The role of helper lipids in lipid nanoparticles (LNPs) designed for oligonucleotide delivery. *Advanced Drug Delivery Reviews* **99**, 129–137 (2016).
50. Wittrup, A. *et al.* Visualizing lipid-formulated siRNA release from endosomes and target gene knockdown. *Nat. Biotechnol.* **33**, 870–876 (2015).
51. Hafez, I. M., Maurer, N. & Cullis, P. R. On the mechanism whereby cationic lipids promote intracellular delivery of polynucleic acids. *Gene Ther.* **8**, 1188–1196 (2001).
52. Semple, S. C. *et al.* Rational design of cationic lipids for siRNA delivery. *Nat. Biotechnol.* **28**, 172–176 (2010).
53. Liu, S. *et al.* Membrane-destabilizing ionizable phospholipids for organ-selective mRNA delivery and CRISPR–Cas gene editing. *Nat. Mater.* **20**, 701–710 (2021).
54. Gilleron, J. *et al.* Image-based analysis of lipid nanoparticle–mediated siRNA delivery, intracellular trafficking and endosomal escape. *Nat. Biotechnol.* **31**, 638–646 (2013).
55. Sahay, G. *et al.* Efficiency of siRNA delivery by lipid nanoparticles is limited by endocytic recycling-supp. *Nat. Biotechnol.* **31**, 653–658 (2013).
56. Kirtane, A. R. *et al.* Nanotechnology approaches for global infectious diseases. *Nat. Nanotechnol.* **16**, 369–384 (2021).
57. Ngan, C. L. & Asmawi, A. A. Lipid-based pulmonary delivery system: a review and future considerations of formulation strategies and limitations. *Drug Deliv. Transl. Res.* **8**, 1527–1544 (2018).
58. Kourtis, I. C. *et al.* Peripherally Administered Nanoparticles Target Monocytic Myeloid Cells, Secondary Lymphoid Organs and Tumors in Mice. *PLoS One* **8**, e61646 (2013).
59. Zhang, Y.-N., Poon, W., Tavares, A. J., McGilvray, I. D. & Chan, W. C. W. Nanoparticle–liver interactions: Cellular uptake and hepatobiliary elimination. *J. Control. Release* **240**, 332–348 (2016).
60. Tsoi, K. M. *et al.* Mechanism of hard-nanomaterial clearance by the liver. *Nat. Mater.* **1**, 1–10 (2016).
61. Poon, W. *et al.* Elimination Pathways of Nanoparticles. *ACS Nano* **13**, 5785–5798 (2019).
62. Allen, T. M., Murray, L., MacKeigan, S. & Shah, M. Chronic liposome administration in mice: effects on reticuloendothelial function and tissue distribution. *J. Pharmacol. Exp. Ther.* **229**, 267–275 (1984).
63. Allen, T. M., Williamson, P. & Schlegel, R. A. Phosphatidylserine as a determinant of reticuloendothelial recognition of liposome models of the erythrocyte surface. *Proc. Natl.*

Acad. Sci. **85**, 8067–8071 (1988).
64. Wake, K., Kawai, Y. & Smedsrod, B. Re-evaluation of the reticulo-endothelial system. *Ital. J. Anat. Embryol.* **106**, 261–269 (2001).
65. Sadauskas, E. *et al.* Kupffer cells are central in the removal of nanoparticles from the organism. *Part. Fibre Toxicol.* **4**, 10 (2007).
66. Tavares, A. J. *et al.* Effect of removing Kupffer cells on nanoparticle tumor delivery. *Proc. Natl. Acad. Sci.* **114**, E10871 LP-E10880 (2017).
67. Sørensen, K. K., Simon-Santamaria, J., McCuskey, R. S. & Smedsrød, B. Liver sinusoidal endothelial cells. *Compr. Physiol.* **5**, 1751–1774 (2015).
68. Li, R. *et al.* Role of liver sinusoidal endothelial cells and stabilins in elimination of oxidized low-density lipoproteins. *Am. J. Physiol. Gastrointest. Liver Physiol.* **300**, G71–G81 (2010).
69. Mates, J. M. *et al.* Mouse Liver Sinusoidal Endothelium Eliminates HIV-Like Particles from Blood at a Rate of 100 Million per Minute by a Second-Order Kinetic Process . *Frontiers in Immunology* **8**, 35 (2017).
70. McCourt, P. A. G. *et al.* The liver sinusoidal endothelial cell hyaluronan receptor and its homolog, stabilin-1 - Their roles (known and unknown) in endocytosis. *Comp. Hepatol.* **3**, S24 (2004).
71. Scherphof, G. L. & Kamps, J. A. The role of hepatocytes in the clearance of liposomes from the blood circulation. *Prog. Lipid Res.* **40**, 149–166 (2001).
72. Sakai-Kato, K., Sakurai, M., Takechi-Haraya, Y., Nanjo, K. & Goda, Y. Involvement of scavenger receptor class B type 1 and low-density lipoprotein receptor in the internalization of liposomes into HepG2 cells. *Biochim. Biophys. Acta - Biomembr.* **1859**, 2253–2258 (2017).
73. Akinc, A. *et al.* Targeted delivery of RNAi therapeutics with endogenous and exogenous ligand-based mechanisms. *Mol. Ther.* **18**, 1357–1364 (2010).
74. Sadauskas, E. *et al.* Protracted elimination of gold nanoparticles from mouse liver. *Nanomedicine* **5**, 162–169 (2009).
75. Cataldi, M., Vigliotti, C., Mosca, T., Cammarota, M. & Capone, D. Emerging Role of the Spleen in the Pharmacokinetics of Monoclonal Antibodies, Nanoparticles and Exosomes. *Int. J. Mol. Sci.* **18**, 1249 (2017).
76. Moghimi, S. M., Hunter, A. C. & Andresen, T. L. Factors controlling nanoparticle pharmacokinetics: an integrated analysis and perspective. *Annu. Rev. Pharmacol. Toxicol.* **52**, 481–503 (2012).
77. Dams, E. T. *et al.* Accelerated blood clearance and altered biodistribution of repeated injections of sterically stabilized liposomes. *J. Pharmacol. Exp. Ther.* **292**, 1071–1079 (2000).
78. Ishida, T. *et al.* Accelerated clearance of a second injection of PEGylated liposomes in mice. *Int. J. Pharm.* **255**, 167–174 (2003).
79. Cheng, T.-L., Wu, P.-Y., Wu, M.-F., Chern, J.-W. & Roffler, S. R. Accelerated Clearance of Polyethylene Glycol-Modified Proteins by Anti-Polyethylene Glycol IgM. *Bioconjug. Chem.* **10**, 520–528 (1999).
80. Wang, J. & Liu, G. Imaging Nano–Bio Interactions in the Kidney: Toward a Better Understanding of Nanoparticle Clearance. *Angew. Chemie Int. Ed.* **57**, 3008–3010 (2018).
81. Du, B., Yu, M. & Zheng, J. Transport and interactions of nanoparticles in the kidneys. *Nat. Rev. Mater.* **3**, 358–374 (2018).
82. Fielding, R. M., Moon-Mcdermott, L., Lewis, R. O. & Horner, M. J. Pharmacokinetics and Urinary Excretion of Amikacin in Low-Clearance Unilamellar Liposomes after a Single or Repeated Intravenous Administration in the Rhesus Monkey. *Antimicrob. Agents Chemother.* **43**, 503 LP – 509 (1999).

83. Bekersky, I. *et al.* Pharmacokinetics, excretion, and mass balance of liposomal amphotericin B (AmBisome) and amphotericin B deoxycholate in humans. *Antimicrob. Agents Chemother.* **46**, 828–833 (2002).
84. Faria, M. *et al.* Minimum information reporting in bio–nano experimental literature. *Nat. Nanotechnol.* **13**, 777–785 (2018).
85. Nel, A. E. *et al.* Understanding biophysicochemical interactions at the nano-bio interface. *Nat. Mater.* **8**, 543–557 (2009).
86. Björnmalm, M., Thurecht, K. J., Michael, M., Scott, A. M. & Caruso, F. Bridging Bio–Nano Science and Cancer Nanomedicine. *ACS Nano* **11**, 9594–9613 (2017).
87. Chonn, A., Semple, S. C. & Cullis, P. R. Association of blood proteins with large unilamellar liposomes in vivo. Relation to circulation lifetimes. *J. Biol. Chem.* **267**, 18759–18765 (1992).
88. Oja, C. D., Semple, S. C., Chonn, A. & Cullis, P. R. Influence of dose on liposome clearance: critical role of blood proteins. *Biochim. Biophys. Acta* **1281**, 31–37 (1996).
89. Cullis, Chonn & Semple. Interactions of liposomes and lipid-based carrier systems with blood proteins: Relation to clearance behaviour in vivo. *Adv. Drug Deliv. Rev.* **32**, 3–17 (1998).
90. Cedervall, T. *et al.* Understanding the nanoparticle-protein corona using methods to quantify exchange rates and affinities of proteins for nanoparticles. *Proc. Natl. Acad. Sci.* **104**, 2050–2055 (2007).
91. Walczyk, D., Bombelli, F. B., Monopoli, M. P., Lynch, I. & Dawson, K. A. What the Cell "Sees" in Bionanoscience. *J. Am. Chem. Soc.* **132**, 5761–5768 (2010).
92. Lundqvist, M. *et al.* Nanoparticle size and surface properties determine the protein corona with possible implications for biological impacts. *Proc. Natl. Acad. Sci. U. S. A.* **105**, 14265 (2008).
93. Tenzer, S. *et al.* Nanoparticle size is a critical physicochemical determinant of the human blood plasma corona: A comprehensive quantitative proteomic analysis. *ACS Nano* **5**, 7155–7167 (2011).
94. Wang, M. *et al.* Nanoparticle–proteome *in vitro* and *in vivo*. *J. Mater. Chem. B* **6**, 6026–6041 (2018).
95. Ritz, S. *et al.* Protein Corona of Nanoparticles: Distinct Proteins Regulate the Cellular Uptake. *Biomacromolecules* **16**, 1311–1321 (2015).
96. Hadjidemetriou, M. *et al.* In Vivo Biomolecule Corona around Blood-Circulating, Clinically Used and Antibody-Targeted Lipid Bilayer Nanoscale Vesicles. *ACS Nano* **9**, 8142–8156 (2015).
97. Pederzoli, F. *et al.* Protein corona and nanoparticles: how can we investigate on? *Wiley Interdiscip. Rev. Nanomedicine Nanobiotechnology* **9**, 1–23 (2017).
98. Weber, C., Morsbach, S. & Landfester, K. Possibilities and Limitations of Different Separation Techniques for the Analysis of the Protein Corona. *Angew. Chemie Int. Ed.* **58**, 12787–12794 (2019).
99. Carrillo-Carrion, C., Carril, M. & Parak, W. J. Techniques for the experimental investigation of the protein corona. *Curr. Opin. Biotechnol.* **46**, 106–113 (2017).
100. Simonsen, J. B. & Münter, R. Pay attention to the biological nanoparticles when studying the protein corona on nanomedicines. *Angew. Chemie Int. Ed.* **59**, 12584–12588 (2020).
101. Vilanova, O. *et al.* Understanding the Kinetics of Protein-Nanoparticle Corona Formation. *ACS Nano* **10**, 10842–10850 (2016).
102. Chenthamara, D. *et al.* Therapeutic efficacy of nanoparticles and routes of administration. *Biomater. Res.* **23**, 20 (2019).
103. Huang, X. *et al.* Effect of injection routes on the biodistribution, clearance, and tumor uptake

of carbon dots. *ACS Nano* **7**, 5684–5693 (2013).
104. Salvati, A. *et al.* Transferrin-functionalized nanoparticles lose their targeting capabilities when a biomolecule corona adsorbs on the surface. *Nat. Nanotechnol.* **8**, 137–143 (2013).
105. Mirshafiee, V., Mahmoudi, M., Lou, K., Cheng, J. & Kraft, M. L. Protein corona significantly reduces active targeting yield. *Chem. Commun. (Camb).* **49**, 2557–2559 (2013).
106. Varnamkhasti, B. S. *et al.* Protein corona hampers targeting potential of MUC1 aptamer functionalized SN-38 core-shell nanoparticles. *Int. J. Pharm.* **494**, 430–444 (2015).
107. Shahabi, S. *et al.* Enhancing Cellular Uptake and Doxorubicin Delivery of Mesoporous Silica Nanoparticles via Surface Functionalization: Effects of Serum. *ACS Appl. Mater. Interfaces* **7**, 26880–26891 (2015).
108. Gunawan, C., Lim, M., Marquis, C. P. & Amal, R. Nanoparticle–protein corona complexes govern the biological fates and functions of nanoparticles. *J. Mater. Chem. B* **2**, 2060–2083 (2014).
109. Bertrand, N. *et al.* Mechanistic understanding of in vivo protein corona formation on polymeric nanoparticles and impact on pharmacokinetics. *Nat. Commun.* **8**, (2017).
110. Saha, K. *et al.* Regulation of Macrophage Recognition through the Interplay of Nanoparticle Surface Functionality and Protein Corona. *ACS Nano* **10**, 4421–4430 (2016).
111. Chinen, A. B., Guan, C. M., Ko, C. H. & Mirkin, C. A. The Impact of Protein Corona Formation on the Macrophage Cellular Uptake and Biodistribution of Spherical Nucleic Acids. *Small* **13**, 10.1002/smll.201603847 (2017).
112. Cai, R. *et al.* Corona of Thorns: The Surface Chemistry-Mediated Protein Corona Perturbs the Recognition and Immune Response of Macrophages. *ACS Appl. Mater. Interfaces* **12**, 1997–2008 (2020).
113. Cheng, X. *et al.* Protein Corona Influences Cellular Uptake of Gold Nanoparticles by Phagocytic and Nonphagocytic Cells in a Size-Dependent Manner. *ACS Appl. Mater. Interfaces* **7**, 20568–20575 (2015).
114. Sebastiani, F. *et al.* Apolipoprotein E Binding Drives Structural and Compositional Rearrangement of mRNA-Containing Lipid Nanoparticles. *ACS Nano* **15**, 6709–6722 (2021).
115. Schöttler, S. *et al.* Protein adsorption is required for stealth effect of poly(ethylene glycol)- and poly(phosphoester)-coated nanocarriers. *Nat. Nanotechnol.* **11**, 372–377 (2016).
116. Chen, F. *et al.* Complement proteins bind to nanoparticle protein corona and undergo dynamic exchange in vivo. *Nat. Nanotechnol.* **12**, 387–393 (2017).
117. Canton, J., Neculai, D. & Grinstein, S. Scavenger receptors in homeostasis and immunity. *Nat. Rev. Immunol.* **13**, 621–634 (2013).
118. Smedsrød, B. Clearance function of scavenger endothelial cells. *Comp. Hepatol.* **3**, S22 (2004).
119. Neyen, C. *et al.* Macrophage Scavenger Receptor A Mediates Adhesion to Apolipoproteins A-I and E. *Biochemistry* **48**, 11858–11871 (2009).
120. Kzhyshkowska, J., Neyen, C. & Gordon, S. Role of macrophage scavenger receptors in atherosclerosis. *Immunobiology* **217**, 492–502 (2012).
121. Zani, I. A. *et al.* Scavenger receptor structure and function in health and disease. *Cells* **4**, 178–201 (2015).
122. PrabhuDas, M. R. *et al.* A Consensus Definitive Classification of Scavenger Receptors and Their Roles in Health and Disease. *J. Immunol.* **198**, 3775–3789 (2017).
123. Nakayama, M. Macrophage Recognition of Crystals and Nanoparticles. *Front. Immunol.* **9**, 103 (2018).
124. Plebanek, M. P. *et al.* Nanoparticle Targeting and Cholesterol Flux Through Scavenger Receptor Type B-1 Inhibits Cellular Exosome Uptake. *Sci. Rep.* **5**, 15724 (2015).

125. França, A. *et al.* Macrophage scavenger receptor A mediates the uptake of gold colloids by macrophages in vitro. *Nanomedicine* **6**, 1175–1188 (2011).
126. Petersen, L. K. *et al.* Amphiphilic nanoparticles repress macrophage atherogenesis: novel core/shell designs for scavenger receptor targeting and down-regulation. *Mol. Pharm.* **11**, 2815–2824 (2014).
127. Campbell, F. *et al.* Directing Nanoparticle Biodistribution through Evasion and Exploitation of Stab2-Dependent Nanoparticle Uptake. *ACS Nano* **12**, 2138–2150 (2018).
128. Arias-Alpizar, G. *et al.* Stabilin-1 is required for the endothelial clearance of small anionic nanoparticles. *Nanomedicine Nanotechnology, Biol. Med.* **34**, 102395 (2021).
129. Beisiegel, U., Weber, W., Ihrke, G., Herz, J. & Stanley, K. K. The LDL-receptor-related protein, LRP, is an apolipoprotein E-binding protein. *Nature* **341**, 162–164 (1989).
130. Shannahan, J. H., Bai, W. & Brown, J. M. Implications of scavenger receptors in the safe development of nanotherapeutics. *Recept. Clin. Investig.* **2**, e811 (2015).
131. Lokhande, A. S., Jahagirdar, P., Dandekar, P. & Devarajan, P. V. Scavenger Receptor and Targeting Strategies BT - Targeted Intracellular Drug Delivery by Receptor Mediated Endocytosis. in (eds. Devarajan, P. V, Dandekar, P. & D'Souza, A. A.) 297–321 (Springer International Publishing, 2019). doi:10.1007/978-3-030-29168-6_10
132. Yin, B., Li, K. H. K., Ho, L. W. C., Chan, C. K. W. & Choi, C. H. J. Toward Understanding *in Vivo* Sequestration of Nanoparticles at the Molecular Level. *ACS Nano* acsnano.8b00141 (2018). doi:10.1021/acsnano.8b00141
133. Sindhwani, S. *et al.* The entry of nanoparticles into solid tumours. *Nat. Mater.* (2020). doi:10.1038/s41563-019-0566-2
134. Patel, S. *et al.* Brief update on endocytosis of nanomedicines. *Adv. Drug Deliv. Rev.* **144**, 90–111 (2019).
135. Degors, I. M. S., Wang, C., Rehman, Z. U. & Zuhorn, I. S. Carriers Break Barriers in Drug Delivery: Endocytosis and Endosomal Escape of Gene Delivery Vectors. *Acc. Chem. Res.* **52**, acs.accounts.9b00177 (2019).
136. Patel, S. *et al.* Boosting Intracellular Delivery of Lipid Nanoparticle-Encapsulated mRNA. *Nano Lett.* **17**, 5711–5718 (2017).
137. Dawidczyk, C. M., Russell, L. M. & Searson, P. C. Nanomedicines for cancer therapy: state-of-the-art and limitations to pre-clinical studies that hinder future developments. *Front. Chem.* **2**, 69 (2014).
138. de Jong, M. & Maina, T. Of mice and humans: are they the same?--Implications in cancer translational research. *J. Nucl. Med.* **51**, 501–504 (2010).
139. Nichols, J. W. & Bae, Y. H. Odyssey of a cancer nanoparticle: from injection site to site of action. *Nano Today* **7**, 606–618 (2012).
140. Francia, G., Cruz-Munoz, W., Man, S., Xu, P. & Kerbel, R. S. Mouse models of advanced spontaneous metastasis for experimental therapeutics. *Nat. Rev. Cancer* **11**, 135–141 (2011).
141. Korangath, P. *et al.* Nanoparticle interactions with immune cells dominate tumor retention and induce T cell–mediated tumor suppression in models of breast cancer. *Sci. Adv.* **6**, eaay1601 (2020).
142. Liu, L. Y. *et al.* Nanoparticle Uptake in a Spontaneous and Immunocompetent Woodchuck Liver Cancer Model. *ACS Nano* **14**, 4698–4715 (2020).
143. Hua, S., de Matos, M. B. C., Metselaar, J. M. & Storm, G. Current Trends and Challenges in the Clinical Translation of Nanoparticulate Nanomedicines: Pathways for Translational Development and Commercialization. *Front. Pharmacol.* **9**, 790 (2018).
144. Sieber, S. *et al.* Zebrafish as a preclinical in vivo screening model for nanomedicines. *Adv.*

Drug Deliv. Rev. **151–152**, 152–168 (2019).
145. Hayashi, Y. *et al.* Differential Nanoparticle Sequestration by Macrophages and Scavenger Endothelial Cells Visualized in Vivo in Real-Time and at Ultrastructural Resolution. *ACS Nano* **14**, 1665–1681 (2020).
146. Haque, E. & Ward, A. C. Zebrafish as a Model to Evaluate Nanoparticle Toxicity. *Nanomater. (Basel, Switzerland)* **8**, 561 (2018).
147. Arias-Alpizar, G. *et al.* Light-triggered switching of liposome surface charge directs delivery of membrane impermeable payloads in vivo. *Nat. Commun.* **11**, 3638 (2020).

Chapter 2

Unbiased Identification of the Liposome Protein Corona Using Photoaffinity Based Chemoproteomics

Protein adsorption to the surface of a nanoparticle can fundamentally alter the character, behavior and fate of a nanoparticle in vivo. Current methods to capture the protein corona rely on physical separation techniques and are unable to resolve key, individual protein-nanoparticle interactions. As a result, the precise link between the "synthetic" and the "biological" identity of a nanoparticle remains unclear. Herein, we report an unbiased photoaffinity-based approach to capture, characterise and quantify the protein corona of liposomes in their native state. Compared to conventional methods, our photoaffinity approach reveals markedly different interacting proteins as well as reduced total protein binding to liposome surfaces. Identified proteins do not follow protein abundancy patterns of human serum, as has been generally reported, but are instead dominated by soluble apolipoproteins – endogenous serum proteins that have evolved to recognise the lipidic surface of circulating lipoproteins. We believe our findings are the most accurate characterization of a liposome's "biological" identity to date but, more fundamentally, reveal liposome-protein binding is, in many cases, significantly less complex than previously thought.

This chapter was published as a research article: R. Pattipeiluhu, S. Crielaard, I. Klein-Schiphorst, B. I. Florea, A. Kros, F. Campbell, ACS Cent. Sci. 2020, **6**, 535.

2.1 Introduction

The protein corona of a nanoparticle describes a subset of proteins that preferentially adsorb to the surface of a nanoparticle upon administration in vivo. Formation of the protein corona creates the "biological identity" of a nanoparticle.[1–3] To some extent, it is the protein corona, not the underlying synthetic surface of a nanoparticle, which the body "sees" and interacts with (**Figure 1a**). The adsorbed protein corona can, therefore, significantly influence the in vivo fate of a nanoparticle,[4,5] for instance, by promoting bodily clearance and/or shielding active targeting ligands displayed from a nanoparticle surface.[6–8] The composition and extent of the protein corona is dependent on the "synthetic identity" of a nanoparticle (e.g. size, surface charge, chemical composition),[9–11] the biological media to which the nanoparticle is exposed,[12,13] and the kinetics of protein binding,[14–17] however, the general formation of a protein corona is believed omnipresent for all types of nanoparticles.[4,18]

The most common method to isolate and identify the protein corona of a nanoparticle involves sedimentation of nanoparticle-protein complexes following incubation in biological fluids, such as (human) serum or blood (**Figure 1b**).[19] Depending on the density of a nanoparticle, this requires centrifugation speeds high enough (typically > 14.000 g) to ensure enough pelleted material for subsequent characterisation. However, subjecting nanoparticle-protein complexes to significant centrifugal force runs the risk of disrupting native and weak protein-nanoparticle interactions, and can induce protein aggregation and/or sedimentation of large, unbound proteins.[20] This, in turn, leads to the capture and inclusion of false positive proteins and a biased profile of protein binding to a nanoparticle surface, often mirroring serum protein abundancy.[21,22] As such, while reported protein corona datasets have highlighted important general differences in serum protein binding based on, for example, nanoparticle size or surface charge,[23] it is not yet possible to identify key individual nanoparticle-protein interactions from the long, empirical lists of proteins typically reported. Characterising the protein corona of liposomes and other lipid nanoparticles is especially problematic, given the low density of these lipidic particles requires higher centrifugal forces than dense (*e.g.* inorganic) nanoparticles. In studies involving lipid nanoparticles, the identified protein corona is typically dominated by highly abundant serum albumin and high molecular weight proteins (*e.g.* complement C3 and α-2-macroglobulin).[10,12,15,24,25]

Herein, an unbiased photoaffinity labelling method to capture the protein corona of liposomes, in their native state, is described (**Figure 1c**). Photoaffinity labeling has been successfully applied in chemoproteomic strategies to study lipid metabolism,[26] identify

inhibitor off-targets and discover new small molecule therapeutics.[27,28] Here, it is introduced to the field of nanotechnology and nanomedicine for the first time. Of the myriad nanoparticle-based drug delivery systems reported, liposomes are the most widely investigated and approved for clinical use.[29,30] In this study, we apply our photoaffinity method to three clinically relevant liposome formulations – AmBisome (anionic), EndoTAG-1 (cationic) and Myocet (neutral) – to assess the influence of liposome surface charge on protein binding. We have recently described, in mechanistic detail, the biodistribution and bodily clearance of these same three liposome formulations *in vivo* (embryonic zebrafish).[31] Following photoaffinity capture and purification of the protein corona, label-free quantitative mass spectrometry revealed distinct and highly reproducible protein corona fingerprints for all three liposome formulations. In contrast to centrifugation protocols, our photoaffinity method identified only a small subset of bound serum proteins, devoid of abundant serum albumin and dominated by apolipoproteins. The dominance of apolipoproteins, adsorbed to the surface of liposomes, over more abundant serum has not before been reported.[15,32,33]

2.2 Results

Probes for photoaffinity labelling (PAL) require two key features:[27] (1) photoactivatable chemical functionality that, upon *in situ* sample irradiation, can covalently cross-link to any molecule/protein in close proximity, and (2) a bioorthogonal handle for conjugation of a reporter molecule or selective pull-down of the probe-protein complex from the biological environment. Both functionalities should be small to avoid significant disruption of the native liposomal system and the potential capture of proteins that would not otherwise bind to the liposome surface. Accordingly, a PAL probe, IKS02, structurally similar to endogenous phosphatidylcholine (PC) phospholipids, was designed and synthesised *via* robust phosphoramidite synthetic protocols (**Figure 1d and Figure S1**). PC lipids are present in virtually all clinically approved liposomal formulations.[34] Within the PAL probe design, the zwitterionic PC lipid headgroup was maintained so as not to alter the surface charge or surface charge density of liposomes containing IKS02.

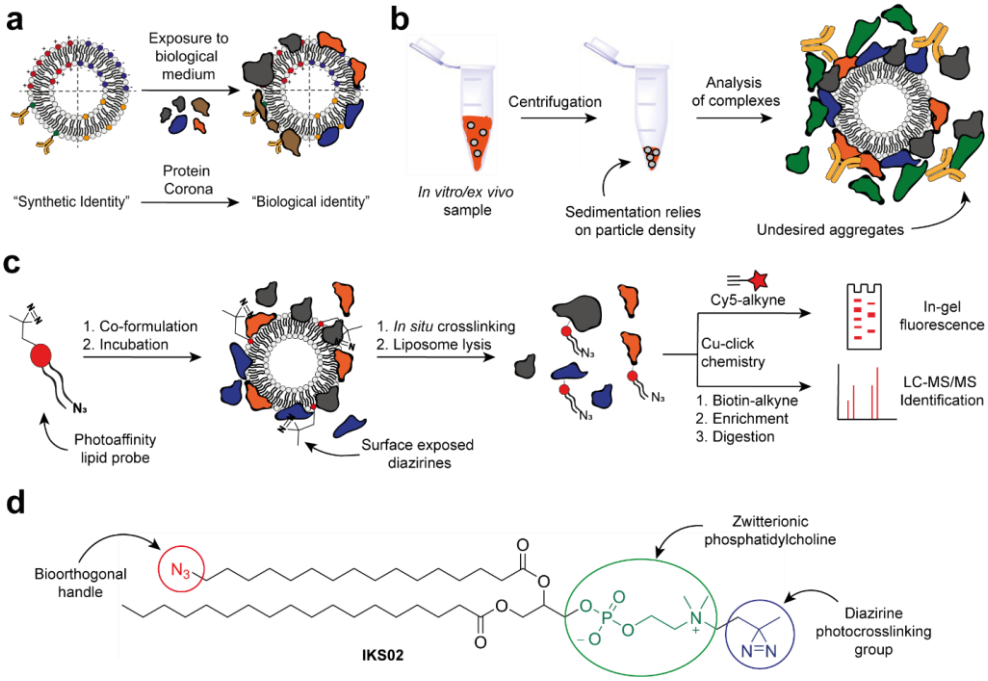


Figure 1. Protein corona identification using photoaffinity based chemoproteomics. (**a**) Liposomes exposed to biological medium are confronted by a wide variety of endogenous proteins, a subset of which preferentially bind to the synthetic surface of the liposome to create the "biological identity" of the liposome. (**b**) Centrifugation protocols to isolate nanoparticle protein complexes rely on efficient sedimentation and can disrupt weak protein-nanoparticle interactions, induce protein aggregation and/or lead to the capture of large, unbound proteins. (**c**) Schematic representation of a photoaffinity labelling (PAL) approach for the capture and identification of a liposome protein corona. (**d**) Bifunctional PAL probe, IKS02, structurally similar to common phosphatidylcholine (PC) phospholipids.

Likewise, the incorporation of long chain fatty acids (> C12) not only mirrors chain lengths typical of most reported (clinical and experimental) liposome formulations but, given the extreme water insolubility of long chain PC lipids, largely excludes any possibility of incorporated IKS02 dissociating from a liposome membrane under physiological conditions.[35] Diazirine functionality was chosen as photoactivatable group given its small size and high photo-efficiency.[36] Irradiation of diazirines with UV-A (~350 nm) light generates a highly reactive carbene intermediate that can spontaneously react with all residues, as well as the backbone, of a surface bound protein. We chose to install diazirine functionality at the phosphatidylcholine headgroup of the lipid probe to maximise the capture of proteins directly interacting with the liposome surface. As bioorthogonal

ligation handle, azide functionality was incorporated at the terminus of one fatty acid chain of the PAL probe. In this position, it is most likely buried within the liposome lipid bilayer, minimising potential unwanted interactions with surface bound proteins. Following photo-crosslinking and liposome solubilisation, azide functionality was used to selectively couple the protein-lipid conjugate to either a fluorescent alkyne-Cy5 probe or an alkyne-biotin label. The latter could be used to selectively pull down and isolate the protein-lipid conjugate from the biological media. In both cases, conjugation reactions were performed using standard bioorthogonal click chemistry protocols.[28,37]

Three liposome formulations, either approved for clinical use or under development (Myocet, AmBisome and EndoTAG-1) were selected to test our photoaffinity method, as well as investigate qualitative and quantitative differences in the adsorbed protein corona as a function of liposome surface charge. Myocet (*lipid composition*: POPC:cholesterol – 55:45, *reported size* (*clinical*): 150-200 nm) is a zwitterionic, neutral liposomal-doxorubicin formulation used in breast cancer therapy.[38] AmBisome (*lipid composition*: DSPC:DSPG:cholesterol – 53:21:26; *size*: 78 nm) is a negatively charged liposomal-amphotericin B formulation used to treat fungal infections.[39] EndoTAG-1 (*lipid composition*: DOTAP:DOPC – 51.5:48.5; *size*: 200 nm) is a positively charged liposomal-paclitaxel formulation that targets the tumor vasculature.[40] Liposomes, formulated without encapsulated drugs and based on the lipid composition of these three formulations, were prepared by thin-film hydration and extrusion. For the photoaffinity method, IKS02 was incorporated within liposome formulations at 5 mol% (approx. 1 probe per 10 nm^2 liposome surface). Dynamic light scattering and zeta potential measurements revealed all liposomes were ~100 nm in diameter (PDI < 0.1) and surface charges were not significantly affected by incorporation of IKS02 (**Table S1**).

Next, gel electrophoresis (SDS-PAGE) was used to resolve the protein corona fingerprint of all three liposome formulations obtained either *via* our photoaffinity method or *via* a conventional centrifugation protocol (**Figure 2**).[10,12,15,24,25,32] In all cases, liposomes were incubated in human serum at 37°C for one hour prior to the capture/isolation of the liposome-protein complex. For the centrifugation protocol, liposome-protein complexes were sedimented (15 min, 17.500 g) and carefully washed to remove unbound proteins present in the supernatant. Pelleted liposome-protein complexes were dissolved in denaturing buffer, resolved by SDS-PAGE (10 µg/well) and visualised by Coomassie Blue staining (**Figure 2a,d**). As negative control, human serum, diluted with buffer containing no liposomes, was subjected to the same centrifugation protocol (**Figure 2c**). From the obtained gels, only cationic EndoTAG-1 liposomes displayed a distinct and unique protein binding profile. In contrast, AmBisome (negative) and Myocet (neutral) liposomes showed

very similar protein fingerprints to the serum only control, with the clearest visible band, at ~70 kDa, corresponding to serum albumin. These results highlight two inseparable and competing flaws of using centrifugation to isolate liposome-protein complexes from serum protein mixtures. On the one hand, efficient sedimentation of nanoparticle-protein complexes relies on a threshold particle density, either of the nanoparticle or the formed nanoparticle-protein complex. In this case, using fluorescently labelled liposomes (DOPE-LR, 1 mol%), a clearly significant fraction of liposomes remained in suspension following centrifugation (15 min, 17.500 g) and was, therefore, excluded from subsequent characterisation (**Figure S2a,b**). Furthermore, in all cases, the measured size of the pelleted liposomes was significantly larger than the original formulation (**Figure S2c-e**). Whether, or not, aggregation adversely affects protein corona formation is, however, unclear given the significant background of large, unbound serum proteins in the pelleted fraction. Alternatively, by increasing centrifugal speeds to achieve greater nanoparticle-protein complex sedimentation, the risk of sedimenting (large), non-adsorbed serum proteins is also increased. This is exemplified by the significant amount of resolved proteins present in the SDS-PAGE of the serum only control (**Figure 2d, far right lane**).

For the photoaffinity method, liposomes containing IKS02 were incubated in serum and subsequently irradiated (15 min, 350 nm, 15 $mWcm^{-2}$) *in situ*. After covalent capture of the protein corona, liposomes were solubilized with detergent (Triton X-100). The crosslinked lipid-protein complexes were then conjugated to a fluorescent, alkyne-Cy5 probe and the fluorescent lipid-protein complex resolved by SDS-PAGE. In-gel fluorescence was used to reveal the subset of proteins that successfully crosslinked to the lipid probe (**Figure 2b,e**). As negative control ("-UV"), liposomes containing IKS02 were not irradiated but otherwise processed identically. In this case, the resolved protein corona fingerprints showed distinct and unique protein profiles, both between formulations as well as compared to the resolved protein corona of the same liposomes isolated *via* centrifugation. In the case of cationic EndoTAG-1 liposomes, multiple unique protein bands, notably at ~10, 28, 40, 45 and 150 kDa, were detected in the "+UV" sample exclusively. In addition, proteins, notably at ~28 and 80 kDa, appear significantly enriched over the "–UV" background. Similarly, unique protein bands, notably at ~20, 28 and 35 kDa, were present for the "+UV" AmBisome formulation. In the case of Myocet, no unique protein labelling over "-UV" background was observed, indicating a possible lack of significant protein binding. Interestingly, the band intensity for serum albumin, at ~70 kDa, for both AmBisome and Myocet formulations, was similar for both the "+UV" sample and "-UV" control, indicating albumin may not constitute a significant proportion of the protein corona of either of these liposome formulations. Background proteins resolved in all three "-UV" control samples

broadly followed protein abundancy patterns of human serum. This suggests background labelling is due to non-selective protein binding and can be attributed to relatively low amounts of crosslinked lipid-protein complexes compared to the total amount of protein in the sample. In addition, background labelling appeared selective for the presence of the copper click catalyst (**Figure S3**). This labelling was minimized by reducing the copper sulfate concentration and increasing chelating agent concentration, as described previously.[41,42] Although complete elimination of background labelling was not achieved, the resolved protein corona of the three liposome formulations isolated *via* our photoaffinity approach clearly show significant differences in both distribution and abundancy of proteins compared to both the negative ("-UV") control, and compared to the resolved protein corona of the same liposome formulations isolated *via* centrifugation.

To characterise the specific composition of the protein coronas visualized by gel electrophoresis, we performed label free, quantitative mass spectrometry on the photoaffinity captured protein corona of EndoTAG-1, AmBisome and Myocet liposomes. Over the past decade, label free quantification (LFQ) has emerged as a straightforward and accurate method to quantify relative protein amounts within complex proteomic samples that do not allow for metabolic labeling, such as human blood or serum.[43] Recently, this method has been used to determine the abundance of proteins within the protein corona of nanoparticles isolated *via* centrifugation.[44] For each liposome formulation, six separate samples were incubated in serum and subsequently irradiated (+UV). Alongside, six control samples were incubated in serum but not irradiated (-UV). The liposomes were solubilized and the captured lipid-protein complexes conjugated to alkyne-functionalized biotin, followed by streptavidin-agarose bead enrichment and on-bead digestion (**Figure 3a**). In all cases, enolase digest (50 fmol) was added to the enriched samples as an internal standard. The samples were resolved using nanoUPLC-MS/MS and peptide fragments were identified and quantified based on the LFQ TOP3-approach using the ISOQuant software.[45,46]

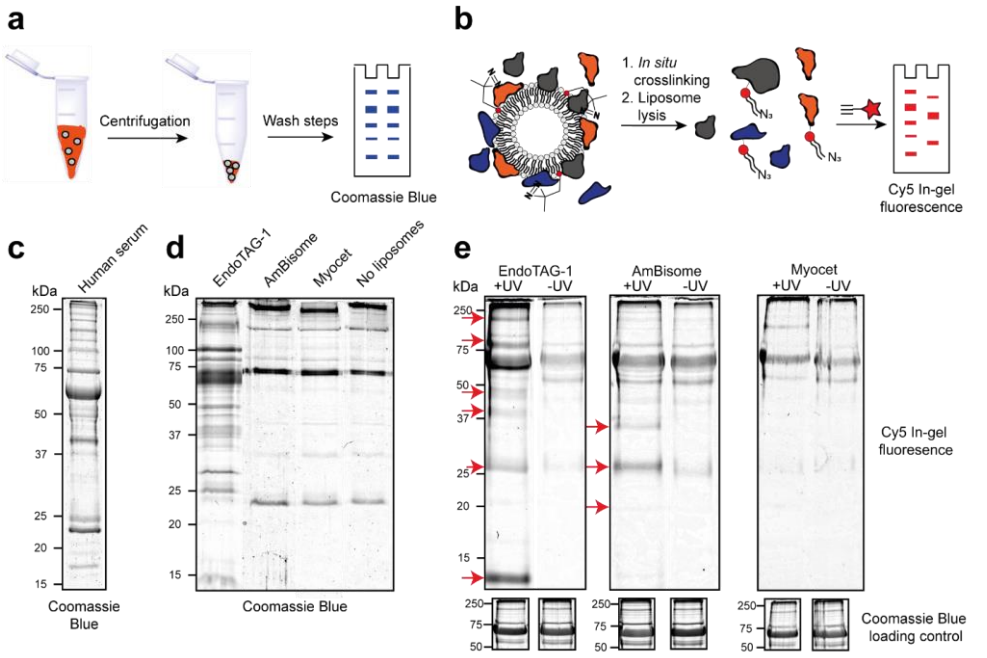


Figure 2. Liposome protein corona fingerprints resolved by gel electrophoresis. (**a**) Schematic representation of the centrifugation protocol. (**b**) Schematic representation of the photoaffinity protocol. (**c**) Gel electrophoresis (SDS-PAGE) of human serum, stained with Coomassie Blue (**d**) SDS-PAGE of the liposome protein coronas, as well as captured proteins of a liposome free control sample, isolated by centrifugation and stained with Coomassie Blue. (**e**) SDS-PAGE of the liposome protein coronas, isolated by photoaffinity method, visualising Cy5 labelled lipid-protein conjugates by in-gel fluorescence. Unique bands highlighted with red arrows. Below: Coomassie Blue loading controls displayed as cropped images. Complete gels displaying all controls and complete Coomassie Blue stained gels displayed in Figure S3.

To gain a high accuracy for the label-free quantification, strict processing parameters were selected. These included a total of six replicates, a minimum peptide score of 6.0, as well as a minimum of three unique identified peptides per protein (**Table S2**). In addition and to ensure that identified proteins were consistently bound to the liposome surface, only proteins that were present in six out of six (+UV) samples were considered for further analysis. All selection criteria can, of course, be modified retrospectively to meet any desired output (see Supplementary files for fully editable raw and processed proteomic datasets). To correct for the background labelling observed in the gel electrophoresis experiments, volcano plots were constructed to identify enriched and statistically significant proteins of the protein corona (**Figure 3b-d**). To ensure statistical significance,

a ratio comparing the average relative protein quantities (expressed in ppm) of +UV versus -UV samples was plotted against its p-value, determined by a t-test followed by a Benjamini-Hochberg correction. Proteins that were significantly enriched (2-fold and $p < 0.05$) over the background were selected as a true part of the protein corona. Proteins completely absent in the background were listed as 'exclusive for +UV', and added to the selection. Finally, selected proteins were ranked based on abundance (**Figures 3b-d, S4**).

In addition, LFQ allows for the absolute quantification of a proteomic sample, in which the amount of the protein is calculated (in fmol) as compared to an internal standard (50 fmol enolase digest). In this case, the sum of the absolute amounts of individual proteins, background corrected and meeting the strict selection criteria, was significantly higher for cationic EndoTAG-1 liposomes than anionic AmBisome or neutral Myocet liposomes (**Figure 3e**). Indeed, the amount of protein adsorbed to the surface of Myocet liposomes was vanishingly small. These results broadly mirror total protein abundancies observed in gel electrophoresis experiments and confirm serum protein adsorption is most prolific on cationic liposome surfaces. In contrast, precise quantitative analysis is not possible for protein coronas isolated *via* centrifugation methods due to the variability in sedimentation efficiency between different liposome formulations.

To verify the accuracy of our photoaffinity approach, we next performed a competition assay in which AmBisome liposomes, containing IKS02, were incubated in pre-defined mixtures of purified serum proteins together with increasing concentrations of unlabeled AmBisome liposomes (**Figure 4a**). As defined protein mixture, apolipoprotein E (APOE, 2 μgmL^{-1}), apolipoprotein A-I (APOA1, 2 μgmL^{-1}) – both of which apparently bound to the surface of AmBisome – were combined with abundant but apparently non-binding serum albumin (ALBU, 25 μgmL^{-1}), transferrin (TRFE, 10 μgmL^{-1}) and prothrombin (THRB, 2 μgmL^{-1}). The relative concentrations of individual proteins was chosen to approximate endogenous serum protein abundance (**Table S3**). In the absence of any competing and unlabeled AmBisome liposomes, our photoaffiinity approach again revealed the selective binding of apoE and apoA1 to the anionic surface of AmBisome liposomes (**Figure 4b**). The relative abundancy of apoE and apoA1 on the surface of the liposomes was comparable to that observed for experiments using human serum with slight variation in absolute values likely reflecting small differences in relative protein concentrations compared to endogenous human serum. Furthermore, this experiment confirmed the complete absence of binding of more abundant serum proteins (*e.g.* ALBU and TRFE) to the surface of AmBisome liposomes (**Figure 4b**).

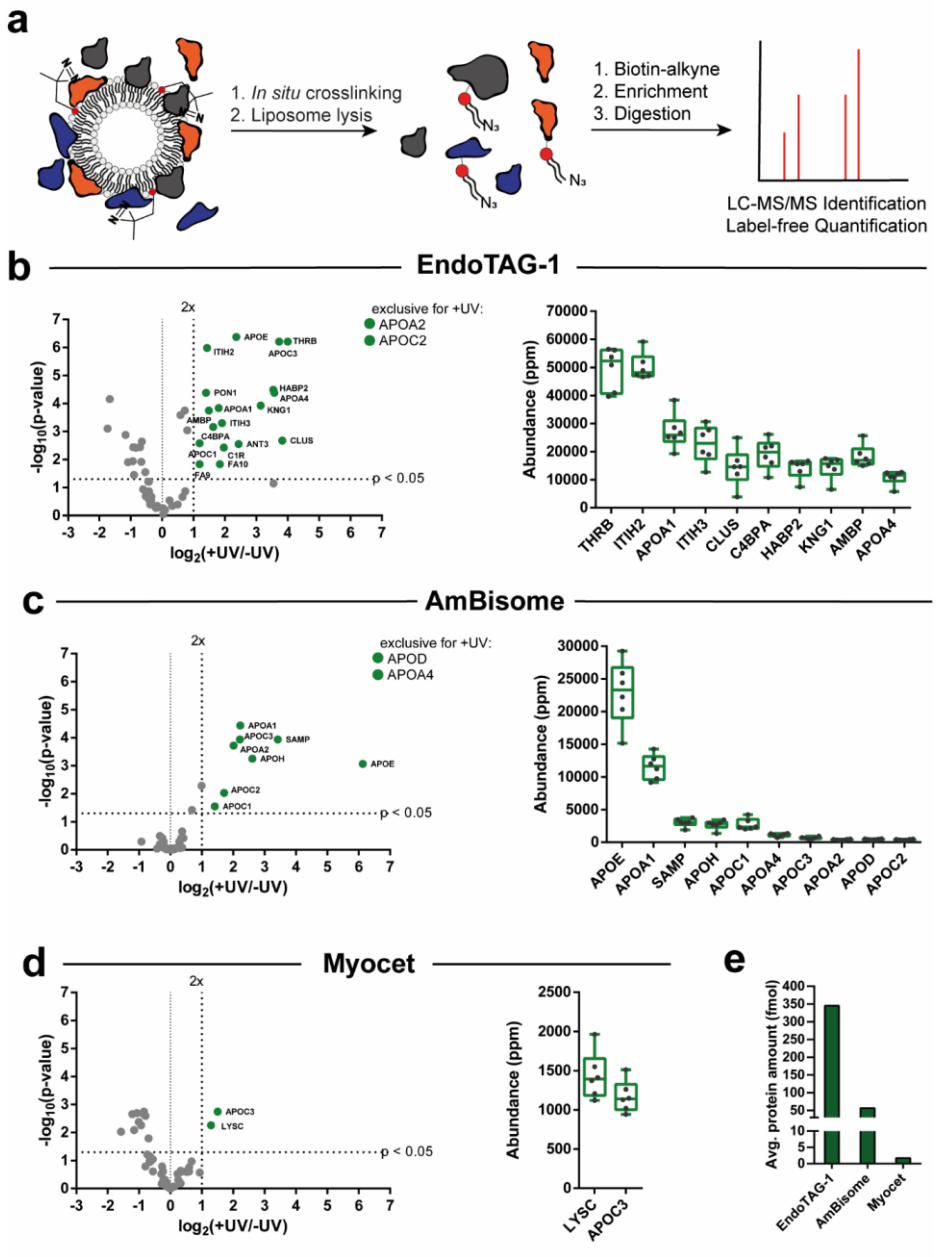


Figure 3. Label free, quantitative identification of the liposome protein corona, isolated *via* photoaffinity method. (**a**) Schematic representation of photoaffinity labelling and enrichment for MS/MS identification of the liposome protein corona. (**b**-**d**) Label free quantitative mass

spectrometry for EndoTAG-1, AmBisome and Myocet liposomes. Volcano plots of enrichment over background (log2(+UV/-UV)) plotted against the statistical significance of this comparison (-log10(p-value)). Proteins meeting all selection criteria labelled in green. Proteins without background labelling are listed as "exclusive for +UV". Abundance plots displaying the replicate abundancies of the top 10 proteins (ppm) within the +UV samples. Complete abundance plots containing all proteins, including -UV abundancy values and tables can be found in Supplementary Figure 5. (**e**) Absolute quantification of protein binding to EndoTAG-1, AmBisome and Myocet liposomes. Values calculated as the average absolute amount of protein of the +UV replicates corrected for the average absolute amount of protein of the -UV replicates.

In the presence of increasing concentrations of unlabeled but otherwise compositonally identical liposomes, our photoaffinity probe captured decreasing amounts of apoE and apoA1 bound to the surface of IKS02-labeled AmBisome liposomes (**Figure 4c**). Importantly, this result confirmed that unlabeled AmBisome liposomes also bind, and compete for, apoE and apoA1, indicating that the incorporation of our photoaffinity probe (5 mol%) within a liposome membrane does not signifcantly affect specific serum protein binding. Again, this experiment confirmed no enrichment of ALBU, THRB or TRFE on the surface of AmBisome (**Figure S5**). Analogous experiments using Myocet confirmed the complete absence of serum proteins at the surface of these liposomes, whereas for EndoTAG-1, selective binding of apoE and apoA1 was again observed (**Figure S6**). However, significant amounts of surface-bound THRB were not captured on the surface of EndoTAG-1, as was the case in human serum. Again, this may be due to an underestimation of the relative concentration of THRB in the predefined protein mixture, but it is noteworthy that THRB was detected here with high statistical significance (+ UV *vs.* – UV), albeit low enrichment. While we have used six biological replicates to reliably determine enrichment at a minimum of 2-fold over the background throughout this study,[47] it may be the case that proteins with high statistical significance (*e.g.* $p < 0.01$) but low enrichment (*e.g.* ~1.5x) should still be considered important components of the liposome protein corona.

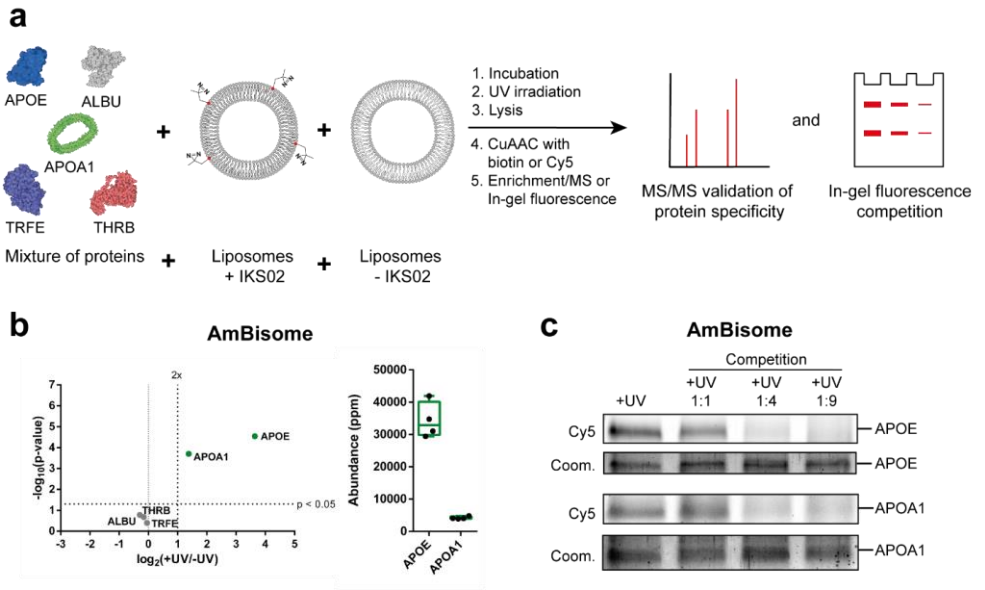


Figure 4. Validation of apolipoprotein E and A1 binding to AmBisome liposomes. (**a**) Liposomes were incubated in a mixture of purified human serum proteins consisting of apolipoprotein E (APOE, 2 μgmL^{-1}), serum albumin (ALBU, 25 μgmL^{-1}), apolipoprotein A-I (APOA1, 2 μgmL^{-1}), transferrin (TRFE, 10 μgmL^{-1}) and prothrombin (THRB, 2 μgmL^{-1}). (**b**) Volcano plot of protein enrichment over background (log2(+UV/-UV)) plotted against the statistical significance of this comparison (-log10(p-value)). Proteins meeting all selection criteria labelled in green. Abundance plot displaying the abundancies of apoE and apoA1 within the +UV samples. (**c**) Competition assay of apolipoprotein E and A1 binding. Increasing concentrations (1:1 to 1:9 molar ratios) of unlabeled AmBisome liposomes were incubated, together with AmBisome liposomes, containing IKS02, in the above pre-defined mixture of human serum proteins. Captured apoE and apoA1 on the surface of IKS02-labeled AmBisome liposomes were separated by SDS-PAGE and visualized by in-gel fluorescence (Cy5). Protein loading determined by Coomassie Blue (coom.). Protein structures were obtained from the protein data bank (PDB): (APOE: 2L7B, APOA1: 1AV1, ALBU: 1E78, THRB: 6C2W, TRFE: 1D3K). Illustrations were generated using Illustrate.[48]

To compare liposome protein coronas isolated *via* centrifugation, six replicates of each liposome formulation were incubated in human serum, centrifuged, washed and resolved with SDS-PAGE, followed by in-gel digestion (**Figure S7**).[49,50] Following digestion, the same nanoUPLC-MS/MS methods and LFQ criteria, as for the photoaffinity labelling, were applied to identify specific, isolated proteins. Given the variability in sedimentation efficiency, isolated proteins from the centrifugation method were ranked on abundancy without background correction (**Figure S8 and Tables S4-7**). For all three liposome

formulations, the number of individually identified proteins present in the protein corona isolated *via* centrifugation were higher than those identified *via* the photoaffinity method (**Figure 4a**). This was most evident for EndoTAG-1 liposomes, where our photoaffinity method identified a total of 20 unique proteins compared to 100+ for centrifugation, and for Myocet liposomes, where our photoaffinity method identified just two proteins compared to 24 for centrifugation.

To further correlate identified proteins to their natural abundance, complete human serum was digested in solution, followed by identification and quantification (**Table S3**). Using this data, the distribution of protein molecular weights and isoelectric points for both methods, and all three liposome formulations, could be compared to the protein composition of the serum sample used in this study (**Figure 5b,c**). In the case of protein molecular weight, protein coronas isolated *via* centrifugation methods showed similar size distributions to that of native serum. In contrast, coronas isolated *via* photoaffinity methods contained no proteins with a molecular weight of >150 kDa, with AmBisome and Myocet binding only <60 kDa proteins. This disparity is most likely due to the sedimentation of large, unbound proteins during centrifugation. In the case of protein isoelectric point (pI), both EndoTAG-1 and AmBisome predominantly bound acidic serum proteins (pI < 7), irrespective of isolation method. Interestingly, there was no significant enrichment of basic serum proteins (pI > 7) on the surface of anionic, AmBisome liposomes. Accordingly, protein pI distributions on the surface of AmBisome and EndoTAG-1 liposomes broadly follow the pI distribution of proteins in human serum, in which the majority of proteins are acidic. This also explains the high amount of total protein binding to cationic, EndoTAG-1 liposomes.

Finally, a heat map was constructed to compare individual proteins present on the surface of each of the three liposome formulations, isolated *via* either centrifugation or photoaffinity methods (**Figure 5d**). Here, the relative abundance of a protein within a sample is displayed for the top 10 most abundant proteins in human serum, as well as the top ten most abundant apolipoproteins. From this heat map, it is clear that protein coronas isolated *via* centrifugation closely follow native protein abundancies in human serum, and human serum albumin (ALBU) and complement component 3 (CO3) are abundantly present in all samples, as well as in the control sample (*i.e.*, no liposomes). In contrast, our photoaffinity method reveals the most abundant serum proteins do not constitute a significant component of the protein corona of any of the three liposomal formulations tested. Instead, isolated protein coronas are dominated by apolipoproteins. These results show that photoaffinity labelling can be used to selectively determine the protein corona of liposomes without a bias towards large abundant proteins.

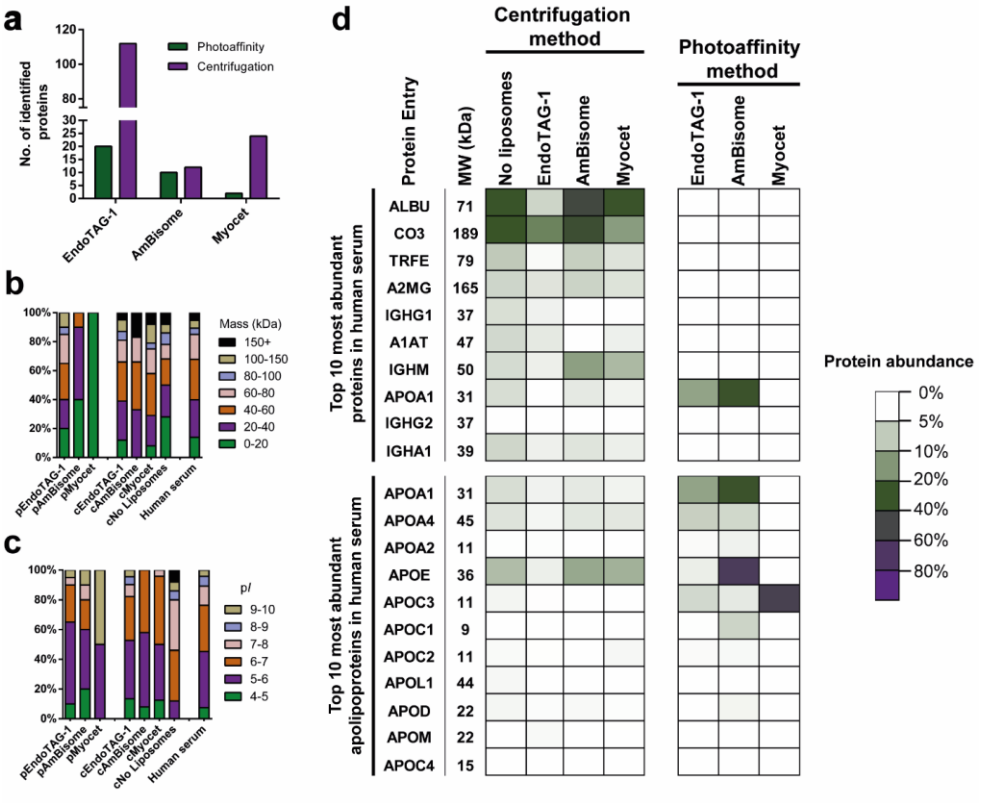


Figure 5. Comparison of liposome protein coronas isolated *via* centrifugation or photoaffinity method. (**a**) Number of distinct serum proteins adsorbed to the surface of EndoTAG-1, AmBisome and Myocet liposomes. (**b**) Molecular weight (in kDa) distributions of identified proteins for each liposome formulation and complete human serum. Photoaffinity samples are labelled 'p' (*e.g.* pEndoTag), centrifugation samples are labelled 'c' (*e.g.* cEndoTag). (**c**) Isoelectric point (pI) distributions of identified proteins for each liposome formulation and complete human serum. (**d**) Heat map displaying the abundancy of proteins associated with individual liposome formulations. For the centrifugation method, protein abundance was calculated as the average abundance (ppm) for every protein over the average total amount of protein in the sample. For the photoaffinity method, protein abundance was calculated as the average abundance (ppm) for every protein over the average total amount of protein (meeting the selection criteria).

2.3 Discussion

The dominance of apolipoproteins on the surface of all three liposome formulations can be rationally explained in terms of endogenous protein function. The evolved function of soluble apolipoproteins is to bind secreted lipoproteins (*e.g.* HDL, LDL, VLDL and chylomicrons), to coordinate the transport and metabolism of endogenous and exogenous (dietary) fats throughout the body.[51] The general structure of a lipoprotein consists of a phospholipid monolayer surrounding a solid lipid core, rich in triglycerides and cholesteryl esters. Following secretion into the bloodstream, lipoproteins can associate with various exchangeable and soluble apolipoproteins (apo), the most abundant being apoA (I, II and IV), apoC (I, II and III) and apoE.[51] Specific apolipoprotein binding to the surface of a lipoprotein is determined by the physicochemical properties of a lipoprotein, in particular its size and curvature, as well as local environmental factors (*e.g.* local apolipoprotein concentrations). The changing apolipoprotein "signature" on the surface of a lipoprotein, throughout its lifecycle, dictates a lipoprotein's fate in the body. Given the natural affinity of soluble apolipoproteins for the surface of endogenous and circulating lipid nanoparticles (*i.e.* lipoproteins), it is perhaps unsurprising that these serum proteins also dominate the protein corona of liposomes.

At a fundamental level, our finding that virtually no serum proteins, including highly abundant serum albumin, bind to the surface of Myocet liposomes suggests that the general formation of a protein corona on a nanoparticle may not always be relevant. Likewise, the enrichment and high abundance of acidic apoE (pI 5.5) on the surface of anionic AmBisome liposomes is unexpected, although can be rationalized by the presence of a cationic heparin binding site on the surface of apoE.[52–54] Overall, while the implications of these findings on *in vivo* liposome fate will require comprehensive mechanistic studies in animal models,[55] the ability to accurately characterize and quantify the protein corona of a liposome in complex biological mixtures, prior to first injections in animals, provides a strong rationale for further *in vivo* experiments.

Finally, it is important to recognize the limitations of our photo-affinity method as described. Given its chemical structure, the IKS02 photoaffinity probe can only be reasonably applied to lipidic (nano)materials (*e.g.* liposomes, micelles, solid lipid particles, lipid-coated particles etc.). Assuming synthetic accessibility, however, there is no reason why a bifunctional probe with separate photoaffinity and conjugation handles could not be designed for other self-assembled, organic materials (*e.g.* polymersomes, hydrogels etc.). More fundamentally, however, **our** photoaffinity approach can only capture the hard protein corona of a liposome (*i.e.* proteins directly adsorbed to the nanoparticle surface)

and will not resolve potentially important proteins of any (outer) "soft" corona that may form.[4,56,57] It is worth noting, however, that in the case of lipoprotein-bound apolipoproteins, biological function relies on direct binding of apolipoprotein to a target receptor/enzyme (e.g. apoE-LDLr mediated uptake of LDL particles in hepatocytes).[51]

In conclusion, our photoaffinity-based chemoproteomics approach enables the capture, identification and quantification of the protein corona of a liposome in its native state. Through this approach, we have revealed liposome protein coronas that are quantitatively and qualitatively different from each other but also significantly less complex than those previously reported. While we have focused on human serum solutions in this study, the ability to capture proteins *in situ* provides a unique opportunity to isolate and characterise the adsorbed protein corona of a liposome, in its native state, in any *ex vivo* or *in vitro* protein sample, such as human blood or plasma, and even *in vivo* (*e.g.* using light transparent zebrafish embryos). Furthermore, light activation can be applied with high spatiotemporal resolution, offering the chance to resolve evolving nanoparticle-protein interactions in both time and space. These features represent a significant technological advance over current methods and, going forward, may enrich our fundamental understanding of the protein corona as well as its impact on nanoparticle behavior and performance *in vitro* and *in vivo*.

2.4 Data availability

The mass spectrometry proteomics data have been deposited to the ProteomeXchange Consortium *via* the PRIDE[58] partner repository with the dataset identifier PXD016229.

2.5 References

1. Lazarovits, J., Chen, Y. Y., Sykes, E. A. & Chan, W. C. W. Nanoparticle-blood interactions: the implications on solid tumour targeting. *Chem. Commun. (Camb).* **51**, 2756–2767 (2015).
2. Cai, R. & Chen, C. The Crown and the Scepter: Roles of the Protein Corona in Nanomedicine. *Adv. Mater.* **1805740**, 1–13 (2018).
3. Nguyen, V. H. & Lee, B.-J. Protein corona: a new approach for nanomedicine design. *Int. J. Nanomedicine* **12**, 3137–3151 (2017).
4. Walkey, C. D. & Chan, W. C. W. W. Understanding and controlling the interaction of nanomaterials with proteins in a physiological environment. *Chem. Soc. Rev.* **41**, 2780–2799 (2012).
5. Nel, A. E. *et al.* Understanding biophysicochemical interactions at the nano-bio interface. *Nat. Mater.* **8**, 543–557 (2009).
6. Bertrand, N. *et al.* Mechanistic understanding of in vivo protein corona formation on polymeric nanoparticles and impact on pharmacokinetics. *Nat. Commun.* **8**, (2017).
7. Oh, J. Y. *et al.* Cloaking nanoparticles with protein corona shield for targeted drug delivery.

Nat. Commun. **9**, 1–9 (2018).
8. Salvati, A. *et al.* Transferrin-functionalized nanoparticles lose their targeting capabilities when a biomolecule corona adsorbs on the surface. *Nat. Nanotechnol.* **8**, 137–143 (2013).
9. Garcia-Alvarez, R., Hadjidemetriou, M., Sanchez-Iglesias, A., Liz-Marzan, L. M. & Kostarelos, K. In vivo formation of protein corona on gold nanoparticles. The effect of their size and shape. *Nanoscale* **10**, 1256–1264 (2018).
10. Corbo, C. *et al.* Unveiling the in Vivo Protein Corona of Circulating Leukocyte-like Carriers. *ACS Nano* **11**, 3262–3273 (2017).
11. Grenier, P., Viana, I. M. de O., Lima, E. M. & Bertrand, N. Anti-polyethylene glycol antibodies alter the protein corona deposited on nanoparticles and the physiological pathways regulating their fate in vivo. *J. Control. Release* **287**, 121–131 (2018).
12. Amici, A. *et al.* In vivo protein corona patterns of lipid nanoparticles. *RSC Adv.* **7**, 1137–1145 (2017).
13. Wang, M. *et al.* Nanoparticle–proteome *in vitro* and *in vivo*. *J. Mater. Chem. B* **6**, 6026–6041 (2018).
14. Casals, E., Pfaller, T., Duschl, A., Oostingh, G. J. & Puntes, V. Time evolution of the nanoparticle protein corona. *ACS Nano* **4**, 3623–3632 (2010).
15. Barrán-Berdón, A. L. *et al.* Time evolution of nanoparticle-protein corona in human plasma: Relevance for targeted drug delivery. *Langmuir* **29**, 6485–6494 (2013).
16. Hadjidemetriou, M., Al-Ahmady, Z. & Kostarelos, K. Time-evolution of in vivo protein corona onto blood-circulating PEGylated liposomal doxorubicin (DOXIL) nanoparticles. *Nanoscale* **8**, 6948–6957 (2016).
17. Cedervall, T. *et al.* Understanding the nanoparticle-protein corona using methods to quantify exchange rates and affinities of proteins for nanoparticles. *Proc. Natl. Acad. Sci.* **104**, 2050–2055 (2007).
18. Docter, D. *et al.* The nanoparticle biomolecule corona: lessons learned – challenge accepted? *Chem. Soc. Rev.* **44**, 6094–6121 (2015).
19. Carrillo-Carrion, C., Carril, M. & Parak, W. J. Techniques for the experimental investigation of the protein corona. *Curr. Opin. Biotechnol.* **46**, 106–113 (2017).
20. Weber, C., Morsbach, S. & Landfester, K. Possibilities and Limitations of Different Separation Techniques for the Analysis of the Protein Corona. *Angew. Chemie Int. Ed.* **58**, 12787–12794 (2019).
21. Lundqvist, M. *et al.* The nanoparticle protein corona formed in human blood or human blood fractions. *PLoS One* **12**, 1–15 (2017).
22. Aggarwal, P., Hall, J. B., McLeland, C. B., Dobrovolskaia, M. A. & McNeil, S. E. Nanoparticle interaction with plasma proteins as it relates to particle biodistribution, biocompatibility and therapeutic efficacy. *Adv. Drug Deliv. Rev.* **61**, 428–437 (2009).
23. Lundqvist, M. *et al.* Nanoparticle size and surface properties determine the protein corona with possible implications for biological impacts. *Proc. Natl. Acad. Sci. U. S. A.* **105**, 14265 (2008).
24. Pozzi, D. *et al.* The biomolecular corona of nanoparticles in circulating biological media. *Nanoscale* **7**, 13958–13966 (2015).
25. Hadjidemetriou, M. *et al.* In Vivo Biomolecule Corona around Blood-Circulating, Clinically Used and Antibody-Targeted Lipid Bilayer Nanoscale Vesicles. *ACS Nano* **9**, 8142–8156 (2015).
26. Gubbens, J. *et al.* Photocrosslinking and Click Chemistry Enable the Specific Detection of Proteins Interacting with Phospholipids at the Membrane Interface. *Chem. Biol.* **16**, 3–14

(2009).
27. Murale, D. P., Hong, S. C., Haque, M. M. & Lee, J. S. Photo-affinity labeling (PAL) in chemical proteomics: A handy tool to investigate protein-protein interactions (PPIs). *Proteome Sci.* **15**, 1–34 (2017).
28. Soethoudt, M. *et al.* Selective Photoaffinity Probe That Enables Assessment of Cannabinoid CB2 Receptor Expression and Ligand Engagement in Human Cells. *J. Am. Chem. Soc.* **140**, 6067–6075 (2018).
29. Allen, T. M. & Cullis, P. R. Liposomal drug delivery systems: from concept to clinical applications. *Adv. Drug Deliv. Rev.* **65**, 36–48 (2013).
30. Bulbake, U., Doppalapudi, S., Kommineni, N. & Khan, W. Liposomal Formulations in Clinical Use: An Updated Review. *Pharmaceutics* **9**, 12 (2017).
31. Campbell, F. *et al.* Directing Nanoparticle Biodistribution through Evasion and Exploitation of Stab2-Dependent Nanoparticle Uptake. *ACS Nano* **12**, 2138–2150 (2018).
32. Tenzer, S. *et al.* Rapid formation of plasma protein corona critically affects nanoparticle pathophysiology. *Nat. Nanotechnol.* **8**, 772 (2013).
33. Capriotti, A. L. *et al.* Analysis of plasma protein adsorption onto DC-Chol-DOPE cationic liposomes by HPLC-CHIP coupled to a Q-TOF mass spectrometer. *Anal. Bioanal. Chem.* **398**, 2895–2903 (2010).
34. Chang, H.-I. & Cheng, M.-Y. Clinically-Proven Liposome-Based Drug Delivery: Formulation, Characterization and Therapeutic Efficacy. *J. Nanomedine. Biotherapeutic Discov.* **01**, 1–8 (2012).
35. Marrink, S.-J., Berger, O., Tieleman, P. & Jähnig, F. Adhesion Forces of Lipids in a Phospholipid Membrane Studied by Molecular Dynamics Simulations. *Biophys. J.* **74**, 931–943 (1998).
36. Pan, S. *et al.* A Suite of "Minimalist" Photo-Crosslinkers for Live-Cell Imaging and Chemical Proteomics: Case Study with BRD4 Inhibitors. *Angew. Chemie - Int. Ed.* **56**, 11816–11821 (2017).
37. Agard, N. J., Baskin, J. M., Prescher, J. A., Lo, A. & Bertozzi, C. R. A Comparative Study of Bioorthogonal Reactions with Azides. *ACS Chem. Biol.* **1**, 644–648 (2006).
38. Batist, G., Barton, J., Chaikin, P., Swenson, C. & Welles, L. Myocet (liposome-encapsulated doxorubicin citrate): a new approach in breast cancer therapy. *Expert Opin. Pharmacother.* **3**, 1739–1751 (2002).
39. Cornely, O. A. *et al.* Liposomal Amphotericin B as Initial Therapy for Invasive Mold Infection : A Randomized Trial Comparing a High – Loading Dose Regimen with Standard Dosing (AmBiLoad Trial). *Clin. Infect. Dis.* **44**, 1289–1297 (2007).
40. Schmitt-Sody, M. *et al.* Neovascular Targeting Therapy. *Clin. Cancer Res.* **9**, 2335 LP – 2341 (2003).
41. Yang, Y., Yang, X. & Verhelst, S. H. L. Comparative analysis of click chemistry mediated activity-based protein profiling in cell lysates. *Molecules* **18**, 12599–12608 (2013).
42. Pickens, C. J., Johnson, S. N., Pressnall, M. M., Leon, M. A. & Berkland, C. J. Practical Considerations, Challenges, and Limitations of Bioconjugation via Azide-Alkyne Cycloaddition. *Bioconjug. Chem.* **29**, 686–701 (2018).
43. Al Shweiki, M. H. D. R. *et al.* Assessment of Label-Free Quantification in Discovery Proteomics and Impact of Technological Factors and Natural Variability of Protein Abundance. *J. Proteome Res.* **16**, 1410–1424 (2017).
44. Docter, D. *et al.* Quantitative profiling of the protein coronas that form around nanoparticles. *Nat. Protoc.* **9**, 2030–2044 (2014).
45. Silva, J. C., Gorenstein, M. V., Li, G., Vissers, J. P. C. & Geromanos, S. J. Absolute

Quantification of Proteins by LCMS E. *Mol. Cell. Proteomics* **5**, 144–156 (2006).
46. Distler, U. *et al.* Drift time-specific collision energies enable deep-coverage data-independent acquisition proteomics. *Nat. Methods* **11**, 167–170 (2014).
47. Old, W. M. *et al.* Comparison of label-free methods for quantifying human proteins by shotgun proteomics. *Mol. Cell. Proteomics* **4**, 1487–1502 (2005).
48. Goodsell, D. S., Autin, L. & Olson, A. J. Illustrate: Software for Biomolecular Illustration. *Structure* **27**, 1716-1720.e1 (2019).
49. Shevchenko, A., Tomas, H., Havliš, J., Olsen, J. V. & Mann, M. In-gel digestion for mass spectrometric characterization of proteins and proteomes. *Nat. Protoc.* **1**, 2856–2860 (2007).
50. Monopoli, M. P., Aberg, C., Salvati, A. & Dawson, K. A. Biomolecular coronas provide the biological identity of nanosized materials. *Nat. Nanotechnol.* **7**, 779–786 (2012).
51. Mahley, R. W., Innerarity, T. L., Rall, S. C. J. & Weisgraber, K. H. Plasma lipoproteins: apolipoprotein structure and function. *J. Lipid Res.* **25**, 1277–1294 (1984).
52. Saito, H. *et al.* Characterization of the heparin binding sites in human apolipoprotein E. *J. Biol. Chem.* **278**, 14782–14787 (2003).
53. Dong, J. *et al.* Interaction of the N-terminal domain of apolipoprotein E4 with heparin. *Biochemistry* **40**, 2826–2834 (2001).
54. Chen, J., Li, Q. & Wang, J. Topology of human apolipoprotein E3 uniquely regulates its diverse biological functions. *Proc. Natl. Acad. Sci. U. S. A.* **108**, 14813–14818 (2011).
55. Lazarovits, J. *et al.* Supervised Learning and Mass Spectrometry Predicts the in Vivo Fate of Nanomaterials. *ACS Nano* **13**, 8023–8034 (2019).
56. Weber, C., Simon, J., Mailänder, V., Morsbach, S. & Landfester, K. Preservation of the soft protein corona in distinct flow allows identification of weakly bound proteins. *Acta Biomater.* **76**, 217–224 (2018).
57. Kari, O. K. *et al.* In situ analysis of liposome hard and soft protein corona structure and composition in a single label-free workflow. *Nanoscale* **12**, 1728–1741 (2020).
58. Vizcaíno, J. A. *et al.* The Proteomics Identifications (PRIDE) database and associated tools: status in 2013. *Nucleic Acids Res.* **41**, D1063–D1069 (2012).

Chapter 3

Anionic Lipid Nanoparticles Preferentially Deliver mRNA to the Hepatic Reticuloendothelial System

Lipid nanoparticles (LNPs) are the leading non-viral technology for the delivery of exogenous RNA to target cells in vivo. Such delivery platforms are exemplified by Onpattro®, an approved LNP-based RNA interference (RNAi) therapy, indicated for polyneuropathies resulting from transthyretin-mediated amyloidosis, administered systemically, and targeted to parenchymal liver cells. The discovery of systemically administered LNP technologies capable of preferential RNA delivery beyond hepatocytes has, however, proved more challenging. Here, preceded by comprehensive mechanistic understanding of nanoparticle biodistribution and clearance, we rationally design an LNP-based mRNA delivery platform to preferentially target the hepatic reticuloendothelial system (RES). Evaluated in embryonic zebrafish, validated in mice and compared to LNP-mRNA systems based on the lipid composition of Onpattro®, RES-targeted LNPs significantly enhance mRNA expression both globally within the liver and specifically within hepatic RES cell types. Hepatic RES targeting required just a single lipid change within the formulation of Onpattro® to switch LNP surface charge from neutral to anionic. This technology opens up new opportunities to treat liver-specific and systemic diseases in which RES cell types play a key role and highlights that rational development of advanced RNA therapies should be proceeded by a robust understanding of the nano-bio interactions involved.

This chapter was submitted as a research article: R. Pattipeiluhu, G. Arias-Alpizar, G. Basha, J. Bussmann, T.H. Sharp, M.A. Moradi, N. Sommerdijk, P.R. Cullis, A. Kros, D. Witzigmann, F. Campbell

3.1 Introduction

RNA therapy relies on cytosolic delivery of exogenous (therapeutic) RNA molecules, *e.g.* mRNA, siRNA, or miRNA, to gain precise control of gene expression within target cells.[1,2] This requires delivery systems to protect, transport and deliver highly charged, immunogenic and membrane impermeable RNA payloads within target cells and tissues in the body. To this end, lipid nanoparticles (LNPs) have emerged as the state-of-the-art, non-viral RNA delivery system for *in vivo* application.[3–5] These technologies are exemplified by Onpattro®, a clinically approved LNP-based RNA interference (RNAi) therapy, administered intravenously (*i.v.*) and used to treat polyneuropathies resulting from transthyretin-mediated amyloidosis (hATTR).[6,7] Onpattro® functions by transiently silencing transthyretin (TTR) expression specifically within hepatocytes through siRNA delivery.[7] Hepatocyte targeting is mediated through the adsorption of soluble apolipoprotein E (apoE) to the surface of a circulating LNP.[8,9] This, in turn, promotes LNP binding to the low density lipoprotein receptor (LDLr),[10] a receptor heavily expressed on the sinusoidal surface of hepatocytes. ApoE-LDLr binding leads to LNP endocytosis and consequent cytosolic siRNA delivery. Cytosolic siRNA release is enhanced by the protonation of ionizable (cationic) lipids within the endosome and subsequent disruption of the endosomal membrane.[11]

Following systemic administration, harnessing apoE-mediated LNP specificity for the delivery of RNA therapeutics (siRNA or mRNA) to hepatocytes is relatively common.[5,10,12–15] However, expanding the scope of LNP-based gene therapies to other hepatic cell types (or non-hepatic cells), to gain access to a greater diversity of disease states, has so far proved more challenging. To meet this challenge, high throughput empirical screening of DNA-barcoded LNPs has revealed formulations that preferentially target extra-hepatic tissues (*e.g.* bone marrow)[16] and cells (*e.g.* T-cells),[17] as well as individual hepatic (*e.g.* liver endothelial) cell types.[18,19] However, while these empirical discoveries have enriched our understanding of the structure-activity landscape of LNP technologies, they have not revealed the fundamental biological mechanisms underpinning LNP transport and preferential cellular uptake *in vivo*. Only this knowledge can enable the rational design of new LNP-based RNA therapies with target cell specificity.[5,20]

Besides hepatocytes (comprising ~80% liver volume), the liver is composed of non-parenchymal liver cells, including Kupffer cells (KCs) and liver sinusoidal endothelial cells (LSECs).[21] Hepatic blood vessels, or sinusoids, connecting the hepatic artery and portal vein to the central vein, are primarily composed of LSECs (~70%) and KCs (~20%).[22,23] Together these two cell types make up the hepatic reticuloendothelial system (RES) whose

primary role is to maintain blood homeostasis through the scavenging of macromolecular waste and pathogens from blood.[24,25] LSECs, in particular, are specialized scavenger endothelial cells (SECs) and have one of the highest endocytic activities of any cell type in the body.[26] These cells are responsible for the clearance of endogenous macromolecules, such as oxidized low-density lipoprotein and hyaluronic acid,[25,27,28] as well as blood borne pathogens.[29,30] In large part, LSEC clearance of macromolecular waste and pathogens is mediated through an array of scavenger receptors (*e.g.* Hyaluronan- and Stabilin-receptors), heavily expressed on the luminal membrane of LSECs.[31–33] As a therapeutic target, LSECs play a crucial role in liver homeostasis, regeneration following acute injury, and in the pathogenesis of various liver diseases, including cirrhosis and liver cancer.[26,34] Additionally, as antigen presenting cells, LSECs are key regulators of hepatic adaptive immunity and systemic immunotolerance, and are therefore promising immunotherapy targets.[35]

Guided by mechanistic understanding of the systemic clearance of *i.v.* administered anionic nanoparticles by hepatic RES cell types,[36] here, we rationally design anionic LNPs to preferentially target and transfect the hepatic RES, *i.e.* scavenger receptor LNPs (srLNPs). This required just a single lipid compositional change within the formulation of Onpattro®. Using the embryonic zebrafish (*Danio rerio*) as convenient, accurate and cost effective *in vivo* model,[37] we qualitatively describe LNP biodistribution, mRNA delivery and expression of an exogenous fluorescent protein *in vivo*, at cellular resolution and in real time, focusing particularly on relative LNP uptake and mRNA expression within SECs, macrophages and hepatocytes of the embryo. Furthermore, we confirm scavenger receptor, Stabilin-1 and -2, mediated uptake of anionic LNPs by SECs. Finally, we validate preferential LNP-mediated mRNA transfection of the hepatic RES in mice.

3.2 Results

Previously, we have shown that *i.v.* administered, anionic nanoparticles (ranging in size from 10-150 nm) are rapidly and extensively cleared from circulation by scavenging endothelial cells (SECs) within the posterior cardinal vein (PCV), caudal *hematopoietic tissue* (CHT) and caudal vein (CV) of a two day old zebrafish embryo.[36] In teleost fish (*i.e.* zebrafish), and other aquatic vertebrates, SECs are not located primarily in the liver (as for LSECs in mammals), but reside in various other organs including scavenging (venous) blood vessels.[38] Mechanistically, anionic nanoparticle recognition and uptake by SECs is mediated by the scavenger receptors, Stabilin-1 (*stab1*) and Stabilin-2 (*stab2*).[36] Stabilin-1 and -2 are strongly expressed by LSECs in the mammalian liver[39] and *i.v.* injection of anionic liposomes in 6-8 week old mice resulted in extensive nanoparticle uptake within these cell

types.[36] In addition to SECs, anionic nanoparticles are also scavenged by blood resident macrophages, both within the CHT of the embryonic zebrafish and within the mouse liver (*i.e.* within KCs).[36,40] All together, these observations indicate that the embryonic zebrafish can be used to qualitatively predict *in vivo* nanoparticle interactions with mammalian RES cell types.

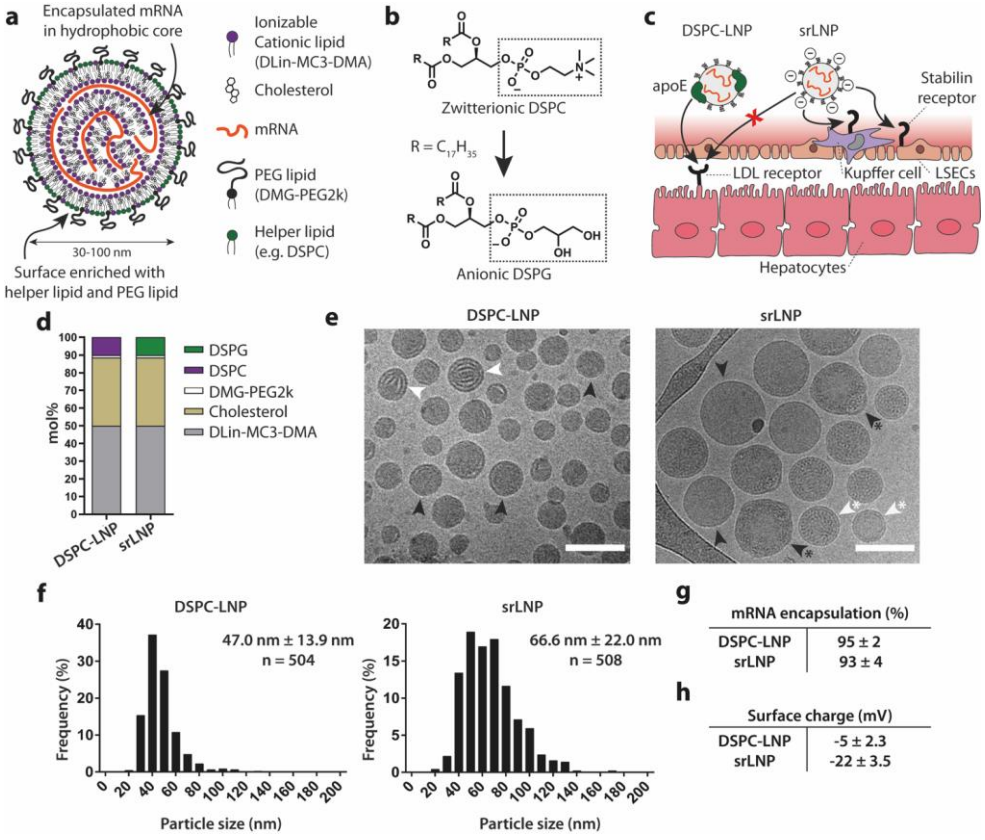


Figure 1. Design and characterization of srLNPs (**a**) Schematic of the structural organization of an LNP containing mRNA, as described previously.[41] Helper phospholipids (typically incorporated at 10 mol%) are enriched at the LNP surface. (**b,c**) Within the liver sinusoids, switching of the helper phospholipid from zwitterionic DSPC (as in ONPATTRO®) to anionic DSPG creates anionic srLNPs that are directed to the hepatic RES, *via* Stabilin receptor mediated recognition and uptake in LSECs. srLNP uptake within hepatic RES cells is further enhanced by the inhibition of apoE-LDLr interactions mediated by anionic phospholipids (*e.g.* DSPG).[42] The mechanism of recognition and uptake of srLNPs by blood resident macrophages (*i.e.* KCs) is not known. (**d**) Lipid composition of DSPC-LNPs (*i.e.* ONPATTRO®) and srLNPs. (**e**) Cryo-EM images of DSPC-LNPs and srLNPs (entrapping capped mRNA-eGFP) shows solid lipid nanoparticle structures. Scale bars: 100 nm.

Internal structures indicated with arrows: lamellar (white), amorphous (black), polymorphous (black*) and unilamellar (white*) (**f**) Size distribution of DSPC-LNPs and srLNPs, as determined by cryo-EM. The values derived from the frequency distribution graphs represent the mean ± s.d. (**g**) mRNA encapsulation efficiency within DSPC-LNPs and srLNPs, as determined by RiboGreen assay. (**h**) Surface charge of DSPC-LNPs and srLNPs, as determined by zeta potential measurements. See **Supporting Table 1** for full biophysical characterization of all formulations used in this study.

In this case, we rationally designed an anionic LNP system to enable preferential genetic manipulation in hepatic RES cells. In general, LNPs consist of five structural components (four lipid reagents and an oligonucleotide payload) that self-assemble to form discrete nanostructures ranging from ~30 to ~150 nm in size (**Figure 1a**).[43] The "hydrophobic" core of an LNP is rich in ionizable lipids (*e.g.* heptatriaconta-6,9,28,31-tetraen-19-yl 4-(dimethylamino) butanoate, DLin-MC3-DMA; 50 mol%)* [asterix denotes in the case of Onpattro®]), cholesterol (38.5 mol%)* and an oligonucleotide payload. The LNP surface (*i.e.* lipid-water interface), in contrast, is rich in helper phospholipids (*e.g.* 1,2-distearoyl-*sn*-glycero-3-phosphocholine, DSPC; 10 mol%)* and lipid-PEG conjugates (*e.g.* 1,2-dimyristoyl-rac-glycero-3-methoxypolyethylene glycol-2000, DMG-PEG2k; 1.5 mol%))*.[41] We therefore hypothesized that switching the helper phospholipid of Onpattro®, from zwitterionic DSPC to anionic 1,2-distearoyl-*sn*-glycero-3-phosphoglycerol (DSPG), would render an LNP surface anionic. In turn, an anionic surface charge would redirect LNP targeting and functional RNA delivery from hepatocytes to the hepatic RES by promoting Stabilin-mediated LNP recognition and uptake in LSECs whilst simultaneously inhibiting hepatocyte apoE-LDLr interactions (**Figure 1b,c**).[42] Hereafter, we refer to DSPG-containing LNPs as srLNPs and LNPs based on the lipid composition of Onpattro® as DSPC-LNPs (**Figure 1d**). In all cases, a nitrogen to phosphate (N:P) ratio of 6:1 was used, as is typical for larger nucleic acid payloads.[44]

Following microfluidic assembly, cryo-electron microscopy (cryo-EM) revealed LNPs with a typical electron-dense core structure (Figure 1e).[45–48] Within DSPC-LNPs (47.0 nm ± 13.9 nm), both amorphous and lamellar core structures were present, whereas the core structure of srLNPs (66.6 nm ± 22.0 nm) contained a mixture of amorphous, unilamellar and polymorphic structures, as has been previously reported for LNP-mRNA systems.[49,50] Particle sizes of both DSPC-LNPs and srLNPs (determined through cryo-EM image analysis) were comparable to the number-weighted average determined by dynamic light scattering (Figure 1f, Supporting Table 1) and, in all cases, mRNA encapsulation efficiencies were >95% (Figure 1g). Importantly, however, srLNPs possessed a significantly more anionic (ζ-potential ~ -20 mV) surface charge compared to DSPC-LNPs (ζ-potential ~ -5 mV), indicative of DSPG exposed at the lipid-water interface (Figure 1h). For detailed

biophysical characterization (*i.e.* size, surface charge, encapsulation efficiencies) of all formulations used in this study, please refer to Supporting Table 1.

To assess LNP biodistribution, DSPC-LNPs and srLNPs containing a fluorescent lipid probe (DOPE-LR, 0.2 mol%) and encaspulating fluorescently tagged mRNA (capped and Cy5-labelled), were injected (*i.v.*, ~10 mM lipid, ~0.2 mg/kg mRNA) in wildtype zebrafish embryos at two days post-fertilisation (dpf) (**Figure 2a**). Confocal imaging of entire live embryos, as well as high resolution, tissue level views to include key scavenging cell types of the embryo within the CV and CHT (**Figure 2b**), revealed distinct biodistribution patterns for both LNP-mRNA formulations at 1.5 hour post injection (hpi) (**Figure 2c-f**). In the case of DSPC-LNPs, particles were mostly freely circulating, with both lipid and mRNA confined to, and homogenously distributed throughout, the vasculature of the embryo (**Figure 2c,d**). In addition, a small fraction of DSPC-LNPs accumulated in blood-resident macrophages within the CHT of the embryo, indicative of low level recognition and uptake by the RES (white arrowheads, **Figure 2d**; confirmed in *mpeg*:mCherry embryos, **Figure S1a-c**). In the case of srLNPs, the majority of injected particles were cleared from circulation at 1.5 hpi, with highly selective accumulation observed within SECs and blood-resident macrophages within the PCV, CHT and CV of the two day old embryo (**Figure 2e,f**; macrophage uptake confirmed in *mpeg*:mCherry embryos, **Figure S1d-f**).

The selective accumulation of srLNPs within scavenging (venous) blood vessels of the embryonic zebrafish closely resembled previously observed biodistributions of anionic liposomes, polymersomes and inorganic nanoparticles, in which nanoparticle uptake within SECs was mediated by Stabilin scavenger receptors.[36] To confirm Stabilin-mediated uptake, srLNPs were injected (*i.v.*) in established *stab1*$^{-/-}$/*stab2*$^{-/-}$ double knockout (KO) zebrafish embryos (2 dpf).[51] Within these mutant embryos, srLNPs predominantly remained in circulation at 1.5 hpi with a small fraction accumulating within blood-resident macrophages of the CHT (**Figure 2g** and (whole embryo) **S2**). This confirmed that srLNPs selectively accumulate within RES cell types of the embryonic zebrafish and that recognition and uptake of srLNPs within SECs, but not macrophages, is mediated by Stabilin receptors. Analogous injections of DSPC-LNPs within double KO embryos did not alter DSPC-LNP biodistribution, with the majority of DSPC-LNPs remaining in circulation (**Figure 2h**, (whole embryo) **S2**). In all cases, both lipid and mRNA fluorescent probes appear fully colocalized at 1.5 hpi, suggesting mRNA remains stably entrapped within the core of both DSPC- and srLNPs in circulation, as well as during cellular recognition and (early) cellular uptake.

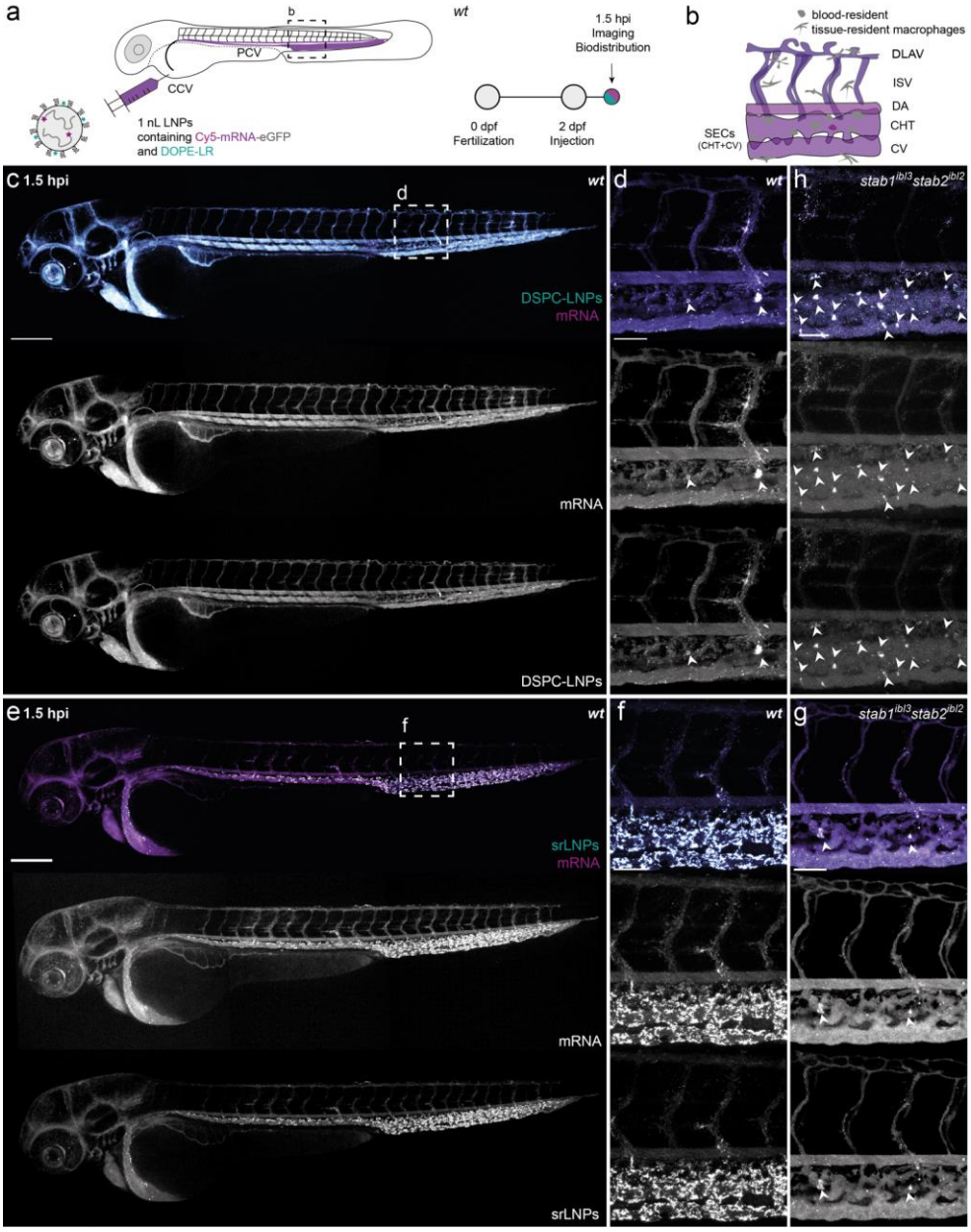


Figure 2. Biodistribution of DSPC-LNPs and srLNPs in two-day old embryonic zebrafish at 1.5 hpi. (**a**) Schematic showing the site of LNP injection (*i.v*) within embryonic zebrafish (2 dpf) and imaging timeframe. LNPs contained DOPE-LR (cyan, 0.2 mol%) as fluorescent lipid probe and Cy5-labelled eGFP mRNA (magenta) as fluorescent mRNA probe. *Injected dose*: ~10 mM lipid, ~0.2 mg/kg

mRNA. *Injection volume*: 1 nL. Major venous blood vessels: CCV – common cardinal vein; PCV – posterior cardinal vein. (**b**) Tissue level schematic of a dorsal region of the embryo containing scavenging cell types (*i.e.* SECs and blood resident macrophages). Blood vessels: DA – dorsal aorta, CHT – caudal hematopoietic tissue; CV – caudal vein; ISV – intersegmental vessel; DLAV - dorsal longitudinal anastomotic vessel. (**c,d**) Whole embryo (10x magnification) and tissue level (40x magnification) views of DSPC-LNP biodistribution within wild-type (AB/TL) embryonic zebrafish (2 dpf) at 1.5 hpi. DSPC-LNPs are mostly freely circulating, confined to, and distributed throughout, the vasculature of the embryo. Low level phagocytotic uptake within blood resident macrophages is highlighted by white arrowheads. (**e,f**) Whole embryo (10x magnification) and tissue level (40x magnification) views of srLNP biodistribution within wild-type (AB/TL) embryonic zebrafish (2 dpf) at 1.5 hpi. srLNPs are mainly associated with SECs within the PCV, CHT and CV of the embryo and are largely removed from circulation at 1.5 hpi. Phagocytotic uptake of both DSPC-LNPs and srLNPs within blood resident macrophages at 1.5 hpi was confirmed by analogous LNP injections in transgenic *mpeg*:mCherry zebrafish embryos, stably expressing mCherry within macrophages (Figure S1). (**g**) Tissue level (40x magnification) view of srLNP biodistribution within double knockout (*stab1*^{ibl3}/*stab2*^{ibl2})[51]zebrafish embryos at 1.5 hpi. Within Stabilin KOs, srLNPs are now mostly freely circulating, with low level phagocytotic uptake within blood resident macrophages highlighted by white arrowheads. (**h**) Tissue level (40x magnification) view of DSPC-LNP biodistribution within double knockout (*stab1*^{ibl3}/*stab2*^{ibl2})[51] zebrafish embryos at 1.5 hpi. Within Stabilin KOs, DSPC-LNPs remain mostly freely circulating, with low level phagocytotic uptake within blood resident macrophages highlighted by white arrowheads. Scale bars: 200 μm (whole embryo) and 50 μm (tissue level).

To assess LNP-mediated delivery of functional mRNA within the embryonic zebrafish, we switched to unlabeled eGFP mRNA (capped, **Figure 3a**), as we consistently observed low mRNA expression levels using Cy5-labeled eGFP (capped) mRNA payloads. This alteration did not significantly change the structure, surface charge or mRNA encapsulation efficiency of LNPs (see **Supporting Table 1**). At 1.5 hpi, srLNPs (~10 mM lipid, ~0.2 mg/kg mRNA) again associated with SECs and blood-resident macrophages within the PCV, CHT and CV of the embryonic zebrafish (**Figure 3b,c**). Given the >2 h timeframe for mRNA delivery, expression and maturation of eGFP,[52,53] low level green fluorescence observed at 1.5 hpi, within the yolk sac and iridophores (pigment cells) of the embryo, is attributed to embryo autofluorescence in the GFP channel.[54] However, at 24 hpi, intense eGFP fluorescence was observed specifically within SECs and blood-resident macrophages of the embryo (Figure 3d,e). This is consistent with the timing reported for eGFP-mRNA delivery and expression using analogous lipid-based delivery systems, whereby the onset of eGFP maturation and fluorescence (*in vitro*) occurs 2-7 h post-incubation and expression levels (fluorescence intensity) continually increase up to 24 h post-treatment.[52 55] Within *stab1*$^{-/-}$/*stab2*$^{-/-}$ KO embryos, srLNP-mediated eGFP expression was observed only within blood-resident

macrophages and not SECs at 24 hpi, confirming macrophage uptake of srLNPs, as for other anionic nanoparticles, is not dependent on Stabilin receptors (**Figure S3**).

For srLNPs, the resulting eGFP expression pattern mirrored srLNP biodistribution at 1.5 hpi (**Figure 2e,f**), confirming successful transport, uptake and cytosolic delivery of functional mRNA within these cells. This is particularly remarkable given SECs have one of the highest endo/lysosomal activities of any cell type in the body,[28,33] and are therefore primed to degrade fragile RNA molecules. Endosomal escape and cytosolic delivery of RNA is widely recognized as one of the major obstacles in the development of effective RNA therapies,[56] with <2% of internalized siRNA (complexed within LNPs based on the lipid composition of Onpattro®) reaching the cytoplasm of HeLa cells (*in vitro*) and hepatocytes (*in vivo*).[57,58] Indeed, the acute extent of mRNA degradation within SECs (as well as potential mRNA degradation in circulation), was confirmed by injection (*i.v.*) of free eGFP-mRNA (capped; both Cy5-labeled and unlabeled) within the zebrafish embryo. This resulted in no significant expression of eGFP within SECs at 24 hpi despite extensive accumulation within these cells at 1.5 hpi, presumably *via* scavenger receptor-mediated uptake of circulating, polyanionic RNA (**Figure S4**).[59]

In the case of DSPC-LNP (~10 mM lipid, ~0.2 mg/kg mRNA) mediated mRNA delivery, widespread eGFP fluorescence was observed throughout the embryo at 24 hpi (**Figure S5**). Combined with the evident lack of cellular accumulation at 1.5 hpi (**Figure 2c,d**), this indicates low-level, non-specific cellular uptake of LNPs based on the lipid composition of Onpattro®, with concurrent mRNA expression across a broad range of cell types, including SECs and blood-resident macrophages. Importantly, however, the liver of the embryonic zebrafish has yet to fully develop at 2 dpf.[60,61] To assess *in vivo* LNP interactions with a functional liver, and potentially corroborate reported hepatocyte targeting of Onpattro® in mammals, we therefore switched to LNP injections in older zebrafish embryos.

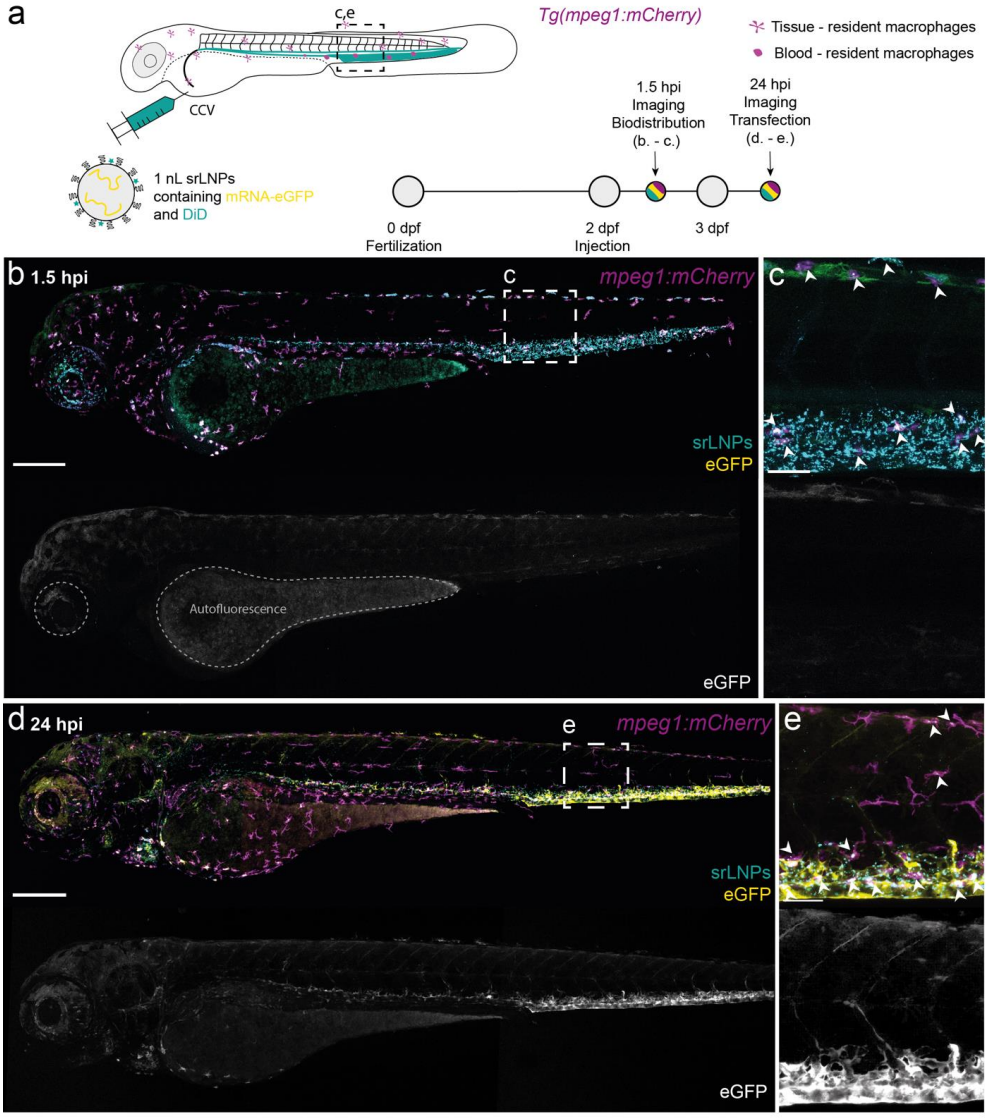


Figure 3. srLNP biodistribution, eGFP-mRNA delivery and eGFP expression within *mpeg1*:mCherry transgenic zebrafish embryos at 1.5 and 24 hpi. (**a**) Schematic showing the site of srLNP injection (*i.v.*) within embryonic zebrafish (2 dpf) and imaging timeframe. srLNPs contained DiD (Cy5, 0.1 mol%) as fluorescent lipid probe and unlabeled, eGFP mRNA (capped) payload. *Injected dose*: ~10 mM lipid, ~0.2 mg/kg mRNA. *Injection volume*: 1 nL. Transgenic Tg(*mpeg1*:mCherry) zebrafish embryos stably express mCherry (magenta) within all macrophages. (**b,c**) Whole embryo (10x magnification) and tissue level (40x magnification) views of srLNP biodistribution and eGFP

expression within the embryonic zebrafish at 1.5 hpi. srLNPs were associated with SECs and blood resident macrophages (white arrowheads) within the PCV, CHT and CV of the embryo. Low level autofluorescence in the GFP channel is highlighted within the yolk sac and pigment cells of the embryo. (**d,e**) Whole embryo and tissue level views of srLNP biodistribution and eGFP expression within the embryonic zebrafish at 24 hpi. At this timepoint, srLNPs remain associated with SECs and blood resident macrophages (white arrowheads) within the PCV, CHT and CV of the embryo. However, intense eGFP expression was now observed specifically within the PCV, CHT and CV confirming successful cytosolic delivery and translation of functional eGFP mRNA within SECs and blood resident macrophages. Scale bars: 200 µm (whole embryo) and 50 µm (tissue level).

From approximately 55 hours post-fertilisation (hpf), the liver of the embryonic zebrafish undergoes a dramatic growth phase. New intrahepatic blood vessels are formed, with blood circulation detected from 72 hpf,[62] and the localised expression of key hepatocyte markers, including transferrin (Tf)[63] and liver fatty acid binding protein (L-FABP),[64] evidently marking maturation of functional hepatoctyes. During this growth phase, anatomical features characteristic of the mammalian liver, and important for the correct processing of lipid nanoparticles, also emerge, including a Space of Disse,[65] the likely presence of a fenestrated endothelium[66] and a functional biliary network (connected to the blood vasculature *via* hepatocytes).[60] These features, combined with a conserved repertoire of lipid transport proteins,[67,68] including apoE, and lipoprotein receptors, including LDLR,[69,70] suggest older (> 72 hpf) zebrafish embryos may offer an attractive *in vivo* model to assess endogenous lipid transport mechanisms, including lipid processing disorders,[71] and probe their prospective role in the fate of LNPs within mammals.

To verify liver development timings and to assess the suitability of the embryonic zebrafish as a predictive *in vivo* model for hepatocyte targeting of nanomedicines, non-PEGylated liposomes (~100 nm), co-formulated with cholesterol-conjugated, human apoE target peptides (Chol-NH-apoE peptide, 5 mol%, see supporting information for synthesis and characterisation), were administered within 3 and 4 day old zebrafish embryos (*L-FABP*:eGFP transgenic line, stably expressing L-FABP-eGFP fusion proteins within hepatocytes) (**Figure 4a,b**). Nanoparticle/macromolecule-conjugated, apoE target peptides (*amino acid sequence*: $(LRKLRKRLL)_2$; tandem-repeat LDLR target sequence (residues 159-167) of human apoE) have been previously shown to interact with LDLr, as well as the low-density lipoprotein receptor-related proteins, LRP1 and LRP2.[72–74] Following liposome (~5 mM) administration within a zebrafish embryo at 3 dpf (74 hpf), no significant fluorescence (eGFP) was observed in the region of the developing liver and apoE-targeted liposomes remained mostly freely circulating (**Figure 4c**). At 4 dpf (98 hpf), however, the liver of the embryo, delineated by transgenic eGFP-L-FABP fluorescence, was

evidently present and *i.v.* adminstered apoE-targeted liposomes now clearly accumulated within the liver vasculature (**Figure 4d-f**). Interestingly, we observed no significant colocalisation of apoE-targeted liposomes and hepatocytes within the liver at 1.5 hpi. This may be due to liposome accumulation within the Space of Disse, as has been described for the hepatic clearance of albumin within embryonic zebrafish at 12 dpf.[66] Crucially, however, unmodified DOPC liposomes did not accumulate within the embryonic liver of either a three- or four-day old embryo, confirming liver accumulation of apoE-targeted liposomes within a four-day old zebrafish embryo was exclusively mediated by apoE target peptides (**Figure S6**). Overall, these observations confirm apoE-mediated targeting of nanoparticles to the liver of the zebrafish embryo is possible from 4 dpf.

After verification of apoE-mediated liver targeting of liposomes, we next injected DSPC-LNPs (~10 mM, ~0.2 mg/kg mRNA, **Figure 5a-e**; ~30 mM, ~0.6 mg/kg mRNA, **Figure 5f-i**) and srLNPs (~30 mM, ~0.6 mg/kg mRNA, **Figure S7**) in four day old zebrafish embryos. In the case of srLNPs, particles remained largely associated within the PCV, CV and CHT of the 4 day old embryo at 1.5 hpi, and exogenous eGFP expression was primarily restricted within ECs of these venous blood vessels at 24 hpi. No significant srLNP accumulation (at 1.5 hpi) or mRNA expression (at 24 hpi) was observed within the liver, confirming RES targeting of srLNPs remains predominant even in the presence of a functional liver.

In the case of DSPC-LNPs (~10 mM), no signficant LNP liver accumulation (1.5 hpi), nor liver specific eGFP expression (24 hpi), was observed within the four day old embryo (**Figure 5b-e**). Increasing the dose threefold (~30 mM), however, did result in significant eGFP expression throughout the entire embryo, including the liver (**Figure 5f-i**). Again, with no apparent liver targeting of DSPC-LNPs at 1.5 hpi, these observations indicate that DSPC-LNPs ineffectively target functional hepatocytes of the embryonic zebrafish *via* endogenous apoE-mediated lipid trafficking pathways. Instead, DSPC-LNPs are liable to low-level non-specific uptake and mRNA delivery and expression across a wide range of cell types, as has been previously observed.[75]

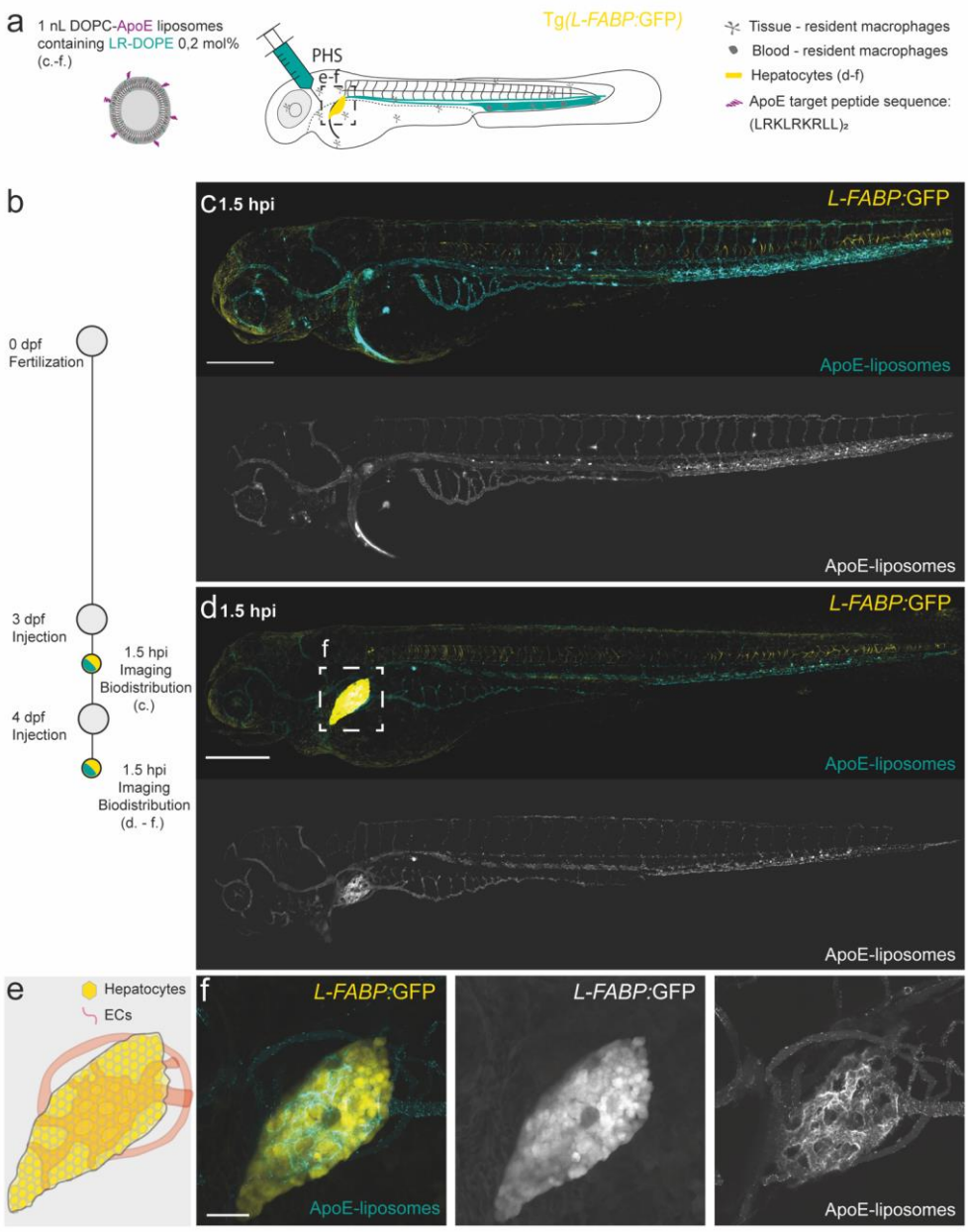


Figure 4. Biodistribution of apoE-targeted liposomes in three- and four-day old zebrafish embryos. (**a**) Schematic showing the site of apoE-targeted liposome injection (*i.v.*) within embryonic zebrafish (at 3 and 4 dpf). Liposomes contained 0.2 mol% DOPE-lissamine rhodamine as fluorescent lipid probe (cyan). *Injected dose*: ~5 mM lipid, ~5 mol% ApoE target ligand (*amino acid primary sequence*:

(LRKLRKRLL)$_2$), *Injection volume*: 1 nL. Transgenic *Tg*(*LFABP*:eGFP) zebrafish embryos stably express eGFP (yellow) within hepatocytes. PHS – primary head sinus. (**b**) Injection and imaging timeframe. (**c,d**) Whole embryo (10x magnification) views of apoE-targeted liposome biodistribution within (**c**) three- and (**d**) four-day old embryonic zebrafish at 1.5 hpi. (**e**) Tissue level schematic of the embryonic liver at 4 dpf. (**f**) Tissue level (40x magnification) views of apoE-targeted liposome biodistribution within the liver of a four-day old embryo. Within the embryonic liver, liposomes appear predominantly associated with ECs and not hepatocytes. Scale bars: 200 µm (whole embryo) and 50 µm (tissue level).

Next, we validated LNP biodistribution and LNP-mediated mRNA expression patterns in mice. In particular, we focused on cell-specific LNP distribution and mRNA expression within the murine liver, the largest RES organ in mammals. For all mouse experiments, LNP-mRNA formulations were injected (*i.v.*) in 8–10-week-old C57BL/6 mice (**Figure 6a**). To assess LNP distribution and functional mRNA delivery within individual hepatic and non-hepatic (*i.e.*, spleen) RES cell types, mice were anesthetized, a trans-cardiac collagenase perfusion performed, (parenchymal and non-parenchymal hepatic) cells were separated and individual cell types detected using cell-specific antibodies (**Figure S8** for representative flow cytometry density plots). To monitor LNP biodistribution across RES cell types and tissues, LNP-mRNA formulations, containing a non-exchangeable, fluorescent lipid probe (DiD, 0.5 mol%), were administered (**Figure 6b**). At 2 hpi, for both DSPC-LNPs and srLNPs (42.75 mg/kg total lipid), we observed striking LNP accumulation within mouse liver cell types (**Figure 6c**) compared to those of the spleen (**Figure S9**) which, although smaller than the liver, is a highly efficient unit of the mononuclear phagocyte system.[76] Notably, both LNP formulations distributed to all individually isolated hepatic cell types, as has previously been described for LNP formulations based on Onpattro®.[77,78] However, srLNPs demonstrated significantly enhanced uptake ($P < 0.001$) within all liver cell types relative to DSPC-LNPs (**Figure 6d**). This confirmed that incorporating anionic DSPG into LNP-mRNA delivery systems both enhances liver tropism in general and leads to a significant shift towards LNP targeting and cellular uptake within hepatic RES cell types.

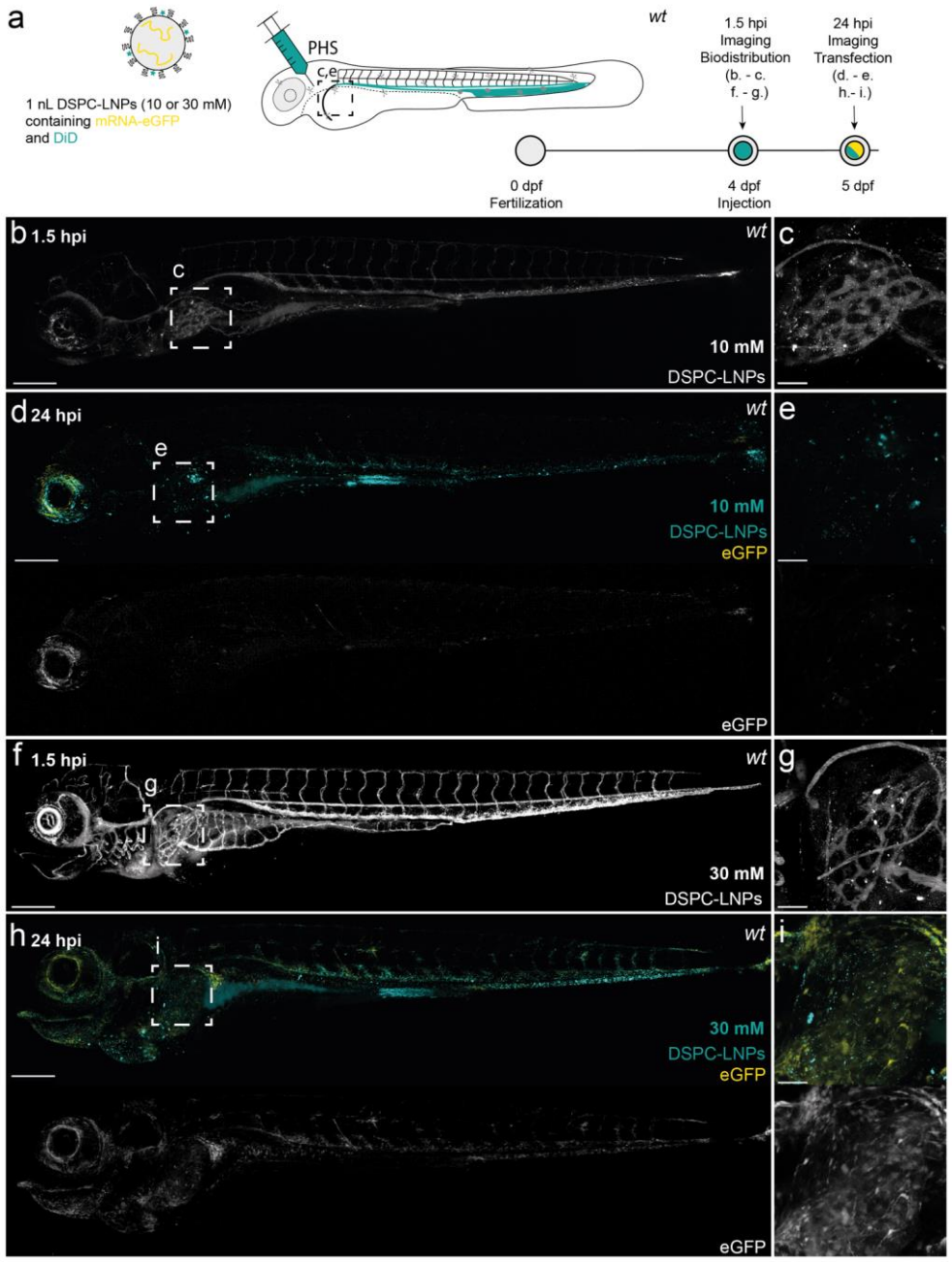


Figure 5. DSPC-LNP (10 and 30 mM) biodistribution and mRNA expression within, four-day old, wildtype (AB/TL) embryonic zebrafish. (**a**) Schematic showing the site of DSPC-LNP injection (*i.v.*) within embryonic zebrafish (4 dpf). DSPC-LNPs contained DiD (0.1 mol%) as fluorescent lipid probe

and unlabeled, eGFP mRNA (capped) payload. Injection and imaging timeframe. *Injection volume*: 1 nL. PHS – primary head sinus (**b,c**) Whole embryo (10x magnification) and tissue level (liver region, 40x magnification) views of DSPC-LNP biodistribution at 1.5 hpi. *Injected dose*: ~10 mM lipid, ~0.2 mg/kg mRNA. LNPs were mostly freely circulating with no significant accumulation in the liver at 1.5 hpi. Intense fluorescent punctae within the liver region are likely due to macrophage uptake. (**d,e**) Whole embryo (10x magnification) and tissue level (liver region, 40x magnification) views of eGFP expression at 24 hpi. (**f,g**) Whole embryo (10x magnification) and tissue level (liver region, 40x magnification) views of DSPC-LNP biodistribution at 1.5 hpi. *Injected dose*: ~30 mM lipid, ~0.6 mg/kg mRNA. At both dosages, LNPs were mostly freely circulating with no significant accumulation in the liver observed at 1.5 hpi. Intense fluorescent punctae within the liver region are likely due to macrophage LNP uptake. (**h,i**) Whole embryo (10x magnification) and tissue level (liver region, 40x magnification) views of eGFP expression at 24 hpi. At 30 mM dosage, low level eGFP fluorescence is observed throughout the embryo, including within the liver region. Confocal microscope settings were identical across all experiments. Scale bars: 200 µm (whole embryo) and 50 µm (tissue level).

To confirm functional mRNA delivery to hepatic RES cells, LNPs entrapping capped mCherry-mRNA (0.25 mg/kg mRNA) were administered (**Figure 6e**). This dosage is in line with other systemically administered LNP-mRNA therapies, including those currently in clinical trials (*e.g.* NCT03829384).[79] Following organ isolation and cell separation at 24 hpi, both srLNPs and DSPC-LNPs yielded comparable mCherry expression in hepatocytes, as well as within splenic RES cell types (**Figure 6f**, **Figure S9**). In contrast, srLNPs yielded significantly enhanced mRNA delivery to hepatic RES cell types relative to DSPC-LNPs ($P < 0.001$) (**Figure 6g**). Importantly, for both srLNPs and DSPC-LNPs, absolute mCherry expression levels within hepatocytes were significantly higher than other cell types analyzed. This apparent disparity between LNP cellular targeting and functional mRNA expression could be explained by the adverse (high) endosomal activity within LSECs and KCs (leading to significant mRNA degradation despite extensive LNP internalization), combined with the high translational efficiency of hepatocytes (leading to significant mRNA expression despite comparably low LNP internalization).[80] Interestingly, a four-fold dosage increase (1 mg/kg mRNA) resulted in significantly enhanced absolute mRNA expression within LSECs relative to hepatocytes and KCs, potentially indicative of dynamic competition between these cell types in recognizing and internalizing circulating LNPs (**Figure S10**). Since no LNP technology has yet demonstrated exclusive targeting to a single cell type *in vivo*, these findings reaffirm the importance of considering not only LNP biodistribution but also cellular physiology (both in the healthy and diseased state) in the development of new LNP technologies with novel targeting function. Overall, our data confirm that charge modifications to an LNP surface leads to preferential targeting of the hepatic RES and a significant increase in the absolute levels of functional mRNA expression within these cell types.

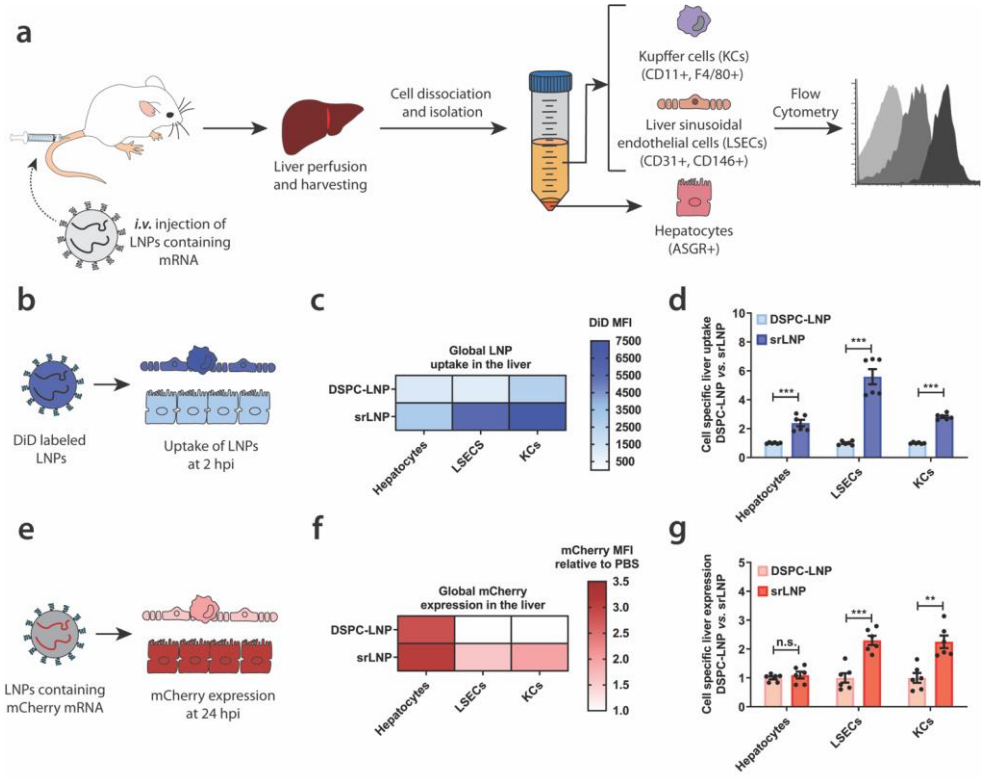


Figure 6. LNP uptake and functional mRNA delivery within different hepatic cell types. (**a**) Schematic illustrating the procedure to isolate different hepatic cell types and determine LNP-mRNA targeting and functional mRNA delivery. Following intravenous LNP-mRNA injection (*i.v*) the liver was perfused with collagenase IV, hepatic cells were isolated and stained with specific antibodies, and flow cytometry was used to analyze LNP uptake and gene expression. Specific antibody markers used to uniquely identify hepatocytes, LSECs and KCs, respectively, are defined in parentheses. (**b**) For intrahepatic biodistribution studies, LNPs contained DiD (0.5 mol%) as fluorescent lipid probe. Cellular uptake of DSPC-LNP and srLNP was assessed following mouse sacrifice at 2 hpi. *Injected dose*: 42.75 mg/kg total lipid. (**c**) Heatmap of global LNP uptake in the liver determined by absolute DiD fluorescence. srLNP demonstrate significantly enhanced LNP uptake within all hepatic cell types, and significant re-direction to hepatic RES compared to DSPC-LNPs. (**d**) Cell specific liver uptake normalized to DSPC-LNP for each cell type. (**e**) For gene expression experiments, LNPs contained capped, mCherry-mRNA. Functional mRNA delivery was assessed based on mCherry fluorescence levels following mouse sacrifice at 24 hpi. (**f**) Heatmap of mCherry expression in different liver cell types following functional mRNA delivery using DSPC-LNP and srLNP. *Injected dose*: 0.25 mg/kg mRNA. (**g**) Cell specific mCherry expression normalized to DSPC-LNP for each cell type. In all cases, n = 6 represents 3 separate liver tissue samples from 2 mice sorted

into individual cell types. Bars and error bars in d and g represent mean ± s.e.m. The data was normalized to the average uptake and expression of DSPC-LNPs within each cell type. Statistical significance was evaluated using a two-tailed unpaired Student's t-test. n.s. = not significant, ** $p < 0.01$, *** $p < 0.001$. Exact P values for d: Hepatocytes P= 0.00011, LSECs P= $1.12*10^{-5}$, KCs P= $3.62*10^{-9}$. Exact P values for g: Hepatocytes P= 0.464, LSECs P= 0.00064, KCs P= 0.0023.

3.3 Discussion

Based on a robust understanding of the nano-bio interactions involved,[36] we have rationally designed an LNP platform capable of preferentially targeting the hepatic RES and enhanced mRNA expression within hepatic RES cell types. Given the importance of the hepatic RES in establishing and maintaining the liver microenvironment, as well as in the pathogenesis of many liver-specific and systemic diseases,[26,81] including (auto)immune diseases,[35] we believe anionic LNP formulations can form the basis of future RNA gene therapies against acquired and inherited diseases in which hepatic RES cell types play a central role.[34] Here, it is important to recognize the extensive refinement of both ionizable[82–84] and sterol lipid components of LNPs[50] (primarily to promote endosomal rupture/escape and cytosolic RNA delivery), as well as chemical modifications to RNA (to improve stability, translation proficiency and reduce immunogenicity), that have already been made.[85–87] These optimized reagents can improve transfection efficiency >10-fold, compared to LNPs based on the lipid composition of Onpattro®,[82,83] meaning anionic, srLNP formulations could, if necessary, be simply retrofitted to widen any potential therapeutic window.

Existing LNP technologies that have demonstrated preferential RNA delivery to non-parenchymal hepatic cell types and/or non-hepatic cells have all been discovered through bottom-up empirical screens. These discoveries have not revealed the biological mechanisms underpinning any observed cellular preference. Preferential delivery of mRNA to liver ECs has, for example, been achieved through the replacement of cholesterol with either cholesteryl oleate or oxidized cholesterol components.[18,19] While these observations may conform to a charge-dependent, Stabilin-mediated mechanism of uptake within LSECs, as has been observed for both OxLDL and AcLDL,[27,88] in the absence of reported zeta potentials, and given both sterol reagents likely predominate within the LNP core, this could equally point to an alternative mechanism of LNP recognition and uptake within hepatic RES cell types. Alternatively, exclusive LNP-mediated RNA delivery to the spleen has been achieved by adding the anionic phospholipid, 18PA (up to 30 mol%), to the lipid composition of Onpattro®.[89] Assuming the measured surface charge of these formulations is also anionic (and given srLNPs showed negligible accumulation within the spleen), this suggests simply rendering an LNP anionic does not necessarily guarantee preferential

uptake within hepatic RES cell types. Overall, these studies highlight the complex interplay between LNP compositional makeup, biophysical properties and structure, and the implications these factors have in determining the *in vivo* fate of an LNP. Given the exploitable chemical space of an LNP is vast, the targeting of innate immune cells and hepatocytes – primed to recognize and internalize waste and/or pathogenic (lipid) particles – may therefore reflect only a small, easily accessible fraction of preferential LNP cellular tropisms. Consequently, the discovery of new LNP platforms capable of preferential cellular targeting beyond RES cells and/or hepatocytes would undoubtedly benefit from a more focused and informed screening approach.

To this end, the elucidation and exploitation of fundamental mechanisms dictating both endogenous and exogenous lipid particle fate *in vivo* can focus and direct empirical screens for new LNP formulations. It is worth emphasizing that all cells rely, to some extent, on systemic lipid transport to ensure correct function. We therefore believe the embryonic zebrafish is a powerful addition to the discovery pipeline for new LNP technologies,[37] both as a screening platform and as a tool to probe fundamental biology. As a screening and optimization tool, zebrafish embryos permit real-time, *in vivo* visualization of total LNP injected doses at cellular resolution. Furthermore, with a conserved repertoire of RES cell types, hepatocytes, soluble lipid transport proteins and receptors, the data acquired within these animals can offer accurate qualitative predictions of cell specific LNP recognition and uptake within key mammalian RES organs. Furthermore, up to 5 dpf, the number of different LNP formulations that can be screened is limited only by practical considerations of time and capacity. As a fundamental tool to elucidate biological mechanisms underpinning LNP transport and RNA delivery, the short generational time of the zebrafish (approx. 3 months), the extensive repertoire of established (fluorescent) transgenic lines and antibodies,[90,91] optimized techniques for genetic manipulation (including CRISPR/Cas)[92] and advanced imaging techniques, enable key nano-bio interactions underpinning LNP fate *in vivo* to be rapidly assessed and confirmed.

In conclusion, the widespread evaluation of LNP-based mRNA therapies as potential prophylactic vaccines,[93,94] notably against COVID-19,[95–98] has provided further proof of the broad therapeutic potential of these platform mRNA technologies. Despite the obvious differences in therapeutic target, mode of action and injection site, however, all LNP-mRNA vaccine candidates to date closely resemble the lipid composition of Onpattro®. In particular, LNP surface lipids (*i.e.* "helper" phospholipids and PEG lipids), cholesterol content and overall lipid composition are strikingly similar between different clinical formulations. Based on our observations, these vaccines can be expected to elicit broad mRNA expression profiles. Indeed, following intramuscular (*i.m.*) injection of an LNP-

mRNA COVID-19 vaccine candidate, mRNA (coding for the receptor binding domain (RBD) of SARS-CoV-2) expression was observed across a broad spectrum of cell types, including intramuscular and hepatic immune cells, as well as hepatocytes.[95] However, while the ability to leverage a wide array of cell types to produce a therapeutic protein may be safe and effective as a systemic secreted therapy (*i.e.* suitable for vaccine application), the lack of LNP designs capable of preferentially delivering RNA to specific diseased cells and tissues in the body remains a major limitation. For although cell specificity of LNP-mRNA systems can be enhanced, for example, through microRNA regulation of mRNA expression,[99] these technologies still rely on LNPs reaching and delivering functional mRNA within target cells at therapeutically relevant doses. To this end, we believe a top-down approach to LNP discovery, based on pre-existing knowledge of the nano-bio interactions, can guide and focus (high throughput) empirical screening. This will surely expedite the necessary discovery of new LNP designs with inherent tropisms for specific and varied cell types.

3.4 References

1. Delivering the promise of RNA therapeutics. *Nat. Med.* **25**, 1321 (2019).
2. Dammes, N. & Peer, D. Paving the Road for RNA Therapeutics. *Trends Pharmacol. Sci.* **41**, 755–775 (2020).
3. Yin, H. *et al.* Non-viral vectors for gene-based therapy. *Nat. Rev. Genet.* **15**, 541–555 (2014).
4. Cullis, P. R. & Hope, M. J. Lipid Nanoparticle Systems for Enabling Gene Therapies. *Mol. Ther.* **25**, 1467–1475 (2017).
5. Kulkarni, J. A., Witzigmann, D., Chen, S., Cullis, P. R. & van der Meel, R. Lipid Nanoparticle Technology for Clinical Translation of siRNA Therapeutics. *Acc. Chem. Res.* **52**, 2435–2444 (2019).
6. Akinc, A. *et al.* The Onpattro story and the clinical translation of nanomedicines containing nucleic acid-based drugs. *Nat. Nanotechnol.* **14**, 1084–1087 (2019).
7. Adams, D. *et al.* Patisiran, an RNAi therapeutic, for hereditary transthyretin amyloidosis. *N. Engl. J. Med.* **379**, 11–21 (2018).
8. Kumar, V. *et al.* Shielding of Lipid Nanoparticles for siRNA Delivery: Impact on Physicochemical Properties, Cytokine Induction, and Efficacy. *Mol. Ther. Nucleic Acids* **3**, e210 (2014).
9. Mui, B. L. *et al.* Influence of Polyethylene Glycol Lipid Desorption Rates on Pharmacokinetics and Pharmacodynamics of siRNA Lipid Nanoparticles. *Mol. Ther. Nucleic Acids* **2**, e139 (2013).
10. Akinc, A. *et al.* Targeted delivery of RNAi therapeutics with endogenous and exogenous ligand-based mechanisms. *Mol. Ther.* **18**, 1357–1364 (2010).
11. Nguyen, J. & Szoka, F. C. Nucleic acid delivery: the missing pieces of the puzzle? *Acc. Chem. Res.* **45**, 1153–1162 (2012).
12. Sato, Y. *et al.* Highly specific delivery of siRNA to hepatocytes circumvents endothelial cell-mediated lipid nanoparticle-associated toxicity leading to the safe and efficacious decrease in the hepatitis B virus. *J. Control. Release* **266**, 216–225 (2017).

13. DeRosa, F. *et al.* Therapeutic efficacy in a hemophilia B model using a biosynthetic mRNA liver depot system. *Gene Ther.* **23**, 699–707 (2016).
14. Ramaswamy, S. *et al.* Systemic delivery of factor IX messenger RNA for protein replacement therapy. *Proc. Natl. Acad. Sci. U. S. A.* **114**, E1941–E1950 (2017).
15. Chen, S. *et al.* Development of lipid nanoparticle formulations of siRNA for hepatocyte gene silencing following subcutaneous administration. *J. Control. Release* **196**, 106–112 (2014).
16. Sago, C. D. *et al.* Nanoparticles That Deliver RNA to Bone Marrow Identified by in Vivo Directed Evolution. *J. Am. Chem. Soc.* **140**, 17095–17105 (2018).
17. Lokugamage, M. P., Sago, C. D., Gan, Z., Krupczak, B. R. & Dahlman, J. E. Constrained Nanoparticles Deliver siRNA and sgRNA to T Cells In Vivo without Targeting Ligands. *Adv. Mater.* **31**, 1902251 (2019).
18. Paunovska, K. *et al.* Analyzing 2,000 in vivo Drug Delivery Data Points Reveals Cholesterol Structure Impacts Nanoparticle Delivery. *ACS Nano* **12**, 8341–8349 (2018).
19. Paunovska, K. *et al.* Nanoparticles Containing Oxidized Cholesterol Deliver mRNA to the Liver Microenvironment at Clinically Relevant Doses. *Adv. Mater.* **31**, e1807748 (2019).
20. Witzigmann, D., Hak, S. & van der Meel, R. Translating nanomedicines: Thinking beyond materials? A young investigator's reply to 'The Novelty Bubble'. *J. Control. Release* **290**, 138–140 (2018).
21. Trefts, E., Gannon, M. & Wasserman, D. H. The liver. *Curr. Biol.* **27**, R1147–R1151 (2017).
22. Wisse, E. An electron microscopic study of the fenestrated endothelial lining of rat liver sinusoids. *J. Ultrastruct. Res.* **31**, 125–150 (1970).
23. Braet, F. & Wisse, E. Structural and functional aspects of liver sinusoidal endothelial cell fenestrae: a review. *Comp. Hepatol.* **1**, 1–17 (2002).
24. Smedsrød, B., Pertoft, H., Gustafson, S. & Laurent, T. C. Scavenger functions of the liver endothelial cell. *Biochem. J.* **266**, 313–327 (1990).
25. Sørensen, K. K., Simon-Santamaria, J., McCuskey, R. S. & Smedsrød, B. Liver sinusoidal endothelial cells. *Compr. Physiol.* **5**, 1751–1774 (2015).
26. Poisson, J. *et al.* Liver sinusoidal endothelial cells: Physiology and role in liver diseases. *J. Hepatol.* **66**, 212–227 (2017).
27. Li, R. *et al.* Role of liver sinusoidal endothelial cells and stabilins in elimination of oxidized low-density lipoproteins. *Am. J. Physiol. Gastrointest. Liver Physiol.* **300**, G71–G81 (2010).
28. Smedsrød, B. Clearance function of scavenger endothelial cells. *Comp. Hepatol.* **3**, S22 (2004).
29. Ganesan, L. P. *et al.* Rapid and Efficient Clearance of Blood-borne Virus by Liver Sinusoidal Endothelium. *PLOS Pathog.* **7**, e1002281 (2011).
30. Mates, J. M. *et al.* Mouse Liver Sinusoidal Endothelium Eliminates HIV-Like Particles from Blood at a Rate of 100 Million per Minute by a Second-Order Kinetic Process . *Frontiers in Immunology* **8**, 35 (2017).
31. Sørensen, K. K. *et al.* The scavenger endothelial cell: a new player in homeostasis and immunity. *Am. J. Physiol. Integr. Comp. Physiol.* **303**, R1217–R1230 (2012).
32. Schledzewski, K. *et al.* Deficiency of liver sinusoidal scavenger receptors stabilin-1 and -2 in mice causes glomerulofibrotic nephropathy via impaired hepatic clearance of noxious blood factors. *J. Clin. Invest.* **121**, 703–714 (2011).
33. McCourt, P. A. G. *et al.* The liver sinusoidal endothelial cell hyaluronan receptor and its homolog, stabilin-1 - Their roles (known and unknown) in endocytosis. *Comp. Hepatol.* **3**, S24 (2004).
34. Wilkinson, A. L., Qurashi, M. & Shetty, S. The Role of Sinusoidal Endothelial Cells in the Axis of Inflammation and Cancer Within the Liver . *Frontiers in Physiology* **11**, 990 (2020).

35. Shetty, S., Lalor, P. F. & Adams, D. H. Liver sinusoidal endothelial cells — gatekeepers of hepatic immunity. *Nat. Rev. Gastroenterol. Hepatol.* **15**, 555–567 (2018).
36. Campbell, F. *et al.* Directing Nanoparticle Biodistribution through Evasion and Exploitation of Stab2-Dependent Nanoparticle Uptake. *ACS Nano* **12**, 2138–2150 (2018).
37. Sieber, S. *et al.* Zebrafish as a preclinical in vivo screening model for nanomedicines. *Adv. Drug Deliv. Rev.* **151–152**, 152–168 (2019).
38. Seternes, T., Sørensen, K. & Smedsrød, B. Scavenger endothelial cells of vertebrates: a nonperipheral leukocyte system for high-capacity elimination of waste macromolecules. *Proc. Natl. Acad. Sci. U. S. A.* **99**, 7594–7597 (2002).
39. Smedsrod, B. Scavenger function of liver sinusoidal endothelial cells. *FASEB J.* **23**, 66.1 (2009).
40. Hayashi, Y. *et al.* Differential Nanoparticle Sequestration by Macrophages and Scavenger Endothelial Cells Visualized in Vivo in Real-Time and at Ultrastructural Resolution. *ACS Nano* **14**, 1665–1681 (2020).
41. Arteta, M. Y. *et al.* Successful reprogramming of cellular protein production through mRNA delivered by functionalized lipid nanoparticles. *Proc. Natl. Acad. Sci. U. S. A.* **115**, E3351–E3360 (2018).
42. Yamamoto, T. & Ryan, R. O. Anionic phospholipids inhibit apolipoprotein E—Low-density lipoprotein receptor interactions. *Biochem. Biophys. Res. Commun.* **354**, 820–824 (2007).
43. Evers, M. J. W. *et al.* State-of-the-Art Design and Rapid-Mixing Production Techniques of Lipid Nanoparticles for Nucleic Acid Delivery. *Small Methods* **2**, 1700375 (2018).
44. Kulkarni, J. A., Witzigmann, D., Leung, J., Tam, Y. Y. C. & Cullis, P. R. On the role of helper lipids in lipid nanoparticle formulations of siRNA. *Nanoscale* **11**, 21733–21739 (2019).
45. Kulkarni, J. A. *et al.* On The Formation and Morphology of Lipid Nanoparticles Containing Ionizable Cationic Lipids and siRNA. *ACS Nano* **12**, 4787–4795 (2018).
46. Leung, A. K. K. *et al.* Lipid nanoparticles containing siRNA synthesized by microfluidic mixing exhibit an electron-dense nanostructured core. *J. Phys. Chem. C* **116**, 18440–18450 (2012).
47. Kulkarni, J. A. *et al.* Fusion-dependent formation of lipid nanoparticles containing macromolecular payloads. *Nanoscale* **11**, 9023–9031 (2019).
48. Crawford, R. *et al.* Analysis of lipid nanoparticles by Cryo-EM for characterizing siRNA delivery vehicles. *Int. J. Pharm.* **403**, 237–244 (2011).
49. Eygeris, Y., Patel, S., Jozic, A. & Sahay, G. Deconvoluting Lipid Nanoparticle Structure for Messenger RNA Delivery. *Nano Lett.* **20**, 4543–4549 (2020).
50. Patel, S. *et al.* Naturally-occurring cholesterol analogues in lipid nanoparticles induce polymorphic shape and enhance intracellular delivery of mRNA. *Nat. Commun.* **11**, 983 (2020).
51. Arias-Alpizar, G. *et al.* Stabilin-1 is required for the endothelial clearance of small anionic nanoparticles. *Nanomedicine Nanotechnology, Biol. Med.* **34**, 102395 (2021).
52. Reiser, A. *et al.* Correlation of mRNA delivery timing and protein expression in lipid-based transfection. *Integr. Biol.* **11**, 362–371 (2019).
53. Balleza, E., Kim, J. M. & Cluzel, P. Systematic characterization of maturation time of fluorescent proteins in living cells. *Nat. Methods* **15**, 47–51 (2018).
54. Lopes, S. *et al.* Leukocyte Tyrosine Kinase Functions in Pigment Cell Development. *PLoS Genet.* **4**, e1000026 (2008).
55. Leonhardt, C. *et al.* Single-cell mRNA transfection studies: Delivery, kinetics and statistics by numbers. *Nanomedicine Nanotechnology, Biol. Med.* **10**, 679–688 (2014).

56. Patel, S. *et al.* Brief update on endocytosis of nanomedicines. *Adv. Drug Deliv. Rev.* **144**, 90–111 (2019).
57. Gilleron, J. *et al.* Image-based analysis of lipid nanoparticle–mediated siRNA delivery, intracellular trafficking and endosomal escape. *Nat. Biotechnol.* **31**, 638–646 (2013).
58. Sahay, G. *et al.* Efficiency of siRNA delivery by lipid nanoparticles is limited by endocytic recycling. *Nat. Biotechnol.* **31**, 653–658 (2013).
59. Miller, C. M. *et al.* Stabilin-1 and Stabilin-2 are specific receptors for the cellular internalization of phosphorothioate-modified antisense oligonucleotides (ASOs) in the liver. *Nucleic Acids Res.* **44**, 2782–2794 (2016).
60. Wilkins, B. J. & Pack, M. Zebrafish models of human liver development and disease. *Compr. Physiol.* **3**, 1213–1230 (2013).
61. Wang, S., Miller, S. R., Ober, E. A. & Sadler, K. C. Making It New Again: Insight Into Liver Development, Regeneration, and Disease From Zebrafish Research. *Curr. Top. Dev. Biol.* **124**, 161–195 (2017).
62. Korzh, S. *et al.* Requirement of vasculogenesis and blood circulation in late stages of liver growth in zebrafish. *BMC Dev. Biol.* **8**, 84 (2008).
63. Mudumana, S. P., Wan, H., Singh, M., Korzh, V. & Gong, Z. Expression analyses of zebrafish transferrin, ifabp, and elastaseB mRNAs as differentiation markers for the three major endodermal organs: liver, intestine, and exocrine pancreas. *Dev. Dyn. an Off. Publ. Am. Assoc. Anat.* **230**, 165–173 (2004).
64. Her, G. M., Chiang, C.-C., Chen, W.-Y. & Wu, J.-L. In vivo studies of liver-type fatty acid binding protein (L-FABP) gene expression in liver of transgenic zebrafish (Danio rerio). *FEBS Lett.* **538**, 125–133 (2003).
65. Yin, C., Evason, K. J., Maher, J. J. & Stainier, D. Y. R. The basic helix-loop-helix transcription factor, heart and neural crest derivatives expressed transcript 2, marks hepatic stellate cells in zebrafish: analysis of stellate cell entry into the developing liver. *Hepatology* **56**, 1958–1970 (2012).
66. Cheng, D., Morsch, M., Shami, G. J., Chung, R. S. & Braet, F. Albumin uptake and distribution in the zebrafish liver as observed via correlative imaging. *Exp. Cell Res.* **374**, 162–171 (2019).
67. Otis, J. P. *et al.* Zebrafish as a model for apolipoprotein biology: comprehensive expression analysis and a role for ApoA-IV in regulating food intake. *Dis. Model. Mech.* **8**, 295–309 (2015).
68. Babin, P. J. *et al.* Both apolipoprotein E and A-I genes are present in a nonmammalian vertebrate and are highly expressed during embryonic development. *Proc. Natl. Acad. Sci.* **94**, 8622–8627 (1997).
69. Liu, C. *et al.* Modeling hypercholesterolemia and vascular lipid accumulation in LDL receptor mutant zebrafish. *J. Lipid Res.* **59**, 391–399 (2018).
70. O'Hare, E. A. *et al.* Disruption of ldlr causes increased LDL-c and vascular lipid accumulation in a zebrafish model of hypercholesterolemia. *J. Lipid Res.* **55**, 2242–2253 (2014).
71. Schlegel, A. Zebrafish Models for Dyslipidemia and Atherosclerosis Research . *Frontiers in Endocrinology* **7**, 159 (2016).
72. Wang, D. *et al.* Engineering a lysosomal enzyme with a derivative of receptor-binding domain of apoE enables delivery across the blood-brain barrier. *Proc. Natl. Acad. Sci. U. S. A.* **110**, 2999–3004 (2013).
73. Jiang, Y., Zhang, J., Meng, F. & Zhong, Z. Apolipoprotein E Peptide-Directed Chimeric Polymersomes Mediate an Ultrahigh-Efficiency Targeted Protein Therapy for Glioblastoma. *ACS Nano* **12**, 11070–11079 (2018).
74. Böckenhoff, A. *et al.* Comparison of five peptide vectors for improved brain delivery of the

lysosomal enzyme arylsulfatase A. *J. Neurosci.* **34**, 3122–3129 (2014).
75. Patton, C., Farr, G. H., An, D., Martini, P. G. V. & Maves, L. Lipid Nanoparticle Packaging Is an Effective and Nontoxic mRNA Delivery Platform in Embryonic Zebrafish. *Zebrafish* **15**, 217–227 (2018).
76. Mayer, L. D., Cullis, P. R. & Bally, M. B. Designing therapeutically optimized liposomal anticancer delivery systems: Lessons from conventional liposomes. in *Medical Applications of Liposomes* 231–257 (Elsevier Science B.V., 1998).
77. Sago, C. D., Krupczak, B. R., Lokugamage, M. P., Gan, Z. & Dahlman, J. E. Cell Subtypes Within the Liver Microenvironment Differentially Interact with Lipid Nanoparticles. *Cell. Mol. Bioeng.* **12**, 389–397 (2019).
78. Shi, B. *et al.* Biodistribution of small interfering RNA at the organ and cellular levels after lipid nanoparticle-mediated delivery. *J. Histochem. Cytochem.* **59**, 727–740 (2011).
79. Moderna Announces Positive Phase 1 Results for the First Systemic Messenger RNA Therapeutic Encoding a Secreted Protein (mRNA-1944). (2019). Available at: https://investors.modernatx.com/news-releases/news-release-details/moderna-announces-positive-phase-1-results-first-systemic. (Accessed: 21st December 2020)
80. Schulze, R. J., Schott, M. B., Casey, C. A., Tuma, P. L. & McNiven, M. A. The cell biology of the hepatocyte: A membrane trafficking machine. *J. Cell Biol.* **218**, 2096–2112 (2019).
81. Ni, Y. *et al.* Pathological process of liver sinusoidal endothelial cells in liver diseases. *World J. Gastroenterol.* **23**, 7666–7677 (2017).
82. Rietwyk, S. & Peer, D. Next-Generation Lipids in RNA Interference Therapeutics. **11**, 7572–7586 (2017).
83. Miao, L. *et al.* Delivery of mRNA vaccines with heterocyclic lipids increases anti-tumor efficacy by STING-mediated immune cell activation. *Nat. Biotechnol.* **37**, 1174–1185 (2019).
84. Hassett, K. J. *et al.* Optimization of Lipid Nanoparticles for Intramuscular Administration of mRNA Vaccines. *Mol. Ther. - Nucleic Acids* **15**, 1–11 (2019).
85. Khvorova, A. & Watts, J. K. The chemical evolution of oligonucleotide therapies of clinical utility. *Nat. Biotechnol.* **35**, 238–248 (2017).
86. Ku, S. H., Jo, S. D., Lee, Y. K., Kim, K. & Kim, S. H. Chemical and structural modifications of RNAi therapeutics. *Adv. Drug Deliv. Rev.* **104**, 16–28 (2016).
87. Shen, X. & Corey, D. R. Chemistry, mechanism and clinical status of antisense oligonucleotides and duplex RNAs. *Nucleic Acids Res.* **46**, 1584–1600 (2017).
88. De Rijke, Y. B., Biessen, E. A., Vogelezang, C. J. & van Berkel, T. J. Binding characteristics of scavenger receptors on liver endothelial and Kupffer cells for modified low-density lipoproteins. *Biochem. J.* **304**, 69–73 (1994).
89. Cheng, Q. *et al.* Selective organ targeting (SORT) nanoparticles for tissue-specific mRNA delivery and CRISPR–Cas gene editing. *Nat. Nanotechnol.* **15**, 313–320 (2020).
90. Staudt, N. *et al.* A panel of recombinant monoclonal antibodies against zebrafish neural receptors and secreted proteins suitable for wholemount immunostaining. *Biochem. Biophys. Res. Commun.* **456**, 527–533 (2015).
91. Burket, C. T. *et al.* Generation and characterization of transgenic zebrafish lines using different ubiquitous promoters. *Transgenic Res.* **17**, 265–279 (2008).
92. Varshney, G. K. *et al.* High-throughput gene targeting and phenotyping in zebrafish using CRISPR/Cas9. *Genome Res.* **25**, 1030–1042 (2015).
93. Pardi, N., Hogan, M. J., Porter, F. W. & Weissman, D. mRNA vaccines — a new era in vaccinology. *Nat. Rev. Drug Discov.* **17**, 261–279 (2018).
94. John, S. *et al.* Multi-antigenic human cytomegalovirus mRNA vaccines that elicit potent

humoral and cell-mediated immunity. *Vaccine* **36**, 1689–1699 (2018).
95. Zhang, N.-N. *et al.* A Thermostable mRNA Vaccine against COVID-19. *Cell* **182**, 1271–1283 (2020).
96. Jackson, L. A. *et al.* An mRNA Vaccine against SARS-CoV-2 — Preliminary Report. *N. Engl. J. Med.* **383**, 1920–1931 (2020).
97. McKay, P. F. *et al.* Self-amplifying RNA SARS-CoV-2 lipid nanoparticle vaccine candidate induces high neutralizing antibody titers in mice. *Nat. Commun.* **11**, 3523 (2020).
98. Lu, J. *et al.* A COVID-19 mRNA vaccine encoding SARS-CoV-2 virus-like particles induces a strong antiviral-like immune response in mice. *Cell Res.* **30**, 936–939 (2020).
99. Jain, R. *et al.* MicroRNAs Enable mRNA Therapeutics to Selectively Program Cancer Cells to Self-Destruct. *Nucleic Acid Ther.* **28**, 285–296 (2018).

Chapter 4

Site Selective Binding of Apolipoprotein E in the Protein Corona of Anionic Liposomes

Protein adsorption to the surface of nanoparticles can change the *in vivo* fate of nanoparticles, for example through facilitating or inhibiting interactions with specific receptors. However, current understanding of the protein corona remains superficial, typically describing the combined effect of multiple proteins, and lacking the mechanistic understanding of individual proteins. A key challenge is deciphering the binding sites and roles of individual proteins within the protein corona of nanoparticles. Herein, we show the site-selective binding of apolipoprotein E (APOE) to anionic nanoparticles. Using a photoaffinity-based chemoproteomic approach, we were able to show the repetitive and reproducible binding of specific proteins in the protein corona of various zwitterionic and anionic liposomes and lipid nanoparticles (LNPs). Furthermore, using a competition experiment revealed that APOE binding to anionic liposomes occurs through its heparin binding domain, while APOE binding to zwitterionic liposomes and LNPs occurs in a non-heparin competitive manner through its lipid binding domain. These results greatly deepen our understanding of protein corona binding to nanoparticles towards a molecular level, and allow for the targeted design of experiments in order to determine the *in vivo* effect of single proteins in the nanoparticle protein corona.

This chapter was prepared as a research article: R. Pattipeiluhu, B.I. Florea, K. Dickie, T.H. Sharp, F. Campbell, A. Kros

4.1 Introduction

The protein corona of nanoparticles describes the preferential adsorption of proteins from a biological medium to the surface of a nanoparticle.[1,2] Here, the alteration from a "synthetic identity" to a "biological identity" of nanoparticles is known to significantly influence the *in vivo* behavior of nanoparticles,[3,4] for example through promotion of bodily clearance mechanisms or shielding active targeting ligands.[5–8] Therefore, the interaction of nanoparticles with cells is, to some extent, believed to be regulated by a protein corona intermediate. The composition and complexity of the protein corona is dependent on the characteristics of the nanoparticle, such as chemical composition, size and surface charge (**Figure 1a**). Furthermore, the biological media to which the nanoparticle is exposed, as well as the kinetics of protein binding are believed to influence the protein composition.[9,10]

These parameters have led researchers to report a large number of protein corona fingerprints, which has revealed their dynamic complexity, but also contributes to the fact that our understanding of the protein corona remains superficial and elusive, typically describing the effect of a combination of proteins, instead of more in-depth understanding of individual proteins.[5,11,12] In addition, commonly applied methods are limited by biased isolation of large and abundant proteins, interference of endogenously present nanoparticles (*e.g.*, HDL, LDL, chylomicrons) and insufficient or non-native isolation of nanoparticle-protein complexes.[13–15] The resulting protein corona fingerprints generated are therefore typically long and empirical lists, displaying high similarity despite large differences in the synthetic identity of the nanoparticles.[7,16–18] Furthermore, the majority of these methods do not allow validation of binding for the discovered hits, hindering the confirmation and in-depth understanding of key nanoparticle-protein interactions. Recently, more research has been dedicated towards the development of new methods for the identification and validation of the protein corona on nanoparticles.[19,20] We have, to this end, developed a bifunctional lipid probe (IKS02, **Figure 1b**) for a photoaffinity-based chemoproteomic approach in order to covalently capture, isolate and identify the protein corona on liposomes in human plasma (**Figure 1c**).[21] Utilizing the covalent capture of adsorbed proteins allowed us to validate the selectivity of protein binding *in vitro*, crucially complementing the initial hit from a complex biological system.

Here, we employ this photoaffinity based chemoproteomics method for the identification of the protein corona on ionizable lipid nanoparticles (LNPs) encapsulating siRNA, which highly complements key nanoparticle-protein interactions described in literature. Furthermore, we are able to compare these findings to liposome formulations with distinct synthetic identities, and consequently pinpoint reproducible and selective binding of

individual proteins. Specifically, we show that apolipoprotein E (APOE) binds to a variety of anionic liposomes, but only a subset of zwitterionic neutral lipidic nanoparticles. Using a competition assay, we reveal that this APOE binding to anionic liposomes occurs site selectively through its heparin binding domain. Our findings display a unique selectivity of an individual protein in the protein corona of various nanoparticles, which contributes to the deeper understanding of nano-bio interactions and will allow for the specific mechanistic evaluation of these nanoparticles *in vivo*.

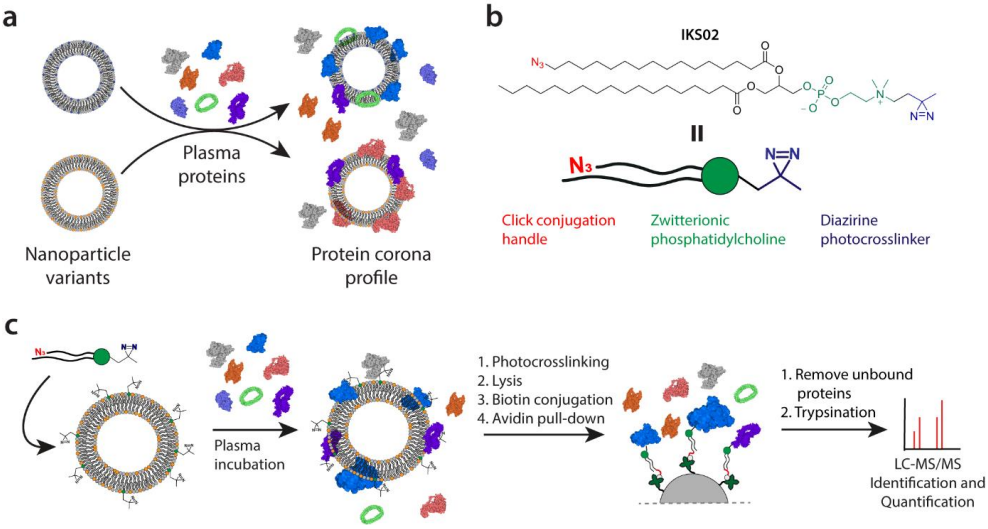


Figure 1. Photoaffinity based chemoproteomic approach for the identification of the liposome protein corona. (**a**) Schematic representation of how nanoparticle variation can lead to alteration of the protein corona profile. (**b**) Structure and schematic of bifunctional lipid probe IKS02, containing a diazirine photo crosslinker, zwitterionic phosphatidylcholine and azide functionality for click chemistry conjugation. (**c**) Methodology for identification of the liposome protein corona by co-formulation with IKS02, followed by incubation, crosslinking, pull-down and LC-MS/MS identification and quantification. Protein structures were obtained from the protein data bank (PDB) and their depiction was generated using Illustrate.[22]

4.2 Results

Our first goal was aimed at expanding the photoaffinity-based chemoproteomic approach for the identification of the protein corona of LNPs. LNPs are multicomponent systems typically consisting of an ionizable lipid (*e.g.*, DLin-MC3-DMA),[23] structural lipid (*e.g.*, cholesterol), helper lipid (*e.g.*, DSPC), PEG lipid and an oligonucleotide payload (*e.g.*, mRNA, siRNA).[24,25] LNPs have realized the transition of RNA therapeutics to the clinic,

serving as state-of-the-art carriers for the cytosolic delivery of RNA molecules. In 2018, Onpattro® was approved as the first RNA interference (RNAi) drug, used for the treatment of hereditary ATTR amyloidosis by delivering siRNA molecules to liver hepatocytes.[26] More recently, LNPs have been utilized for the delivery of mRNA for the safe and efficient development of prophylactic vaccines against SARS-CoV-2.[27,28] Currently, there is a large variety of LNP formulations being studied, composed of typically novel or proprietary ionizable lipids (ILs).[29]

In our approach, we studied the Onpattro® formulation, with its siRNA cargo Patisiran®,[30] for two distinct reasons. Firstly, the organization of lipids within this formulation has been studied in-depth, showing that the surface of this nanoparticle is enriched with 1,2-distearoyl-sn-glycero-3-phosphocholine (DSPC) and 1,2-Dimyristoyl-*rac*-glycero-3-methoxypolyethylene glycol-2000 (DMG-PEG2000) (**Figure 2a**).[31] In addition, it has been shown that exchanging DSPC in this formulation with similar analogues keeps this surface enrichment intact.[32] With IKS02 being a close mimic of DSPC, we hypothesized that this lipid would be sufficiently enriched at the surface of these LNPs in order to enable crosslinking of the protein corona. Secondly, the importance of APOE is known in relation to its *in vivo* effect, where its presence in plasma is required for the efficient uptake of LNPs and silencing the target protein in liver hepatocytes through the lipoprotein-receptor family.[33,34] Together, these findings suggest a crucial role for the binding of APOE to the LNP surface and thereby serves as a fitting positive control for our identification method. To this end, we incorporated IKS02 at 5 mol%, exchanging for DSPC, and performed the assembly using conventional microfluidic procedures. Cryogenic transmission electron microscopy (cryoTEM), dynamic light scattering (DLS) and ζ-potential measurements of LNPs formulated with IKS02, compared to the native Onpattro® formulation, revealed no significant changes in nanoparticle morphology, size and surface charge (**Figure 2b,c and Table S1**). Following assembly, LNPs were incubated in full human plasma for 1 hour at 37 °C, followed by crosslinking with UV-A light (350 nm, 15 min) to capture the adsorbed proteins. The mixture was lysed, the proteins were precipitated and biotin was conjugated to the crosslinked lipid-protein conjugates through copper-catalyzed click chemistry, followed by pull-down using avidin-agarose beads. Finally, on-bead digestion allowed for the LC-MS/MS identification and quantification of the proteins. In order to correctly identify hits from this method, a negative control in which the sample is not irradiated with UV-A light was employed, allowing for a comparison to the background labeling observed due to the copper catalyzed click chemistry. The quantified proteins are displayed in a volcano plot describing the abundance (>1.5-fold) and statistical significance ($p < 0.05$) of proteins in the "+UV" sample over the "-UV" control (**Figure 2d**). Proteins meeting these

criteria are selected as hits and can be sorted based on relative abundance derived from their label free quantification within the sample (**Figure 2e**). From these results, APOE is positively identified at a relative abundance of ~25%. Furthermore, the protein corona of Onpattro® is dominated by other apolipoproteins, such as APOA1 and apoB. These findings highlight the large similarity of this LNP formulation to endogenous nanoparticles such as low-density lipoprotein (LDL), and support the fact that this LNPs exploits similar endogenous uptake mechanisms through a protein corona intermediate.

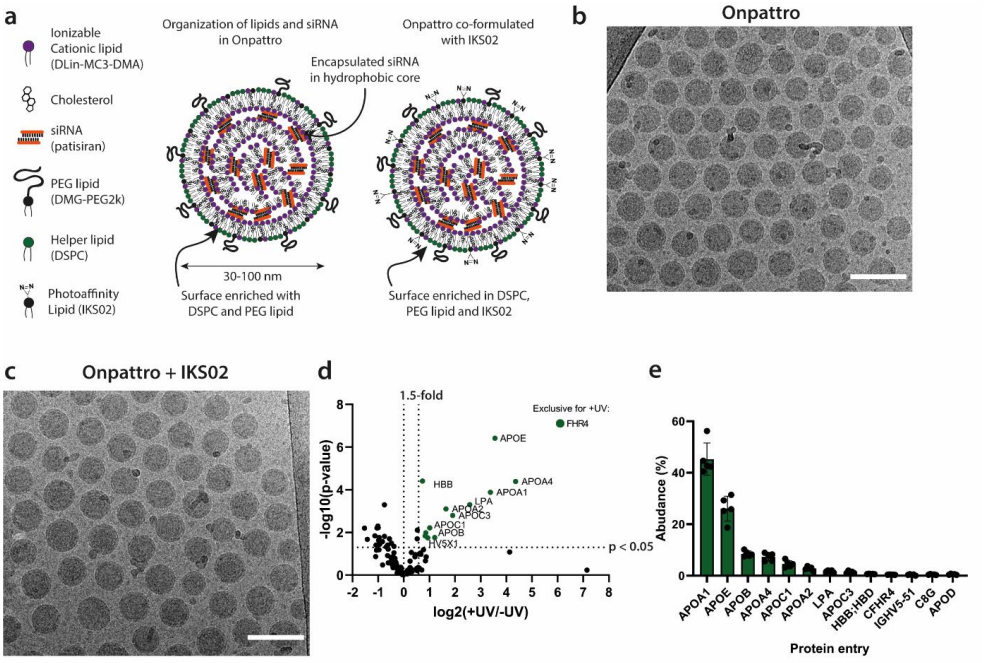


Figure 2. Application of photoaffinity based chemoproteomic approach for the identification of the protein corona of LNPs. (**a**) Schematic representation of the lipid organization in LNPs. Surface enriched DSPC can be replaced by IKS02. (**b,c**) CryoTEM images of native Onpattro and Onpattro co-formulated with 5 mol% of IKS02. Scale bars are 100 nm. (**d**) Volcano plot of identified proteins of "+UV" and "-UV". Hits were selected when meeting the criteria for for p-values ($p < 0.05$) and enrichment (>1.5-fold) and are displayed in green. (**e**) Protein abundance of identified hits described in **d**. Bar plots and errors bars represent the average ($n = 5$) and standard deviation.

Previously, we have reported the protein corona of anionic liposomes, with the lipid composition of AmBisome®,[35,36] where APOE was found as the most abundant protein of its protein corona.[21] The high abundancy of a single protein on two very distinct lipid surfaces, anionic AmBisome® vs. zwitterionic neutral Onpattro®, raises the question to

what extent APOE binding is determined by surface charge. Although liposomes and LNPs both have solvent-exposed lipidic surfaces, they differ significantly in their structural organization. Liposomes are unilamellar vesicles with an aqueous core in which a bilayer structure is exposed to the exterior. LNPs, however, are solid core structures that contain a lipid monolayer enriched with PEGylated lipids on their surface (**Figure 2a**). Since the assembly of liposomes with distinct physiochemical properties (*e.g.*, size, rigidity, surface charge) can be achieved with a higher degree of precision and flexibility over LNPs, we assessed multiple liposomal formulations in order to probe the repetitive binding of APOE and other proteins in their protein corona (**Figure 3a**).

Firstly, we selected a liposomal formulation with a similar behavior to Onpattro®, serving as a positive control of liposomes exhibiting an APOE dependent uptake mechanism. Liposomes composed of zwitterionic neutral 1,2-distearoyl-*sn*-glycero-3-phosphocholine (DSPC, 60 mol%) and cholesterol (40 mol%) were reported to have a >20-fold reduced uptake into liver hepatocytes in APOE-deficient mice,[37] highlighting the importance of APOE binding for its *in vivo* fate. Secondly, we selected an anionic liposome formulation based on the lipid composition of Mepact® (30PS), composed of anionic 1,2-dioleoyl-*sn*-glycero-3-phospho-L-serine (DOPS, 30 mol%) and zwitterionic lipid 1-palmitoyl-2-oleoyl-glycero-3-phosphocholine (POPC, 70 mol%), used with its active ingredient Mifamurtide in the clinic for the treatment of high-grade resectable non-metastatic osteosarcoma.[38] As controls of anionic lipid type and surface charge, we also included liposomal formulations where DOPS was replaced with the anionic lipid 1,2-dioleoyl-*sn*-glycero-3-phospho-(1′-rac-glycerol) (DOPG, 30PG) or the zwitterionic lipid 1,2-dioleoyl-*sn*-glycero-3-phosphocholine (DOPC, 30PC) (**Figure 3b**). Furthermore, we systematically varied the ratio of anionic and zwitterionic lipid in these formulations to determine to what extend surface charge density would affect protein binding (**Figure 3a**, 10PS, 95PS, 10PG, 50PG, 70PG, 95PG, 95PC). All liposomal formulations contained 5 mol% of the photoaffinity probe IKS02 and were assembled using standard thin film hydration and extrusion protocols, yielding monodisperse liposomes with an average size of ~100 nm (PDI < 0.120) (**Table S1**). All formulations were processed through our photoaffinity based chemoproteomic workflow and the criteria for the positive identification of protein hits from their respective volcano plots was equal to those applied for the determination of the Onpattro® protein corona (**Figures S1-4**). From the combination of these identified hits, we constructed a heatmap displaying the relative abundance of all proteins within their respective protein corona (**Figure S5**). Overall, the obtained protein coronas of these liposomal formulations are generally dominated by the identification of apolipoproteins (**Figure 3c**).

When comparing the anionic liposomes, a more negative ζ-potential for PG liposomes (10PG, 30PG, 50PG, 70PG, 95PG), led to a clear a clear increase in total number of proteins in the protein corona, albeit at an increased amount of identified proteins at low abundance (< 2%) (**Figure 3d, Figure S5**). Nevertheless, for 30PS and 95PS, which showed similar strongly anionic surface potentials, no significant increase in number of proteins in their respective corona was observed (**Figure 3d, Figure S5**). These results indicate that protein corona complexity on anionic liposomes is not only dependent on the surface charge density, but also on lipid headgroup structure.

The rather sparse protein corona obtained for PS-containing liposomes, compared to PG-containing liposomes, may be a consequence of the biological role of PS, which must remain exposed. In nature, PS lipids are commonly present in negatively-charged biological membranes, predominantly in the inner leaflet or the subcellular compartments of healthy cells, where they function as signaling molecules for downstream processes.[39,40] However, PS lipids can be exposed extracellularly by the help of lipid scramblases during biological processes such as apoptosis.[41,42] In vivo, PS lipids must be directly engaged by specific receptors of phagocytic cells (*e.g.* macrophages) to mediate recognition, without being masked by proteins bound to the exposed PS.[42,43] Furthermore, the absence of a dense or complex protein corona supports the *in vivo* recognition and selective uptake by macrophages and other phagocytic cells which is reported for the Mepact® formulation.[38,44,45]

For the weakly anionic (10PS, 10PG) and zwitterionic liposomes (DSPC-Chol, 30PC, 95PC), the number of bound proteins varied widely. For example, 10PG was completely devoid of positive protein identification, whereas APOA1 was the only identified hit in the case of 10PS. Furthermore, zwitterionic 30PC also shows a low amount of protein binding and is similar to our previous protein corona determined on POPC-Cholesterol (50 mol% POPC, 45% mol% cholesterol, 5 mol% IKS02).[21] Nevertheless, 95PC and DSPC-Chol showed an increase in total numbers of protein binding. Although the antifouling behavior of zwitterionic neutral nanoparticles and surfaces is a frequently described phenomenon,[46–48] in the case of zwitterionic liposomes other membrane characteristics such as rigidity or solvent exposed hydrophobicity might also play a role in the binding affinity towards plasma proteins.

From the identified apolipoproteins across all formulations, it is apparent that apolipoprotein A-1 (APOA1) and APOE showed the most repetitive and reproducible binding. In the case of DSPC-Chol, we positively identified the binding of APOE, as expected due to its importance in *in vivo* fate of these liposomes.[37] Nevertheless, the APOE

binding was not observed for the other zwitterionic liposomes. In the case of anionic liposomes, positive APOE binding was observed across all strongly anionic formulations irrespective of headgroup structure (PS or PG), but not for weakly anionic liposomes (10PS, 10PG). This indicates that the binding of APOE to anionic liposomes has a certain threshold requirement for surface charge density.

In the case of APOA1, positive binding is observed for all formulations besides DSPC-Chol, 30PC and 10PG. APOA1 is a 28 kDa protein and a major component of high-density lipoproteins (HDL), where it plays important roles in promoting cellular cholesterol efflux, binding lipids, activating lecithin cholesterol acyltransferase, and aiding in the structural stability of mature HDL that interacts with specific receptors and lipid transfer proteins.[49] APOA1 is known to interact with zwitterionic and anionic lipid surfaces through both headgroup and hydrophobic interactions, due to the multiple structural conformations it can adopt.[50–52] Its primary identified lipid bound structure consists of pseudo-continuous amphipathic α-helices, forming a toroidal structure (**Figure S6**, PDB: 1AV1).[53] APOA1 has hydrophobic patches and a large amount of charged residues across its surface to facilitate the binding to lipidic surfaces. However, APOA1 does not have specific binding domains for other biomolecules. The high affinity of APOA1 towards lipid surfaces, both anionic and zwitterionic, explains the high abundance of this protein in the protein corona of multiple liposomal formulations. However, the large number interaction possibilities of APOA1 with lipid surfaces makes it difficult to determine why APOA1 is absent in the protein corona of certain liposomes.

APOE is a 36 kDa glycoprotein and associated with nearly all lipoproteins in human plasma (*e.g.*, LDL, HDL, Chylomicrons).[54,55] One of the key functions of APOE is mediating the binding of lipoproteins in plasma to specific cell-surface receptors (*e.g.*, LDLr, LRP), allowing the internalization of APOE-containing lipoprotein particles. In order to exhibit this role, APOE has an amphipathic α-helical C-terminal domain critical for the binding to lipoproteins (**Figure 3e**).[56,57] Binding of lipoproteins promotes a structural change, facilitated through a flexible hinge domain, to the putative "open state" of APOE (**Figure 3e**). This lipidated and open state of APOE exposes a LDLr-binding region,[58,59] containing a heparan sulfate proteoglycan (HSPG) recognition sequence.[60] The recognition of cell-surface HSPGs is required for the binding and uptake of APOE-containing lipoproteins by transfer to lipoprotein receptors or through HSPG directly.[61–63] Furthermore, an additional heparin binding-site is present on the "closed state" of APOE, containing a variety of lysine (Lys-143, Lys-146 and Lys-233) and arginine (Arg-142, Arg-145, and Arg-147) residues.[64,65] In this binding-site, Lys-233 is critical for effective heparin binding in the closed state, but also

overlaps with the C-terminal lipid binding region. Here, we hypothesized that APOE binding to anionic liposomes might occur through this surface exposed heparin binding domain.

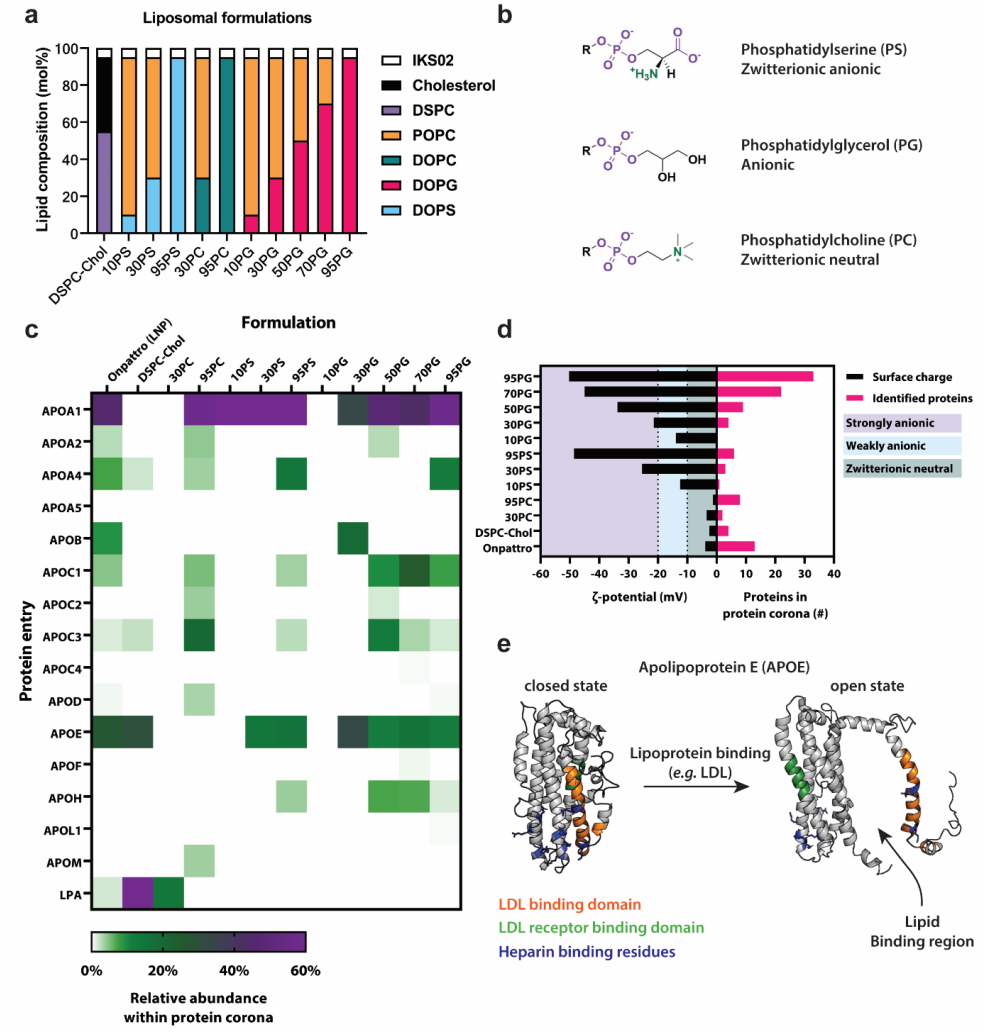


Figure 3. Protein corona identification of zwitterionic and anionic liposomes. (**a**) Lipid type and composition of liposomal formulations in the screen of protein corona fingerprints. (**b**) Chemical structures of anionic and zwitterionic lipid headgroups. Moieties responsible for anionic charge displayed in purple and for cationic charge in green. (**c**) Heatmap displaying the LFQ abundance of the identified protein corona of all liposomal formulations and Onpattro®. The abundance is displayed as relative to other proteins within the protein corona. (**d**) Surface charge (ζ-potential)

and number of identified proteins in the protein corona of all liposomal formulations and Onpattro®. (**e**) Different structural conformations of APOE and important binding domains and residues. Cationic residues on the surface indicated in blue make up the heparin binding domain.[64] Interaction of the LDL binding domain (orange) upon binding to lipoproteins leads to the reorganization of the protein into an "open state" which exposes the LDL receptor binding domain critical for cellular uptake.[66] PDB entry 2L7B is used for APOE closed state,[65] the open state has been generated using PyMOL.

In order to validate the binding specificity of APOE and APOA1 to liposomes and LNPs, and the possible role of specific domains on liposome binding, we performed a competition assay using a mixture of purified human proteins and potential competitors (**Figure 4a**). The protein mixture was composed of APOE and APOA1, and complemented with abundant plasma proteins that were not identified as positive hits in their protein coronas; specifically prothrombin (THRB), transferrin (TRFE) and albumin (ALBU). Within this mixture, the ratio of proteins was chosen to reflect their natural abundance in plasma.[67] In this assay, liposomes or LNPs of interest containing IKS02 were added to the mixture, followed by the addition of a competitor, and incubated at 37 °C for 1 hour. After irradiation and click chemistry conjugation with a fluorescent dye (Cy5-alkyne), the binding of proteins and potential inhibition by the competitors was determined by in-gel fluorescence (**Figure 4a**). In the case of anionic liposome formulations, 30PS and 30PG were selected and showed very similar competitive binding to APOE. In these cases, the binding of APOE and APOA1 was validated by its presence in the "+UV" lane and absence in "-UV", while the other proteins remained at background levels in both cases (**Figure 4b,c**). Competition with heparin (5:1 heparin:APOE, mol:mol) was enough to completely abolish the binding of APOE to both of these liposomes. Moreover, this competitive binding led to an increase in APOA1 signal, confirming that APOA1 does not bind anionic liposomes through any form of heparin binding domain. Furthermore, competition with native DSPC-Chol or 30PC liposomes did not affect APOE or APOA1 binding to these anionic liposomes.

In the case of zwitterionic 30PC, we did not observe any positive labeling of proteins, confirming the lack of binding affinity of all selected proteins to these liposomes, in agreement with our initial experiment in human plasma (**Figure 4d**). In the case of DSPC-Chol and Onpattro®, the validation was also in line with our initial screen, showing a positive binding of APOE in both cases, but a lack of APOA1 binding in the case of DSPC-Chol (**Figure 4e,f**). For these formulations, the competition with heparin showed no decrease in APOE binding. However, the addition of 30PG did lead to competition for APOE binding in the case of DSPC-Chol. This indicates that APOE binding to anionic liposomes through its heparin binding domain has a higher affinity than through its lipid

binding region, likely due to stronger electrostatic interactions of the surface exposed cationic residues with the anionic lipids compared to hydrophobic driven interaction of the lipid binding region. Altogether, the high degree of competition between heparin and anionic liposomes shows that APOE binds to anionic liposomes through its surface exposed heparin binding domain. Given the critical importance of residue Lys-233 in heparin binding, which overlaps with the C-terminal lipid binding domain,[63,64] this would likely lead to a "locked closed state" of APOE due to the strong electrostatic interaction with all the residues (**Figure 4g**). The binding of APOE to spherical zwitterionic lipoproteins surfaces is known to occur in a multi-step reversible process in which the hydrophobic interaction of the lipid binding domain and flexible hinge regions facilitate a structural change.[66,68] Therefore, we assume that APOE binding to DSPC-Chol and Onpattro® occurs through its lipid binding region, similar to the binding to zwitterionic lipoproteins, resulting in a non-competitive binding with heparin (**Figure 4g**).

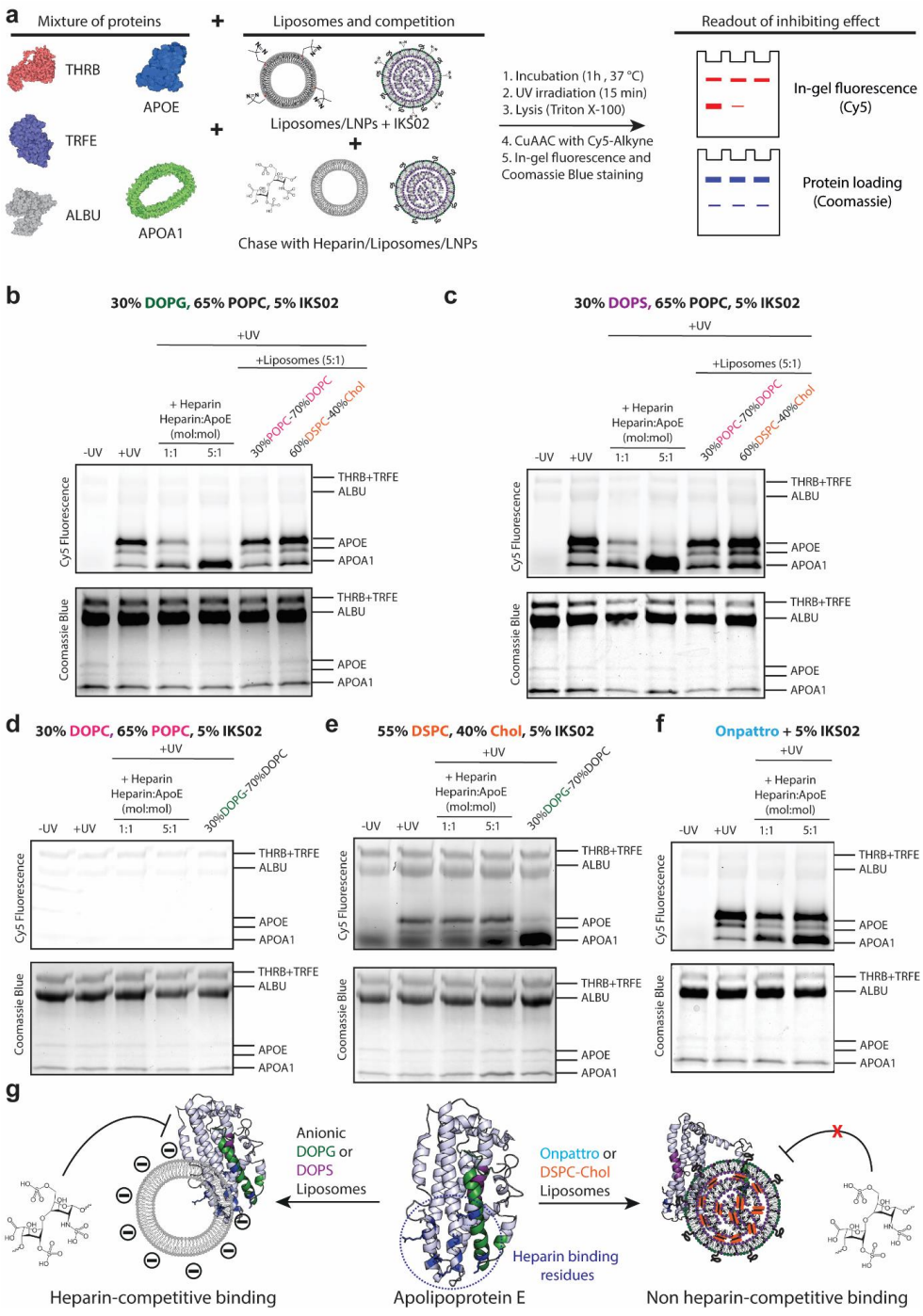

a
Mixture of proteins
THRB
APOE
TRFE
ALBU
APOA1
Liposomes and competition
Liposomes/LNPs + IKS02
Chase with Heparin/Liposomes/LNPs
1. Incubation (1h , 37 °C)
2. UV irradiation (15 min)
3. Lysis (Triton X-100)
4. CuAAC with Cy5-Alkyne
5. In-gel fluorescence and Coomassie Blue staining
Readout of inhibiting effect
In-gel fluorescence (Cy5)
Protein loading (Coomassie)
b
30% DOPG, 65% POPC, 5% IKS02
c
30% DOPS, 65% POPC, 5% IKS02
+UV
+Liposomes (5:1)
+ Heparin Heparin:ApoE (mol:mol)
-UV
+UV
1:1
5:1
30%POPC-70%DOPC
60%DSPC-40%Chol
Cy5 Fluorescence
Coomassie Blue
THRB+TRFE
ALBU
APOE
APOA1
d
30% DOPC, 65% POPC, 5% IKS02
30%DOPG-70%DOPC
e
55% DSPC, 40% Chol, 5% IKS02
f
Onpattro + 5% IKS02
g
Anionic DOPG or DOPS Liposomes
Onpattro or DSPC-Chol Liposomes
Heparin binding residues
Heparin-competitive binding
Apolipoprotein E
Non heparin-competitive binding

Figure 4. Site selective binding of APOE to anionic liposomes. (**a**) Schematic representation of the employed competition assay. Protein structures were obtained from the PDB (entries: THRB = 6C2W[69], TRFE = 1D3K[70], ALBU = 1E78[71], APOA1 = 1AV1[53], APOE = 2L7B[65]) and illustrations were generated using Illustrate.[22] (**b**-**f**) In-gel fluorescence (Cy5) and Coomassie Blue stained SDS-PAGE gels of competition experiments. APOE appears as two distinct bands on SDS-PAGE, due to the presence of its glycosylated (36 kDa) and non-glycosylated (34 kDa) form.[72] (**g**) Schematic representation of the competitive binding of heparin to anionic liposomes 30PG and 30PS, and the lack thereof in the case of DSPC-Chol and Onpattro. Heparin binding residues are displayed in blue. Lipid binding region is displayed in green. LDLr binding is displayed in purple.

4.3 Discussion

Using a photoaffinity-based chemoproteomics approach, we have identified and validated the recurring binding of various proteins on liposomes and LNPs. In particular, we have been able to validate the positive binding of APOE on Onpattro® LNPs and DSPC-Chol liposomes, for which their importance has been described in literature. Furthermore, we have shown to what extent APOE binding is repetitive among zwitterionic and anionic liposomes. Finally, we were able to use the photoaffinity approach in combination with a competition assay in order to determine that APOE binds strongly-anionic liposomes through its heparin binding domain. In addition, binding to zwitterionic liposomes and LNPs occurs non-competitively with heparin, likely in a similar manner as APOE binding and structural reorganization to spherical lipoproteins.

While the current understanding of the protein corona is known at a superficial level, typically describing the effect of a set of proteins, with these results we have gained important insights into specific protein-nanoparticle interactions. Understanding site-selective binding of a single protein to LNPs in plasma will allow us to probe the effect on its fate *in vivo*. While the effect of APOE in the uptake of liver hepatocytes has been shown for zwitterionic liposomes such as DSPC-Chol,[37] of particular interest is understanding to which extent binding of APOE to anionic liposomes has on its uptake *in vivo*. Previous work has shown that anionic nanoparticles are preferentially taken up through scavenger receptors (*e.g.*, stabilin-1,2) preferentially expressed by cells of the reticuloendothelial system (RES).[32,73,74] However, the intermediate function of APOE is not understood. In future work, we aim to compare the biodistribution of anionic and zwitterionic liposomes in wildtype and APOE knockout (*apoe*$^{-/-}$) mice in order to examine the role of APOE on the uptake by liver cells.

With the current widespread application of multiple LNP-based therapeutics, such as the nascent prophylactic vaccines against SARS-CoV-2, we believe that this system can be used

for screening protein coronas on other LNP formulations. The ability to validate specific protein binding, and gain more insight into their relevant binding domains and resulting cell uptake pathways will aid our understanding of the nano-bio interface at a much deeper level, improving the *in vivo* fate prediction of LNPs and liposomal formulations.

4.4 References

1. Cai, R. & Chen, C. The Crown and the Scepter: Roles of the Protein Corona in Nanomedicine. *Adv. Mater.* **1805740**, 1–13 (2018).
2. Walkey, C. D. & Chan, W. C. W. W. Understanding and controlling the interaction of nanomaterials with proteins in a physiological environment. *Chem. Soc. Rev.* **41**, 2780–2799 (2012).
3. Lundqvist, M. *et al.* The nanoparticle protein corona formed in human blood or human blood fractions. *PLoS One* **12**, 1–15 (2017).
4. Monopoli, M. P., Aberg, C., Salvati, A. & Dawson, K. A. Biomolecular coronas provide the biological identity of nanosized materials. *Nat. Nanotechnol.* **7**, 779–786 (2012).
5. Salvati, A. *et al.* Transferrin-functionalized nanoparticles lose their targeting capabilities when a biomolecule corona adsorbs on the surface. *Nat. Nanotechnol.* **8**, 137–143 (2013).
6. Bertrand, N. *et al.* Mechanistic understanding of in vivo protein corona formation on polymeric nanoparticles and impact on pharmacokinetics. *Nat. Commun.* **8**, 777 (2017).
7. Gunawan, C., Lim, M., Marquis, C. P. & Amal, R. Nanoparticle–protein corona complexes govern the biological fates and functions of nanoparticles. *J. Mater. Chem. B* **2**, 2060–2083 (2014).
8. Chinen, A. B., Guan, C. M., Ko, C. H. & Mirkin, C. A. The Impact of Protein Corona Formation on the Macrophage Cellular Uptake and Biodistribution of Spherical Nucleic Acids. *Small* **13**, 1603847 (2017).
9. Vilanova, O. *et al.* Understanding the Kinetics of Protein-Nanoparticle Corona Formation. *ACS Nano* **10**, 10842–10850 (2016).
10. Casals, E., Pfaller, T., Duschl, A., Oostingh, G. J. & Puntes, V. Time evolution of the nanoparticle protein corona. *ACS Nano* **4**, 3623–3632 (2010).
11. Oh, J. Y. *et al.* Cloaking nanoparticles with protein corona shield for targeted drug delivery. *Nat. Commun.* **9**, 1–9 (2018).
12. Tenzer, S. *et al.* Rapid formation of plasma protein corona critically affects nanoparticle pathophysiology. *Nat. Nanotechnol.* **8**, 772 (2013).
13. Weber, C., Morsbach, S. & Landfester, K. Possibilities and Limitations of Different Separation Techniques for the Analysis of the Protein Corona. *Angew. Chemie Int. Ed.* **58**, 12787–12794 (2019).
14. Simonsen, J. B. & Münter, R. Pay attention to the biological nanoparticles when studying the protein corona on nanomedicines. *Angew. Chemie Int. Ed.* **59**, 12584–12588 (2020).
15. Kristensen, K. *et al.* Isolation methods commonly used to study the liposomal protein corona suffer from contamination issues. *Acta Biomater.* **65**, In press (2021).
16. Pozzi, D. *et al.* The biomolecular corona of nanoparticles in circulating biological media. *Nanoscale* **7**, 13958–13966 (2015).
17. Bigdeli, A. *et al.* Exploring Cellular Interactions of Liposomes Using Protein Corona Fingerprints and Physicochemical Properties. *ACS Nano* **10**, 3723–3737 (2016).
18. Walkey, C. D. *et al.* Protein Corona Fingerprinting Predicts the Cellular Interaction of Gold

and Silver Nanoparticles. *ACS Nano* **8**, 2439–2455 (2014).
19. Zhang, Y., Wu, J. L. Y., Lazarovits, J. & Chan, W. C. W. An Analysis of the Binding Function and Structural Organization of the Protein Corona. *J. Am. Chem. Soc.* **142**, 8827–8836 (2020).
20. Chu, Y. *et al.* Deciphering Protein Corona by scFv-Based Affinity Chromatography. *Nano Lett.* **21**, 2124–2131 (2021).
21. Pattipeiluhu, R. *et al.* Unbiased Identification of the Liposome Protein Corona using Photoaffinity-based Chemoproteomics. *ACS Cent. Sci.* **6**, 535–545 (2020).
22. Goodsell, D. S., Autin, L. & Olson, A. J. Illustrate: Software for Biomolecular Illustration. *Structure* **27**, 1716–1720 (2019).
23. Jayaraman, M. *et al.* Maximizing the potency of siRNA lipid nanoparticles for hepatic gene silencing in vivo. *Angew. Chemie - Int. Ed.* **51**, 8529–8533 (2012).
24. Cullis, P. R. & Hope, M. J. Lipid Nanoparticle Systems for Enabling Gene Therapies. *Mol. Ther.* **25**, 1467–1475 (2017).
25. Witzigmann, D. *et al.* Lipid nanoparticle technology for therapeutic gene regulation in the liver. *Adv. Drug Deliv. Rev.* **159**, 344–363 (2020).
26. Akinc, A. *et al.* The Onpattro story and the clinical translation of nanomedicines containing nucleic acid-based drugs. *Nat. Nanotechnol.* **14**, 1084–1087 (2019).
27. Jackson, L. A. *et al.* An mRNA Vaccine against SARS-CoV-2 — Preliminary Report. *N. Engl. J. Med.* **383**, 1920–1931 (2020).
28. Zhang, N.-N. *et al.* A Thermostable mRNA Vaccine against COVID-19. *Cell* **182**, 1271–1283 (2020).
29. Rietwyk, S. & Peer, D. Next-Generation Lipids in RNA Interference Therapeutics. **11**, 7572–7586 (2017).
30. Adams, D. *et al.* Patisiran, an RNAi therapeutic, for hereditary transthyretin amyloidosis. *N. Engl. J. Med.* **379**, 11–21 (2018).
31. Arteta, M. Y. *et al.* Successful reprogramming of cellular protein production through mRNA delivered by functionalized lipid nanoparticles. *Proc. Natl. Acad. Sci. U. S. A.* **115**, E3351–E3360 (2018).
32. Pattipeiluhu, R. *et al.* Anionic Lipid Nanoparticles Preferentially Deliver mRNA to the Hepatic Reticuloendothelial System. *Chapter 3, This Thesis* (2021).
33. Akinc, A. *et al.* Targeted delivery of RNAi therapeutics with endogenous and exogenous ligand-based mechanisms. *Mol. Ther.* **18**, 1357–1364 (2010).
34. Sabnis, S. *et al.* A Novel Amino Lipid Series for mRNA Delivery: Improved Endosomal Escape and Sustained Pharmacology and Safety in Non-human Primates. *Mol. Ther.* **26**, 1509–1519 (2018).
35. Bekersky, I. *et al.* Pharmacokinetics, excretion, and mass balance of liposomal amphotericin B (AmBisome) and amphotericin B deoxycholate in humans. *Antimicrob. Agents Chemother.* **46**, 828–833 (2002).
36. Bulbake, U., Doppalapudi, S., Kommineni, N. & Khan, W. Liposomal Formulations in Clinical Use: An Updated Review. *Pharmaceutics* **9**, 12 (2017).
37. Yan, X. *et al.* The role of apolipoprotein E in the elimination of liposomes from blood by hepatocytes in the mouse. *Biochem. Biophys. Res. Commun.* **328**, 57–62 (2005).
38. Fidler, I. J., Sone, S., Fogler, W. E. & Barnes, Z. L. Eradication of spontaneous metastases and activation of alveolar macrophages by intravenous injection of liposomes containing muramyl dipeptide. *Proc. Natl. Acad. Sci.* **78**, 1680–1684 (1981).
39. Yeung, T. *et al.* Membrane Phosphatidylserine Regulates Surface Charge and Protein Localization. *Science* **319**, 210–213 (2008).

40. Arumugam, S. & Kaur, A. The Lipids of the Early Endosomes: Making Multimodality Work. *Chembiochem* **18**, 1053–1060 (2017).
41. Hanayama, R. *et al.* Autoimmune Disease and Impaired Uptake of Apoptotic Cells in MFG-E8-Deficient Mice. *Science* **304**, 1147–1150 (2004).
42. Allen, T. M., Williamson, P. & Schlegel, R. A. Phosphatidylserine as a determinant of reticuloendothelial recognition of liposome models of the erythrocyte surface. *Proc. Natl. Acad. Sci.* **85**, 8067–8071 (1988).
43. Lemke, G. How macrophages deal with death. *Nat. Rev. Immunol.* **19**, 539–549 (2019).
44. Ando, K., Mori, K., Corradini, N., Redini, F. & Heymann, D. Mifamurtide for the treatment of nonmetastatic osteosarcoma. *Expert Opin. Pharmacother.* **12**, 285–292 (2011).
45. Mori, K., Ando, K. & Heymann, D. Liposomal muramyl tripeptide phosphatidyl ethanolamine: a safe and effective agent against osteosarcoma pulmonary metastases. *Expert Rev. Anticancer Ther.* **8**, 151–159 (2008).
46. Debayle, M. *et al.* Zwitterionic polymer ligands: an ideal surface coating to totally suppress protein-nanoparticle corona formation? *Biomaterials* **219**, 119357 (2019).
47. Safavi-Sohi, R. *et al.* Bypassing Protein Corona Issue on Active Targeting: Zwitterionic Coatings Dictate Specific Interactions of Targeting Moieties and Cell Receptors. *ACS Appl. Mater. Interfaces* **8**, 22808–22818 (2016).
48. Sanchez-Cano, C. & Carril, M. Recent Developments in the Design of Non-Biofouling Coatings for Nanoparticles and Surfaces. *International Journal of Molecular Sciences* **21**, 1007 (2020).
49. Frank, P. G. & Marcel, Y. L. Apolipoprotein A-I: structure-function relationships. *J. Lipid Res.* **41**, 853–872 (2000).
50. Sparks, D. L., Lund-Katz, S. & Phillips, M. C. The charge and structural stability of apolipoprotein A-I in discoidal and spherical recombinant high density lipoprotein particles. *J. Biol. Chem.* **267**, 25839–25847 (1992).
51. Sparks, D. L., Frank, P. G. & Neville, T. A. Effect of the surface lipid composition of reconstituted LPA-I on apolipoprotein A-I structure and lecithin: cholesterol acyltransferase activity. *Biochim. Biophys. Acta* **1390**, 160–172 (1998).
52. Sparks, D. L., Davidson, W. S., Lund-Katz, S. & Phillips, M. C. Effect of cholesterol on the charge and structure of apolipoprotein A-I in recombinant high density lipoprotein particles. *J. Biol. Chem.* **268**, 23250–23257 (1993).
53. Borhani, D. W., Rogers, D. P., Engler, J. A. & Brouillette, C. G. Crystal structure of truncated human apolipoprotein A-I suggests a lipid-bound conformation. *Proc. Natl. Acad. Sci.* **94**, 12291–12296 (1997).
54. Mahley, R. W. Apolipoprotein E: cholesterol transport protein with expanding role in cell biology. *Science* **240**, 622–630 (1988).
55. Huang, Y., Weisgraber, K. H., Mucke, L. & Mahley, R. W. Apolipoprotein E: diversity of cellular origins, structural and biophysical properties, and effects in Alzheimer's disease. *J. Mol. Neurosci.* **23**, 189–204 (2004).
56. Huang, Y. & Mahley, R. W. Apolipoprotein E: structure and function in lipid metabolism, neurobiology, and Alzheimer's diseases. *Neurobiol. Dis.* **72 Pt A**, 3–12 (2014).
57. Weisgraber, K. H. Apolipoprotein E: structure-function relationships. *Adv. Protein Chem.* **45**, 249–302 (1994).
58. Innerarity, T. L., Friedlander, E. J., Rall, S. C. J., Weisgraber, K. H. & Mahley, R. W. The receptor-binding domain of human apolipoprotein E. Binding of apolipoprotein E fragments. *J. Biol. Chem.* **258**, 12341–12347 (1983).

59. Wilson, C., Wardell, M. R., Weisgraber, K. H., Mahley, R. W. & Agard, D. A. Three-dimensional structure of the LDL receptor-binding domain of human apolipoprotein E. *Science* **252**, 1817–1822 (1991).
60. Mahley, R. W. & Huang, Y. Atherogenic remnant lipoproteins: role for proteoglycans in trapping, transferring, and internalizing. *J. Clin. Invest.* **117**, 94–98 (2007).
61. Futamura, M. *et al.* Two-step mechanism of binding of apolipoprotein E to heparin: implications for the kinetics of apolipoprotein E-heparan sulfate proteoglycan complex formation on cell surfaces. *J. Biol. Chem.* **280**, 5414–5422 (2005).
62. Narita, M. *et al.* Cellular catabolism of lipid poor apolipoprotein E via cell surface LDL receptor-related protein. *J. Biochem.* **132**, 743–749 (2002).
63. Libeu, C. P. *et al.* New insights into the heparan sulfate proteoglycan-binding activity of apolipoprotein E. *J. Biol. Chem.* **276**, 39138–39144 (2001).
64. Saito, H. *et al.* Characterization of the heparin binding sites in human apolipoprotein E. *J. Biol. Chem.* **278**, 14782–14787 (2003).
65. Chen, J., Li, Q. & Wang, J. Topology of human apolipoprotein E3 uniquely regulates its diverse biological functions. *Proc. Natl. Acad. Sci. U. S. A.* **108**, 14813–14818 (2011).
66. Frieden, C., Wang, H. & Ho, C. M. W. A mechanism for lipid binding to apoE and the role of intrinsically disordered regions coupled to domain-domain interactions. *Proc. Natl. Acad. Sci. U. S. A.* **114**, 6292–6297 (2017).
67. Farrah, T. *et al.* A high-confidence human plasma proteome reference set with estimated concentrations in PeptideAtlas. *Mol. Cell. Proteomics* **10**, M110.006353 (2011).
68. Nguyen, D., Dhanasekaran, P., Phillips, M. C. & Lund-Katz, S. Molecular Mechanism of Apolipoprotein E Binding to Lipoprotein Particles. *Biochemistry* **48**, 3025–3032 (2009).
69. Chinnaraj, M. *et al.* Structure of prothrombin in the closed form reveals new details on the mechanism of activation. *Sci. Rep.* **8**, 2945 (2018).
70. Yang, A. H. *et al.* Crystal structures of two mutants (K206Q, H207E) of the N-lobe of human transferrin with increased affinity for iron. *Protein Sci.* **9**, 49–52 (2000).
71. Bhattacharya, A. A., Curry, S. & Franks, N. P. Binding of the general anesthetics propofol and halothane to human serum albumin. High resolution crystal structures. *J. Biol. Chem.* **275**, 38731–38738 (2000).
72. Lee, Y. *et al.* Glycosylation and sialylation of macrophage-derived human apolipoprotein E analyzed by SDS-PAGE and mass spectrometry: Evidence for a novel site of glycosylation on SER290. *Mol. Cell. Proteomics* **9**, 1968–1981 (2010).
73. Campbell, F. *et al.* Directing Nanoparticle Biodistribution through Evasion and Exploitation of Stab2-Dependent Nanoparticle Uptake. *ACS Nano* **12**, 2138–2150 (2018).
74. Arias-Alpizar, G. *et al.* Stabilin-1 is required for the endothelial clearance of small anionic nanoparticles. *Nanomedicine Nanotechnology, Biol. Med.* **34**, 102395 (2021).

Chapter 5

Paracrystalline Inverted Lipid Phases Encapsulating siRNA Enhance Lipid Nanoparticle Mediated Transfection

Efficient cytosolic delivery of RNA molecules remains a formidable barrier for RNA therapeutic strategies. Lipid nanoparticles (LNPs) serve as state-of-the-art carriers that can deliver RNA molecules intracellularly, as exemplified by the recent implementation of several vaccines against SARS-CoV-2. Using a bottom-up rational design approach, we assemble LNPs that contain programmable lipid phases encapsulating small interfering RNA (siRNA). A combination of cryogenic transmission electron microscopy, cryogenic electron tomography and small-angle X-ray scattering reveals that we can form inverse hexagonal structures, which are present in a paracrystalline nature within the LNP core. Comparison with lamellar LNPs reveals that the presence of inverse hexagonal phases enhances the intracellular silencing efficiency over lamellar structures. We then demonstrate that lamellar LNPs exhibit an *in situ* transition from a lamellar to inverse hexagonal phase upon interaction with anionic membranes, whereas LNPs containing pre-programmed paracrystalline hexagonal phases bypass this transition for a more efficient one-step delivery mechanism, explaining the increased silencing effect. This rational design of LNPs with defined lipid structures aids in the understanding of the nano-bio interface and adds substantial value for new avenues of LNP design, optimization and use.

This chapter was submitted as a research article: R. Pattipeiluhu, Y. Zeng, M.R.M. Hendrix, I.K. Voets, A. Kros, T.H. Sharp

5.1 Introduction

RNA therapy relies on delivery of exogenous (therapeutic) RNA molecules, such as messenger (mRNA) or small interfering RNA (siRNA), to control disease-relevant gene expression.[1–3] For efficient functional cytosolic delivery to, and release within, target cells, these highly charged, immunogenic and membrane-impermeable RNA molecules require the use of delivery systems.[4–6] To this end, ionizable lipid nanoparticles (LNPs) serve as state-of-the-art vehicles that can package, protect and release RNA molecules inside cells.[7,8] LNPs have realized the translation of RNA therapeutics to the clinic, highlighted by the approval of Onpattro®,[9] enabling RNA interference (RNAi) therapy for the treatment of polyneuropathies resulting from transthyretin-mediated amyloidosis.[10] In addition, this platform has been successfully expanded for the delivery of other RNA molecules, yielding safe and effective mRNA-based vaccines for SARS-CoV-2.[11,12]

LNPs are multicomponent systems typically composed of an ionizable cationic lipid (IL), phospholipid, cholesterol, PEG-lipid and an nucleic acid payload, formulated through rapid microfluidic mixing.[13,14] At a pH below its pKa, the ionizable lipids enable electrostatic complexation of anionic nucleic acid molecules, followed by self-assembly and buffer exchange to physiological pH to form nanostructures with a core-shell structure in the range of ~30-150 nm.[15] The LNP core is considered "hydrophobic", being rich in ionizable lipids, cholesterol and its nucleic acid payload, in contrast, the LNP surface (*i.e.* lipid-water interface) is rich in helper phospholipids and lipid-PEG conjugates.[16] Intracellular unpacking and delivery to the cytosol of the encapsulated RNA molecules relies on endosomal acidification and *in situ* protonation of the ILs, leading to an electrostatic interaction with the endosomal membrane.[17] Disruption of the LNP structure and endosomal membrane is crucial for sufficient cytosolic RNA delivery.[18,19] However, in this process the majority (≥98%) of RNA molecules delivered with LNP systems remain trapped inside endosomal and lysosomal compartments, leading to degradation or efflux out of the cell.[20,21] To this end, empirical studies exploring the chemical space of LNP components, for example the diversification of IL structures,[22–27] or the variation of helper and PEG-lipids,[28–32] has been pursued in order to improve LNP mediated transfection efficiency. More recently, similar studies have been coupled with biophysical characterization of lipid structures in LNPs, aiming to understand the importance of LNP lipid organization and structure on their biological activity.[33,34] However, characterization and identification of defined lipid structures in LNPs, and the mechanistic understanding of these how structures affect LNP-endosome interaction and RNA delivery into the cytoplasm, remains

elusive. Nevertheless, a fundamental understanding of these mechanisms can aid the development of more potent LNP nanomedicines.

Here, we present bottom-up rational design of LNPs with defined lipid superstructures encapsulating siRNA, in order to accurately study their structure-activity relationship. Using cryogenic transmission electron microscopy (cryoTEM), cryogenic electron tomography (cryoET) and small angle X-ray scattering (SAXS), we identify and characterize defined lamellar, paracrystalline inverted hexagonal or mixed lipid-RNA structures in the core of LNPs, and are able to successfully differentiate between empty lipid structures and those containing siRNA. By combining cryoTEM and SAXS, we gain insights into the thermal stability of these structures and demonstrate that thermally-stable paracrystalline inverse hexagonal lipid phases encapsulating siRNA enhance the LNP-mediated transfection efficiency over lamellar variants. Our data supports the notion that lamellar LNP formulations induce an *in situ* transition from a lamellar to inverse hexagonal phase upon interaction with anionic membranes, whereas LNPs with pre-programmed inverse hexagonal phases can bypass this transition for a more efficient one-step delivery mechanism. We believe that our rational approach and biophysical characterization will yield new avenues for LNP design and development and can improve the efficiency of RNA therapeutics.

5.2 Results

The formation of lipid superstructures is dictated by the composition and ratio of different lipids with distinctive biophysical properties, such as transition temperature, charge, hydrophobicity and intrinsic curvature.[35] This is utilized in the field of nanomedicine in order to generate non-lamellar and crystalline lipid nanoparticles.[36,37] For example, the formation of inverted lipid structures is dependent on an abundance of lipids that possess a intrinsic negative ($R_o < 0$) curvature, such as the lipid 1,2-dioleoyl-sn-glycero-3-phosphoethanolamine (DOPE) (**Figure 1a**).[38] Here, we aimed to rationally design LNP systems containing lamellar or inverted structures encapsulating siRNA in order to assess their biophysical properties and structure-activity relationship. We envisioned that generation of lamellar or inverted phases in the core of LNPs could be achieved by manipulation of the DOPE lipid content (mol%), substituting for cholesterol (**Figure 1b,c**). We chose three different formulations, in which the molar ratios of the model ionizable lipid (IL) 1,2-dioleoyl-3-dimethylammonium-propane (DODAP) and PEG lipid 1,2-dimyristoyl-sn-glycero-3-phosphoethanolamine-N-methoxypolyethylene glycol-2000 (DMPE-PEG2000) were kept constant, while varying in DOPE content at 10, 30 and 49 mol% (**Figure 1c, Figure S1**). These formulations are referred to as 10PE-LNP, 30PE-LNP

and 49PE-LNP respectively. The small interfering RNA (siRNA) molecule Patisiran®,[10] used in the clinically approved LNP formulation Onpattro®,[9] was chosen a model oligonucleotide cargo (**Table S1**). Duplexed siRNA molecules for therapeutic purposes are short (~18-22 base pairs),[39] display high structural similarity and are less prone to structural deformation or the formation of secondary structures compared to mRNA,[40] which aids in the formation of predictable and reproducible lipid-RNA structures. LNP formulations were assembled with different ionizable lipid (nitrogen, N) to siRNA ratios (phosphate, P) ratios, being: no RNA, NP = 6 and NP = 1 (noted as 10PE-LNP-noRNA, 10PE-LNP-NP6 or 10PE-LNP-NP1, *etc.*). A NP ratio of 6 is commonly applied for oligonucleotide payloads such as siRNA or mRNA in order to achieve a sufficient encapsulated dose with high encapsulation efficiency,[41] whereas a NP ratio of 1 is known to have surpassed the maximum encapsulation capacity of RNA molecules in LNPs.[42] We performed a comparative analysis of these LNPs in order to determine the independent effects of RNA content and lipid composition on the formation of lipid-RNA superstructures. Conventional microfluidic mixing procedures were used to fabricate the LNPs (**Figure S2**). After dialysis, the hydrodynamic radius and surface charge of the LNPs were determined by dynamic light scattering (DLS) and zeta potential measurements, respectively (**Table S2**). Formulations with an NP ratio of 6 or 1 showed the formation of 100-150 nm particles with a polydispersity index (PDI) < 0.120, in which particle size slightly increased concomitantly with DOPE content. Assembly of 30PE-LNP-noRNA and 49PE-LNP-noRNA showed formation of larger and more polydisperse particles. In all cases, the surface charge varied between -1 to -5 mV, indicating the formation of zwitterionic neutral LNPs in PBS buffer, reflecting the expected formal charge of the lipid combination at physiological pH.

In order to gain insights into the formation of lipid structures in these formulations, we combined SAXS as bulk method with cryoTEM imaging to assess the difference in nanoscale structures of the assembled LNPs. All 10PE-LNP SAXS profiles displayed a Bragg reflection at a scattering vector $\mathbf{q} \sim 0.1$ Å^{-1}, which was most pronounced at NP1. This is a hallmark of the formation of a defined structure for all NP ratios and its amplification by an increase in siRNA content in the assembly (**Figure 1d**). The associated cryoTEM revealed the formation of lamellar structures in all three formulations, in which 10PE-LNP-NP1 formed concentric circles extending to the LNP core (Black arrows, **Figure 1g, Figure S3a**). For 10PE-LNP-NP6 and 10PE-LNP-noRNA, structure formation was limited to several lamellar rings on the periphery, surrounding an amorphous core (**Figure S4**). When dialysis was performed with a molecular weight cut-off (MWCO) below the size of the siRNA (MWCO = 10 kDa) to exchange buffer but retain free RNA for effective encapsulation efficiency (EE%) determination, an EE% of roughly 50% indicated successful

saturation of encapsulation of 10PE-LNPs at a NP ratio of 1 (**Figure S5a**). Our data showing the amplification of lamellar structures and saturation of encapsulation are in line with previously reported LNPs with comparable lipid compositions and NP ratios.[15,42]

When the DOPE content was increased to 30 mol% (30PE-LNP variants), the Bragg reflection shifted towards smaller **q** values, indicating transition away from lamellar structures (**Figure 1e**). Two maxima around $q \sim 0.1$ Å^{-1} are distinguishable for 30PE-LNP-noRNA and 30PE-LNP-NP6, whereas 30PE-LNP-NP1 showed a broad shoulder instead, suggesting that multiple structures may coexist. For 30PE-LNP-NP1, cryoTEM revealed the formation of various repeating and distinguishable structures. Similar to 10PE-LNP-NP1, lamellar structures could be identified (Black arrows, **Figure 1h, Figure S3b**) but, in addition, also non-lamellar structures were observed (White arrows, **Figure 1h**). In the case of 30PE-LNP-NP6 and 30PE-LNP-noRNA, similar lamellar and non-lamellar structures were observed (**Figure S6**). However, following the trend of the 10PE-LNP variants, these structures were less defined and the lamellar rings showed a lower signal amplification in the presence of siRNA compared to those observed in 30PE-LNP-NP1.

When the DOPE content was increased further to 49 mol% (49PE-LNP variants), the $\mathbf{q} \sim 0.1$ Å^{-1} reflection again shifted to lower **q** values (**Figure 1f**). In this case, both 49PE-LNP-NP1 and 49PE-LNP-noRNA showed discernable Bragg reflections. These occurred at lower $\boldsymbol{q}$ values for 49PE-LNP-NP1 than for 49PE-LNP-noRNA, indicating a difference in structure and/or domain size. The LNP-49PE-NP6 profile displays the principal reflections of both 49PE-LNP-NP1 and 49PE-LNP-noRNA, albeit less pronounced, indicating the formation of a mixture of the corresponding structures. In all of the LNP-49PE variants, cryoTEM revealed the sole formation of non-lamellar like structures (**Figure 1i, Figures S3c and S7**). Similar to 10PE-LNP-NP1, the 30PE-LNP-NP1 and 49PE-LNP-NP1 formulations displayed saturation of encapsulation, indicated by an EE% of roughly 50% (**Figure S5**). For all formulations, the large excess of siRNA could be removed by dialysis with a MWCO larger than free siRNA of 1 MDa, in order to avoid interference of unencapsulated siRNA in further experiments.

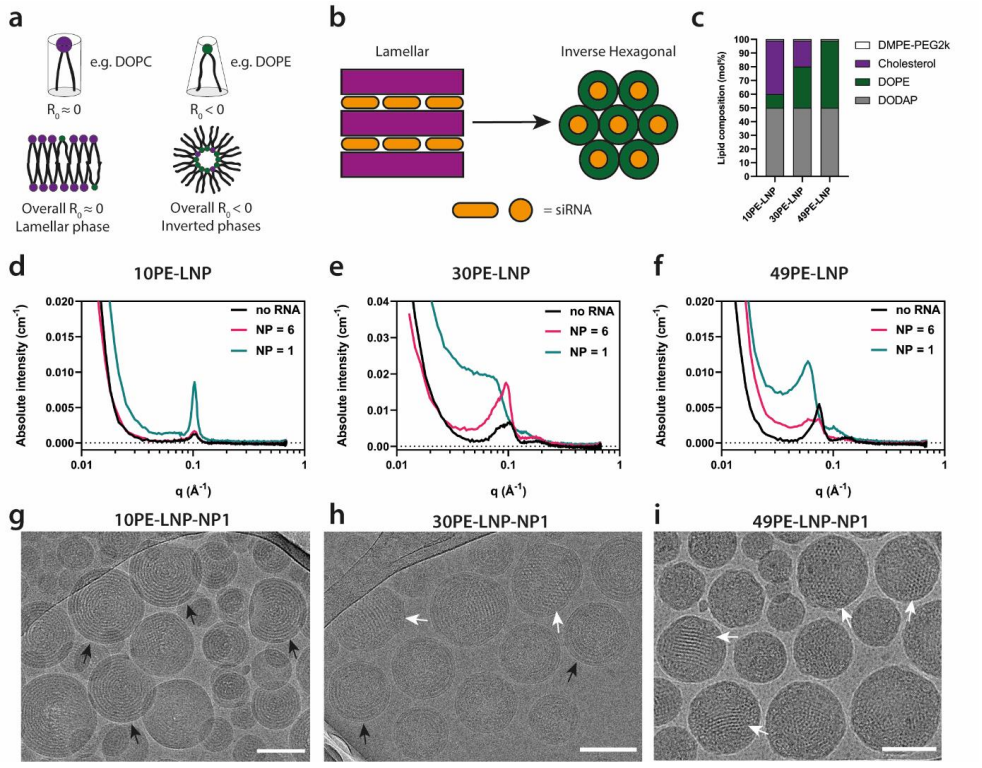


Figure 1. Design of LNPs containing defined lipid phases. (**a**) Curvature in lipid mixtures is driven by the composition of lipids with various curvature profiles Compositions with larger amounts of lipids with a $R_o < 0$ lead to the formation of inverted phases. (**b**) Lamellar structures can transition towards inverted phases by the increase of DOPE lipid content. (**c**) LNP compositions designed to form lamellar and inverted lipid structures encapsulating siRNA used in this study. (**d**-**f**) SAXS profiles of the LNP compositions shown in c, at different NP ratios. (**g**-**i**) Representative cryoTEM images of the LNPs compositions in c, at NP ratio = 1. Scale bars are 100 nm.

Since 10PE-LNP, 30PE-LNP and 49PE-LNP assembled with an NP ratio of 1 formed particles of similar sizes, along with clearly defined lipid structures, they were subjected to comparative and in-depth structural analysis. For each of the formulations, a large number of single particles ($n > 75$) showing clear structural properties were selected from cryoTEM images and categorized based on structural similarity. The regions of interest were subjected to a fast Fourier transform (FFT), yielding the reciprocal lattice from which the repeating distance of a structure could be determined. In the case of 10PE-LNP-NP1, only lamellar concentric rings were observed throughout the sample. These structures displayed clear diffraction, as well as higher-order maxima, of the reciprocal space repeating unit,

specifically at 6.38 nm, 3.19 nm and 2.08 nm (**Figure 2a**). The initial scattering vector at 6.38 nm represents the lattice spacing of the primitive cell. Analyzing all of the selected single particles allowed us to construct a violin plot, revealing the variation in lamellar lattice spacing (**Figure 2b**). The mean lattice spacing of the lamellar structure is 5.88 nm ± 0.65 nm (n = 84). The large deviation in observed lattice spacings, which range from 4.20 nm to 6.90 nm, is not well reflected in the SAXS profile of 10PE-LNP-NP1, which displays a narrow peak at $q \sim 0.1$ Å^{-1} (**Figure 1d**). In contrast to bulk SAXS measurements, cryoTEM imaging displays the structures within individual LNPs, which can present multiple orientations along the imaging axis. Consequently, this deviation in lattice spacings can be explained by an out-of-plane rotation of the lamellae to the electron beam, in which rotated lattices appear narrower (**Figure 2c**). Nevertheless, a preferential orientation for the lamellar spacing in vitreous water is observed and reflected by the median of 6.18 nm. This value closely reflects the expected values of lamellar lipid bilayers containing (phospho)lipids with similar carbon tail lengths (C_{18}) and cholesterol complexing oligonucleotides.[43,44]

For 30PE-LNP-NP1 samples, we identified three distinguishable and repetitive structures: hexagons, straight lines and lamellae (**Figure 2d**). Lattice spacing analysis of the individual structures in 30PE-LNP-NP1 revealed a high similarity for the straight lines and hexagons, at 5.78 nm ± 0.14 nm and 5.77 nm ± 0.14 nm respectively (**Figure 2e**). These values are slightly smaller than the mean lattice spacings of a = 6.26 nm ± 0.18 nm observed for 10PE-LNP-NP1. Interestingly, LNPs with a hexagonal and lamellar structure were found to co-exist, and in some cases, these structures were visualized within the same particle (**Figure S8**). This coexistence of LNPs with different structures and LNPs displaying coexisting structures within the same particle yields a broad scattering signal in the 30PE-LNP-NP1 SAXS profile instead of well-defined, distinguishable Bragg reflections (**Figure 1e**). For 49PE-LNP-NP1, hexagonal and straight-line structures similar to 30PE-LNP-NP1 were observed (**Figure 2f**). However, the presence of concentric lamellar structures was no longer observed. This absence of lamellar structures can be attributed to our rational design, given the high amount of DOPE lipids that possess a negative intrinsic curvature in the 49PE-LNP formulations. Quantification of the structures in 49PE-LNP-NP1 also yielded a high similarity in lattice spacing for straight lines and hexagons, at 6.10 nm ± 0.13 nm and 6.03 nm ± 0.12 nm respectively. This is in line with the presence of a very pronounced Bragg peak in the 49PE-LNP-NP1 SAXS pattern. Altogether, the observation of straight lines and hexagonal structures in 30PE-LNP-NP1 and 49PE-LNP-NP1 clearly indicates the presence of an inverse hexagonal tubular structure, imaged from different viewpoints by cryoTEM (**Figure 2h**). The expansion of the lattice of the inverted hexagonal

phase from a = 5.78 nm ± 0.14 nm for 30PE-LNP-NP1 to a = 6.06 nm ± 0.13 nm for 49PE-LNP-NP1, can be explained by the increase in C_{18}-tailed DOPE and concomitant reduction in cholesterol content.[45]

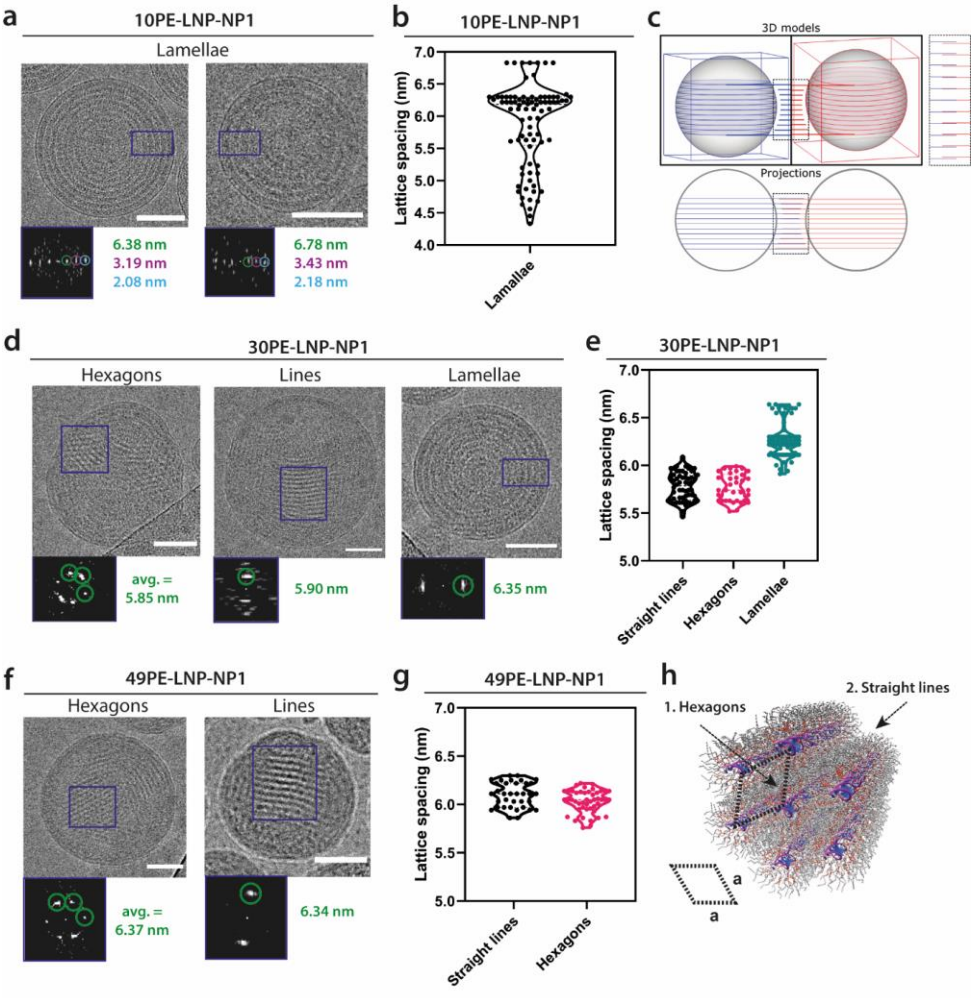


Figure 2. Identification and quantification of lipid-siRNA structures in LNPs. (**a**) cryoTEM of representative structures found in 10PE-LNP-NP1. FFT values represent the [100] structure and higher-order reflections. Scale bars are 50 nm. (**b**) Quantification of lamellar spacings (n = 84, 5.88 nm ± 0.65 nm, median = 6.18 nm). Values are derived from the first-order reflections in the FFT of 10PE-LNP-NP1. (**c**) Schematic representation of lamellar structures at different tilt angles. Projection of lattices shown in red appear narrower than blue due to out of plane rotation of the LNPs. Dashed box shows a magnification of the indicated regions. (**d**) CryoTEM of individual

particles displayed representative structures found in 30PE-LNP-NP1. Scale bars are 50 nm. (**e**) Quantification of lattice spacings of the different structures displayed in d: straight lines (n = 56, 5.78 nm ± 0.14 nm), hexagons (n = 34, 5.77 nm ± 0.14 nm) and lamellae (n = 78, 6.26 nm ± 0.18 nm). (**f**) CryoTEM of individual particles displaying representative structures found in 49PE-LNP-NP1. Scale bars are 50 nm. (**g**) Quantification of lattice spacings of the different structures displayed in f: hexagons (n = 46, 6.03 ± 0.12 nm) and straight lines (n = 35, 6.10 ± 0.13 nm). (**h**) Atomistic model of inverse hexagonal lipid structures with associated primitive cell. The lattice spacings derived from cryoTEM images are denoted as **a**.

Following identification and characterization of paracrystalline inverse hexagonal structures inside of LNPs using combined SAXS and cryoTEM, we sought to investigate the effect of siRNA content on the assembly pathway and three-dimensional architecture of the LNPs. Assembly of 49PE-LNPs without siRNA (49PE-LNP-noRNA) or with an NP ratio of 6 (49PE-LNP-NP6) both yielded straight lines and hexagonal structures similar to 49PE-LNP-NP1, but with different dimensions (**Figure 3a, Figure S7**). Single particle lattice spacing analysis on these structures revealed a single population for 49PE-LNP-noRNA with an average lattice spacing of 4.78 nm ± 0.11 nm, and a bimodal distribution for 49PE-LNP-NP6 with an average of 4.84 nm ± 0.16 nm for the lower population and an average of 6.20 nm ± 0.17 nm for the higher population (**Figure 3b**). The lattice spacing of the lower population of the 49PE-LNP-NP6 is highly similar to the 49PE-LNP-noRNA distribution, whereas the lattice spacing of the higher population is highly similar to that of 49PE-LNP-NP1. This widening of the lattice spacing for the higher distribution of 49PE-LNP-NP6 and 49PE-LNP-NP1 over that of the lower population of 49PE-LNP-NP6 and 49PE-LNP-noRNA is due to encapsulation of siRNA within in the tubular structure, with the change being close to the calculated width (~2 nm) of a free siRNA molecule (**Figure S1b**). These therefore represent 'empty' and 'filled' hexagonally-packed tubular structures (**Figure 3c**).

Furthermore, no combination of 'empty' and 'filled' structures within the same LNP was observed with cryoTEM, suggesting that a non-saturating amount of siRNA during assembly gives rise to two parallel assembly pathways. DLS measurements indicated that 49PE-LNPs assembled without siRNA are larger and more polydisperse in dimension than LNPs assembled with a NP ratio of 1 (**Table S2**). To examine this more closely, we compared the particle diameters of 'empty' and 'filled' 49PE-LNP variants determined by cryoTEM (**Figure S9**). In line with the DLS results, we found that 'filled' LNPs tend to be smaller and more monodisperse (D = 117 nm ± 33 nm and D = 118 nm ± 22 nm for 49PE-LNP-NP6-filled and 49PE-LNP-NP1, respectively) than 'empty' particles (D = 224 nm ± 70 nm and D = 257 nm ± 95 nm for 49PE-LNP-NP6-empty and 49PE-LNP-noRNA, respectively). In addition, 49PE-LNP-noRNA shows the formation of empty tubular

structures throughout the LNP core that were longer than the filled structures in the case of 49PE-LNP-NP1 (**Figure S7b,d**). Although the exact mechanisms underlying LNP assembly remain elusive and beyond the scope of this work,[15,42,46] we hypothesize that DODAP and DOPE can form inverted hexagonal phases in the absence of siRNA, leading to the formation longer tubular structures which in turn favors the formation of larger LNPs. In the presence of siRNA, which is ~5 nm in length, the formation of long tubular structures requires the alignment of multiple siRNA molecules that, along with the electrostatic interaction between DODAP and siRNA, make it more prone to disruption and leads to the formation of smaller LNPs with paracrystalline order comprising shorter tubes.

In addition to the inverse hexagonal tubular structures formed in 49PE-LNP-noRNA, we also identified a spherical structure that was able to co-exist in the same particle with inverse hexagonal tubular structures (**Figure S10a**). CryoET revealed the formation of two independent structures within the same LNP, and showed that the spheres resided at the periphery, in regions without inverse hexagonal tubes (**Figure 3d,e**). In addition, cryoET slices of an individual LNP showed that these spherical structures with a size of ~8-10 nm can be hexagonally packed (**Figure S11**). These spheres are reminiscent of an inverse micellar phase with an aqueous core.[47] In our case, inverse micelles consisting of DODAP and DOPE with the hydrophobic tails point outwards surrounding a large aqueous core accurately reflect the formed structure. In order to determine to what end the SAXS profiles reflected the formed phases we calculated the d-spacing using of the q_{max} values for each of the distinguishable peaks. Due to the co-existence of phases, the first and second order Bragg peaks could reflect [1,0] and [1,1] of one of the structures, or the [1,0] and [1,0] of the two individual hexagonally packed structures (spheres or tubes) (**Figure S10b**). Assuming a single structure, an average d-spacing of 8.48 nm was found, closely reflecting the average size of the inverse micellar structures identified in cryoET (**Figure S10c,d**), whilst calculations assuming two structures revealed that the d-spacing of the second order peak was ~4.95 nm, similar to the average lattice spacing of the inverse hexagonal tubular structures derived from cryoTEM (**Figure 3b**). Together, these results indicate that the peaks in the SAXS profiles represent an overlap of two coexisting structures. Although the resolution of SAXS may be insufficient for the accurate determination of multiple coexisting structural states, it still serves as a qualitative bulk measurement for the relative comparison of structural changes between LNP formulations. Furthermore, the increased lattice spacing in the case of 49PE-LNP-NP1 compared to 49PE-LNP-noRNA is confirmed by a shift in the SAXS profile to lower q_{max} values, of which the same analysis yields and average d-spacing of 6.22 nm (**Figure S10e,f**). A similar shift of the first order peak was observed, suggesting the presence of hexagonally packed spheres with an average d-spacing

of 10.71 nm in the case of 49PE-LNP-NP1. However, inverse micellar structures as found in 49PE-LNP-noRNA were not identified in the case of 49PE-LNP-NP1 using cryoTEM. Nevertheless, we did identify polymorphic-like structures that appear as disordered in cryoTEM (**Figure S10g,h**). Since the particles of 49PE-LNP-NP1 are significantly smaller than 49PE-LNP-noRNA, the identification of ~10 nm structures might be problematic in cryoTEM due to the lack of space at the LNP periphery, leading to a decreased repeatability and less order.

To explore the structural organization in 49PE-LNP-NP1, we used cryoET and identified the polymorphic and inverse hexagonal structures within a single LNP (**Figure 3f**). Inverse hexagonally packed structures were present throughout the core of the LNP, whereas the amorphous structures appeared on the LNP periphery, similar to the spherical structures in 49PE-LNP-noRNA, where they form an interface between the well-ordered core and amorphous lipid membrane. Isosurface reconstruction of the tomogram reveals the paracrystalline nature of the inverse hexagonal phases, appearing in both straight lines and hexagonal orientations within the same particle (**Figure 3g**). The electron density of the tomogram fitted with a siRNA-lipid structure (50:50 mol% DODAP:DOPE) shows a clear overlap of the maximum electron density with the siRNA molecules (**Figure 3h**). Altogether, these results confirm the successful assembly of inverse hexagonal phases, encapsulating siRNA, in the core of LNPs.

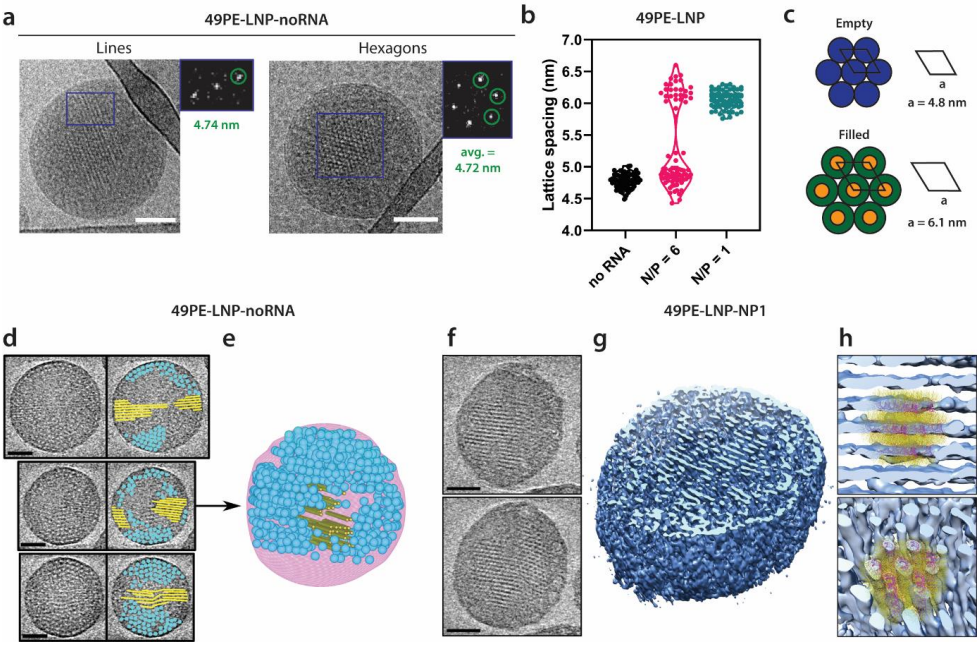


Figure 3. Identification of filled and empty inverse hexagonal structures. (**a**) Representative cryoTEM and FFTs of 49PE-LNP-noRNA showing two distinct structures: straight lines and hexagons. Scale bars are 50 nm. (**b**) Quantification of lattice spacings of structures found in 49PE-LNP at different RNA amounts: no RNA (n = 63, 4.78 nm ± 0.11 nm), NP = 6 (total: n = 77, 5.31 nm ± 0.67, low population: n = 50, 4.84 nm ± 0.16 nm, high population: n = 27, 6.20 nm ± 0.17 nm) and NP = 1 (n = 81, 6.06 nm ± 0.13 nm). (**c**) Schematic representation of 'empty' and 'filled' inverted hexagonal structures. (**d**) CryoET slices of 3 separate 49PE-LNP-noRNA particles. Identified spherical and tubular structures in each slice are indicated as blue circles and yellow lines respectively. Scale bars are 50 nm. (**e**) Reconstruction of the three-dimensional tomogram shown as the middle LNP in d. (**f**) CryoET slices through an individual 49PE-LNP-NP1 particle. EM images represent slices at two different heights of the tomogram, showing straight lines (top) and hexagonally packed regions (bottom). Scale bars are 50 nm. (**g**) Surface rendering indicates internal paracrystalline structures. (**h**) Fitted siRNA-lipid models to the electron density derived from cryoET, showing different orientations of the same structure (RNA in purple, lipid tails in yellow).

The formation and characterization of LNPs is typically performed and reported at room temperature (RT, 25 °C). However, once applied at a physiological temperature (37 °C), the change in temperature can influence lipid structures and LNP performance. Therefore, we explored the stability of the lipid superstructures in 10PE-LNP-NP1, 30PE-LNP-NP1 and 49PE-LNP-NP1 at these temperatures using SAXS. Each LNP sample was subjected to three 6h measurements and two 1h temperature ramps to collect data at 25 °C before heating to 37 °C, and once again at 25 °C after heating. Interestingly, the Bragg reflection characteristic for the lamellar structure in 10PE-LNP-NP1 was only visible at room temperature before heating, while it was completely abolished at 37 °C and did not recover upon cooling down back to room temperature (**Figure 4a**). In addition, no other Bragg reflections were observed. The loss of the lamellar structure and its transformation into a more disordered phase thus appears irreversible. By contrast, neither 30PE-LNP-NP1 nor 49PE-LNP-NP1 exhibited a significant change in their SAXS profiles collected at 25°C and 37 °C (**Figure 4b,c**).

As a control formulation, we designed a LNP that would maintain its lamellar structure upon heating to 37 °C. We hypothesized that substitution of the ionizable lipid DODAP in 10PE-LNP-NP1 with its fully saturated analogue 1,2-distearoyl-3-dimethylammonium-propane (DSDAP), while keeping the rest of the lipids and NP ratio constant, would increase the overall transition temperature of the LNP formulation and lead to the formation of rigid lamellar structures (10PE-DS-LNP-NP1, **Figure 4d,e**). This formulation showed a similar scattering signal compared to 10PE-LNP-NP1 at 25 °C, but no significant decrease when measured at 37 °C or after heating at 25 °C (**Figure 4f**). We probed the dynamic structural changes in 10PE-LNP-NP1 and 10PE-DS-LNP-NP1 by collecting SAXS

profiles at 25 °C, followed by measurements at 37 °C in intervals of 1 hour over a total time of 12 hours (**Figure 4g,h and Figure S12**). For 10PE-LNP-NP1, the scattering signal decreased rapidly after 1 hour and was largely absent after 3-4 hours, whereas the scattering signal for 10PE-DS-LNP-NP1 remained generally unchanged over the complete 12-hour period. To confirm and visualize the structural changes in 10PE-LNP-NP1, cryoTEM imaging was performed after incubation for 1 hour at 37 °C, revealing the formation of polymorphic and amorphous structures, with a small amount of lamellar structure still present (**Figure 4i**). For 10PE-DS-LNP-NP1, cryoTEM imaging showed the formation of spherical and disk-like LNPs containing lamellar structures at 25 °C (**Figure 4j**). Notably, lamellar structures were not present as concentrical rings that extended to the core of the LNP, as found in 10PE-LNP-NP1, but instead showed the formation of amorphous structure in the LNP core. This is likely due to the severe decrease in bending capability of lamellar structures containing the saturated and rigid DSDAP lipid. In addition, the observed structures of 10PE-DS-LNP-NP1 remained visible after a 1-hour incubation at 37 °C (**Figure 4k**), in agreement with the respective SAXS profiles.

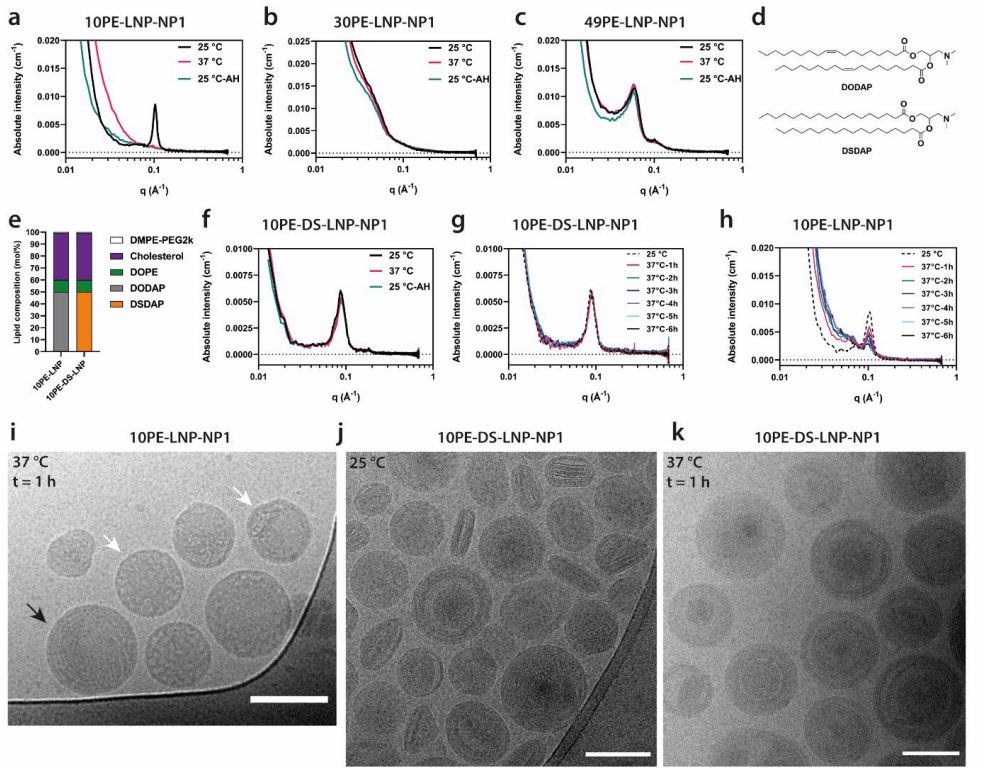


Figure 4. The effect of temperature on LNP core structure. (**a**-**c**) SAXS profiles of LNP-10PE-NP1, LNP-30PE-NP1 and LNP-49PE-NP1 at 25 °C, 37 °C and 25 °C after heating (AH) (**d**) Chemical structures of the ionizable lipids DODAP and DSDAP (**e**) Lipid compositions for the rigidification of thermolabile lamellar 10PE-LNP-NP1 to a rigid formulation 10PE-DS-LNP-NP1. (**f**) SAXS profiles of 10PE-DS-LNP-NP1 at 25 °C, 37 °C and 25 °C after heating (AH) (**g,h**) SAXS profiles 10PE-DS-LNP-NP1 and 10PE-LNP-NP1 at 25 °C, and at 1 hour intervals at 37 °C. (**i**) CryoTEM of 10PE-LNP-NP1 after incubation at 37 °C for 1 hour. White arrows indicate the formation of polymorphic and amorphous structures, black arrows indicate lamellar structure. Scale bar is 100 nm. (**j,k**) CryoTEM of 10PE-DS-LNP-NP1 at 25 °C and after incubation at 37 °C for 1 hour. Scale bars are 100 nm.

After characterization of LNPs, we assessed the intracellular silencing efficiency of LNPs containing rigid lamellar (10PE-DS-LNP-NP1), thermolabile lamellar (10PE-LNP-NP1), mixed (30PE-LNP-NP1) or paracrystalline inverted hexagonal phases (49PE-LNP-NP1). The efficiency of LNP mediated transfection was determined by the silencing of GFP tagged to the endogenous proteins CD63 and UBE21, in HeLa and U2OS cells respectively.[48,49] In order to monitor the difference in uptake between formulations, a small amount of the non-exchangeable lipid dye 1,1′-dioctadecyl-3,3,3′,3′-tetramethylindodicarbocyanine (DiD, 0.1 mol%) was added to the formulations during formation. These LNPs, encapsulating the siRNA for GFP, were added to the cells at various doses of encapsulated siRNA (0 – 83 nM) and incubated for 24 hours, after which the medium was refreshed and the cells were allowed to grow for another 48 hours in order to deplete the GFP that was expressed before the addition of LNPs (**Figure 5a**). At 72 hours, the cells were collected and fluorescence-activated cell sorting (FACS) was performed to quantify both the absolute uptake of LNPs, based on the mean fluorescence intensity (MFI) of the DiD dye, and the silencing efficiency relative to PBS treated cells from the MFI of GFP. A colorimetric cell-viability study (MTT) performed at 72 hours showed that the viability of both cultured cell lines remained unaffected by any of the LNP formulations across all doses (**Figure S13**).

For the U2OS-UBE21-GFP cell line, uptake of LNPs was similar in all cases up to 50 nM (**Figure 5a**), but clear differences in GFP fluorescence were observed (**Figure 5b**). Here, 49PE-LNP-NP1 showed the most GFP silencing across all doses, followed by LNP-30PE-NP1 and LNP-10PE-NP1. Finally, the rigid lamellar LNP-10PE-DS-NP1 showed poor transfection relative to the other formulations, where only the highest concentration of 83 nM led to more than 50% GFP silencing. For the latter, this observation of increased saturation in ionizable cationic lipids leading to less efficient cellular transfection closely reflects previous reports.[50] In the HeLa-CD63-eGFP cell line, similar uptake and silencing efficiency trends were observed for all formulations up to 25 nM (**Figure 5c**). Similar trends

of silencing efficiency were observed to the U2OS cell line, in which 49PE-LNP-NP1 and 30PE-LNP-NP1 performed the best, despite lower cellular uptake at higher doses (50 nM and 83 nM). However, in this cell line, 10PE-LNP-NP1 and 10PE-DS-LNP-NP1 exhibited similar silencing efficiencies suggesting that there is little difference in silencing between the rigid and thermo-labile lamellar structures.

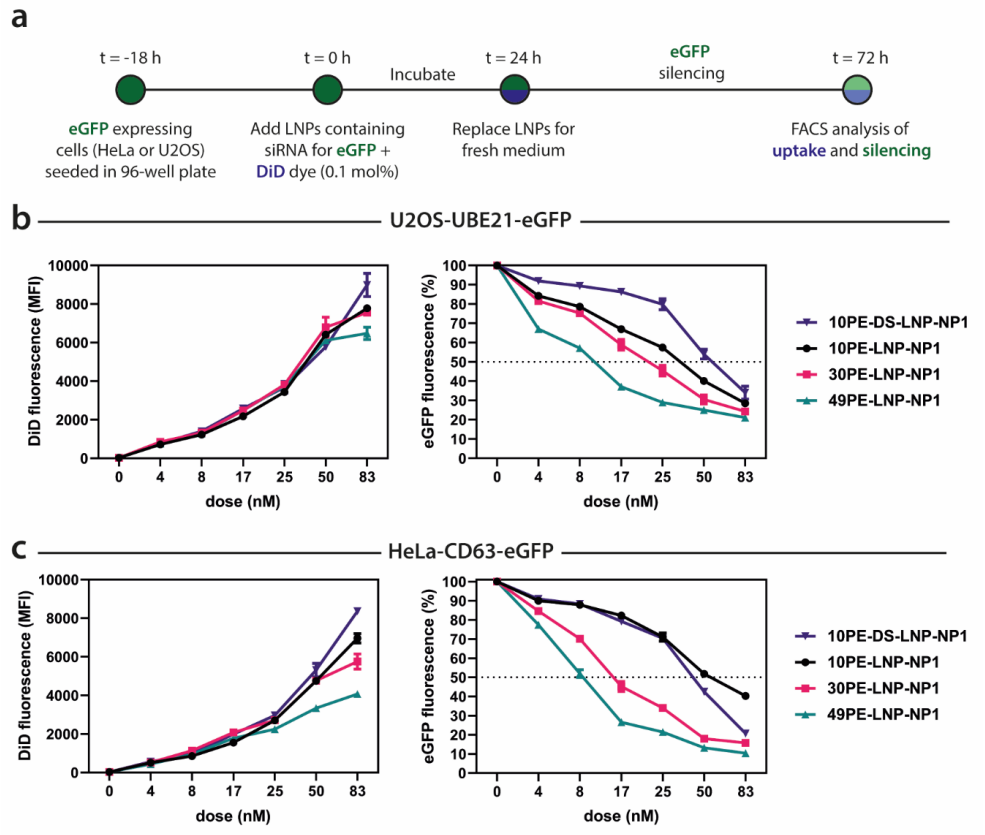


Figure 5. Intracellular silencing of eGFP with lamellar and paracrystalline inverted hexagonal LNPs. (**a**) Schematic representation of the cell culture eGFP silencing experiment. Cells are incubated with LNPs for 24 hours, followed by medium replacement and culturing for an additional 48 hours. At 72 hours, the cells are collected and analyzed using FACS for LNP uptake and eGFP silencing. (**b,c**) LNP uptake and eGFP silencing in U2OS-UBE21-eGFP or HeLa-CD63-eGFP cell lines. LNP uptake is quantified based on the mean fluorescence intensity (MFI) of DiD in the cells. The relative eGFP fluorescence (%) is quantified as the MFI of GFP in the treated cells compared to PBS treated cells. All data points are the average of a triplicate and error bars reflect the standard deviation.

After establishing a clear trend in transfection efficiency when comparing LNPs with defined lipid structures, we sought to gain more mechanistic insights into the LNP-membrane interaction. Interactions between LNPs and endosomal membranes are driven by an electrostatic interaction of negatively charged membranes and protonated LNPs in an acidic endosomal environment.[17] Therefore, we studied the interaction of LNPs with anionic large unilamellar vesicles (LUVs) that mimic endosomal membranes. The lipid composition of endosomal membranes is complex, dynamic and dependent on cell type, typically rich in (zwitterionic) neutral lipids such as phosphatidylcholine (PC), phosphatidylethanolamine (PE) and cholesterol (Chol),[51] along with lipids that have a formal negative charge such as phosphatidylserine (PS) and phosphatidylinositol (PI).[52,53] A lipid composition of PC:PE:PS:Chol:PI at a ratio of 50:27:10:10:3 mol% was chosen, where purified lipid extracts with variable lipid chain lengths for each of the phospholipids were used, to reflect the high variability of lipid chain length and saturation in natural membranes (see **Supplementary Information**). These unilamellar model membranes were assembled using thin-film hydration, followed by multiple freeze-thawing cycles and extrusion. CryoTEM, DLS and Zeta Potential measurements confirmed the formation of monodisperse anionic LUVs of ~100-150 nm (**Figure S14, Table S2**).

We first sought to investigate the effect that the different LNP lipid compositions had on lipid mixing with our model membranes. To this end, we added two DOPE lipid-conjugated fluorophores, Nitrobenzoxadiazole (PE-NBD) and Lissamine Rhodamine B (PE-LR) to the composition of the LUVs at 1.5 mol% each, substituting for PE. These fluorophores form a Fluorescence Resonance Energy Transfer (FRET) pair, in which PE-LR quenches the fluorescence of PE-NBD when they are in close proximity. Upon lipid mixing between LNP and LUVs, the lipid-conjugated fluorophores will be separated leading to dequenching of the PE-NBD fluorescence over time (**Figure 6a**). When lipid mixing was performed at a typical endosomal pH of 6.0 at 37 °C,[54] all LNPs displayed lipid mixing with the acceptor liposomes, but a clear trend was observed showing that an increase in DOPE content displayed faster lipid mixing kinetics as well as a higher total lipid mixing efficiency (**Figure 6b**). Furthermore, the rigid lamellar formulation LNP-10PE-DS-NP1 showed the lowest lipid mixing kinetics and efficiency. In all cases, no active lipid mixing was observed at a physiological pH of 7.4 at 37 °C, confirming the need for a pH below the pKa of DODAP for the initiation of the LNP-LUV interaction (**Figure 6b**). The trend of lipid mixing efficiency closely correlates to the observed silencing efficiencies observed in cell culture (**Figure 4b,c**), where 49PE-LNP-NP1 is the most efficient for both lipid mixing and silencing.

Next, we explored the alteration of the defined lipid structures upon lipid mixing of LNPs with LUVs. Judging from the FRET based assay, lipid mixing reached an equilibrium after

~30 minutes. Therefore, we visualized the LNP-LUV interaction with cryoTEM after 1 and 7 hours and used SAXS in the intermediate period of 6 hours to determine the preservation of defined lipid structures (**Figure 6c**). The very inefficient lipid mixing of 10PE-DS-LNP-NP1 was reflected in the SAXS profile, showing a minor decrease in lamellar signal compared to 10PE-DS-LNP-NP1 before mixing (**Figure S15a,b**). In addition, cryoTEM revealed the docking of LNPs to LUVs but lacking further fusion or structural change, at both 1 and 7 hours. (**Figure S15c,d**).

In the case of 10PE-LNP-NP1, the respective SAXS profile showed a decrease in the lamellar signal after mixing (**Figure 6d**). The SAXS profile also shows the increase of a distinguishable peak at a lower q-value, suggesting the formation of additional structures. CryoTEM revealed that these LNPs interact with LUVs and form inverted hexagonal structures at the LNP-LUV interface, while also retaining characteristics of lamellar structures as determined by FFT analysis (**Figure 6f, Figure S17**). Furthermore, these structures remain visible after incubation with LUVs after 7 hours, indicating preservation of the lipid structures. The first order peaks of both lamellar and inverse hexagonal structures will appear as a signal at a q-value of ~0.1, making it difficult to distinguish the contribution of these structures to the observed signal. Nevertheless, a complete abolishment of the lamellar structures as seen for 10PE-LNP-NP1 alone is not observed, indicating that the thermal stability of these structures is increased upon lipid mixing with the acceptor LUVs.

For 30PE-LNP-NP1 mixed with LUVs, the measured SAXS profile showed complete abolishment of the broad 30PE-LNP-NP1 signal present before mixing while primarily yielding a signal at a q-value of ~0.1 (**Figure S16a,b**). CryoTEM at both 1 and 7 hours show the primary formation of inverted hexagonal structures and straight lines, although some lamellar structures were also identified (**Figure S16c,d**). Finally, for 49PE-LNP-NP1, the SAXS profile showed the complete abolishment of the signal corresponding to the first order signal of the larger structures, yielding a clearly defined peak corresponding to the first order peak of the inverse hexagonal tubular structures (**Figure 6e, Figure S10e**). CryoTEM showed the sole formation of crystalline inverse hexagonal phases, visualized as hexagons or straight lines (**Figure 6g, Figure S18**). Furthermore, these structures remained clearly visible after 7 hours, confirming preservation upon interaction with LUVs and the thermal stability of these structures.

From these results, we propose a mechanism that explains the observations of enhanced lipid mixing and transfection of LNPs with paracrystalline inverse hexagonal over lamellar phases, and to what extent it might impact intracellular siRNA delivery (**Figure 6h**). After

an initial interaction of LNPs with acceptor LUVs triggered by the protonation of ionizable lipids (ILs) at acidic pH, the LNPs follow two different pathways for the delivery of their cargo. In the case of 10PE-LNP-NP1, an *in situ* transition of lamellar to inverse hexagonal phase takes place at the LNP-LUV intersection, which allows for membrane disruption and the eventual escape of RNA molecules from the LNP (**Figure 6h, pathway 1**). These findings are complementary to the rationale for which membrane-disrupting ILs or LNP formulations were designed, in which ILs form non-lamellar structures with the anionic lipids of the acceptor membrane.[18,19] Other factors that will play a role in LNPs with lamellar structures can be the overall fluidity of the lipid mixture and the pKa of the IL. [22,25] Although the formation of pre-programmed inverse hexagonal phases in LNPs has not been reported before, permanently cationic lipid-oligonucleotide complexes, named lipoplexes, show a degree of similarity to our system.[55–57] Here, lipoplexes containing inverse hexagonal phases encapsulating double-stranded DNA (dsDNA) interacting with acceptor giant unilamellar vesicles (GUVs, ~20 μm) are shown to generate near complete lipid mixing towards a lamellar acceptor membrane.[44] However, the visualization of lipoplex-membrane complexes at the nanoscale has not been reported. More recently, molecular dynamics simulations of inverse hexagonal lipoplexes containing dsDNA interacting with anionic membranes show how dsDNA is able to escape from the lipoplex.[58] These results align directly with our observation of retention of the pre-programmed inverse hexagonal phase upon interaction with the LUVs. Therefore, derived from our cryoTEM and SAXS data, we suggest that these structures bypass the initial lamellar-to-inverse hexagonal phase transition that is occurring for 10PE-LNP-NP1, instead generating a more efficient 1-step process of siRNA delivery directly from the inverse hexagonal phase (**Figure 6h, pathway 2**). An important observation is, although the presence of paracrystalline H_{II} phases improves lipid mixing and transfection efficiency, complete fusion of the LNP-LUV systems does not occur, leaving a large amount of siRNA complexed in thermodynamically stable siRNA-lipid structures. Although our *in vitro* model is a simplified version of the LNP-membrane interaction and lacks the presence of the complex dynamic intracellular environment, these observations and proposed mechanism may provide a contributing factor to the poor endosomal escape of RNA molecules (≤ 2%) from the endosome into the cytosol.[17,20,21]

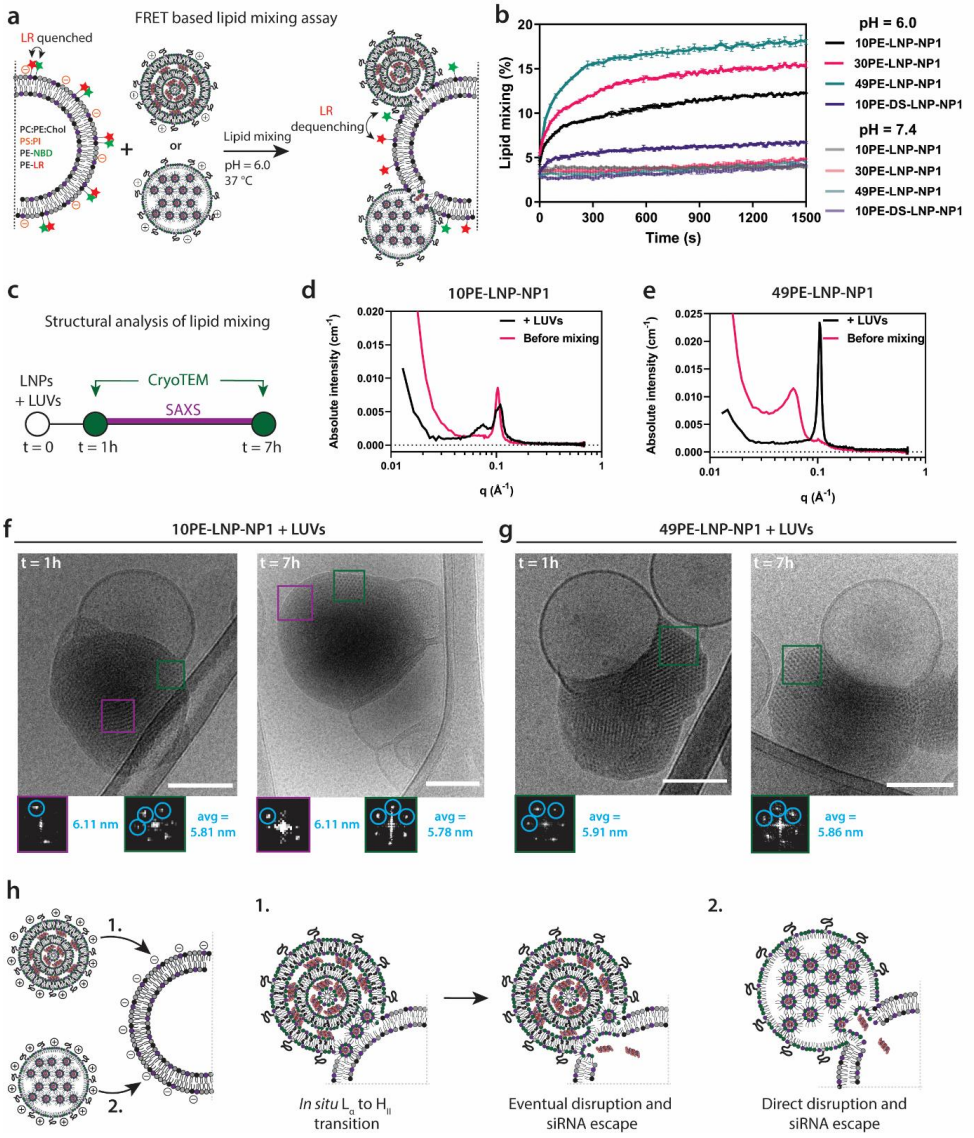


Figure 6. Interaction of LNPs with anionic LUVs. (**a**) Schematic representation of the FRET based lipid mixing assay. LNPs are mixed with anionic acceptor liposomes containing two lipid conjugated fluorophores (PE-NBD and PE-LR), after which the dequenching of PE-NBD is measured over time. (**b**) Lipid mixing results of LNPs (250 µM) mixed with anionic LUVs (125 µM) at pH 6.0 and 7.4 cryoTEM, performed at 37 °C for 25 minutes. Plotted data is the average of a triplicate in which error bars represent the standard deviation. (**c**) Schematic representation of the structural analysis of lipid

mixing between LNPs and LUVs. CryoTEM imaging was performed after an incubation of 1 hour at 37 °C. Similarly, SAXS measurements over a time span of 6 hours were started after an incubation of 1 hour at 37 °C. (**d,e**) SAXS profiles of 10PE-LNP-NP1 or 49PE-LNP-NP1 mixed with LUVs. (**f,g**) Representative cryoTEM images of 10PE-LNP-NP1 or 49PE-LNP-NP1 mixed with LUVs. Scale bars are 100 nm (**h**) Schematic representation of a proposed mechanism explaining the increased lipid mixing and transfection efficiency of LNPs with pre-programmed inverse hexagonal phases compared to LNPs with lamellar phases.

5.3 Discussion

Using bottom-up rational design of defined lipid superstructures, we have generated LNPs with paracrystalline inverse hexagonal lipid structures actively encapsulating siRNA and with enhanced transfection efficiency over LNPs containing lamellar structures. Due to the inherent complexity of lipid behavior in LNPs during and after nanoparticle assembly, an in-depth characterization combining cryoTEM, SAXS and cryoET was employed to determine the effects of lipid composition, RNA content, temperature and membrane interaction on the formation and stability these structures. Endosomal escape remains a tremendous barrier for the improvement of LNP-based RNA therapeutics, yet our data shows that, through inducing pre-programmed lipid phases, transfection efficiency can be enhanced. This may play a crucial role for widespread applications. Here, it is important to recognize the extensive efforts in the exploration of the chemical space of ionizable lipids[24,25,59], and other LNPs components for the promotion of endosomal escape of RNA molecules.[33,34] Since the formation of non-lamellar lipid structures is driven by total lipid composition of these multicomponent systems, and therefore not exclusively on specific ILs, we believe that our approach for inducing inverse hexagonal structures can be retrofitted to LNPs with other ILs or components, albeit it at different lipid concentrations or RNA content, to increase their LNP potency, which will allow additional exploration of the structural space of LNPs. Consequently, the large variety of natural and synthetic lipids also generates possibilities for the rational design of other defined lipid structures.[36,60,61]

LNPs are currently applied in a widespread of LNP-RNA therapeutic approaches,[62–65] for example in the form of prophylactic vaccines against COVID-19.[11,12,66,67] It will be of great interest to expand the defined structural space of LNPs containing RNA molecules with a more complex and less predictable structure than siRNA (*e.g.* mRNA and single guide RNA). To this end, bottom-up approaches of LNP design and application, based on rational design and the mechanistic understanding of the nano-bio interactions, can help to predict and understand of these structures. Finally, mechanistic knowledge about lipid superstructures containing RNA molecules, and their behavior with endosomal

membranes, will enable the predictions of LNP potency from a bottom-up based approach in which LNP formulations are assessed with biophysical methods before their application to *in vitro* or *in vivo* systems, opening up another avenue of LNP design and optimization.

5.4 References

1. Delivering the promise of RNA therapeutics. *Nat. Med.* **25**, 1321 (2019).
2. Lieberman, J. Tapping the RNA world for therapeutics. *Nat. Struct. Mol. Biol.* **25**, 357–364 (2018).
3. Wang, F., Zuroske, T. & Watts, J. K. RNA therapeutics on the rise. *Nature reviews. Drug discovery* **19**, 441–442 (2020).
4. Yin, H. *et al.* Non-viral vectors for gene-based therapy. *Nat. Rev. Genet.* **15**, 541–555 (2014).
5. Nguyen, J. & Szoka, F. C. Nucleic acid delivery: the missing pieces of the puzzle? *Acc. Chem. Res.* **45**, 1153–1162 (2012).
6. Jones, C. H., Chen, C. K., Ravikrishnan, A., Rane, S. & Pfeifer, B. A. Overcoming nonviral gene delivery barriers: Perspective and future. *Mol. Pharm.* **10**, 4082–4098 (2013).
7. Cullis, P. R. & Hope, M. J. Lipid Nanoparticle Systems for Enabling Gene Therapies. *Mol. Ther.* **25**, 1467–1475 (2017).
8. Rajabi, M. & Mousa, S. A. Lipid Nanoparticles and their Application in Nanomedicine. *Curr. Pharm. Biotechnol.* **17**, 662–672 (2016).
9. Akinc, A. *et al.* The Onpattro story and the clinical translation of nanomedicines containing nucleic acid-based drugs. *Nat. Nanotechnol.* **14**, 1084–1087 (2019).
10. Adams, D. *et al.* Patisiran, an RNAi therapeutic, for hereditary transthyretin amyloidosis. *N. Engl. J. Med.* **379**, 11–21 (2018).
11. Jackson, L. A. *et al.* An mRNA Vaccine against SARS-CoV-2 — Preliminary Report. *N. Engl. J. Med.* **383**, 1920–1931 (2020).
12. McKay, P. F. *et al.* Self-amplifying RNA SARS-CoV-2 lipid nanoparticle vaccine candidate induces high neutralizing antibody titers in mice. *Nat. Commun.* **11**, 3523 (2020).
13. Evers, M. J. W. *et al.* State-of-the-Art Design and Rapid-Mixing Production Techniques of Lipid Nanoparticles for Nucleic Acid Delivery. *Small methods* **1700375**, 1–20 (2018).
14. Leung, A. K. K., Tam, Y. Y. C., Chen, S., Hafez, I. M. & Cullis, P. R. Microfluidic Mixing: A General Method for Encapsulating Macromolecules in Lipid Nanoparticle Systems. *J. Phys. Chem. B* **119**, 8698–8706 (2015).
15. Kulkarni, J. A. *et al.* On The Formation and Morphology of Lipid Nanoparticles Containing Ionizable Cationic Lipids and siRNA. *ACS Nano* **12**, 4787–4795 (2018).
16. Arteta, M. Y. *et al.* Successful reprogramming of cellular protein production through mRNA delivered by functionalized lipid nanoparticles. *Proc. Natl. Acad. Sci. U. S. A.* **115**, E3351–E3360 (2018).
17. Wittrup, A. *et al.* Visualizing lipid-formulated siRNA release from endosomes and target gene knockdown. *Nat. Biotechnol.* **33**, 870–876 (2015).
18. Semple, S. C. *et al.* Rational design of cationic lipids for siRNA delivery. *Nat. Biotechnol.* **28**, 172–176 (2010).
19. Liu, S. *et al.* Membrane-destabilizing ionizable phospholipids for organ-selective mRNA delivery and CRISPR–Cas gene editing. *Nat. Mater.* **20**, 701–710 (2021).
20. Gilleron, J. *et al.* Image-based analysis of lipid nanoparticle–mediated siRNA delivery, intracellular trafficking and endosomal escape. *Nat. Biotechnol.* **31**, 638–646 (2013).

21. Sahay, G. *et al.* Efficiency of siRNA delivery by lipid nanoparticles is limited by endocytic recycling. *Nat. Biotechnol.* **31**, 653–658 (2013).
22. Jayaraman, M. *et al.* Maximizing the potency of siRNA lipid nanoparticles for hepatic gene silencing in vivo. *Angew. Chemie - Int. Ed.* **51**, 8529–8533 (2012).
23. Lokugamage, M. P., Sago, C. D., Gan, Z., Krupczak, B. R. & Dahlman, J. E. Constrained Nanoparticles Deliver siRNA and sgRNA to T Cells In Vivo without Targeting Ligands. *Adv. Mater.* **31**, 1902251 (2019).
24. Miao, L. *et al.* Delivery of mRNA vaccines with heterocyclic lipids increases anti-tumor efficacy by STING-mediated immune cell activation. *Nat. Biotechnol.* **37**, 1174–1185 (2019).
25. Rietwyk, S. & Peer, D. Next-Generation Lipids in RNA Interference Therapeutics. **11**, 7572–7586 (2017).
26. Love, K. T. *et al.* Lipid-like materials for low-dose, in vivo gene silencing. *Proc. Natl. Acad. Sci.* **107**, 9915–9915 (2010).
27. Whitehead, K. A. *et al.* Degradable lipid nanoparticles with predictable in vivo siRNA delivery activity. *Nat. Commun.* **5**, 1–10 (2014).
28. Cheng, X. & Lee, R. J. The role of helper lipids in lipid nanoparticles (LNPs) designed for oligonucleotide delivery. *Advanced Drug Delivery Reviews* **99**, 129–137 (2016).
29. Kulkarni, J. A., Witzigmann, D., Leung, J., Tam, Y. Y. C. & Cullis, P. R. On the role of helper lipids in lipid nanoparticle formulations of siRNA. *Nanoscale* **11**, 21733–21739 (2019).
30. Chen, S. *et al.* Influence of particle size on the in vivo potency of lipid nanoparticle formulations of siRNA. *J. Control. Release* **235**, 236–244 (2016).
31. Paunovska, K. *et al.* A Direct Comparison of in Vitro and in Vivo Nucleic Acid Delivery Mediated by Hundreds of Nanoparticles Reveals a Weak Correlation. *Nano Lett.* **18**, 2148–2157 (2018).
32. Chen, S. *et al.* Development of lipid nanoparticle formulations of siRNA for hepatocyte gene silencing following subcutaneous administration. *J. Control. Release* **196**, 106–112 (2014).
33. Patel, S. *et al.* Naturally-occurring cholesterol analogues in lipid nanoparticles induce polymorphic shape and enhance intracellular delivery of mRNA. *Nat. Commun.* **11**, 983 (2020).
34. Eygeris, Y., Patel, S., Jozic, A. & Sahay, G. Deconvoluting Lipid Nanoparticle Structure for Messenger RNA Delivery. *Nano Lett.* **20**, 4543–4549 (2020).
35. Marsh, D. Intrinsic curvature in normal and inverted lipid structures and in membranes. *Biophys. J.* **70**, 2248–2255 (1996).
36. Zhai, J., Fong, C., Tran, N. & Drummond, C. J. Non-Lamellar Lyotropic Liquid Crystalline Lipid Nanoparticles for the Next Generation of Nanomedicine. *ACS Nano* **13**, 6178–6206 (2019).
37. Mouritsen, O. G. Lipids, curvature, and nano-medicine. *Eur. J. Lipid Sci. Technol.* **113**, 1174–1187 (2011).
38. Marrink, S. J. & Mark, A. E. Molecular view of hexagonal phase formation in phospholipid membranes. *Biophys. J.* **87**, 3894–3900 (2004).
39. Hu, B. *et al.* Therapeutic siRNA: state of the art. *Signal Transduct. Target. Ther.* **5**, 101 (2020).
40. Lipfert, J. *et al.* Double-stranded RNA under force and torque: Similarities to and striking differences from double-stranded DNA. *Proc. Natl. Acad. Sci.* **111**, 15408–15413 (2014).
41. Belliveau, N. M. *et al.* Microfluidic Synthesis of Highly Potent Limit-size Lipid Nanoparticles for In Vivo Delivery of siRNA. *Mol. Ther. Nucleic Acids* **1**, e37 (2012).
42. Kulkarni, J. A. *et al.* Spontaneous, solvent-free entrapment of siRNA within lipid nanoparticles. *Nanoscale* **12**, 23959–23966 (2020).

43. Rädler, J. O., Koltover, I., Salditt, T. & Safinya, C. R. Structure of DNA-Cationic Liposome Complexes: DNA Intercalation in Multilamellar Membranes in Distinct Interhelical Packing Regimes. *Science* **275**, 810–814 (1997).
44. Koltover, I., Salditt, T., Rädler, J. O. & Safinya, C. R. An Inverted Hexagonal Phase of Cationic Liposome-DNA Complexes Related to DNA Release and Delivery. *Science* **281**, 78–81 (1998).
45. Chen, Z. & Rand, R. P. The influence of cholesterol on phospholipid membrane curvature and bending elasticity. *Biophys. J.* **73**, 267–276 (1997).
46. Kulkarni, J. A. *et al.* Fusion-dependent formation of lipid nanoparticles containing macromolecular payloads. *Nanoscale* **11**, 9023–9031 (2019).
47. Shearman, G. C. *et al.* A 3-D Hexagonal Inverse Micellar Lyotropic Phase. *J. Am. Chem. Soc.* **131**, 1678–1679 (2009).
48. Jongsma, M. L. M. *et al.* An ER-Associated Pathway Defines Endosomal Architecture for Controlled Cargo Transport. *Cell* **166**, 152–166 (2016).
49. Qiao, X. *et al.* Uncoupling DNA damage from chromatin damage to detoxify doxorubicin. *Proc. Natl. Acad. Sci.* **117**, 15182–15192 (2020).
50. Heyes, J., Palmer, L., Bremner, K. & MacLachlan, I. Cationic lipid saturation influences intracellular delivery of encapsulated nucleic acids. *J. Control. Release* **107**, 276–287 (2005).
51. Symons, J. L. *et al.* Lipidomic atlas of mammalian cell membranes reveals hierarchical variation induced by culture conditions, subcellular membranes, and cell lineages. *Soft Matter* **17**, 288–297 (2021).
52. Yeung, T. *et al.* Membrane Phosphatidylserine Regulates Surface Charge and Protein Localization. *Science* **319**, 210–213 (2008).
53. Arumugam, S. & Kaur, A. The Lipids of the Early Endosomes: Making Multimodality Work. *Chembiochem* **18**, 1053–1060 (2017).
54. Maxfield, F. R. Role of endosomes and lysosomes in human disease. *Cold Spring Harb. Perspect. Biol.* **6**, a016931 (2014).
55. Ma, B., Zhang, S., Jiang, H., Zhao, B. & Lv, H. Lipoplex morphologies and their influences on transfection efficiency in gene delivery. *J. Control. Release* **123**, 184–194 (2007).
56. Safinya, C. R. *et al.* Cationic liposome-DNA complexes: From liquid crystal science to gene delivery applications. *Philos. Trans. R. Soc. A Math. Phys. Eng. Sci.* **364**, 2573–2596 (2006).
57. Majzoub, R. N., Ewert, K. K. & Safinya, C. R. Cationic liposome–nucleic acid nanoparticle assemblies with applications in gene delivery and gene silencing. *Philos. Trans. R. Soc. A Math. Phys. Eng. Sci.* **374**, 20150129 (2016).
58. Bruininks, B. M. H., Souza, P. C. T., Ingolfsson, H. & Marrink, S. J. A molecular view on the escape of lipoplexed DNA from the endosome. *Elife* **9**, e52012 (2020).
59. Hassett, K. J. *et al.* Optimization of Lipid Nanoparticles for Intramuscular Administration of mRNA Vaccines. *Mol. Ther. - Nucleic Acids* **15**, 1–11 (2019).
60. Amar-yuli, I. *et al.* Hexosome and Hexagonal Phases Mediated by Hydration and Polymeric Stabilizer. *Langmuir* **23**, 3637–3645 (2007).
61. Demurtas, D. *et al.* Direct visualization of dispersed lipid bicontinuous cubic phases by cryo-electron tomography. *Nat. Commun.* **6**, 1–8 (2015).
62. Pardi, N., Hogan, M. J., Porter, F. W. & Weissman, D. mRNA vaccines — a new era in vaccinology. *Nat. Rev. Drug Discov.* **17**, 261–279 (2018).
63. Trepotec, Z., Lichtenegger, E., Plank, C., Aneja, M. K. & Rudolph, C. Delivery of mRNA Therapeutics for the Treatment of Hepatic Diseases. *Mol. Ther.* **27**, 794–802 (2019).
64. Samaridou, E., Heyes, J. & Lutwyche, P. Lipid nanoparticles for nucleic acid delivery: Current perspectives. *Adv. Drug Deliv. Rev.* **154–155**, 37–63 (2020).

65. Mout, R., Ray, M., Lee, Y. W., Scaletti, F. & Rotello, V. M. In Vivo Delivery of CRISPR/Cas9 for Therapeutic Gene Editing: Progress and Challenges. *Bioconjug. Chem.* **28**, 880–884 (2017).
66. Zhang, N.-N. *et al.* A Thermostable mRNA Vaccine against COVID-19. *Cell* **182**, 1271–1283 (2020).
67. Lu, J. *et al.* A COVID-19 mRNA vaccine encoding SARS-CoV-2 virus-like particles induces a strong antiviral-like immune response in mice. *Cell Res.* **30**, 936–939 (2020).

Chapter 6

Summary and outlook

The overarching goal of the research presented in this thesis was to add fundamental knowledge, as well as exploit prior knowledge, to understand and manipulate lipid-based nanomedicine at the bio-nano interface. To this end, the work described herein has focused on two themes, specifically: 1. protein adsorption to lipid-based nanoparticles in biological media and 2. the improvement of RNA delivery selectivity and efficiency using ionizable lipid nanoparticles (LNPs). In order to achieve this, an ensemble of chemical, biophysical and biological methodologies was employed. This chapter will summarize the key discoveries, their implications for the field and provide an outlook on advancing the research topics.

6.1 The (un)importance of the protein corona

In **Chapter 2**, a new method for the determination of protein adsorption to liposomes in biological media was described. Here, a bifunctional photoaffinity based lipid was synthesized which allows for co-formulation in liposomal formulations and *in situ* crosslinking with adsorbed proteins to their surface through a photo-active diazirine moiety. Following this, the azide moiety allowed for click-chemistry conjugation with a fluorophore to visualize the subset of protein binding with gel-electrophoresis, or with a biotin group for the isolation of crosslinked lipid-protein complexes. The isolated proteins were digested and identified and quantified using label-free proteomics. Significantly, compared to physical isolation methods, this avoids the isolation and inclusion of highly abundant and/or heavy, unbound serum proteins.[1–3] This approach also allowed for the identification and validation of key individual liposome-protein interactions. In particular, validation of identified proteins hits is required to exclude false-positive identification, which was problematic using previous physical isolation methods.

Chapter 4 expanded the work using the photoaffinity based method for protein corona determination towards LNPs encapsulating RNA, accurately identifying key individual protein-nanoparticle interactions that have a proven effect on the *in vivo* fate of LNPs. Generation of such a positive control served as an important milestone in laying the foundation of this methodology, and highlighted its potential for the use in mechanistic understanding of the protein corona. Furthermore, this method yielded more insights into key protein-nanoparticle interactions. In particular, using a competition assay it was shown that apolipoprotein E binds anionic LNPs site-selectively through its surface exposed heparin binding domain. The ability to uncover the molecular selectivity of a single protein to chemically-distinct nanoparticles is pivotal to elucidate protein selectivity, and provides another layer of depth to explain and predict the *in vivo* fate of nanoparticles.

As described in Chapters 2 and 4, it is possible that previous common protein corona determination methodologies can be intrinsically flawed, or lack the possibility for validation. Consequently, the research field regarding the protein corona may be dominated by false-positive data and hypotheses. In addition, the field is quickly transcending from a "protein" corona towards a "biomolecular" corona, involving the adsorption of other biomolecules (*e.g.*, polysaccharides, small molecules, lipids) to nanoparticles.[4,5] However, the importance of these interactions are still subject to heavy speculation. Therefore, more effort should be dedicated to developing unbiased identification methods and generating multiple lines of evidence for the validation of binding and the effect in a biological system (**Figure 1a**). To this end, further exploitation of the chemical biology toolbox used for small molecules to study nanomaterials at the bio-nano interface,[6] for example via chemoproteomic discovery and mapping of binding hotspots,[7,8] can serve as a useful methodology for further advancement of the field. Beyond the methodology, the obtained results from the chapters in this thesis give some important insights into protein corona formation on lipid-based nanoparticles, which can help shape future research in the field.

Firstly, the protein corona profiles reported in this thesis are typically dominated by apolipoproteins over more abundant serum proteins, which can be rationally explained by the evolved function of soluble apolipoproteins to bind lipidic surfaces of endogenous lipoproteins. As evolution has led to a carefully orchestrated network of protein-protein and protein-membrane interactions, the identification of exotic interactions that would inhibit endogenous functions should be carefully examined.[9]

Secondly, a dominant opinion within the field is that the protein corona is omnipresent for all nanoparticles and heavily impacts *in vivo* fate. In some cases, the protein corona is schematically drawn to fully decorate the nanoparticle.[10] However, these illustrations often lack experimental proof and can heavily bias the view of protein corona importance. In contrast, some of the protein corona profiles reported in this thesis show a near-to-complete absence of protein adsorption. Although the exact determinants of this have not been elucidated, it does provide evidence that in some cases it is not the protein corona, but the underlying synthetic identity of the nanoparticle that is interacting with cellular receptors or membranes.

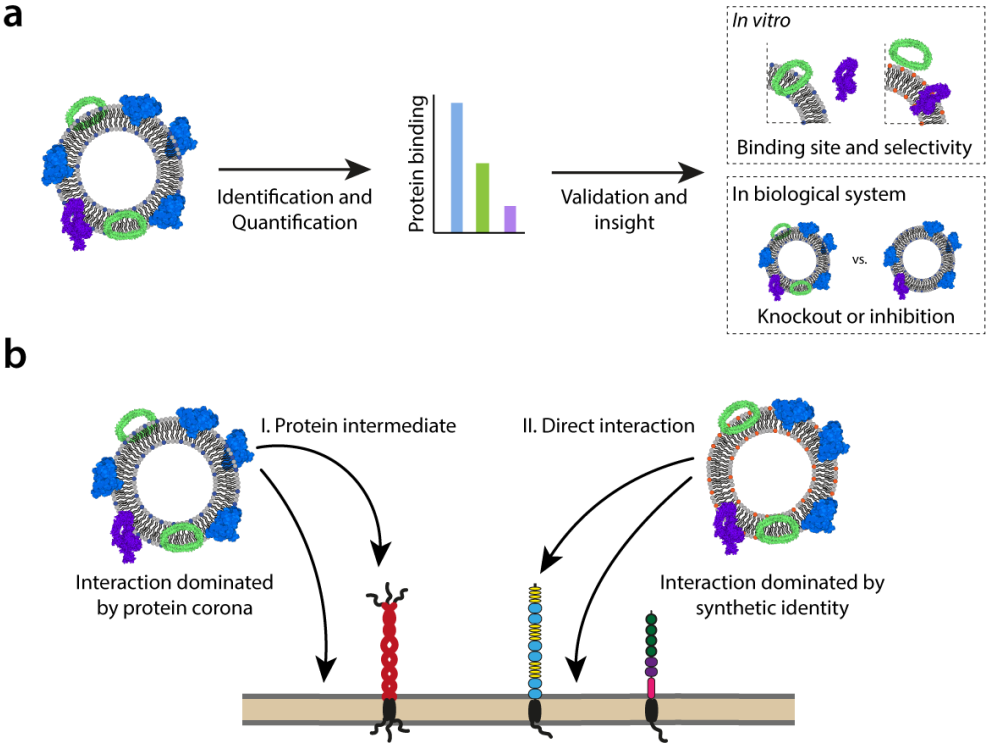


Figure 1. Important considerations for studying protein-nanoparticle interactions. (**a**) Methods should focus on the correct identification of protein binding and allow for validation with multiple lines of evidence. In the case of similar protein binding, probing binding sites can facilitate deeper understanding of key protein-nanoparticle interactions (**b**) The presence of a protein corona might not be critical for the nanoparticle fate *in vivo*, and direct nanoparticle-receptor/membrane interactions should not be excluded.

For the future of the field, it is important that multiple scenarios of protein binding and implications for their *in vivo* fate are considered when validating results (**Figure 1b**). Firstly, in the scenario that the protein corona does indeed play a role in the cellular uptake, an intermediate function of these proteins with receptors, or the direct interaction with cellular membranes, has to be considered. Secondly, there might be scenarios where even dominantly binding proteins do not play a role in the cellular uptake of nanoparticles. In this case, the direct interaction of the nanoparticle surface with receptors, or a direct interaction with the cellular membrane has to be considered. Here, the above-mentioned topics regarding the validation of protein both *in vitro* and *in vivo* will play an important

role. Altogether, the understanding of the protein corona is complicated and heavy interdisciplinary, requiring a careful in-depth examination with the proper tools.

6.2 Lipid nanoparticle design and understanding

In **Chapter 3**, an anionic LNP formulation was designed and evaluated for the preferential delivery of mRNA to the reticuloendothelial system (RES). This strategy relied on prior knowledge regarding the receptor mediated clearance of anionic liposomes, as well as biophysical knowledge of lipid organization in multicomponent LNPs. The strength of this approach was the ability to redirect the delivery of mRNA from liver hepatocytes to the RES starting from a commercial LNP formulation, by the rational change of a single lipid in its composition. *In vivo* prescreening studies in embryonic zebrafish allowed for real time fluorescent imaging of biodistribution and transfection. Additional studies in genetically engineered embryonic zebrafish provided multiple lines of evidence regarding the receptor specific uptake of these LNPs into scavenger endothelial cells and macrophages. Finally, these data were supported by translational studies into mice, showing similar selectivity and effectivity of delivering mRNA to the RES.

Chapter 5 described the fabrication of LNPs containing pre-programmed inverse hexagonal lipid phases encapsulating siRNA. Here, intrinsic properties of lipid mixtures were used to fabricate non-lamellar structures in LNPs for the first time. Using a variety of biophysical methods, including cryogenic electron microscopy and small-angle X-ray scattering, the fabrication of these structures was validated. In addition, the effect of lipid composition, RNA content and temperature on their formation, three-dimensional organization and stability was determined. The generation of LNPs with distinct internal lipid structures allowed for comparison of transfection efficiency. Furthermore, a mechanistic study on the interaction with endosomal model membranes suggests that inverted phases contribute to a more efficient one-step release mechanism by bypassing an initial lamellar to inverse hexagonal transition.

Together, these results demonstrated alternative approaches for LNP design, in which generating or exploiting bio-nano interactions play an important role. In general, the future of nanomedicine research would greatly benefit from more in-depth understanding of LNP fabrication and their interactions with different interfaces.[11,12] Common approaches for LNP development are typically empirical, relying on the generation of libraries, for example by chemically diversifying the components or through empirical formulation variation (**Figure 2a**). The direct *in vivo* evaluation is typically labour intensive and expensive, but can generate the selection of promising LNP formulations for efficient delivery to specific

cell types or organs. Nevertheless, mechanistic explanation in hindsight is troublesome due the size of the screen, large variation in biophysical properties between LNP formulations and obscurity to which bio-nano interfaces play a crucial role in their output. Therefore, alternative workflows should be employed for the mechanistic understanding and rational discovery of LNPs.

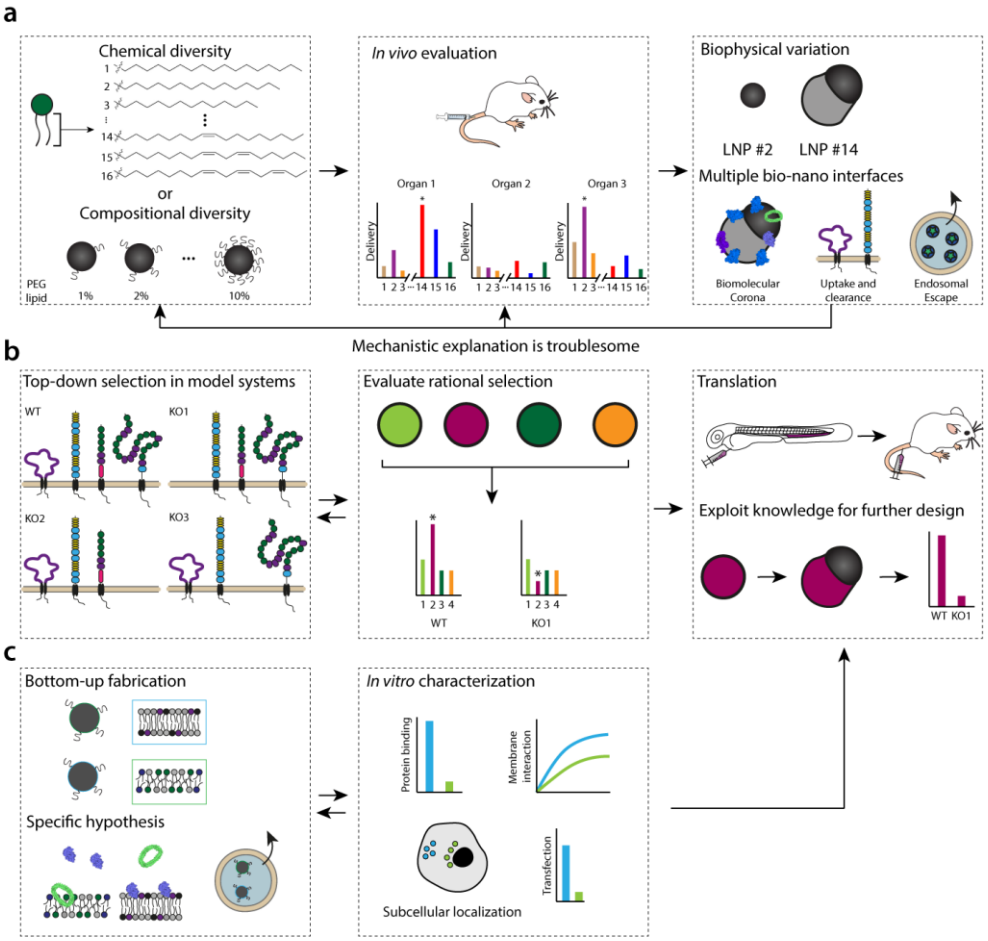


Figure 2. Workflows for mechanistic understanding of LNPs at the bio-nano interface (**a**) Common empirical approach based on the screening of LNPs makes retrospective mechanistic explanation troublesome. (**b**) Top-down selection of for example receptor targets coupled with rational selection of nanoparticles can gain useful information for further translation and new design. (**c**) Bottom-up design of LNPs and the determination of their effect on isolated bio-nano interfaces can help gain more understanding for translation and LNP design.

Firstly, the cellular uptake processes can be addressed systematically in a top-down approach (**Figure 2b**). Here, pre-existing knowledge on the uptake of endogenous nanoparticles through a variety of receptors (*e.g.*, lipoprotein receptors, scavenger receptors) can be used to generate model systems that allow for determining their individual effects. A selection of nanoparticles with distinct chemical and biophysical properties can aid in the validation of the effect and selectivity of these processes. The selection of nanoparticles and receptor targets works bidirectionally, in which information from one screen can help select targets in the other. Finally, once dominant effects are obtained, this knowledge can be used for further translation into other models, or for the design of other nanomedicine that will work through the same mechanism.

Secondly, the influence of LNP components and biophysical characteristics on specific bio-nano interfaces can be studied (**Figure 2c**). Herein, bottom-up fabrication of LNPs with defined characteristics has to be coupled with extensive characterization. The selection of a specific hypothesis (*e.g.*, protein binding, endosomal escape) allows for the use of isolated *in vitro* experiments and leads to stronger conclusions about the effect on individual bio-nano interfaces. Finally, this knowledge can be used for further translation of specific formulations, or be exploited for further design. Altogether, the field of LNP-based RNA therapeutics holds great promise for the treatment of a widespread of diseases. One of the ways of unlocking this potential is by relying more on systematic approaches of their mechanistic behaviour, besides solely empirical screens.

6.3 References

1. Weber, C., Morsbach, S. & Landfester, K. Possibilities and Limitations of Different Separation Techniques for the Analysis of the Protein Corona. *Angew. Chemie Int. Ed.* **58**, 12787–12794 (2019).
2. Simonsen, J. B. & Münter, R. Pay attention to the biological nanoparticles when studying the protein corona on nanomedicines. *Angew. Chemie Int. Ed.* **59**, 12584–12588 (2020).
3. Kristensen, K. *et al.* Isolation methods commonly used to study the liposomal protein corona suffer from contamination issues. *Acta Biomater.* **65**, In press (2021).
4. Monopoli, M. P., Aberg, C., Salvati, A. & Dawson, K. A. Biomolecular coronas provide the biological identity of nanosized materials. *Nat. Nanotechnol.* **7**, 779–786 (2012).
5. Francia, V., Schiffelers, R. M., Cullis, P. R. & Witzigmann, D. The Biomolecular Corona of Lipid Nanoparticles for Gene Therapy. *Bioconjug. Chem.* **31**, 2046–2059 (2020).
6. Shieh, P. Navigating the Biological-Material Interface with the Guide of Chemical Biology. *ChemBioChem* **22**, 481–482 (2021).

7. Piazza, I. *et al.* A machine learning-based chemoproteomic approach to identify drug targets and binding sites in complex proteomes. *Nat. Commun.* **11**, 4200 (2020).
8. Smith, E. & Collins, I. Photoaffinity labeling in target- and binding-site identification. *Future Med. Chem.* **7**, 159–183 (2015).
9. Zhang, Y., Wu, J. L. Y., Lazarovits, J. & Chan, W. C. W. An Analysis of the Binding Function and Structural Organization of the Protein Corona. *J. Am. Chem. Soc.* **142**, 8827–8836 (2020).
10. Dawson, K. A. & Yan, Y. Current understanding of biological identity at the nanoscale and future prospects. *Nat. Nanotechnol.* **16**, 229–242 (2021).
11. Poon, W., Kingston, B. R., Ouyang, B., Ngo, W. & Chan, W. C. W. A framework for designing delivery systems. *Nat. Nanotechnol.* **15**, 819–829 (2020).
12. Woythe, L., Tito, N. B. & Albertazzi, L. A quantitative view on multivalent nanomedicine targeting. *Adv. Drug Deliv. Rev.* **169**, 1–21 (2021).

Appendix 1

Supplementary Information to Chapter 2

1. Supplementary Figures and Tables

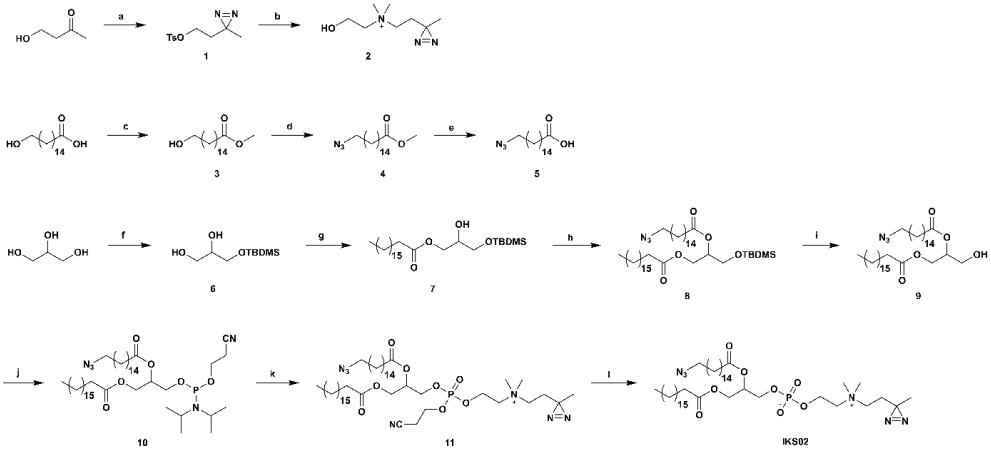
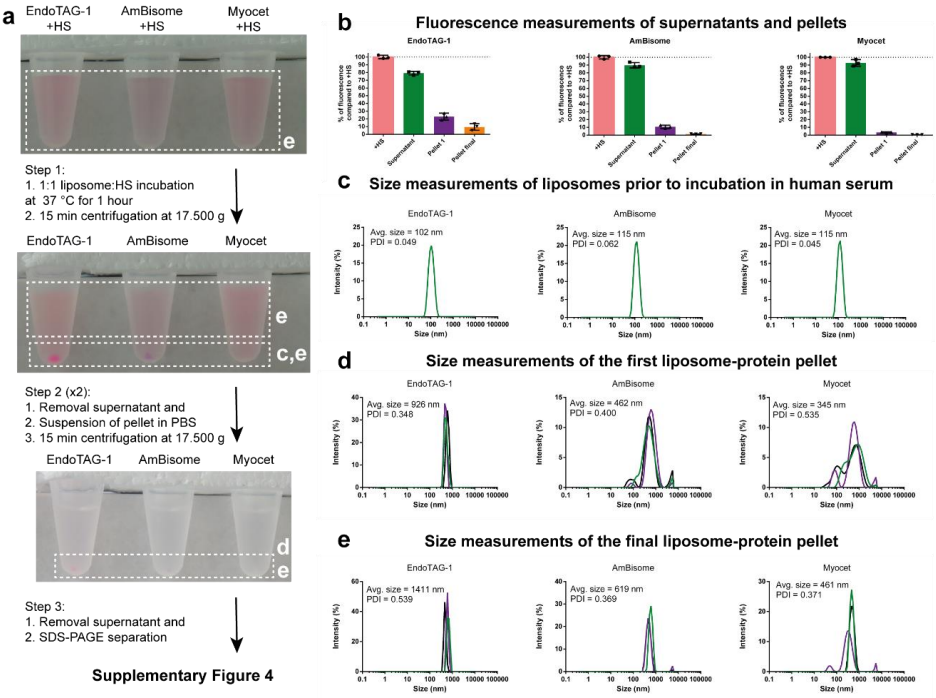


Figure S1. Synthesis scheme of the PAL probe IKS02. Reagents and conditions: (**a**) 1. 7N NH_3 in methanol; 2. NH_2OSO_3H; 3. I_2, Et_3N; 4. TsCl, pyridine, 20% over 4 steps; (**b**) DMEA, acetone, quant.; (**c**) AcCl, MeOH, 92%; (**d**) 1. MsCl, Et_3N, DCM; 2. NaN_3, DMF, 70 °C, 91% over 2 steps; (**e**) 4M NaOH, dioxane, 95%; (f) tBDMSCl, imidazole, DCM:DMF (1:1), -18 °C, 34%; (**g**) Stearic acid, DCC, DMAP, DCM, 76%; (h) 5, DCC, DMAP, DCM, 64%; (**i**) $Et_3N{\cdot}3HF$, THF, quant.; (**j**) $PCl(OCH_2CH_2CN)(NiPr_2)$, Et_3N, DCM, 74%; (**k**) 1. 2, imidazole, DCM; 2. tBuOOH, DCM, 10% over 2 steps; (**l**) $tBuNH_2$, DCM, 48%. Detailed procedures are described in the Chemical Synthesis section of the Supplementary Information.



Supplementary Figure 4

Figure S2. Sedimentation of liposome-protein complexes. (**a**) Liposomes containing 1 mol% fluorescent lipid (DOPE-LR) were incubated in human serum at a 1:1 ratio, followed by centrifugation for 15 minutes at 17,500 g. The supernatant was removed, the pellet was resuspended in PBS and the centrifugation and wash step repeated twice. After the last removal of the supernatant, the liposome-protein complexes were resolved on SDS-PAGE as shown in Figure S7. (**b**) Fluorescence measurements of supernatant and pellet from the steps described in a. Pellets were resuspended in PBS. All samples were performed in triplicate. Fluorescence of DOPE-LR (560 ex./583 em.) was determined using a fluorescence plate reader (Tecan M200, Tecan Life Sciences). (**c**) Dynamic Light Scattering (DLS) size measurements of the extruded liposomes prior to incubation in human serum. (**d**) DLS size measurements of the liposome-protein pellet after the first centrifugation step. (**e**) DLS size measurements of the liposome-protein pellet after the final centrifugation step. Pellets were re-suspended in PBS (100 µL) for DLS measurements.

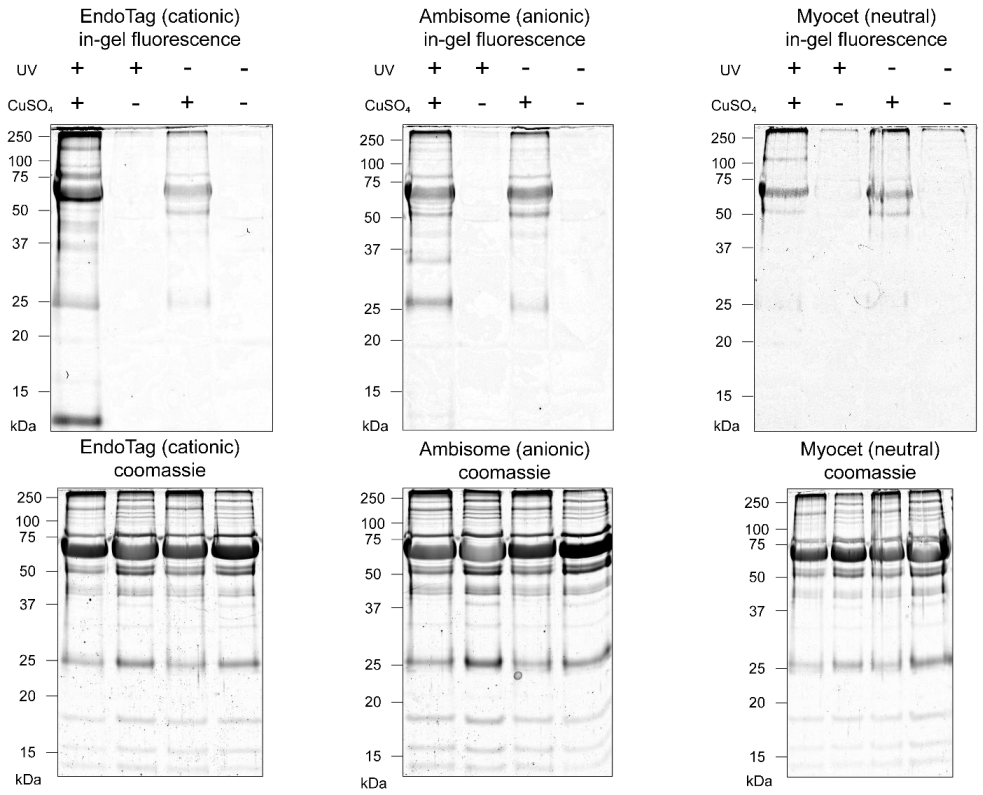
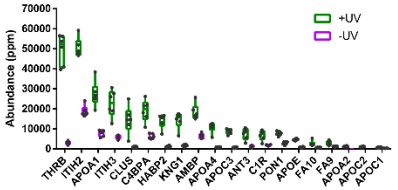


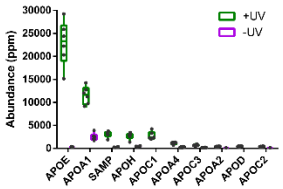
Figure S3. In-gel fluorescence and Coomassie stained SDS-PAGE gels for the photoaffinity method, displaying the fluorescently labelled protein corona (in-gel fluorescence) and the total protein content (Coomassie Blue). 10 µg total protein was loaded in each lane, as determined by BCA assay. Gels were run on a 10% polyacrylamide gel as described in the Biological Methods & Proteomics section.

EndoTAG-1



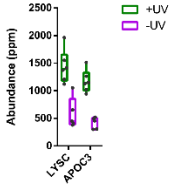
Abundance	Protein name	Protein entry	IEP	MW (kDa)	average ppm -UV	average ppm +UV
1	Prothrombin	THRB	5.54	72	3101	49658
2	Inter-alpha-trypsin inhibitor heavy chain H2	ITIH2	6.43	107	18647	50201
3	Apolipoprotein A-I	APOA1	5.44	31	7831	27202
4	Inter-alpha-trypsin inhibitor heavy chain H3	ITIH3	5.39	100	6056	22664
5	Clusterin	CLUS	5.87	53	1023	14509
6	C4b-binding protein alpha chain	C4BPA	7.02	69	6198	19139
7	Hyaluronan-binding protein 2	HABP2	6.11	65	1187	14124
8	Kininogen-1	KNG1	6.38	73	1639	14413
9	Protein AMBP	AMBP	5.9	40	6520	18286
10	Apolipoprotein A-IV	APOA4	5.12	45	929	10798
11	Apolipoprotein C-III	APOC3	5.06	11	659	8709
12	Antithrombin-III	ANT3	6.33	53	1398	7563
13	Complement C1r subcomponent	C1R	5.8	82	1766	6873
14	Serum paraoxonase/arylesterase 1	PON1	4.93	40	2906	7662
15	Apolipoprotein E	APOE	5.49	36	902	4623
16	Coagulation factor X	FA10	5.59	56	718	2562
17	Coagulation factor IX	FA9	5.19	53	1199	2735
18	Apolipoprotein A-II	APOA2	6.64	11	71	1159
19	Apolipoprotein C-II	APOC2	4.44	11	0	1064
20	Apolipoprotein C-I	APOC1	9.43	9	314	717

AmBisome



Abundance	Protein name	Protein entry	IEP	MW (kDa)	average ppm -UV	average ppm +UV
1	Apolipoprotein E	APOE	5.49	36	326	22878
2	Apolipoprotein A-I	APOA1	5.44	31	2469	11527
3	Serum amyloid P-component	SAMP	6.13	26	284	3038
4	Beta-2-glycoprotein 1	APOH	7.87	40	438	2682
5	Apolipoprotein C-I	APOC1	9.43	9	1024	2730
6	Apolipoprotein A-IV	APOA4	5.12	45	0	1589
7	Apolipoprotein C-III	APOC3	5.06	11	245	1130
8	Apolipoprotein A-II	APOA2	6.64	11	170	686
9	Apolipoprotein D	APOD	4.87	22	0	435
10	Apolipoprotein C-II	APOC2	4.44	11	119	390

Myocet



Abundance	Protein name	Protein entry	IEP	MW (kDa)	average ppm -UV	average ppm +UV
1	Lysozyme C	LYSC	9.34	17	587	1438
2	Apolipoprotein C-III	APOC3	5.06	11	414	1170

Figure S4. Abundance profiles for proteins meeting the selection criteria. Displayed as plots, showing the protein entry and abundancy in both +UV and -UV samples, as well as in table format.

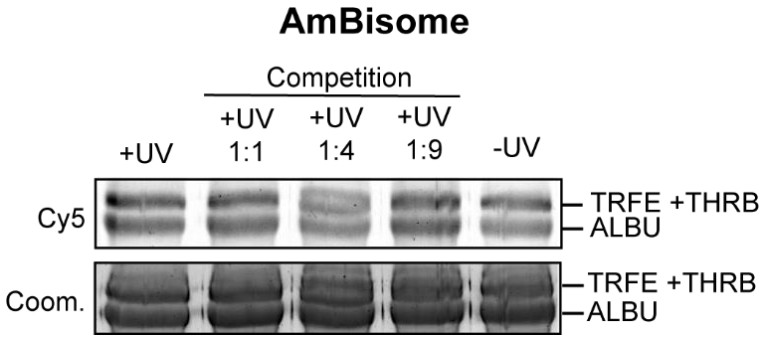


Figure S5. Competitive binding of human serum albumin (ALBU), transferrin (TRFE) and prothrombin (THRB). Increasing concentrations (1:1 to 1:9 molar ratios) of unlabeled AmBisome liposomes were incubated, together with AmBisome liposomes containing IKS02 (5 mol%), in a predefined mixture of purified human serum proteins (see Figure 4). Captured proteins were separated by SDS-PAGE and visualized by in-gel fluorescence (Cy5). Protein loading determined by Coomassie Blue (coom.).

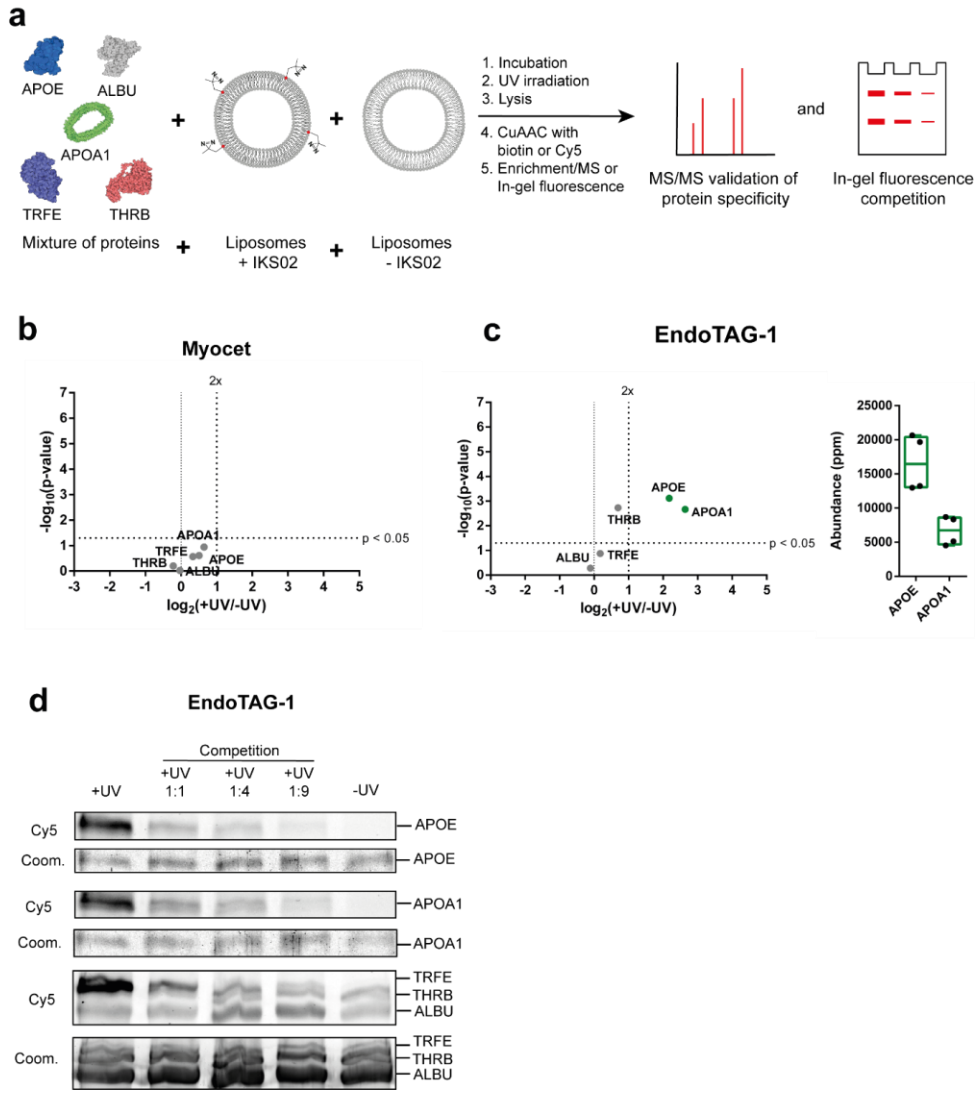


Figure S6. Validation of apolipoprotein E and A1 binding to Myocet and EndoTAG-1 liposomes. (**a**) Liposomes, containing 5 mol% IKS02, were incubated in a mixture of purified human serum proteins consisting of apolipoprotein E (APOE, 2 µgmL-1), serum albumin (ALBU, 25 µgmL-1), apolipoprotein A-I (APOA1, 2 µgmL-1), transferrin (TRFE, 10 µgmL-1) and prothrombin (THRB, 2 µgmL-1). (**b,c**) Volcano plot of protein enrichment over background (log2(+UV/-UV)) plotted against the statistical significance of this comparison (-log10(p-value)). Proteins meeting all selection criteria labelled in green. For EndoTAG-1, abundance plot of apoE and apoA1 within the +UV samples. (**d**) Competition assay of apolipoprotein E and A1 binding. Increasing concentrations (1:1 to 1:9 molar ratios) of

unlabelled EndoTAG-1 liposomes were incubated, together with EndoTAG-1 liposomes containing IKS02 (5 mol%), in the above predefined mixture of purified human serum proteins. Captured apoE and apoA1 on the surface of IKS02-labeled EndoTAG-1 liposomes were separated by SDS-PAGE and visualized by in-gel fluorescence (Cy5). Protein loading determined by Coomassie Blue (coom.). Protein structures were obtained from the protein data bank (PDB): APOE: 2L7B, APOA1: 1AV1, ALBU: 1E78, THRB: 6C2W, TRFE: 1D3K). Illustrations were generated using Illustrate.

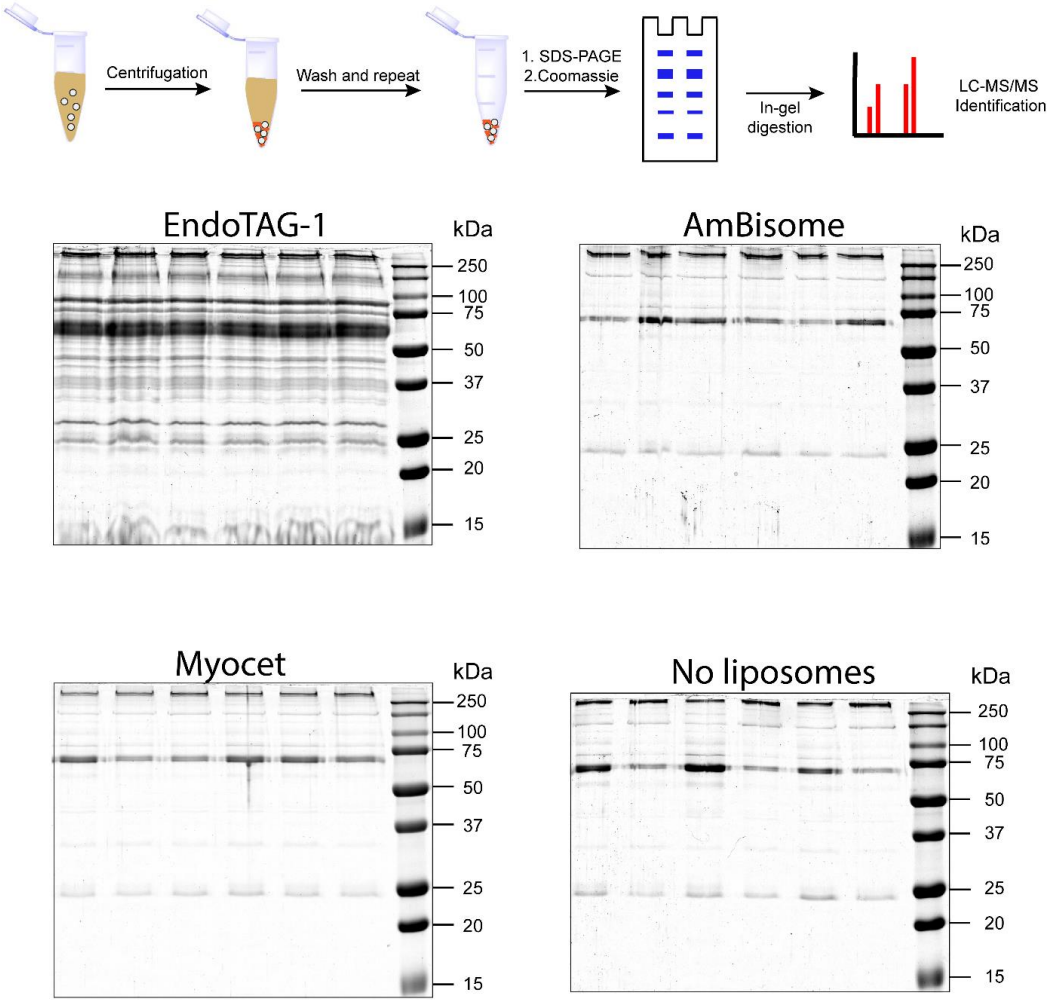


Figure S7. Gel electrophoresis (SDS-PAGE) of protein coronas isolated via centrifugation, displaying Coomassie Blue stained replicates (n=6) used for in-gel digestion. The total amount of liposome-protein complexes isolated by centrifugation were loaded in each lane without correction. Gels were run on a 10% polyacrylamide gel as described in the Biological Methods & Proteomics section.

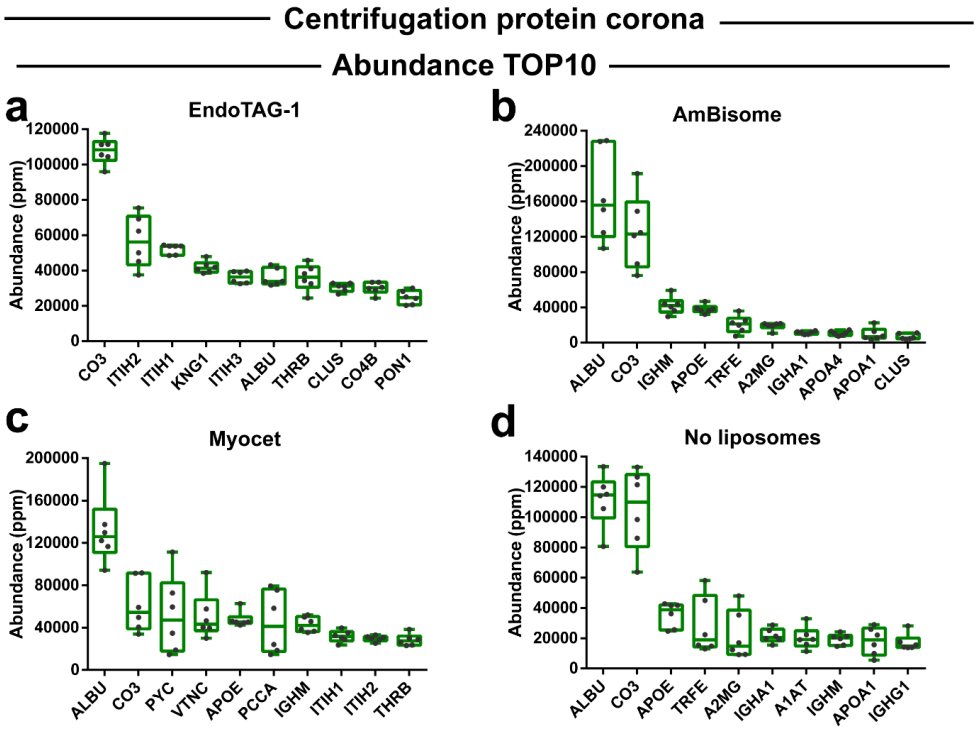


Figure S8. Top 10 most abundant proteins in the corona determined by the centrifugation method for each formulation as well as the negative control in which buffer without liposomes was added to the serum. Complete abundancy lists can be found as table format in Tables S4-7.

Formulation name	Lipid composition (mol%)	Size avg. (nm)	PDI	Zeta Potential (mV)
Myocet	55% POPC: 45% Cholesterol	105.3	0.034	-7.4 ± 2.1
AmBisome	53% DSPC : 21% DSPG : 26% Cholesterol	107.2	0.087	-24.5 ± 3.2
EndoTAG-1	51.5% DOTAP : 48.5% DOPC	101.4	0.044	+41.6 ± 4.6
Myocet + IKS02	50% POPC : 45% Cholesterol : 5% IKS02	102.1	0.042	-6.5 ± 1.8
AmBisome + IKS02	48% DSPC : 21% DSPG : 26% Cholesterol : 5% IKS02	104.8	0.079	-23.3 ± 2.7
EndoTAG-1 + IKS02	51.5% DOTAP : 43.5% DOPC : 5% IKS02	108.6	0.053	+43.2 ± 3.9
Myocet + DOPE-LR	54% POPC : 45% Cholesterol : 1% DOPE-LR	99.1	0.089	-5.2 ± 3.0
AmBisome + DOPE-LR	52% DSPC : 21% DSPG : 26% Cholesterol : 1% DOPE-LR	101.7	0.092	-28.9 ± 5.0
EndoTAG-1 + DOPE-LR	51.5% DOTAP : 47.5% DOPC : 1% DOPE-LR	104.5	0.063	+46.6 ± 5.9

Formulations in clinic/trials

Formulation name	Lipid composition (mol%)	Size avg. (nm)	Surface charge	Encapsulated drug
Myocet	54% POPC : 45% Cholesterol : 1% DOPE-LR	150-200 nm	zwitterionic neutral	Doxorubicin
AmBisome	53% DSPC : 21% DSPG : 26% Cholesterol	78 nm	anionic	Amphotericin B
EndoTAG-1	51.5% DOTAP : 48.5% DOPC	200 nm	cationic	Paclitaxel

Table S1. Dynamic Light Scattering and zeta potential measurements for the formulations used in this study. All formulations were made through thin film hydration and extrusion described in the Biological Methods & Proteomics section of the Supplementary Information. Liposome composition and size of formulations used in clinic or clinical trials obtained from Ref. 1.

ISOQuant Configuration

parameter	value
isoquant.pluginQueue.name	design project and run ISOQuant analysis
process.peptide.deplete.PEP_FRAG_2	false
process.peptide.deplete.CURATED_0	false
process.peptide.statistics.doSequenceSearch	false
process.emrt.minIntensity	1000
process.emrt.minMass	500
process.emrt.rt.alignment.match.maxDeltaMass.ppm	10
process.emrt.rt.alignment.match.maxDeltaDriftTime	2
process.emrt.rt.alignment.normalizeReferenceTime	true
process.emrt.rt.alignment.maxProcesses	24
process.emrt.rt.alignment.referenceRun.selectionMethod	AUTO
process.emrt.clustering.preclustering.orderSequence	MTMTMT
process.emrt.clustering.preclustering.maxDistance.mass.ppm	6.06E-6
process.emrt.clustering.preclustering.maxDistance.time.min	0.202
process.emrt.clustering.preclustering.maxDistance.drift	2.02
process.emrt.clustering.distance.unit.mass.ppm	6.0E-6
process.emrt.clustering.distance.unit.time.min	0.2
process.emrt.clustering.distance.unit.drift.bin	2
process.emrt.clustering.dbscan.minNeighborCount	1
process.identification.peptide.minReplicationRate	2
process.identification.peptide.minScore	6
process.identification.peptide.minOverallMaxScore	0
process.identification.peptide.minSequenceLength	6
process.identification.peptide.acceptType.PEP_FRAG_1	true
process.identification.peptide.acceptType.IN_SOURCE	false
process.identification.peptide.acceptType.MISSING_CLEAVAGE	false
process.identification.peptide.acceptType.NEUTRAL_LOSS_H20	false
process.identification.peptide.acceptType.NEUTRAL_LOSS_NH3	false
process.identification.peptide.acceptType.PEP_FRAG_2	false
process.identification.peptide.acceptType.DDA	true
process.identification.peptide.acceptType.VAR_MOD	false
process.identification.peptide.acceptType.PTM	false
process.annotation.peptide.maxSequencesPerEMRTCluster	1
process.annotation.protein.resolveHomology	true
process.annotation.peptide.maxFDR	0.01
process.annotation.useSharedPeptides	unique
process.normalization.lowess.bandwidth	0.3
process.normalization.orderSequence	XPIR
process.normalization.minIntensity	3000
process.quantification.peptide.minMaxScorePerCluster	0
process.quantification.peptide.acceptType.IN_SOURCE	false
process.quantification.peptide.acceptType.MISSING_CLEAVAGE	false
process.quantification.peptide.acceptType.NEUTRAL_LOSS_H20	false
process.quantification.peptide.acceptType.NEUTRAL_LOSS_NH3	false
process.quantification.peptide.acceptType.PEP_FRAG_1	true
process.quantification.peptide.acceptType.PEP_FRAG_2	false
process.quantification.peptide.acceptType.VAR_MOD	false
process.quantification.peptide.acceptType.PTM	false
process.quantification.peptide.acceptType.DDA	true
process.quantification.topx.degree	3
process.quantification.topx.allowDifferentPeptides	false
process.quantification.minPeptidesPerProtein	3
process.quantification.absolute.standard.entry	ENO1_YEAST
process.quantification.absolute.standard.fmol	50
process.quantification.topx.allowDifferentPeptides	false
process.quantification.absolute.standard.entry	ENO1_YEAST
process.quantification.absolute.standard.fmol	50
process.quantification.maxProteinFDR	0.01

Table S2. ISOQuant label-free quantification (LFQ) configuration based on the TOP3 approach.

Human serum

Abundance	Protein name	Protein entry	IEP	MW (kDa)	average ppm
1	Serum albumin	ALBU	5.89	71.4	26.08
2	Complement C3	CO3	5.99	188.7	65.56
3	Serotransferrin	TRFE	6.78	79.3	29.71
4	Alpha-2-macroglobulin	A2MG	6.04	164.7	58.25
5	Immunoglobulin heavy constant gamma 1	IGHG1	8.20	36.6	16.61
6	Alpha-1-antitrypsin	A1AT	5.25	46.9	19.39
7	Immunoglobulin heavy constant mu	IGHM	6.37	50.1	21.16
8	Apolipoprotein A-I	APOA1	5.44	30.8	14.74
9	Immunoglobulin heavy constant gamma 2	IGHG2	7.45	36.5	17.66
10	Vitamin D-binding protein	VTDB	5.16	54.5	23.22
11	Immunoglobulin heavy constant alpha 1	IGHA1	6.09	38.5	18.53
12	Immunoglobulin kappa constant	IGKC	6.13	11.9	10.02
13	Complement factor H	CFAH	6.21	143.8	54.33
14	Inter-alpha-trypsin inhibitor heavy chain H2	ITIH2	6.43	106.9	42.45
15	Apolipoprotein A-IV	APOA4	5.12	45.4	21.84
16	Complement factor B	CFAB	6.69	86.9	36.53
17	Haptoglobin	HPT	6.15	45.9	23.01
18	Immunoglobulin heavy constant gamma 3	IGHG3	7.79	42.3	22.70
19	Plasminogen	PLMN	6.93	93.3	39.75
20	C4b-binding protein alpha chain	C4BPA	7.02	69.1	32.04
21	Complement C4-B	CO4B	6.90	194.3	74.06
22	Plasma protease C1 inhibitor	IC1	6.11	55.4	27.83
23	Antithrombin-III	ANT3	6.33	53.1	27.46
24	Beta-2-glycoprotein 1	APOH	7.87	39.6	23.83
25	Hemopexin	HEMO	6.60	52.4	28.01
26	Enolase 1	ENO1	6.19	46.9	26.35
27	Immunoglobulin heavy constant gamma 4	IGHG4	7.13	36.5	23.53
28	Inter-alpha-trypsin inhibitor heavy chain H4	ITIH4	6.56	103.6	46.05
29	Complement C5	CO5	6.11	190.0	75.04
30	Gelsolin	GELS	5.87	86.1	40.66
31	Alpha-1-antichymotrypsin	AACT	5.19	47.8	28.00
32	Transthyretin	TTHY	5.42	16.0	17.81
33	Apolipoprotein A-II	APOA2	6.64	11.3	16.98
34	Inter-alpha-trypsin inhibitor heavy chain H1	ITIH1	6.35	101.8	47.40
35	Angiotensinogen	ANGT	5.88	53.4	31.44
36	Complement C1s subcomponent	C1S	4.66	78.2	39.63
37	Prothrombin	THRB	5.54	71.5	38.02
38	Ceruloplasmin	CERU	5.35	123.1	55.47
39	Apolipoprotein E	APOE	5.49	36.3	26.92
40	Heparin cofactor 2	HEP2	6.47	57.2	34.57
41	Alpha-2-HS-glycoprotein	FETUA	5.35	40.1	28.83
42	Hemoglobin subunit alpha	HBA	9.20	15.3	22.17
43	Apolipoprotein C-III	APOC3	5.06	10.9	19.64
44	Hemoglobin subunit beta	HBB	6.91	16.1	22.34
45	Complement C1r subcomponent	C1R	5.80	81.7	44.15
46	Complement C1q subcomponent subunit B	C1QB	8.87	26.9	27.27
47	N-acetylmuramoyl-L-alanine amidase	PGRP2	7.29	62.8	39.03
48	Alpha-2-antiplasmin	A2AP	5.87	54.9	36.26
49	Complement C1q subcomponent subunit C	C1QC	8.54	26.0	27.85
50	Complement C4-A	CO4A	6.68	194.4	83.69

Table S3. Abundancy of proteins in human serum determined with LFQ based on the TOP3 approach, analysed with the ISOQuant software.

51	Histidine-rich glycoprotein	HRG	7.13	60.5	39.56
52	Clusterin	CLUS	5.87	53.1	36.98
53	Alpha-1B-glycoprotein	A1BG	5.50	54.8	37.77
54	Leucine-rich alpha-2-glycoprotein	A2GL	6.53	38.4	32.98
55	Serum amyloid P-component	SAMP	6.13	25.5	28.88
56	Kininogen-1	KNG1	6.38	73.0	45.14
57	Immunoglobulin heavy constant alpha 2	IGHA2	5.85	37.4	33.41
58	Haptoglobin-related protein	HPTR	6.71	39.5	34.75
59	Coagulation factor XII	FA12	7.55	70.1	45.54
60	Apolipoprotein C-I	APOC1	9.43	9.3	26.25
61	Corticosteroid-binding globulin	CBG	5.61	45.3	37.31
62	Apolipoprotein C-II	APOC2	4.44	11.3	25.91
63	Protein AMBP	AMBP	5.90	39.9	36.27
64	CD5 antigen-like	CD5L	5.15	39.6	36.26
65	Serum paraoxonase/arylesterase 1	PON1	4.93	39.9	36.61
66	Complement component C9	CO9	5.28	64.7	45.31
67	Apolipoprotein L1	APOL1	5.49	44.0	38.84
68	Vitronectin	VTNC	5.45	55.1	42.85
69	Vitamin K-dependent protein S	PROS	5.35	77.2	50.51
70	Afamin	AFAM	5.55	71.0	48.85
71	Apolipoprotein D	APOD	4.87	21.6	32.48
72	Immunoglobulin J chain	IGJ	4.91	18.6	31.82
73	Pigment epithelium-derived factor	PEDF	5.97	46.5	41.82
74	Carboxypeptidase B2	CBPB2	7.54	49.0	43.51
75	Kallistatin	KAIN	7.58	48.7	43.76
76	Plasma kallikrein	KLKB1	8.10	73.5	52.53
77	Properdin	PROP	7.75	53.8	46.18
78	Complement factor I	CFAI	7.31	68.1	51.15
79	Insulin-like growth factor-binding protein complex acid labile subunit	ALS	6.37	66.8	50.72
80	Carboxypeptidase N subunit 2	CPN2	5.59	61.4	49.00
81	Retinol-binding protein 4	RET4	5.68	23.4	36.68
82	Thyroxine-binding globulin	THBG	5.88	46.7	44.85
83	Apolipoprotein M	APOM	5.63	21.6	36.74
84	Serum amyloid A-4 protein	SAA4	9.41	14.9	36.09
85	Alpha-1-acid glycoprotein 1	A1AG1	4.74	23.7	37.83
86	Alpha-1-acid glycoprotein 2	A1AG2	4.85	23.9	38.25
87	Lumican	LUM	6.19	38.8	43.99
88	Immunoglobulin heavy constant delta	IGHD	8.10	42.8	46.30
89	Zinc-alpha-2-glycoprotein	ZA2G	5.66	34.5	43.05
90	Immunoglobulin lambda variable 1-51	LV151	6.86	12.5	36.45
91	Apolipoprotein C-IV	APOC4	9.13	14.9	38.34
92	Tetranectin	TETN	5.38	22.9	40.11
93	Hemoglobin subunit delta	HBD	8.23	16.2	39.13

Table S3. Continued.

Abundance	Protein name	Protein entry	IEP	MW (kDa)	average ppm
1	Serum albumin	ALBU	5,89	71	166624
2	Complement C3	CO3	5,99	189	125283
3	Immunoglobulin heavy constant mu	IGHM	6,37	50	42156
4	Apolipoprotein E	APOE	5,49	36	38054
5	Serotransferrin	TRFE	6,78	79	20767
6	Alpha-2-macroglobulin	A2MG	6,04	165	18900
7	Immunoglobulin heavy constant alpha 1	IGHA1	6,09	39	11451
8	Apolipoprotein A-IV	APOA4	5,12	45	10705
9	Apolipoprotein A-I	APOA1	5,44	31	9582
10	Clusterin	CLUS	5,87	53	6738
11	Haptoglobin	HPT	6,15	46	6114
12	Apolipoprotein D	APOD	4,87	22	2933

Table S4. Protein abundancy for the AmBisome protein corona from the centrifugation method determined with LFQ based on the TOP3 approach, analysed with the ISOQuant software.

Myocet

Abundance	Protein name	Protein entry	IEP	MW (kDa)	average ppm
1	Serum albumin	ALBU	5.89	71	132524
2	Complement C3	CO3	5.99	189	61074
3	Pyruvate carboxylase_ mitochondrial	PYC	6.41	130	51995
4	Vitronectin	VTNC	5.45	55	51013
5	Apolipoprotein E	APOE	5.49	36	47754
6	Propionyl-CoA carboxylase alpha chain_ mitochondrial	PCCA	7.27	81	45110
7	Immunoglobulin heavy constant mu	IGHM	6.37	50	43059
8	Inter-alpha-trypsin inhibitor heavy chain H1	ITIH1	6.35	102	31785
9	Inter-alpha-trypsin inhibitor heavy chain H2	ITIH2	6.43	107	29841
10	Prothrombin	THRB	5.54	72	28366
11	Alpha-2-macroglobulin	A2MG	6.04	165	17305
12	Serotransferrin	TRFE	6.78	79	16843
13	Apolipoprotein A-IV	APOA4	5.12	45	14697
14	Clusterin	CLUS	5.87	53	11392
15	Immunoglobulin heavy constant alpha 1	IGHA1	6.09	39	10089
16	Alpha-1-antitrypsin	A1AT	5.25	47	9162
17	Haptoglobin	HPT	6.15	46	7963
18	Serum paraoxonase/arylesterase 1	PON1	4.93	40	7590
19	Apolipoprotein A-I	APOA1	5.44	31	7056
20	Hyaluronan-binding protein 2	HABP2	6.11	65	5028
21	Apolipoprotein C-II	APOC2	4.44	11	4953
22	Heparin cofactor 2	HEP2	6.47	57	3657
23	Apolipoprotein D	APOD	4.87	22	1762
24	Dermcidin	DCD	6.14	11	1472

Table S5. Protein abundancy for the Myocet protein corona from the centrifugation method determined with LFQ based on the TOP3 approach, analysed with the ISOQuant software.

No liposomes

Abundance	Protein name	Protein entry	IEP	MW (kDa)	average ppm
1	Serum albumin	ALBU	5.89	71	111535
2	Complement C3	CO3	5.99	189	104869
3	Apolipoprotein E	APOE	5.49	36	35444
4	Serotransferrin	TRFE	6.78	79	28106
5	Alpha-2-macroglobulin	A2MG	6.04	165	21894
6	Immunoglobulin heavy constant alpha 1	IGHA1	6.09	39	21604
7	Alpha-1-antitrypsin	A1AT	5.25	47	20143
8	Immunoglobulin heavy constant mu	IGHM	6.37	50	19366
9	Apolipoprotein A-I	APOA1	5.44	31	18041
10	Immunoglobulin heavy constant gamma 1	IGHG1	8.2	37	17181
11	Apolipoprotein A-IV	APOA4	5.12	45	14567
12	Haptoglobin	HPT	6.15	46	12884
13	Clusterin	CLUS	5.87	53	12679
14	Complement C4-B	CO4B	6.9	194	8851
15	Complement C4-A	CO4A	6.68	194	8448
16	Vitronectin	VTNC	5.45	55	7579
17	Complement component C9	CO9	5.28	65	6327
18	Lactotransferrin	TRFL	8.02	80	5262
19	Apolipoprotein C-III	APOC3	5.06	11	5039
20	Lysozyme C	LYSC	9.34	17	4995
21	Gelsolin	GELS	5.87	86	4868
22	Apolipoprotein D	APOD	4.87	22	4548
23	Apolipoprotein L1	APOL1	5.49	44	4278
24	Alpha-1-antichymotrypsin	AACT	5.19	48	4244
25	Inter-alpha-trypsin inhibitor heavy chain H1	ITIH1	6.35	102	3949
26	Prothrombin	THRB	5.54	72	3850
27	Inter-alpha-trypsin inhibitor heavy chain H4	ITIH4	6.56	104	3623
28	Immunoglobulin kappa constant	IGKC	6.13	12	3404
29	Complement factor B	CFAB	6.69	87	3360
30	Serum paraoxonase/arylesterase 1	PON1	4.93	40	3319
31	Zinc-alpha-2-glycoprotein	ZA2G	5.66	34	2927
32	Dermcidin	DCD	6.14	11	2892
33	Apolipoprotein C-II	APOC2	4.44	11	2849
34	Kininogen-1	KNG1	6.38	73	2766
35	Polymeric immunoglobulin receptor	PIGR	5.44	84	2617
36	Desmoglein-1	DSG1	4.72	115	2596
37	Serum amyloid A-4 protein	SAA4	9.41	15	2372
38	Beta-2-glycoprotein 1	APOH	7.87	40	2063
39	Immunoglobulin heavy constant gamma 3	IGHG3	7.79	42	1923
40	Immunoglobulin J chain	IGJ	4.91	19	1624
41	Prolactin-inducible protein	PIP	8.1	17	1374
42	Cystatin-A	CYTA	5.22	11	1330
43	Annexin A1	ANXA1	6.67	39	1125
44	Zymogen granule protein 16 homolog B	ZG16B	7.56	23	1070
45	Hemoglobin subunit beta	HBB	6.91	16	1020
46	Apolipoprotein A-II	APOA2	6.64	11	993
47	Protein S100-A8	S10A8	6.65	11	726
48	Alpha-1-acid glycoprotein 1	A1AG1	4.74	24	657
49	Apolipoprotein C-IV	APOC4	9.13	15	653
50	Apolipoprotein C-I	APOC1	9.43	9	369

Table S6. Background protein abundancy of the centrifugation method, determined with LFQ based on the TOP3 approach, analysed with the ISOQuant software.

EndoTag

Abundance	Protein name	Protein entry	IEP	MW (kDa)	average ppm
1	Complement C3	CO3	5.99	189	107751
2	Inter-alpha-trypsin inhibitor heavy chain H2	ITIH2	6.43	107	56604
3	Inter-alpha-trypsin inhibitor heavy chain H1	ITIH1	6.35	102	52182
4	Kininogen-1	KNG1	6.38	73	41911
5	Inter-alpha-trypsin inhibitor heavy chain H3	ITIH3	5.39	100	36208
6	Serum albumin	ALBU	5.89	71	36107
7	Prothrombin	THRB	5.54	72	36037
8	Clusterin	CLUS	5.87	53	30526
9	Complement C4-B	CO4B	6.9	194	30066
10	Serum paraoxonase/arylesterase 1	PON1	4.93	40	24734
11	Alpha-2-macroglobulin	A2MG	6.04	165	23372
12	Ceruloplasmin	CERU	5.35	123	20035
13	Alpha-1-antitrypsin	A1AT	5.25	47	19392
14	Antithrombin-III	ANT3	6.33	53	19378
15	Gelsolin	GELS	5.87	86	16063
16	Hyaluronan-binding protein 2	HABP2	6.11	65	14756
17	Apolipoprotein E	APOE	5.49	36	14519
18	Vitronectin	VTNC	5.45	55	14243
19	Immunoglobulin heavy constant mu	IGHM	6.37	50	13398
20	Complement C1s subcomponent	C1S	4.66	78	12534
21	Complement C4-A	CO4A	6.68	194	12532
22	Plasma protease C1 inhibitor	IC1	6.11	55	12190
23	Immunoglobulin heavy constant alpha 1	IGHA1	6.09	39	12126
24	Inter-alpha-trypsin inhibitor heavy chain H4	ITIH4	6.56	55	11681
25	Heparin cofactor 2	HEP2	6.47	57	11613
26	Immunoglobulin heavy constant gamma 1	IGHG1	8.2	37	11328
27	Apolipoprotein A-I	APOA1	5.44	31	10414
28	Complement C1r subcomponent	C1R	5.8	82	7903
29	Complement C5	CO5	6.11	190	7690
30	Histidine-rich glycoprotein	HRG	7.13	61	7685
31	Protein AMBP	AMBP	5.9	40	7498
32	Apolipoprotein A-IV	APOA4	5.12	45	7359
33	Apolipoprotein F	APOF	5.31	36	6835
34	Vitamin K-dependent protein Z	PROZ	5.59	46	6812
35	Lumican	LUM	6.19	39	6654
36	C-reactive protein	CRP	5.32	25	6423
37	Vitamin K-dependent protein C	PROC	5.85	53	6359
38	Coagulation factor IX	FA9	5.19	53	6183
39	Complement component C9	CO9	5.28	65	5813
40	Beta-Ala-His dipeptidase	CNDP1	4.98	57	5729
41	Vitamin K-dependent protein S	PROS	5.35	77	5542
42	Alpha-2-antiplasmin	A2AP	5.87	55	5530
43	Apolipoprotein M	APOM	5.63	22	5496
44	Serotransferrin	TRFE	6.78	79	4806
45	Haptoglobin	HPT	6.15	46	4769
46	Thrombospondin-1	TSP1	4.53	133	4165
47	Coagulation factor X	FA10	5.59	56	3970
48	Alpha-1-antichymotrypsin	AACT	5.19	48	3725
49	Immunoglobulin kappa constant	IGKC	6.13	12	3478
50	Phosphatidylcholine-sterol acyltransferase	LCAT	5.69	50	3298

Table S7. Protein abundancy for the EndoTAG-1 protein corona from the centrifugation method determined with LFQ based on the TOP3 approach, analysed with the ISOQuant software.

51	Complement factor H	CFAH	6.21	144	3160
52	Ficolin-3	FCN3	6.25	33	3065
53	Apolipoprotein D	APOD	4.87	22	2992
54	Angiotensinogen	ANGT	5.88	53	2944
55	Cartilage oligomeric matrix protein	COMP	4.16	85	2936
56	Protein Z-dependent protease inhibitor	ZPI	8.6	51	2681
57	Apolipoprotein A-II	APOA2	6.64	11	2512
58	Galectin-3-binding protein	LG3BP	4.95	66	2411
59	Lipopolysaccharide-binding protein	LBP	6.27	54	2373
60	Endoplasmin	ENPL	4.56	93	2312
61	C4b-binding protein alpha chain	C4BPA	7.02	69	2268
62	Secreted phosphoprotein 24	SPP24	8.39	25	2140
63	Apolipoprotein C-II	APOC2	4.44	11	2136
64	Thrombospondin-4	TSP4	4.25	109	2072
65	Haptoglobin-related protein	HPTR	6.71	40	1926
66	Plasma serine protease inhibitor	IPSP	9.75	46	1885
67	Apolipoprotein C-III	APOC3	5.06	11	1831
68	Platelet glycoprotein Ib alpha chain	GP1BA	5.87	72	1663
69	Selenoprotein P	SEPP1	7.72	43	1613
70	Mannan-binding lectin serine protease 1	MASP1	5.16	81	1608
71	CD5 antigen-like	CD5L	5.15	40	1454
72	Apolipoprotein L1	APOL1	5.49	44	1426
73	Complement C1q subcomponent subunit C	C1QC	8.54	26	1420
74	SPARC-like protein 1	SPRL1	4.53	76	1310
75	Hemopexin	HEMO	6.6	52	1299
76	Insulin-like growth factor-binding protein complex acid labile subunit	ALS	6.37	67	1292
77	Immunoglobulin heavy constant gamma 3	IGHG3	7.79	42	1283
78	Serum paraoxonase/lactonase 3	PON3	5.11	40	1244
79	Transthyretin	TTHY	5.42	16	1191
80	Alpha-1B-glycoprotein	A1BG	5.5	55	1184
81	Phosphatidylinositol-glycan-specific phospholipase D	PHLD	5.92	93	1124
82	Immunoglobulin heavy constant alpha 2	IGHA2	5.85	37	1085
83	Immunoglobulin heavy constant gamma 2	IGHG2	7.45	37	1085
84	Vitamin D-binding protein	VTDB	5.16	55	1066
85	Alpha-2-HS-glycoprotein	FETUA	5.35	40	1002
86	Complement C1q subcomponent subunit B	C1QB	8.87	27	996
87	Fermitin family homolog 3	URP2	6.57	77	955
88	Complement component C6	CO6	6.37	108	954
89	Complement factor B	CFAB	6.69	87	864
90	Carboxypeptidase N subunit 2	CPN2	5.59	61	854
91	Prenylcysteine oxidase 1	PCYOX	5.78	57	841
92	C4b-binding protein beta chain	C4BPB	4.87	29	772
93	14-3-3 protein zeta/delta	1433Z	4.53	28	561
94	Complement C1q subcomponent subunit A	C1QA	9.45	26	543
95	Pregnancy zone protein	PZP	5.96	165	530
96	Serum amyloid P-component	SAMP	6.13	26	527
97	Lysozyme C	LYSC	9.34	17	517
98	Kallistatin	KAIN	7.58	49	514
99	Immunoglobulin heavy constant gamma 4	IGHG4	7.13	36	455
100	Extracellular superoxide dismutase [Cu-Zn]	SODE	6.17	26	442
101	Immunoglobulin J chain	IGJ	4.91	19	402
102	N-acetylmuramoyl-L-alanine amidase	PGRP2	7.29	63	359
103	Beta-2-glycoprotein 1	APOH	7.87	40	342
104	Retinol-binding protein 4	RET4	5.68	23	200
105	Zinc-alpha-2-glycoprotein	ZA2G	5.66	34	200
106	Hemoglobin subunit beta	HBB	6.91	16	174
107	Prolactin-inducible protein	PIP	8.1	17	168
108	Alpha-1-acid glycoprotein 2	A1AG2	4.85	24	159
109	Dermcidin	DCD	6.14	11	130
110	Apolipoprotein C-IV	APOC4	9.13	15	110
111	Protein S100-A8	S10A8	6.65	11	90
112	Apolipoprotein C-I	APOC1	9.43	9	57

Table S7. Continued.

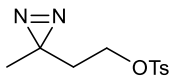
2. Materials and Methods

Chemical synthesis

General

All solvents and reagents were obtained from common commercial sources (Sigma Aldrich, Acros Organics, Alfa Aesar, Fluka, Merck) and used as received without further purification, unless stated otherwise. All reactions were performed under a nitrogen atmosphere, unless stated otherwise. Column chromatography was performed using silica gel (40-63 µm, 60 Å, Screening Devices, The Netherlands) or high purity silica gel (40-63 µm, 60 Å, Sigma-Aldrich). TLC analysis was performed on Merck silica gel 60/Kieselguhr F_{254}, 0.25 mm TLC plates. Compounds were visualized by UV adsorption or $KMnO_4$ stain (K_2CO_3 (15 g), $KMnO_4$ (2 g), and H_2O (200 mL)). ^1H, ^{13}C and ^{31}P NMR spectra were recorded on a Bruker AV 400 MHz or 850 MHz spectrometer. Chemical shifts are reported in ppm (δ), relative to the deuterated solvent as internal standard. Data are reported as follows: chemical shifts (δ), multiplicity (s = singlet, d = doublet, dd = doublet of doublet, t = triplet, q = quartet, br s= broad singlet, m = multiplet), coupling constants (J) reported in Hz. High resolution mass spectra were recorded by direct injection (2 µL of a 1 mM solution in methanol) using a mass spectrometer (Thermo Finnigan LTQ Orbitrap) with an electrospray ion source run in positive mode (source voltage 3.5 kV, sheath gas flow 10, capillary temperature 250°C), and with a resolution R = 60,000 at m/z 400 (mass range m/z = 150-2,000) and dioctylphthalate (m/z = 391.28428) as a "lock mass". The high-resolution mass spectrometer was calibrated prior to measurements with a calibration mixture (Thermo Finnigan).

methyl-3H-diazirin-3-yl)ethyl 4-methylbenzenesulfonate (1)[2]

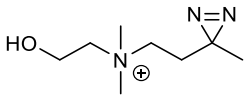


To 7N methanolic ammonia (11.2 mL, 79 mmol, 7 eq.) was added 4-hydroxybutan-2-one (0.98 mL, 11.35 mmol, 1 eq.) at 0 °C under nitrogen atmosphere. After stirring at 0 °C for 2.5 hours, the solution turned dark yellow. To the solution was added hydroxylamine-O-sulfonic acid (1.48 g, 13.05 mmol, 1.1 eq.) in methanol (9.7 mL) dropwise. The solution turned light yellow and was stirred overnight at room temperature until a white suspension was formed. The solid was filtered off and the ammonia was evaporated by gently blowing nitrogen through the solution. The solution was cooled down to 0 °C and to the solution

was added triethylamine (1.6 mL, 11.35 mmol, 1 eq.), then was added in portions molecular iodine (±2 g) until the brown colour persisted. After 2 hours, the solution was quenched by the addition of brine (40 ml) and extracted with diethyl ether (3x). The organic layers were combined, washed with sodium thiosulfate (1x) and brine (1x). The organic layer was dried over anhydrous sodium sulfate and evaporated under reduced pressure. To the crude was added pyridine (8 mL) and *p*-toluenesulfonylchloride (2.30 g, 12 mmol, 1.1 eq.). After stirring overnight at room temperature, the solution was poured onto ice (120 g). The solution was quenched with concentrated hydrogen chloride (10 mL), which was added dropwise. The mixture was extracted with diethyl ether (3x). The organic layers were combined and washed with saturated sodium bicarbonate (1x) and brine (1x). The collected organic layers were dried over anhydrous sodium sulfate and concentrated under reduced pressure. Flash column chromatography (silica gel, 8% ethyl acetate in petroleum ether) yielded **1** (640 mg, 2.50 mmol, 20%).

TLC: R_f = 0.4 (dichloromethane/methanol, 80:20 v/v). **^{1}H NMR** (400 MHz, $CDCl_3$) δ 7.81 (d, J = 8.3 Hz, 2H), 7.36 (d, J = 8.0 Hz, 2H), 3.94 (t, J = 6.4 Hz, 2H), 2.45 (s, 3H), 1.66 (t, J = 6.4 Hz, 2H), 0.99 (s, 3H). **^{13}C NMR** (100 MHz, $CDCl_3$) δ 145.17, 130.04, 128.08, 125.37, 65.23, 34.27, 23.50, 21.78, 19.88.

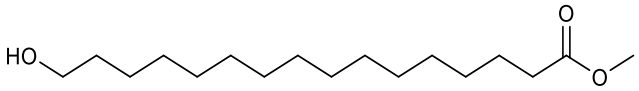
2-hydroxy-N,N-dimethyl-N-(2-(3-methyl-3H-diazirin-3-yl)ethyl)ethan-1-aminium (2)[2]



To a solution of **1** (200 mg, 0.78 mmol, 1.1 eq.) in acetonitrile (700 µl) was added 2-dimethylaminoethanol (72 µl, 0.71 mmol, 1 eq.). After stirring overnight at 80 °C, additional **13** (10 mg, 0.039 mmol, 0.55 eq.) was added. After stirring overnight at 80 °C, the mixture was concentrated under reduced pressure to give the yellow/brown solid **2** (134 mg, 0.78 mmol, quant).

^{1}H NMR (400 MHz, MeOD) δ 7.71 (d, J = 8.2 Hz, 2H), 7.25 (d, J = 8.0 Hz, 2H), 4.02 – 3.89 (m, 2H), 3.50 – 3.44 (m, 2H), 3.43 – 3.40 (m, 2H), 3.13 – 3.09 (m, 4H), 2.38 (s, 3H), 1.88 – 1.80 (m, 2H), 1.07 (s, 2H). **^{13}C NMR** (100 MHz, MeOD) δ 143.62, 141.73, 129.87, 126.93, 66.43, 61.33, 56.81, 52.33, 52.29, 52.25, 29.28, 21.31, 19.35, 0.81.

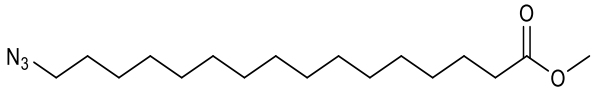
Methyl 16-hydroxyhexadecanoate (3)



To a solution of 16-hydroxyhexadecanoic acid (1.70 g, 6.6 mmol, 1 eq.) in methanol (100 mL) was added acetyl chloride (3.24 mL, 44.7 mmol, 8 eq.) at 0 °C. After stirring overnight, additional acetyl chloride (3 mL, 41.4 mmol) was added. Monitoring by TLC showed complete conversion after 2 hours. The mixture was then concentrated under reduced pressure and dissolved in dichloromethane. The solution was washed with a saturated sodium bicarbonate solution (2x), water (2x) and brine (1x). Every aqueous phase was extracted with dichloromethane (1x). The organic layers were combined, dried over anhydrous sodium sulfate and evaporated under reduced pressure, yielding **3** as a white solid (1.73 g, 6.06 mmol, 92%).

R_f = 0.8 (Pentanes/Ethyl acetate, 75:25 v/v). **^{1}H NMR** (400 MHz, $CDCl_3$) δ 3.66 (s, 3H), 3.63 (t, J = 6.6 Hz, 2H), 2.30 (t, J = 7.6 Hz, 2H), 1.66 – 1.50 (m, 4H), 1.38 – 1.19 (m, 22H). **^{13}C NMR** (100 MHz, $CDCl_3$) δ 63.24, 51.60, 34.26, 32.94, 29.77, 29.76, 29.74, 29.72, 29.57, 29.39, 29.29, 25.87, 25.17, 25.10

Methyl 16-azidohexadecanoate (4)[3]



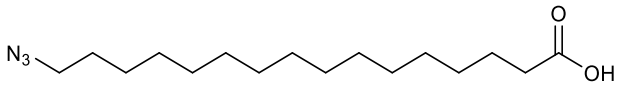
To a solution of **3** (1.70 g, 6.06 mmol) and triethylamine (5.07 mL, 36.4 mmol, 6 eq.).in methanol (100 mL) was added methanesulfonyl chloride (1.88 mL, 24.2 mmol, 4 eq.) dropwise at 0 °C. After addition, the mixture was allowed to warm to room temperature and monitoring by TLC showed complete conversion of the starting materials after 3 hours. The mixture was concentrated under reduced pressure, dissolved in dichloromethane and the solution was washed with a saturated sodium bicarbonate solution (1x), water (1x) and brine (1x). The organic layer was dried over anhydrous sodium sulfate and evaporated under reduced pressure, yielding the mesylate intermediate which was taken to the next step without further purification.

To a solution of mesylate intermediate in N,N-dimethylformamide (40 mL) was added sodium azide (2.15 g, 33 mmol) and the solution was stirred at 70 °C for 2 hours. The mixture was concentrated under reduced pressure, dissolved in DCM and washed with water (3x), a saturated sodium bicarbonate solution (1x) and brine (1x). The organic layer

was dried over anhydrous sodium sulfate and evaporated under reduced pressure. Flash column chromatography (silica gel,5-10% ethyl acetate in pentane) yielded **4** as a white solid (1.71 g, 5.51 mmol, 91%)

R_f = 0.8 (Pentanes/Ethyl acetate, 75:15 v/v). **^{1}H NMR** (400 MHz, $CDCl_3$) δ 3.66 (s, 3H), 3.25 (t, *J* = 8 Hz, 2H), 2.29 (t, *J* = 8 Hz, 2H), 1.66 - 1.59 (m, 4H), 1.42- 1.25 (m, 22H). **^{13}C NMR** (100 MHz, $CDCl_3$) δ 174.43, 51.61, 51.56, 34.24, 29.75, 29.71, 29.66, 29.61, 29.57, 29.38, 29.38, 28.96

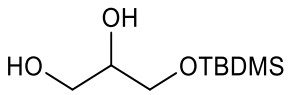
16-Azidohexadecanoic acid (5)[3]



To a solution of **4** (1.70 g, 5.49 mmol) in tetrahydrofuran and dioxane (1:1, 15 mL) was added a 4M NaOH solution (15 mL) and the reaction was stirred at room temperature overnight. The mixture was diluted with ethyl acetate (200 mL) and washed with a 1M HCl solution (2x), water (1x) and brine (1x). The organic layer was dried over anhydrous sodium sulfate and concentrated under reduced pressure yielding **5** as a white solid (1.62 g, 5.21 mmol, 95%)

R_f = 0.2 (Pentanes/Ethyl acetate, 75:25 v/v). **^{1}H** NMR (400 MHz, $CDCl_3$) δ 3.25 (t, *J* = 8 Hz, 2H), 2.34 (t, *J* = 8 Hz, 2H), 1.66 - 1.59 (m, 4H), 1.35- 1.25 (m, 22H). **^{13}C** NMR (100 MHz, $CDCl_3$) δ 180.53, 51.60, 29.74, 29.70, 29.66, 29.60, 29.55, 29.36, 29.28, 29.17, 28.95, 26.84, 24.78

3-((tert-Butyldimethylsilyl)oxy)propane-1,2-diol (6)

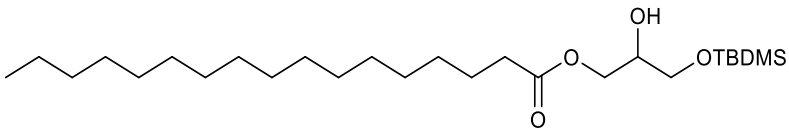


To a solution of *tert*-Butyldimethylsilyl chloride (1.0 gram, 6.6 mmol, 1 eq.) in dichloromethane (25 mL) was added dropwise a solution of glycerol (17.8 gram, 198.6 mmol, 30 eq.) and imidazole (1.35 gram, 19.8 mmol, 3 eq.) in dichloromethane (30 mL) and DMF (12 mL) at -18 °C. After stirring the solution for one hour at -18 °C, water (50 mL) was added. The resulting mixture was extracted with dichloromethane (3x). The organic layers were combined and washed with water (1x) and brine (1x), dried over anhydrous sodium sulfate and evaporated under reduced pressure. Flash column chromatography

(silica gel, 40% ethyl acetate in pentane) yielded **6** as a transparent oil (478 mg, 2.27 mmol, 34%).

R_f = 0.54 (Pentane/Ethyl acetate, 50:50 v/v). **^{1}H NMR** (400 MHz, $CDCl_3$) δ 3.81 – 3.55 (m, 5H), 0.90 (s, 9H), 0.08 (s, 6H). **^{13}C NMR** (100 MHz, $CDCl_3$) δ 71.71, 64.89, 64.35, 64.19, 25.98, 18.39, -5.34.

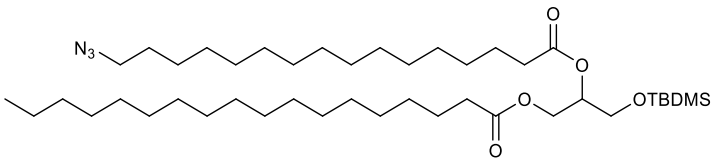
3-((*tert*-Butyldimethylsilyl)oxy)-2-hydroxypropyl propionate (7)



To a solution of stearic acid (295 mg, 1.04 mmol, 0.7 eq.) in dichloromethane (8 mL) were added N,N′-dicyclohexylcarbodiimide (257 mg, 1.04 mmol, 0.7 eq.) and 4-dimethylaminopyridine (90 mg, 0.74 mmol, 0.5 eq.). After stirring for 30 minutes at room temperature, the solution was cooled down to 0 °C. To the cooled solution was added 5 (310 mg, 1.48 mmol, 1 eq.). The solution was stirred at 0 °C for 30 min, allowed to warm up to room temperature and stirred overnight. The formed suspension was filtered and the filtrate was washed with saturated sodium bicarbonate solution (2x), water (2x) and brine (1x). The separate aqueous layers were extracted with dichloromethane (1x). The combined organic layers were dried over anhydrous sodium sulfate and evaporated under reduced pressure. Flash column chromatography (silica gel, 6% ethyl acetate in pentane), yielded 6 as a mixture of regioisomers (2°:1° = 7:43, determined by 1H-NMR) (374 mg, 0.790 mmol, 76%).

R_f = 0.65 & 0.7 (Pentane/Ethyl acetate, 80:20 v/v). **^{1}H NMR** (400 MHz, $CDCl_3$) δ 4.19 – 4.05 (m, 1H), 3.92 – 3.84 (m, 1H), 3.84 – 3.72 (m, 1H), 3.67 (dd, J = 10.1, 4.6 Hz, 1H), 3.60 (dd, J = 10.1, 5.6 Hz, 1H), 2.33 (t, J = 7.6 Hz, 2H), 1.70 – 1.55 (m, 2H), 1.25 (s, 28H), 0.94 – 0.77 (m, 12H), 0.07 (d, J = 2.6 Hz, 6H). **^{13}C NMR** (100 MHz, $CDCl_3$) δ 174.13, 74.38, 65.12, 63.81, 63.02, 62.70, 34.55, 34.34, 32.07, 29.84, 29.82, 29.80, 29.75, 29.61, 29.51, 29.42, 29.29, 25.97, 25.09, 22.84, 14.27, -5.33.

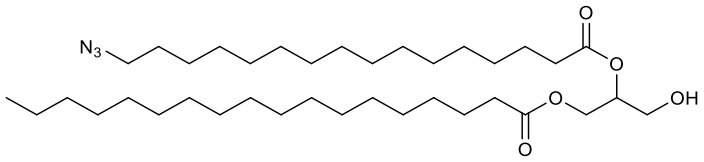
2-((16-Azidohexadecanoyl)oxy)-3-((tert-butyldimethylsilyl)oxy)propyl stearate (8)



To a solution of **5** (221 mg, 0.746 mmol, 1.05 eq.) in dichloromethane (8 mL), were added N,N′-dicyclohexylcarbodiimide (185 mg, 0.746 mmol, 1.05 eq.) and 4-dimethylaminopyridine (65 mg, 0.530 mmol, 0.75 eq.). After stirring for 30 minutes at room temperature, **7** was added (336 mg, 0.751 mmol, 1 eq.) and the solution was stirred overnight. The formed suspension was filtered and the organic phase was washed with saturated sodium bicarbonate solution (2x), water (2x) and brine (1x). The combined organic layers were dried over anhydrous sodium sulfate and evaporated under reduced pressure. Flash column chromatography (silica gel, 1.5% ethyl acetate in pentane) yielded **12** (340 mg, 0.452 mmol, 64%) as a mixture of regioisomers.

R_f = 0.3 (Pentane/Ethyl acetate, 95:5 v/v). **^{1}H NMR** (400 MHz, $CDCl_3$) δ 5.17 – 4.95 (m, 1H), 4.33 (dd, J = 11.8, 3.7 Hz, 1H), 4.15 (dd, J = 11.8, 6.3 Hz, 1H), 3.79 – 3.54 (m, 2H), 3.25 (t, J = 7.0 Hz, 2H), 2.29 (dd, J = 7.9, 7.1, 2.1 Hz, 4H), 1.68 – 1.51 (m, 6H), 1.25 (s, 50H), 0.96 – 0.76 (m, 12H), 0.07 (s, 6H). **^{13}C NMR** (100 MHz, $CDCl_3$) δ 173.61, 173.26, 71.80, 62.58, 61.58, 51.62, 34.49, 34.30, 32.07, 29.84, 29.81, 29.79, 29.77, 29.69, 29.63, 29.51, 29.44, 29.30, 29.27, 29.25, 28.98, 26.86, 25.08, 25.05, 22.83, 14.26, -5.36 (d, J = 4.2 Hz).

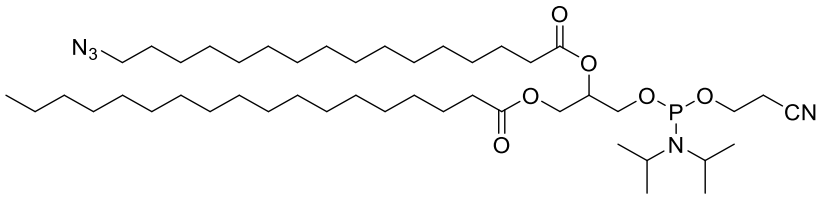
2-((16-Azidohexadecanoyl)oxy)-3-hydroxypropyl stearate (9)



To a solution of **8** (340 mg, 0.452 mmol, 1 eq.) in acetonitrile: tetrahydrofuran (1:1, 8 mL) was added triethylamine trihydrofluoride (0.74 mL, 4.52 mmol, 10 eq.). After stirring overnight at room temperature, the solution was quenched on ice with a saturated sodium bicarbonate solution. After extraction with dichloromethane (4x), the organic layers were combined, dried over anhydrous sodium sulfate and concentrated under reduced pressure. Flash column chromatography (silica gel, 20% ethyl acetate in pentane) yielded **9** (289 mg, 0.452 mmol, quant) as a mixture of regioisomers.

R_f = 0.8 (Pentane/Ethyl acetate, 80:20 v/v). **^{1}H NMR** (400 MHz, $CDCl_3$) δ 5.08 (p, J = 5.0 Hz, 1H), 4.32 (dd, J = 11.9, 4.5 Hz, 1H), 4.24 (dd, J = 11.9, 5.6 Hz, 1H), 4.21 – 4.13 (m, 1H), 3.75 – 3.71 (m, 1H), 3.25 (t, J = 7.0 Hz, 2H), 2.38 – 2.29 (m, 4H), 1.66 – 1.55 (m, 8H), 1.35 – 1.21 (m, 48H), 0.88 (t, J = 6.4 Hz, 3H). **^{13}C NMR** (101 MHz, $CDCl_3$) δ 72.24, 62.11, 61.71, 51.64, 34.44, 34.26, 32.08, 29.85, 29.81, 29.79, 29.77, 29.69, 29.63, 29.52, 29.42, 29.40, 29.31, 29.27, 29.24, 28.99, 26.87, 25.09, 25.04, 22.85, 14.28.

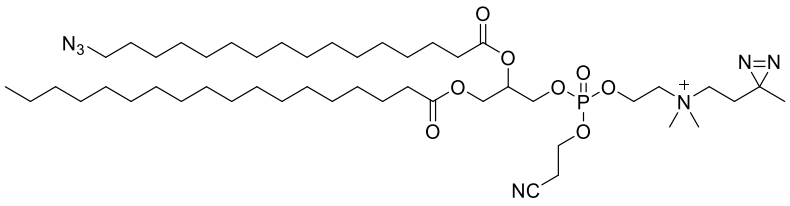
2-((16-azidohexadecanoyl)oxy)-3-(((2-cyanoethoxy)(diisopropylamino)phosphanyl)oxy)propyl stearate (10)



A solution of **13** (200 mg, 0.313 mmol, 1 eq.) and diisopropylethylamine (329 µl, 1.88 mmol, 6 eq.) in dry dichloromethane (5 mL) was dried over freshly oven-dried 3Å molecular sieves and stored under nitrogen atmosphere. The mixture was transferred to a dry flask under nitrogen atmosphere and to the solution was added 2-cyanoethyl N,N-diisopropylchlorophosphoramidite (250 mg, 1.056 mmol, 3 eq.). After stirring for 1.5 hours the solution was concentrated under reduced pressure until 600 mbar. Flash column chromatography, (high purity silica gel pre-treated with 5% triethylamine in pentane, 3% ethyl acetate and 3% Et_3N in pentane) yielded **16** (194 mg, 0.231 mmol, 74%)**.** The product was stored in 20% triethylamine in dichloromethane (2 mL) under nitrogen atmosphere overnight. For the next reaction, the product was concentrated under reduced pressure until 60 mbar for maximum 10 minutes.

R_f = 0.6 (Pentane/Ethyl acetate/Et_3N, 90:7:3 v/v/v)). **^{1}H NMR** (400 MHz, $CDCl_3$) δ 4.29 – 4.06 (m, 2H), 3.92 – 3.72 (m, 2H), 3.67 – 3.54 (m, 1H),3.25 (t, J = 7.0 Hz, 1H), 2.63 (td, J = 6.5, 2.3 Hz, 2H), 2.54 (q, J = 7.2 Hz, 4H), 2.30 (tt, J = 7.0, 3.5 Hz, 4H), 1.68 – 1.54 (m, 6H), 1.32 – 1.18 (m, 50H), 1.17 (q, J = 2.9 Hz, 12H), 0.87 (t, J = 6.8 Hz, 3H). **^{13}C NMR** (100 MHz, $CDCl_3$) δ 173.61, 69.68, 69.52, 64.03, 58.64, 58.46, 51.63, 46.38, 43.43, 43.31, 34.30 (d, J = 4.3 Hz), 32.07, 29.82 (d, J = 4.6 Hz), 29.66 (d, J = 5.9 Hz), 29.51, 29.45, 29.30, 28.98, 26.86, 25.03, 24.75, 24.65, 24.57, 22.83, 14.27, 11.69. ^{31}P NMR (162 MHz, $CDCl_3$) δ 150.08, 149.50.

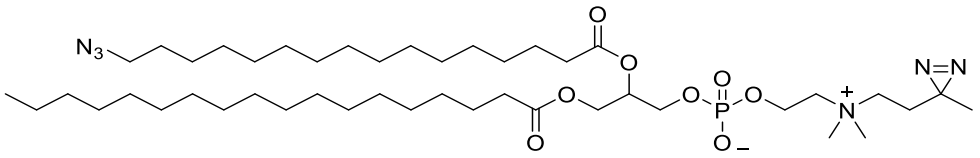
2-(((2-((16-azidohexadecanoyl)oxy)-3-(stearoyloxy)propoxy)(2-cyanoethoxy)phosphoryl)oxy)-n,n-dimethyl-n-(2-(3-methyl-3h-diazirin-3-yl)ethyl)ethan-1-aminium (11)



A solution of **10** (194 mg, 0.231 mmol, 1 eq.) in dry dichloromethane (5 mL) was dried over freshly oven-dried 3Å molecular sieves under nitrogen atmosphere. To the solution were added **2** (79 mg, 0.231 mmol, 1 eq.) and tetrazole (1.03 mL, 0.462 mmol, 2 eq.). After stirring for 45 minutes, additional tetrazole (0.51 mL, 0.231 mmol, 1eq.) and **15** (20 mg, 0.058 mmol, 0.25 eq.) were added. After 1 hour, ^{31}P-NMR indicated complete conversion of the starting material (main peak shifted from 150 ppm to 140 ppm) to the solution was added *tert*-Butyl hydroperoxide (66 µL, 0.347 mmol, 1.5 eq.). After 45 minutes, ^{31}P-NMR showed oxidation was complete (peak shifted from 140 ppm to -3 ppm), the solution was diluted with dichloromethane and washed with saturated sodium bicarbonate (1x) and brine (1x). The collected organic layers were dried over anhydrous sodium sulfate and concentrated under reduced pressure. Flash column chromatography (high purity silica gel, 10% methanol in dichloromethane) yielded **11** (20.5 mg, 5.54 µmol, 10%).

R$_f$ = 0.3 (dichloromethane/methanol, 80:20 v/v). **^{1}H NMR** (400 MHz, $CDCl_3$) δ 4.88 – 4.63 (m, 2H), 4.50 – 4.31 (m, 3H), 4.27 – 4.12 (m, 4H), 3.65 (d, J = 5.4 Hz, 2H), 3.40 (s, 6H), 3.25 (t, J = 7.0 Hz, 2H), 3.11 (qd, J = 7.3, 4.8 Hz, 4H), 2.90 (s, 2H), 2.43 – 2.26 (m, 4H), 1.90 (s, 2H), 1.65 – 1.52 (m, 6H), 1.25 (s, 50H), 1.17 (s, 3H), 0.87 (t, J = 6.7 Hz, 3H). **^{31}P NMR** (162 MHz, $CDCl_3$) δ -2.68, -3.33. **ESI-HRMS** (*m/z*) $C_{48}H_{91}N_7O_8P^+$: $[M]^+$ calculated: 925.27, found: 923.98.

2-((16-azidohexadecanoyl)oxy)-3-(stearoyloxy)propyl(2-(dimethyl(2-(3-methyl-3h-diazirin-3-yl)ethyl)ammonio)ethyl) phosphate (iks02)



To a solution of **17** (10.26 mg, 11.08 µmol) in dry dichloromethane (3 mL) was added a mixture of *tert*-butylamine and dichloromethane (1:1, 100 µL) and the mixture was stirred at room temperature for 3 hours. The solution was concentrated under reduced pressure. The product was purified with column chromatography (high purity silica gel, 17% methanol in dichloromethane) and yielded **IKS02** as a white solid (5.66 mg, 5.32 µmol, 48%).

R$_f$ = 0.3 (dichloromethane/methanol, 70:30 v/v). **^{1}H NMR** (850 MHz, $CDCl_3$) δ 4.55 (s, 1H), 4.40 (s, 3H), 4.27 (dd, J = 11.7, 5.3 Hz, 2H), 4.24 (dd, J = 11.5, 4.6 Hz, 2H), 4.01 (s, 1H), 3.86 (s, 2H), 3.58 (t, J = 8.4 Hz, 2H), 3.30 (s, 6H), 3.25 (t, J = 7.0 Hz, 2H), 2.31 (t, J = 7.7 Hz, 6H), 1.87

(q, J = 8.8 Hz, 2H), 1.59 (h, J = 7.1 Hz, 6H), 1.33 – 1.18 (m, 48H), 1.15 (s, 3H), 0.88 (t, J = 7.1 Hz, 3H). **^{31}P NMR** (162 MHz, $CDCl_3$) δ -1.82. **ESI-HRMS** (*m*/*z*) $C_{45}H_{87}N_6O_8P$: $[M]^+$ calculated: 871.1780, found: 871.63958.

Biological methods and proteomics

General

All solvents and reagents were obtained from common commercial sources (Sigma Aldrich, Acros Organics, Alfa Aesar, Fluka, Merck) and used without further purification, unless stated otherwise. Dynamic light scattering and zeta potential measurements were performed on a Malvern Zetasizer Nano ZS. For light irradiation, a CaproBox™ (Caprotec Bioanalytics GmbH) was used with a wavelength of 350 nm and applying a 300 nm light filter. Human serum was purchased from Sigma-Aldrich (Non Heat Inactivated, Human Male AB plasma, USA origin, sterile-filtered, product code: H4522) with a protein concentration of 60.2 µg/µl determined by a Pierce BCA Protein Assay Kit (Thermo Scientific). The serum was aliquoted, snap-frozen with liquid nitrogen and stored for a maximum of 6 months at -80 °C. Albumin from human serum (SRP6182), Human transferrin (T3309) and recombinant human apolipoprotein E3 (SRP4696) were purchased from Sigma-Aldrich. Human prothrombin (RP-43087) was purchased from Thermo-Fisher Scientific. Recombinant human Apolipoprotein A1 (ab50239) was purchased from Abcam B.V. (Amsterdam, The Netherlands).

Evaporation of solvents with a vacuum centrifuge was performed using an Eppendorf speedvac (Eppendorf Concentrator Plus 5301). Sequencing grade modified trypsin was purchased from Promega (product code = V5111). Acetonitrile (LC-MS grade) and methanol (LC-MS grade) were purchased from Biosolve. Formic acid (LC-MS grade) was purchased from Actu-All Chemicals. BioSpin columns were purchased from Bo-Rad. The Empore C18 47-mm extraction disks (model 2215) were purchased from 3M™ Purification. Enolase digest standard was purchased from Waters MassPREP™.

Liposome preparation

Lipids were combined from stock solutions (10 mM in $CHCl_3$:MeOH 1:1 v/v) at the desired molar ratios. The solvents were evaporated under a nitrogen flow and traces of solvents were removed *in vacuo* for at least 30 minutes. Lipid films were hydrated with the desired volume of 20 mM HEPES (pH 7.4), vortexed and warmed to 65 °C for 5 minutes. The mixture was extruded thirteen times through two stacked 100 nm polycarbonate membranes (Nucleopore Track-Etch, Whatman) using an Avanti Mini Extruder (Avanti

Polar Lipids). Size and surface charge were measured by Dynamic Light Scattering (DLS) and Zeta Potential measurement and liposomes were stored in the dark at 4 °C for no longer than two weeks.

Photoaffinity method

Incubation, crosslinking and click chemistry

Liposomes containing the photoaffinity probe (25 µL, 5 mM) were added to pre-warmed human serum (37 °C, 25 µL, 60.26 mg/ml protein) and incubated in the dark at 37 °C for 1 hour. For every liposome formulation, twelve replicates were prepared. Half of the replicates were irradiated with 350 nm light for 15 minutes, while cooling. The other replicates were kept at room temperature in the dark for 15 minutes. Afterwards, the liposomes were solubilized by addition of 10 µL 0.2% Triton X-100 in ultrapure water and incubation for 30 minutes. The samples were diluted by adding 140 µL of 0.1% SDS in ultrapure water. Aliquots of 100 µL were taken and protein precipitation was performed according to Wessel and Flügge.[4] Briefly, ultrapure water (400 µL), methanol (650 µL), chloroform (200 µL) and ultrapure water (150 µL) were added sequentially, followed by vigorous vortexing and centrifugation (3000 *g*, 10 min, rt). The liquid layers were removed, the pellet resuspended with methanol (600 µL) and centrifuged (14,000 *g*, 5 min, rt). The supernatant was discarded and the pellet was dissolved in HEPES buffer containing 0.5% SDS (200 µL, 100 mM, pH 8.0).

A BCA assay was performed to determine the protein concentration and the samples were diluted to a volume of 450 µL with HEPES buffer with 0.5% SDS (100 mM, pH 8.0) with a protein concentration of 0.5-1.0 mg/mL. For each protein sample, click reagent mixture (50 µL) was added from a 10x concentrated stock to give a final concentration of 100 µM $CuSO_4$, 1000 µM sodium ascorbate, 500 µM THPTA, 5000 µM aminoguanidine and 20 µM Cy5-alkyne or Biotin-alkyne, followed by incubation at room temperature for 1 hour. Methanol (650 µL), chloroform (150 µL) and ultrapure water (150 µL) were added sequentially, the mixture vortexed and centrifuged (3000 *g*, 10 min, rt). The liquid layers were removed, resuspended with methanol (600 µL) and centrifuged (14,000 *g*, 5 min, rt). The pellet was air-dried at room temperature for 5-10 minutes and resuspended in freshly prepared denaturing buffer (250 µL, 6 M urea, 25 mM NH_4HCO_3) and used for in-gel fluorescence imaging or enrichment. Alternatively, samples were snap-frozen with liquid nitrogen and stored for no longer than 2 weeks at -80 °C.

SDS-Page and in-gel fluorescence imaging

Protein concentration was determined by BCA assay prior to loading samples for in-gel fluorescence. To a volume corresponding to 10 µg of protein was added Laemmli buffer (4x stock) and the proteins were resolved on a 12.5% PA gel at 180 V. The subset of fluorescent proteins was imaged on a Typhoon FLA 9500 (GE Healthcare), followed by staining of all the proteins with Coomassie Brilliant Blue R-250 staining solution (Bio-Rad) and imaging on a ChemiDoc MP system (Bio-Rad).

Reduction and alkylation

To lipid-protein samples conjugated to biotin, 5 µL (1 M DTT; 20 mM final concentration) was added. Samples were vortexed, centrifuged and incubated at 56 °C while shaking (600 rpm) for 30 minutes. The samples were allowed to cool down to room temperature, after which 40 µl 0.5 M iodoacetamide (80 mM final concentration) was added and the samples incubated at room temperature in the dark for 30 minutes. Afterwards, 20 µL 1 M DTT (100 mM final concentration) was added and the samples were vortexed and incubated at 56 °C for 5 minutes. Reduced and alkylated proteins were used directly for avidin bead enrichment.

Enrichment and on-bead digestion

Avidin agarose beads (50% slurry, 100 µL per sample, Thermo Fisher Scientific) were washed three times with PBS (10 mL PBS per 400 µL slurry), centrifuging at 2500 *g* for 3 minutes. The beads were resuspended in PBS (1 mL PBS per 100 µL slurry) and divided over 15 mL tubes in 1 mL fractions. An additional 2 mL PBS was added to each tube, after which the denatured and alkylated protein samples were added and the samples were shaken gently in an overhead shaker at RT for at least 3 hours. Beads were pelleted (2,500 g, 5 min) and the supernatant discarded. The beads were washed twice with SDS in PBS (0.5% w/v, 10 mL), three times with PBS (10 mL) and twice with ultrapure water (10 mL). In between each washing step, the samples were vortexed, centrifuged (2,500 g, 5 min) and the supernatants were discarded. The washed beads were resuspended in 250 µL on-bead digestion buffer (100 mM TRIS pH 8.0, 100 mM NaCl, 1 mM $CaCl_2$ and 2% v/v acetonitrile (LC-MS grade)) and transferred to 1.5 mL low-binding Eppendorf tubes, after which 10 µL 0.1 µg/µL trypsin was added and the samples were incubated at 37 °C while shaking (950 rpm) overnight. To the samples was added 12.5 µL formic acid, after which they were loaded onto Bio-Spin columns (Bio-Rad) and the flow-through was collected by centrifugation

(2,500 g, 2 min) in low-binding Eppendorf tubes. The samples were desalted using the StageTips procedure described below.

Protein binding validation experiment

Human serum albumin (ALBU, 25 µg), transferrin (TRFE, 10 µg), apolipoprotein A1 (APOA1, 2 µg), apolipoprotein E3 (APOE, 2 µg) and prothrombin (THRB, 2 µg) were mixed in a total volume of 17.5 µL (PBS) for each replicate. To each replicate was added liposomes containing IKS02 (7.5 µL, 5 mM). For competition experiments, liposomes without IKS02 added were according to the competitive ratio (5 mM, 1:1 = 7.5 µL, 1:4 = 30 µL, 1:9 = 67.5 µL). The mixture was incubated at 37 °C for 1 hour followed by liposome solubilisation with 1% Triton X-100 (5 µL). Proteins were precipitated by addition of ultrapure water, up to a volume of 100 µL, methanol (100 µL) and chloroform (50 µL), followed by vigorous vortexing and centrifugation (3000 g, 10 min, rt). The liquid layers were removed, the pellet resuspended with methanol (200 µL) and centrifuged (14,000 g, 5 min, rt). The supernatant was discarded and the pellet was dissolved in HEPES buffer (45 µL, 100 mM, pH 8.0). For each protein sample, click reagent mixture (5 µL) was added from a 10x concentrated stock to give a final concentration of 100 µM $CuSO_4$, 1000 µM sodium ascorbate, 500 µM THPTA, 5000 µM aminoguanidine and 20 µM Cy5-alkyne or Biotin-alkyne, followed by incubation at room temperature for 1 hour. Protein precipitation was repeated as prior to the click reaction and the pellet was dissolved in PBS (50 µL) from which an aliquot was taken to perform a BCA assay. For in-gel fluorescence measurement, aliquots containing 10 µg protein were analysed by SDS-PAGE and in-gel fluorescence as described before. For MS/MS experiments, aliquots containing 20 µg protein were taken for reduction and alkylation and further steps as described before.

Centrifugation method

Centrifugation, washing and SDS-Page

The centrifugation method for protein corona determination was performed as previously described.[5–7] Briefly, human serum (100 µL, 60.26 µg/µL protein) was thawed on ice and warmed to 37 °C prior to incubation with liposomes (100 µL, 1 mg/mL) at 37 °C in low-binding Eppendorf tubes for one hour. The samples were centrifuged (17,500 g, 15 min) and the supernatant was discarded. The pellets were washed by dissolving in PBS (100 µL, pH 7.4) and centrifugation (17,500 g, 15 min). This washing step was performed two more times, after which the pellets were dissolved in 1% SDS containing Laemmli buffer (20 µL), denatured at 95 °C for 5 minutes and resolved on a 12.5% poly acrylamide gel. The gel was

fixed and stained using Coomassie Brilliant Blue R-250 staining solution, imaged on a ChemiDoc MP system (Bio-Rad) followed by in-gel reduction, alkylation and digestion as described below.

In-gel reduction, alkylation and digestion

The SDS-PAGE gel lanes were cut in in pieces of approximately 3 mm and transferred to 1.5 mL low-binding Eppendorf tubes. The gel pieces were washed with 25 mM NH_4HCO_3/acetonitrile (95:5, v/v) (400 µL) for 30 minutes and twice with 50 mM NH_4HCO_3/acetonitrile (50:50 v/v, 400 µL) for 30 minutes. The gel pieces were dehydrated by the addition of acetonitrile (300 µL, 10 min), after which the liquids were removed and the gel pieces were dried with a vacuum centrifuge. The gel pieces were hydrated with a 10 mM DTT in 100 mM NH_4HCO_3 solution (200 µL) and incubated at 56 °C for 1 hr. The excess liquid was removed, 55 mM IAA in 100 mM NH_4HCO_3 (200 µL) added and the solution incubated at room temperature in the dark for 45 minutes. The gel pieces were subsequently washed with 100 mM NH_4HCO_3 (200 µL) for 10 minutes and acetonitrile (200 µL) for 10 minutes. These washing steps were repeated two more times and the pieces were dried with a vacuum centrifuge.

The gel pieces were hydrated with digestion buffer (200 µL, 5 ng/µL trypsin in 50 mM NH_4HCO_3/acetonitrile 90:10 v/v) and incubated at 37 °C overnight. Formic acid in 50 mM NH_4HCO_3 (100 µL, 5:95 v/v) was added and the supernatants of the corresponding gel lanes were combined. To the gel pieces was added a solution of acetonitrile/50 mM NH_4HCO_3/formic acid (50:45:5 v/v, 100 µL) followed by incubation at room temperature for 45 minutes. The gel pieces were sonicated for 5 minutes and the supernatants were combined with the previous supernatants of the corresponding gel lanes. This last extraction step was performed one more time. Finally, a solution of acetonitrile/50 mM NH_4HCO_3/formic acid (90:5:5 v/v, 100 µL) was added and incubated at room temperature for 5 minutes. The supernatants were combined and dried using a vacuum centrifuge. The protein digests were dissolved in 100 µL StageTip solution A (0.5% (v/v) formic acid in ultrapure water) and desalted, using the StageTip procedure described below, before analysis by UPLC MS/MS.

In-solution reduction, alkylation and digestion

Six aliquots of human serum (20 µL, 60.26 mg/ml protein) were precipitated according to Wessel and Flügge[4]. Briefly, ultrapure water (480 µL), methanol (650 µL), chloroform (200 µL) and ultrapure water (150 µL) were added sequentially, followed by vigorous vortexing

and centrifugation (3000 *g*, 10 min, RT). The liquid layers were removed, the pellet resuspended with methanol (600 µL) and centrifuged (14,000 *g*, 5 min, RT). The supernatant was discarded and the pellet was dissolved in freshly prepared denaturing buffer (250 µL, 6M Urea and 25 mM $NaHCO_3$). A BCA assay was performed to determine the protein concentration and aliquots were taken corresponding to 100 µg of protein, followed by dilution to 100 µL with denaturing buffer. To the sample was added 5 µL 0.2 M DTT and the sample was incubated at 56 °C for 30 minutes, followed by the addition of 25 µL 0.2 M Iodoacetamide and incubation at room temperature for 30 minutes. An additional 20 µL 0.2 M DTT was added and the sample was incubated at 56 °C for 5 minutes. Aliquots of 22.5 µL (15 µg of protein) were transferred to low-binding Eppendorf tubes and diluted to 200 µL with digestion buffer (100 mM TRIS pH 8.0, 100 mM NaCl, 1 mM $CaCl_2$ and 2% v/v acetonitrile (LC-MS grade)), to reduce the urea concentration to ~0.6 M, after which 3 µL, 0.1 µg/µL trypsin (1:50 w/w trypsin:protein) was added and the samples were incubated at 37 °C while shaking (950 rpm) overnight. After digestion, 10 µL formic acid was added and the samples were desalted using the StageTip procedure described below.

StageTip desalting

The protein digest desalting procedure was conducted as previously described.[8] Briefly, C_{18} extraction disks (47 mm) were placed in 200 µL pipette tips. These StageTips were conditioned, loaded, washed and eluted, following the scheme below. The eluted fractions were collected into low-binding Eppendorf tubes, dried using a vacuum centrifuge and stored at -20 °C or immediately prepared for UPLC-MS/MS measurements.

STAGE	**BUFFER**
Conditioning 1	50 µL MeOH (LC-MS grade)
Conditioning 2	50 µL StageTip solution B: 0.5% (v/v) formic acid, 80% (v/v) acetonitrile and 19.5% ultrapure water
Conditioning 3	50 µL StageTip solution A: 0.5% (v/v) formic acid in ultrapure water
Loading	Sample
Washing	100 µL StageTip solution A
Elution	100 µL StageTip solution B

NanoUPLC-MS/MS analysis

LC-MS was performed as described previously.[9] Peptide samples were dissolved in 50 µL LC-MS sample solution (ultrapure water:acetonitrile:formic acid 97:3:0.1) containing 10 fmol/µL enolase digest as an internal standard for label-free quantification. DMSO was not added to the LC solvents. Instead, a lower source temperature (80 °C instead of 100 °C) was used. A trap–elute protocol was used, in which a digest is loaded on a trap column and eluted and separated on the analytical column. The samples were brought on this trap column at a flow rate of 10 µl/min with 99.5% solvent A for 2 min, after which the column was switched to the analytical column. The peptide separation was achieved using a multistep concave gradient based on the gradients described elsewhere.[10] After washing with 90% solvent B, the column was re-equilibrated to initial conditions.

The detailed protocol is specified below:

TIME (MIN)	GRADIENT COMPOSITION (%B)	FLOW RATE (NL/MIN)
0	1.0	300
2.4	1.0	300
4.2	5.0	300
10.2	7.6	300
15.6	10.3	300
21	13.1	300
25.8	16.1	300
30.6	19.2	300
35.4	22.4	300
40.2	25.7	300
45	29.1	300
49.8	32.6	300
54	36.2	300

58.2	40.0	300
58.8	90.0	300
60.3	90.0	300
61.2	90.0	300
61.5	1.0	300
70.8	1.0	300

The rear seals of the pump were flushed every 30 min with 10% (v/v) ACN. [Glu1]-fibrinopeptide B (GluFib) was used as a lock mass compound. The auxiliary pump of the LC system was used to deliver this peptide to the reference sprayer (0.2 µl/min). As MS acquisition method, UDMS^{e} method was set up as described previously.[10] Briefly, these settings include that the mass range was set from 50 to 2,000 Da, with a scan time of 0.6 s in positive resolution mode. To be able to use the low-energy MS mode, the collision energy was set to 4 V in the trap cell. Besides, the transfer cell collision energy was ramped using drift-time-specific collision energies for the elevated energy scan[11]. The lock mass was sampled every 30 s.

MS acquisition method

The Synapt G2Si mass spectrometer (Waters) operating with Masslynx for acquisition and PLGS for peptide identification was used for analysis. The following settings in positive resolution mode were used: source temperature of 80°C, capillary voltage 3.0 kV, nano flow gas of 0.25 Bar, purge gas 250 L/h, trap gas flow 2.0 ml/min, cone gas 100 L/h, sampling cone 25V, source offset 25, lock mass acquiring was done with a mixture of Leu Enk (556.2771) and Glu Fib (785.84265), lock spray voltage 2.5 kV, Glufib fragmentation was used as calibrant. An UDMS^{e} data-independent acquisition method was used for analysis. Briefly, the mass range is set from 50 to 2,000 Da with a scan time of 0.6 seconds in positive, resolution mode. The collision energy is set to 4 V in the trap cell for low-energy MS mode. For the elevated energy scan, the transfer cell collision energy is ramped to higher collision energies and data is recorded. The lock mass was sampled every 30 seconds and used for accurate determination of parent ions mass after peak picking. The PLGS search engine was used for peptide identification against the Uniprot human database to which the streptavidin, avidin, yeast enolase and trypsin sequences were manually added. The ISOQuant software[10] was used for label free quantification of proteins using 50 fmol of yeast enolase digest as benchmark.

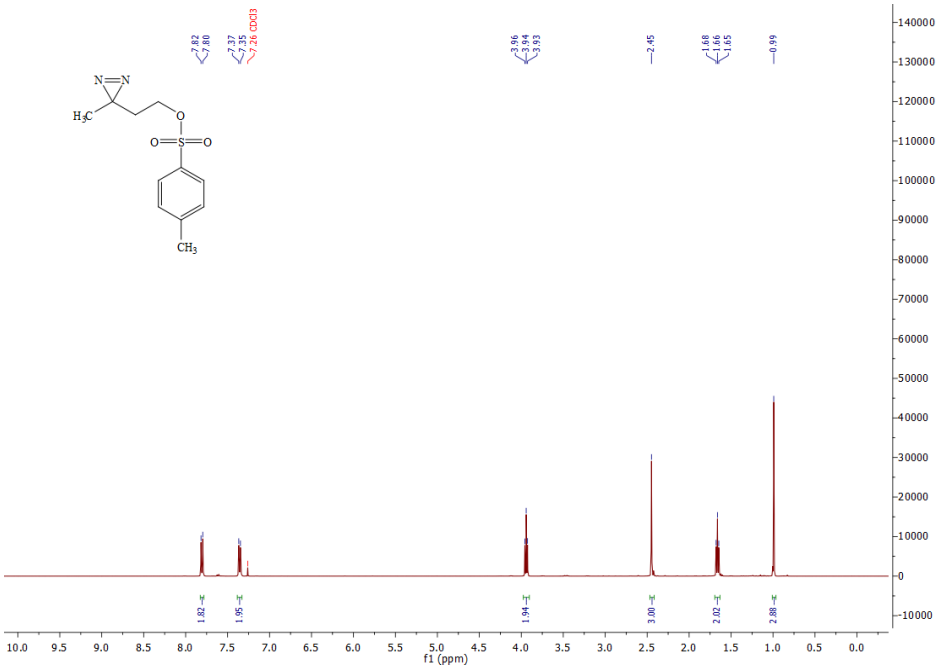
Proteomic analysis

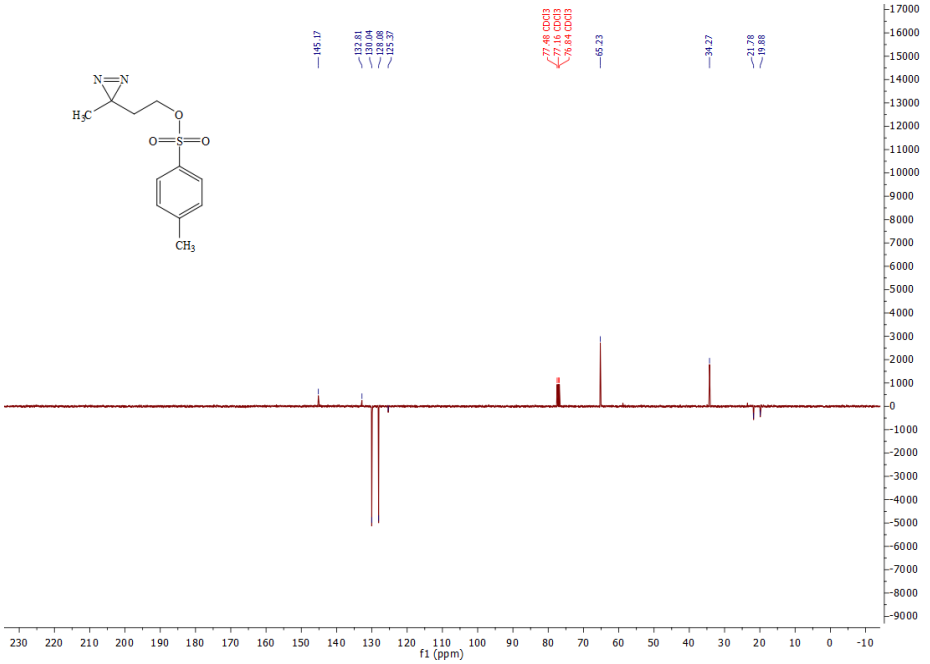
Configuration parameters for label-free quantification (LFQ) in the ISOQuant software are listed in Supplementary Table 2. For quantification, +UV and –UV replicates for all samples were compared in separate groups. The protein lists were filtered by excluding proteins that are considered as contamination (e.g. keratins), non-endogenous (e.g. trypsin, avidin) or non-reproducible (not present in six out of six +UV or centrifugation samples). For the volcano plots, the ratio of average ppm for each protein was calculated and is displayed as a logarithmic value (^{2}log). Furthermore, the p-value was determined by multiple t-tests comparing the replicates of each group using the GraphPad Prism software. In addition, a Benjamini-Hochberg correction was applied to adjust the p-value for multiple comparisons. The final adjusted p-value is displayed as a logarithmic value (^{10}log). Proteins that were exclusive for +UV samples or did not occur more than once in the –UV samples, making a t-test impossible, were labelled as 'exclusive' and are listed next to the volcano plot. Abundance plots were generated by plotting the ppm values of all six replicates. Similar statistical analysis was performed for validation experiments, with slight modifications: (1) the number of replicates here was four, but proteins still had to be present in four out of four replicates. (2) A Benjamini-Hochberg correction was no longer performed as the processing did not require a high amount of comparisons for the t-test. Instead, p-values were directly taken from t-tests and displayed as the logarithmic value (^{10}log).

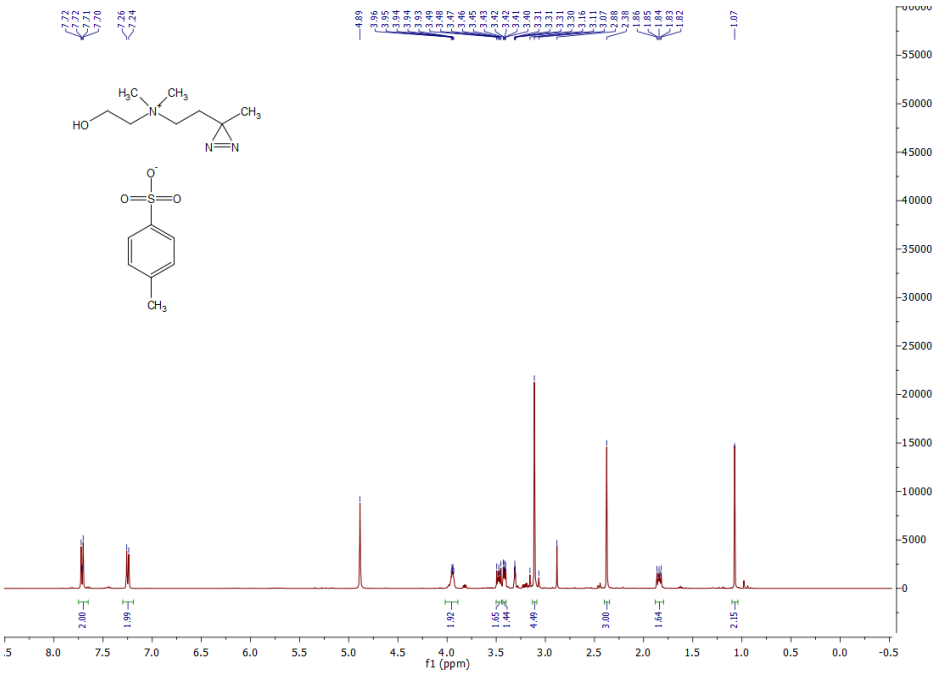
Absolute quantification was achieved from the same LFQ in ISOQuant, based on a comparison to the internal standard (ENLS digest, 50 fmol). The proteins that passed the criteria for the volcano plots were selected. The average absolute amount of these proteins in the +UV samples was corrected for the average in the –UV samples. For heat map construction, the sum of ppm values for all 'accepted' proteins within the sample was taken and the relative abundance of every protein was calculated as a ratio expressed in percentages of this value. For the photoaffinity method, the proteins within the enrichment and p-value boundaries of the volcano plot were considered as 'accepted'. For the centrifugation method, all besides the initially filtered proteins were considered as 'accepted'. Fully processed proteomic data for all samples is provided in two separate excel spreadsheets.

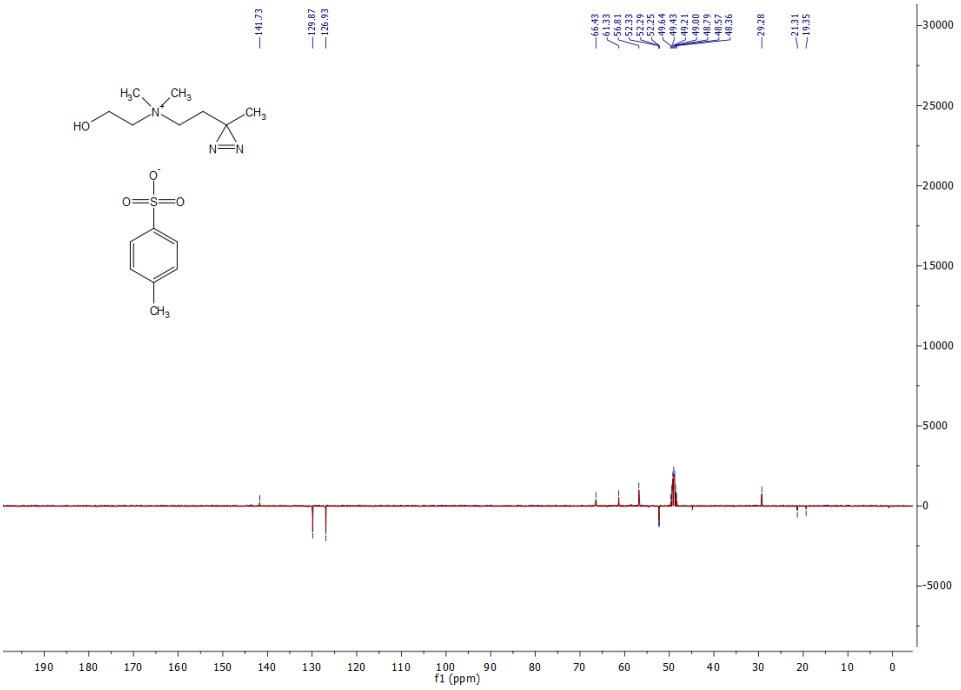
The mass spectrometry proteomics data have also been deposited to the ProteomeXchange Consortium via the PRIDE[12] partner repository with the dataset identifier PXD016229.

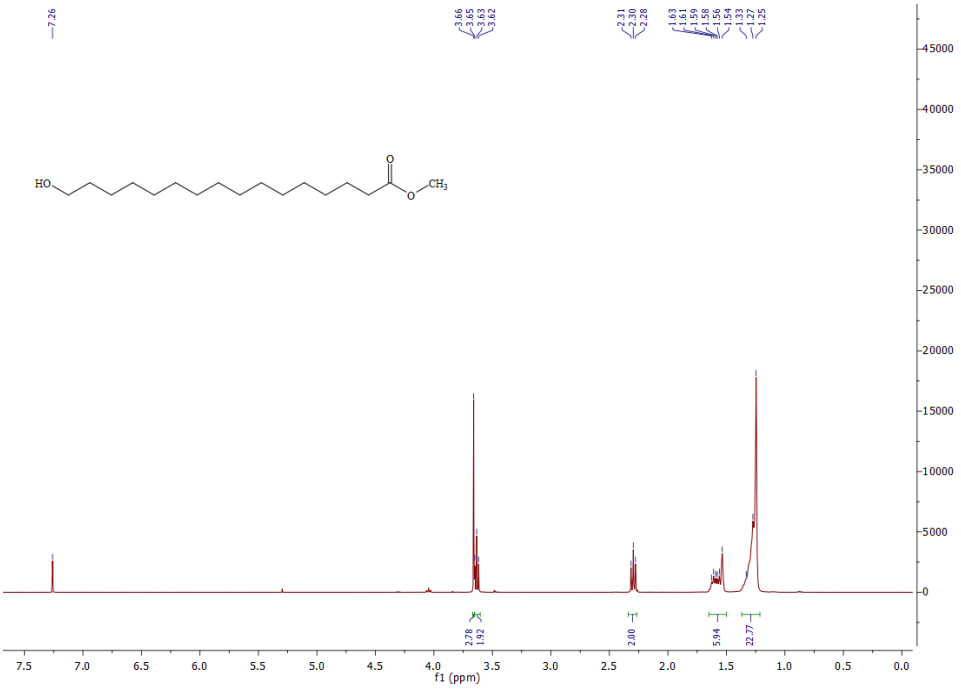
3. NMR and MS spectra

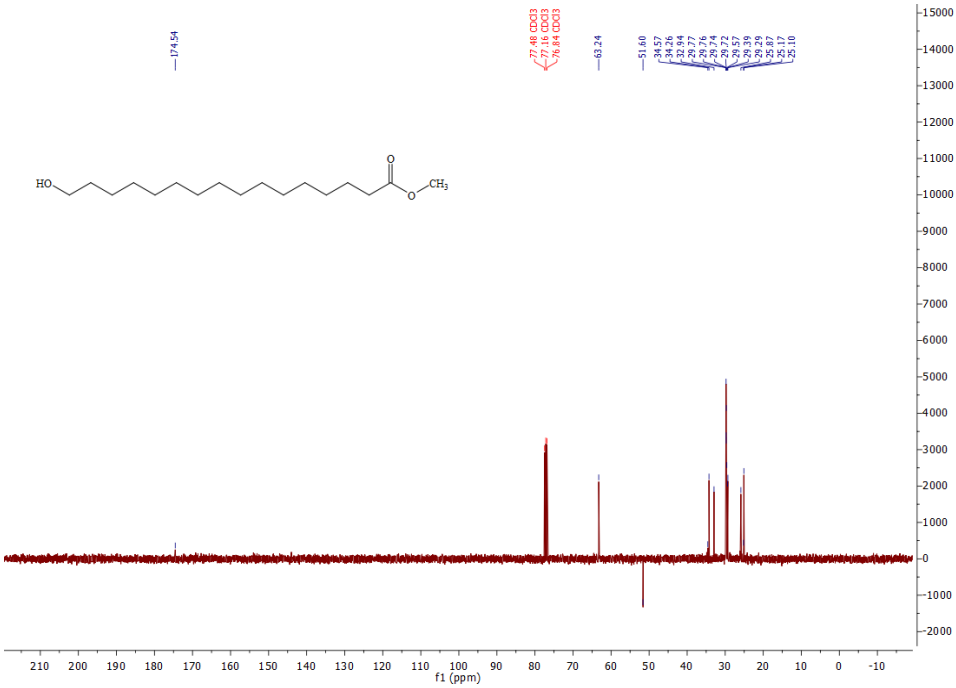


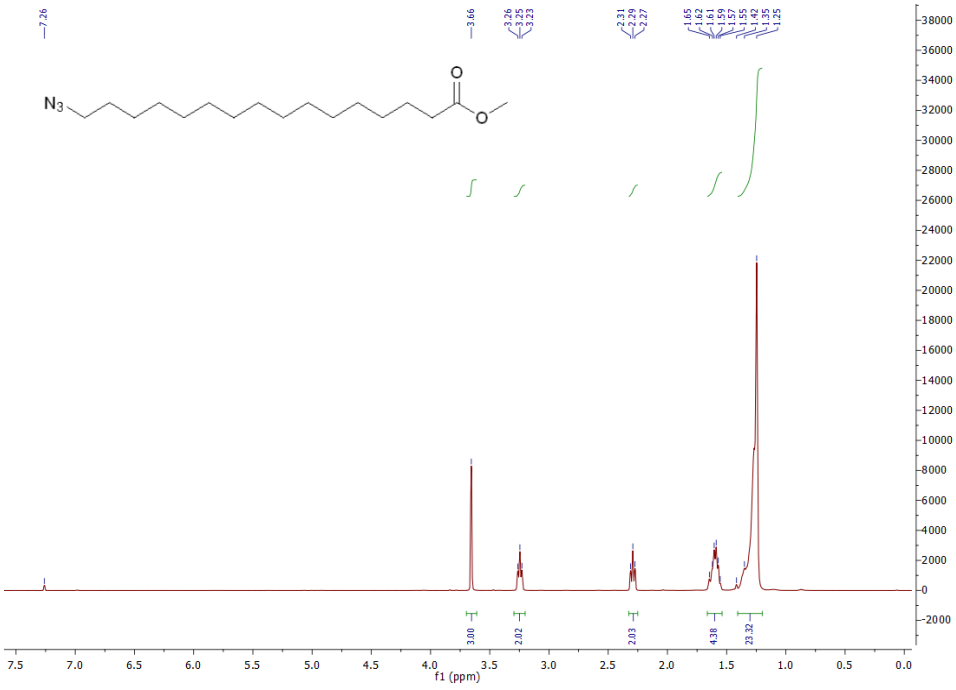

145.17
133.61
130.04
128.88
125.37
77.48 CDCl3
77.16 CDCl3
76.84 CDCl3
65.23
34.27
21.78
19.88
f1 (ppm)

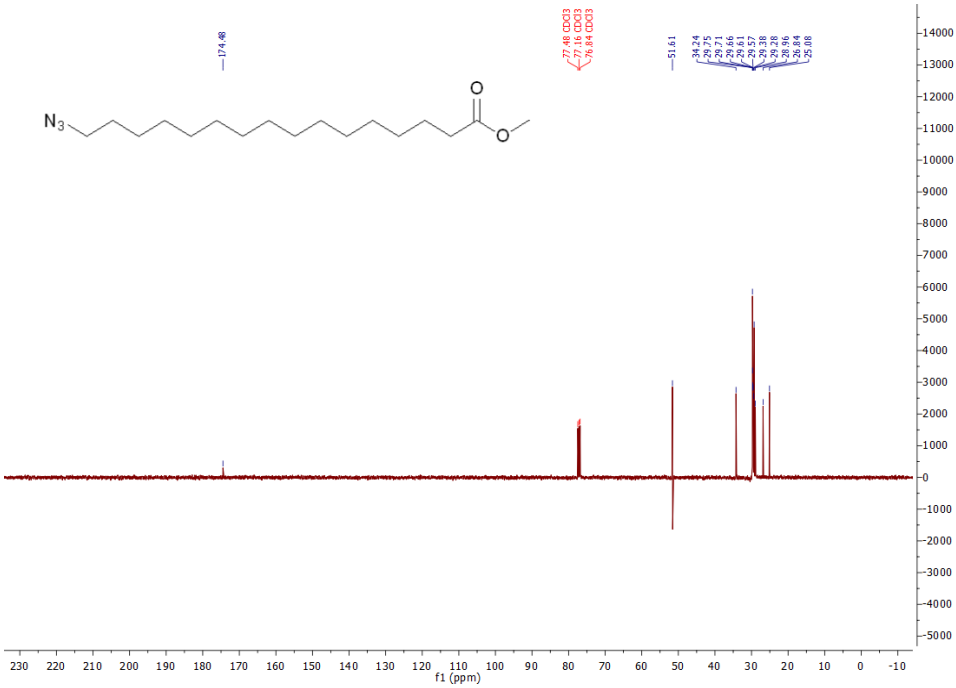

7.72
7.72
7.71
7.70
7.26
7.24
4.89
3.96
3.95
3.94
3.94
3.93
3.49
3.48
3.47
3.46
3.45
3.43
3.42
3.42
3.41
3.40
3.31
3.31
3.30
3.16
3.11
3.07
2.88
2.38
1.86
1.85
1.84
1.83
1.82
1.07
2.00
1.99
1.92
1.65
1.44
4.49
3.00
1.64
2.15
f1 (ppm)

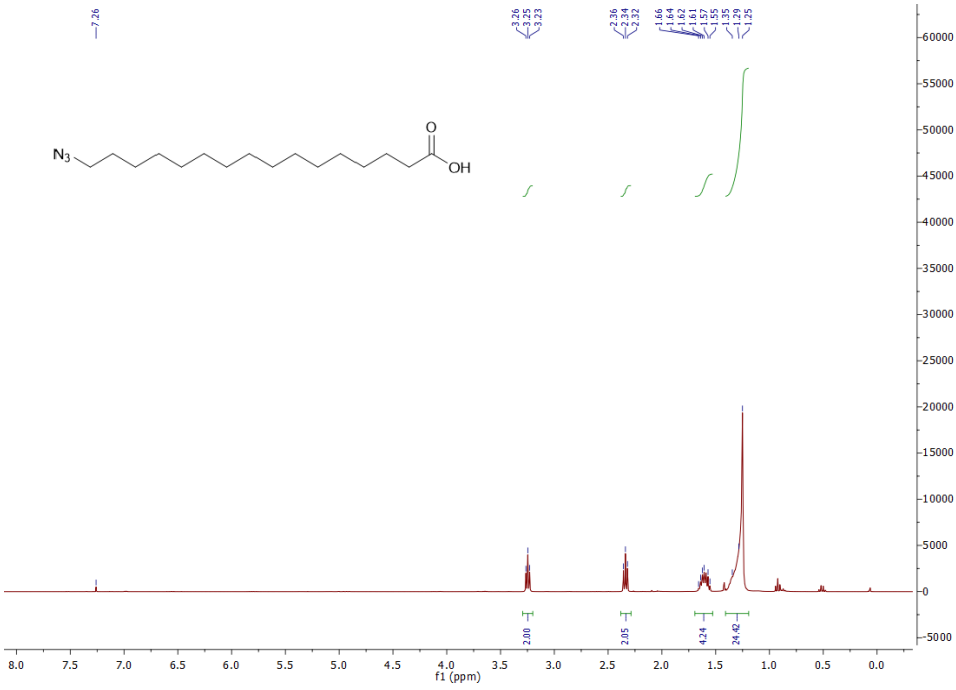

141.73
129.87
126.93
66.43
63.33
56.81
52.33
52.29
51.25
49.64
49.43
49.21
49.00
48.79
48.57
48.36
29.28
21.31
19.35
HO
H_3C
CH_3
N
CH_3
N=N
O
O=S=O
CH_3
f1 (ppm)

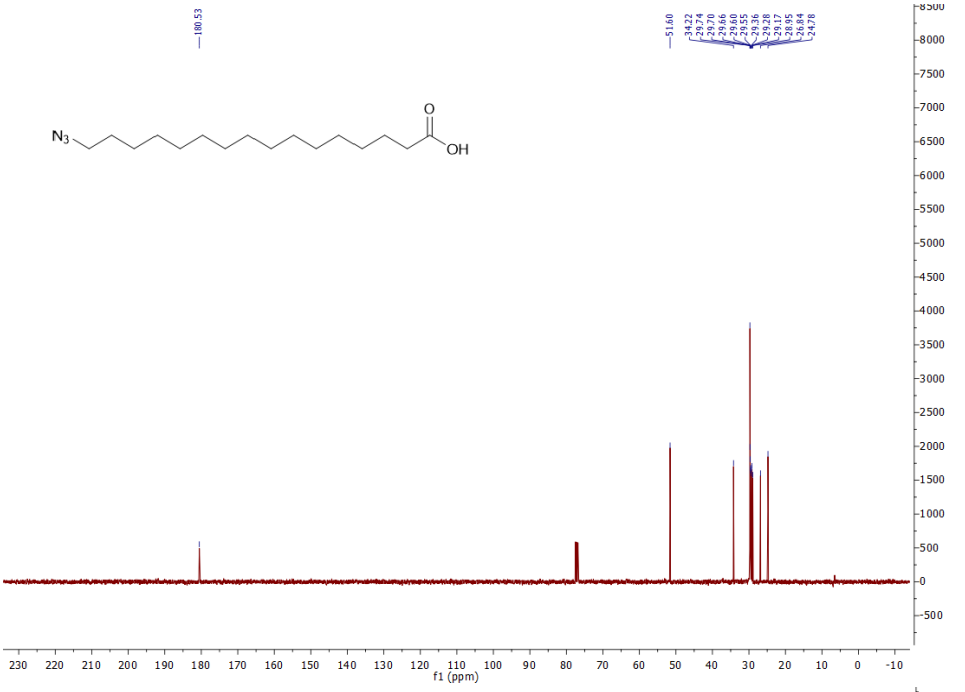

7.26
3.66
3.65
3.63
3.62
2.31
2.30
2.28
1.63
1.61
1.59
1.58
1.56
1.54
1.33
1.27
1.25
HO
O
O
CH_3
2.78
1.92
2.00
5.94
22.77
f1 (ppm)

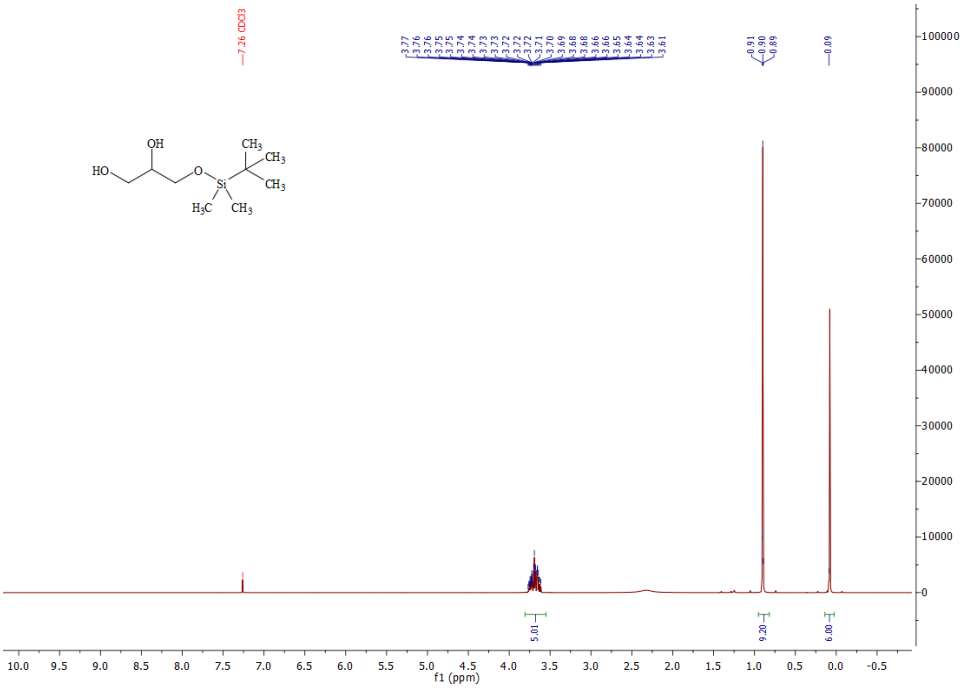

174.54
77.48 CDCl3
77.16 CDCl3
76.84 CDCl3
63.24
51.60
34.57
34.26
32.94
32.77
29.76
29.74
29.72
29.57
29.38
29.29
25.87
25.17
25.10
HO
O
O
CH3
f1 (ppm)

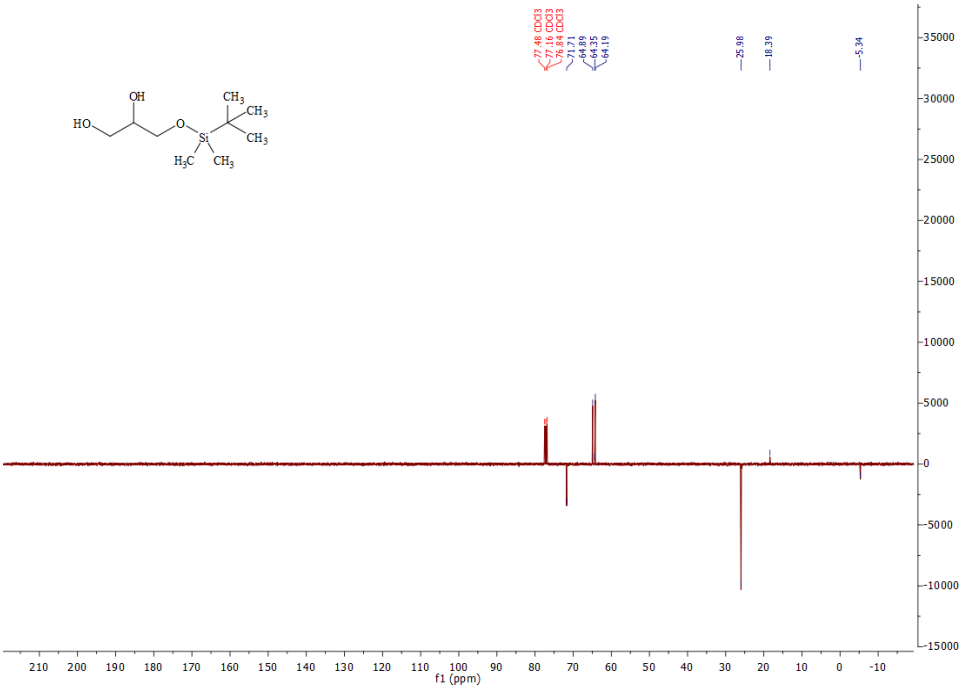

7.26
3.66
3.26
3.25
3.23
2.31
2.29
2.27
1.65
1.62
1.61
1.59
1.57
1.55
1.42
1.35
1.25
N3
O
O
3.00
2.02
2.03
4.38
23.32
f1 (ppm)

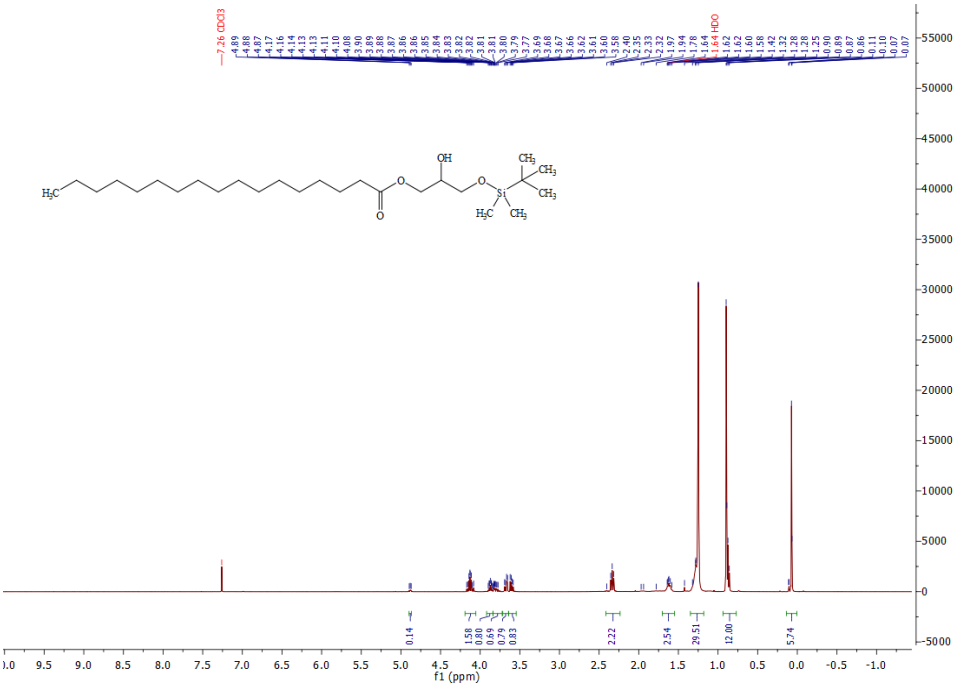

174.48
77.48 CDCl3
77.16 CDCl3
76.84 CDCl3
51.61
34.24
30.75
29.71
29.66
29.61
29.57
29.38
29.28
28.96
26.84
25.08
O
O
N3
f1 (ppm)

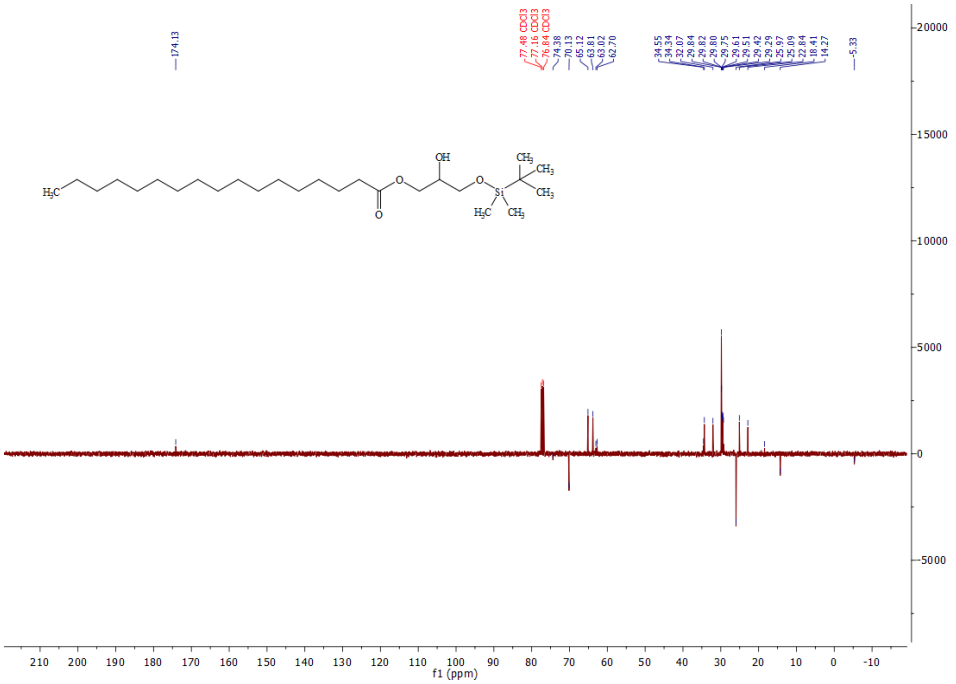

7.26
3.26
3.25
3.23
2.36
2.34
2.32
1.66
1.64
1.62
1.61
1.57
1.55
1.35
1.29
1.25
O
OH
N3
2.00
2.05
4.24
24.42
f1 (ppm)

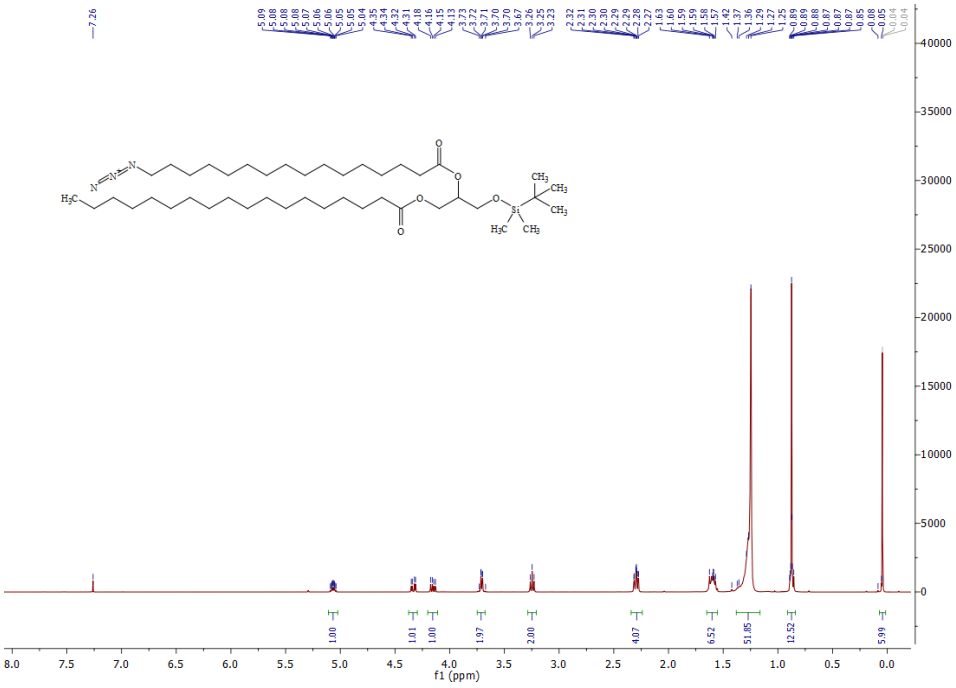

180.53
51.60
34.22
29.74
29.70
29.66
29.60
29.55
29.36
29.28
29.17
28.95
26.84
24.78
N3
O
OH
f1 (ppm)

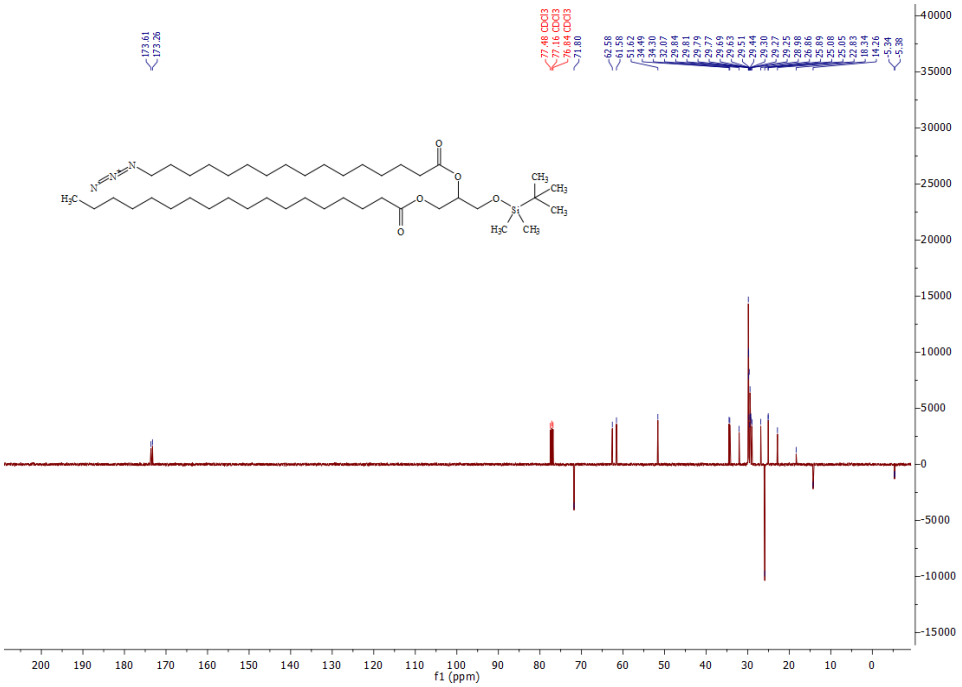

7.26 CDCl3
3.77
3.76
3.76
3.75
3.75
3.74
3.74
3.73
3.73
3.72
3.72
3.72
3.71
3.70
3.69
3.68
3.68
3.66
3.66
3.65
3.64
3.64
3.63
3.61
0.91
0.90
0.89
0.09
OH
HO
O
Si
CH3
CH3
CH3
H3C
CH3
5.01
9.20
6.00
f1 (ppm)

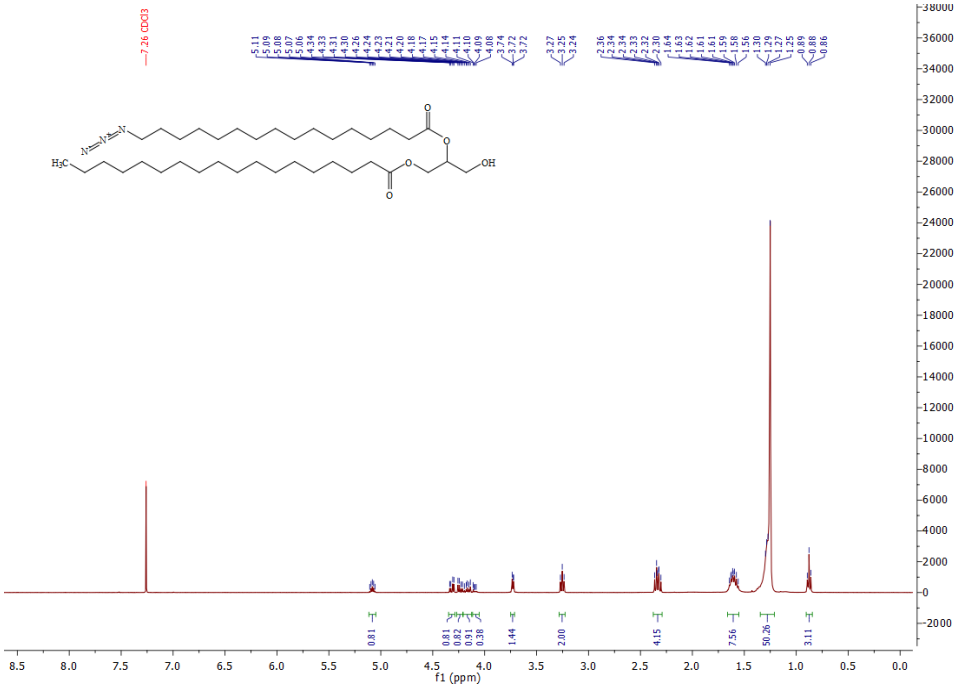

77.48 CDCl3
77.16 CDCl3
76.84 CDCl3
71.71
64.89
64.55
64.19
25.98
18.39
-5.34
f1 (ppm)

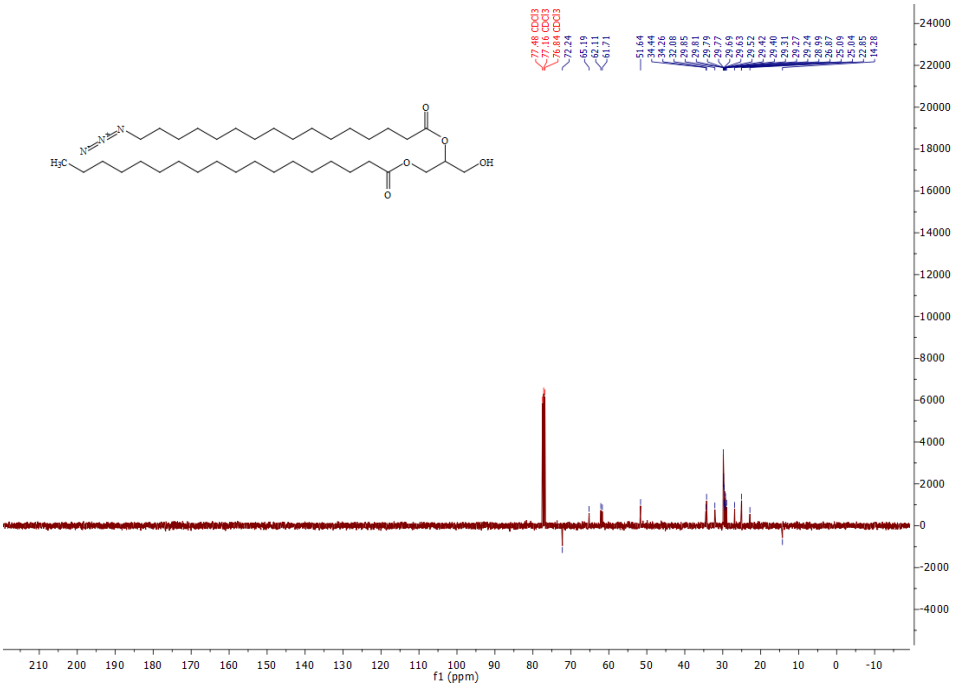

7.26 CDCl3
1.64 HDO
0.14
1.58
0.80
0.69
0.79
0.83
2.22
2.54
29.51
12.00
5.74
f1 (ppm)

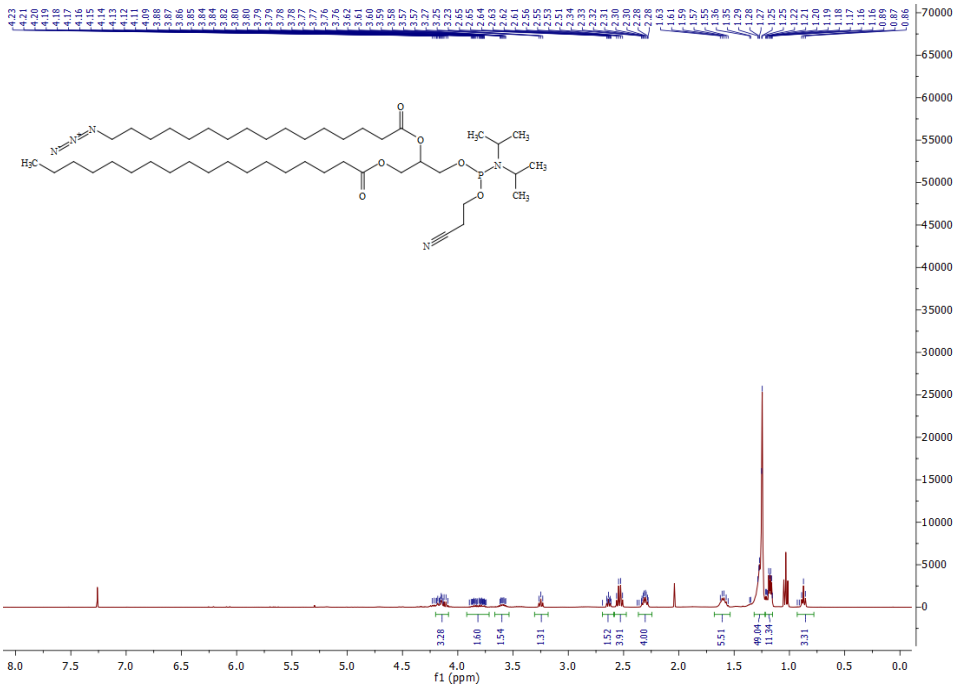

174.13
77.48 CDCl3
77.16 CDCl3
76.84 CDCl3
74.38
70.13
65.12
63.81
63.02
62.70
34.55
34.34
32.07
29.84
29.82
29.80
29.75
29.61
29.51
29.42
29.29
25.97
25.69
22.84
18.41
14.27
-5.33
OH
CH3
CH3
CH3
H3C
CH3
Si
O
O
O
H3C
f1 (ppm)

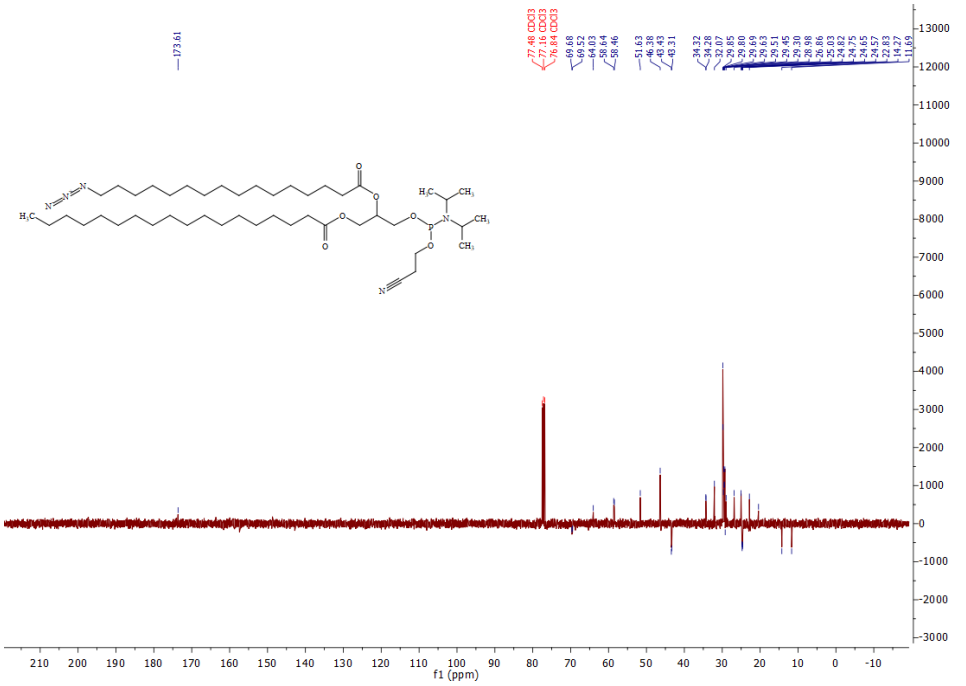

7.26
5.09
5.08
5.08
5.08
5.07
5.06
5.06
5.05
5.05
5.04
4.35
4.34
4.32
4.31
4.18
4.16
4.15
4.13
3.73
3.72
3.71
3.71
3.70
3.67
3.26
3.25
3.23
2.32
2.31
2.31
2.30
2.29
2.29
2.29
2.23
1.63
1.60
1.59
1.59
1.58
1.57
1.42
1.37
1.36
1.26
1.25
0.89
0.88
0.88
0.87
0.87
0.87
0.85
0.08
0.05
0.04
0.04
1.00
1.01
1.00
1.97
2.00
4.07
6.52
51.85
12.52
5.99
f1 (ppm)

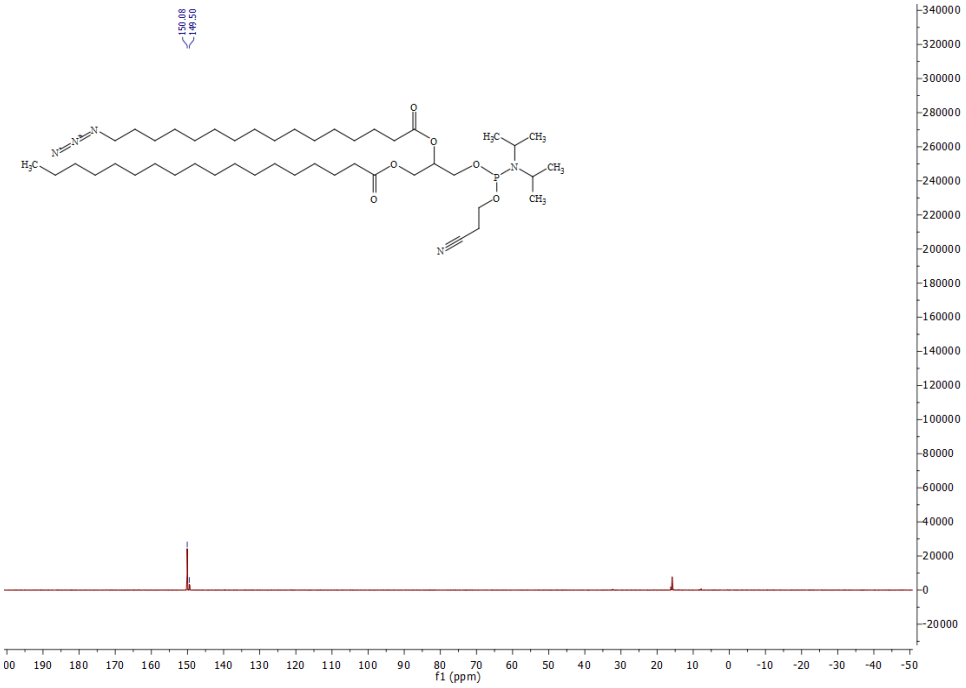

173.61
173.26
77.48 CDCl3
77.16 CDCl3
76.84 CDCl3
71.80
62.58
61.58
51.62
34.49
34.30
32.07
29.84
29.81
29.79
29.77
29.69
29.63
29.51
29.44
29.30
29.27
29.25
28.98
26.86
25.69
25.08
25.05
22.83
18.34
14.26
-5.34
-5.38
f1 (ppm)

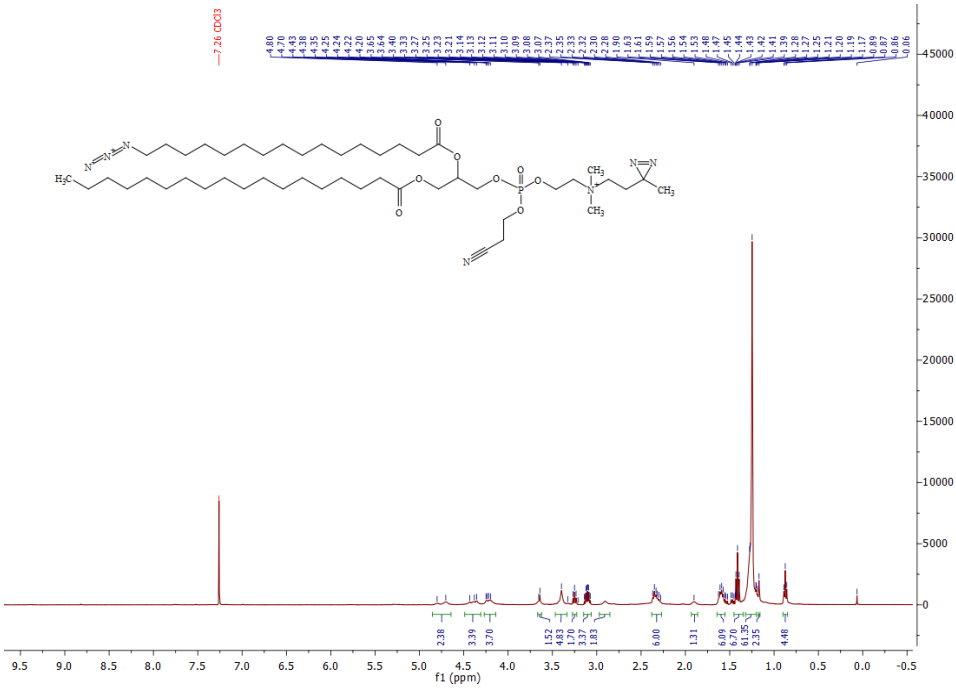

7.26 CDCl3
5.11
5.09
5.08
5.07
5.06
4.34
4.33
4.31
4.30
4.26
4.24
4.23
4.21
4.20
4.18
4.17
4.15
4.14
4.11
4.10
4.09
4.08
3.74
3.72
3.72
3.27
3.25
3.24
2.36
2.34
2.34
2.33
2.32
2.30
1.64
1.63
1.62
1.61
1.61
1.59
1.56
1.56
1.30
1.29
1.27
1.25
0.89
0.88
0.86
0.81
0.82
0.81
0.38
1.44
2.00
4.15
7.56
50.26
3.11
f1 (ppm)

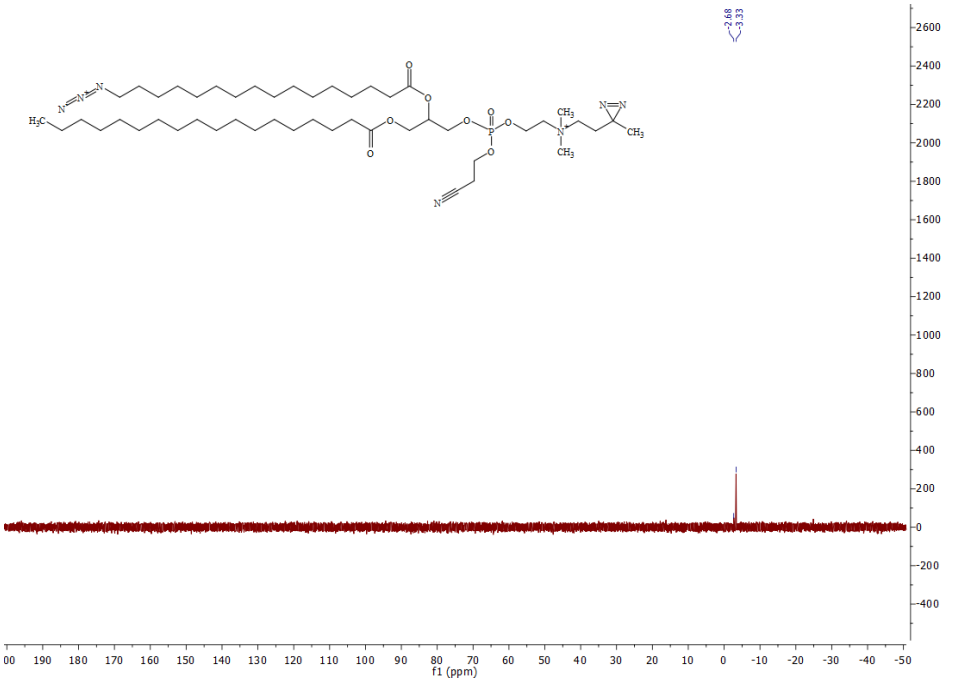

77.48 CDCl3
77.16 CDCl3
76.84 CDCl3
72.24
65.19
62.11
61.71
51.64
34.44
34.26
32.08
29.85
29.81
29.79
29.77
29.69
29.63
29.52
29.42
29.40
29.31
29.27
29.24
28.99
28.87
25.09
25.04
22.85
14.28
f1 (ppm)

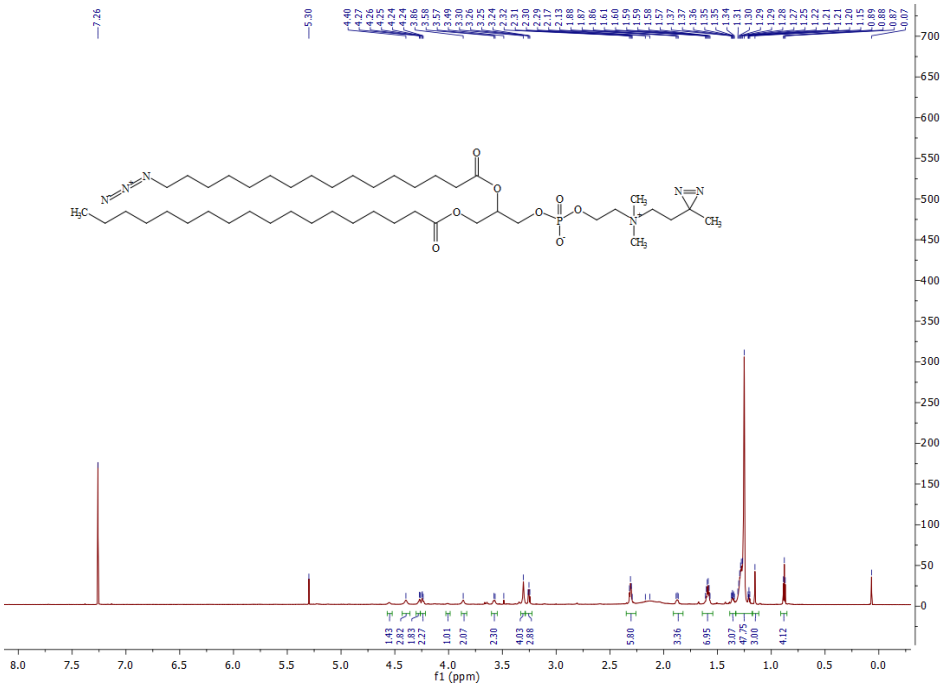

3.28
1.60
1.54
1.31
1.52
3.91
4.00
5.51
40.04
11.34
3.31
f1 (ppm)

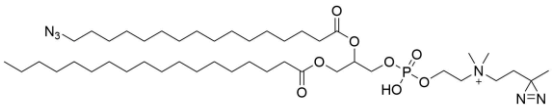

173.61
77.48 CDCl3
77.16 CDCl3
76.84 CDCl3
69.68
69.52
64.03
58.64
58.46
51.63
46.38
43.43
43.31
34.32
34.28
32.07
29.85
29.80
29.69
29.63
29.51
29.45
29.30
28.98
28.86
25.03
24.82
24.75
24.65
24.57
22.83
14.27
11.69
f1 (ppm)


150.08
149.50
f1 (ppm)

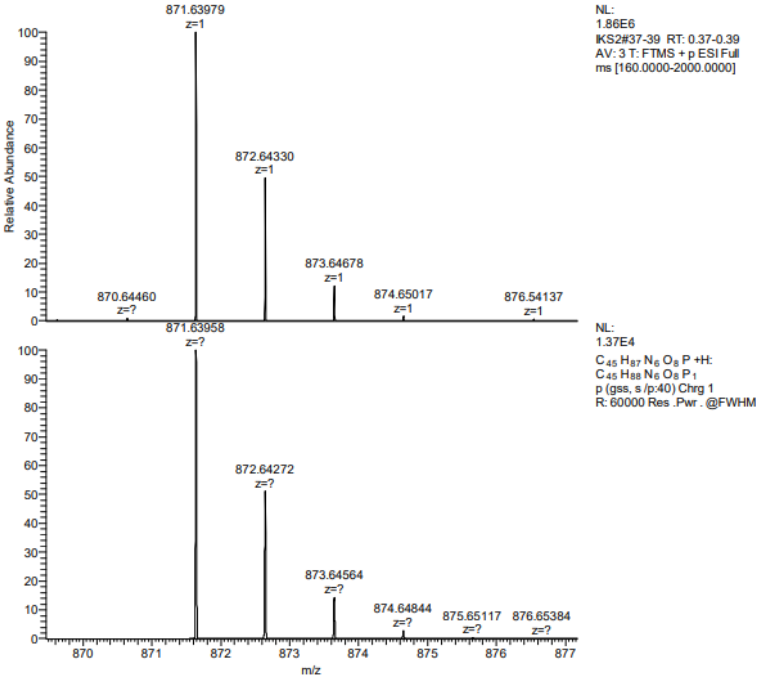

7.26 CDCl3
f1 (ppm)


2.68
3.33
f1 (ppm)


7.26
5.30
1.82
f1 (ppm)



Exact Mass: 871,64



4. References

1. Bulbake, U., Doppalapudi, S., Kommineni, N. & Khan, W. Liposomal Formulations in Clinical Use: An Updated Review. *Pharmaceutics* 9, 12 (2017).
2. Shen, K. *et al.* Diazirines as Potential Molecular Imaging Tags: Probing the Requirements for Efficient and Long-Lived SABRE-Induced Hyperpolarization. *Angew. Chemie Int. Ed.* 56, 12112–12116 (2017).
3. Heal, W. P. *et al.* Bioorthogonal chemical tagging of protein cholesterylation in living cells. *Chem. Commun.* 47, 4081–4083 (2011).
4. Wessel, D. & Flügge, U. I. A method for the quantitative recovery of protein in dilute solution in the presence of detergents and lipids. *Anal. Biochem.* 138, 141–143 (1984).
5. Bigdeli, A. *et al.* Exploring Cellular Interactions of Liposomes Using Protein Corona Fingerprints and Physicochemical Properties. *ACS Nano* 10, 3723–3737 (2016).
6. Capriotti, A. L. *et al.* Analysis of plasma protein adsorption onto DC-Chol-DOPE cationic liposomes by HPLC-CHIP coupled to a Q-TOF mass spectrometer. *Anal. Bioanal. Chem.* 398, 2895–2903 (2010).
7. Barrán-Berdón, A. L. *et al.* Time evolution of nanoparticle-protein corona in human plasma: Relevance for targeted drug delivery. *Langmuir* 29, 6485–6494 (2013).
8. Rappsilber, J., Mann, M. & Ishihama, Y. Protocol for micro-purification, enrichment, pre-fractionation and storage of peptides for proteomics using StageTips. *Nat. Protoc.* 2, 1896–1906 (2007).
9. van Rooden, E. J. *et al.* Mapping in vivo target interaction profiles of covalent inhibitors using chemical proteomics with label-free quantification. *Nat. Protoc.* 13, 752–767 (2018).
10. Distler, U., Kuharev, J., Navarro, P. & Tenzer, S. Label-free quantification in ion mobility-enhanced data-independent acquisition proteomics. *Nat. Protoc.* 11, 795–812 (2016).
11. Distler, U. *et al.* Drift time-specific collision energies enable deep-coverage data-independent acquisition proteomics. *Nat. Methods* 11, 167–170 (2014).
12. Vizcaíno, J. A. *et al.* The Proteomics Identifications (PRIDE) database and associated tools: status in 2013. *Nucleic Acids Res.* 41, D1063–D1069 (2012).

Appendix 2

Supplementary Information to Chapter 3

1. Supplementary Figures and Tables

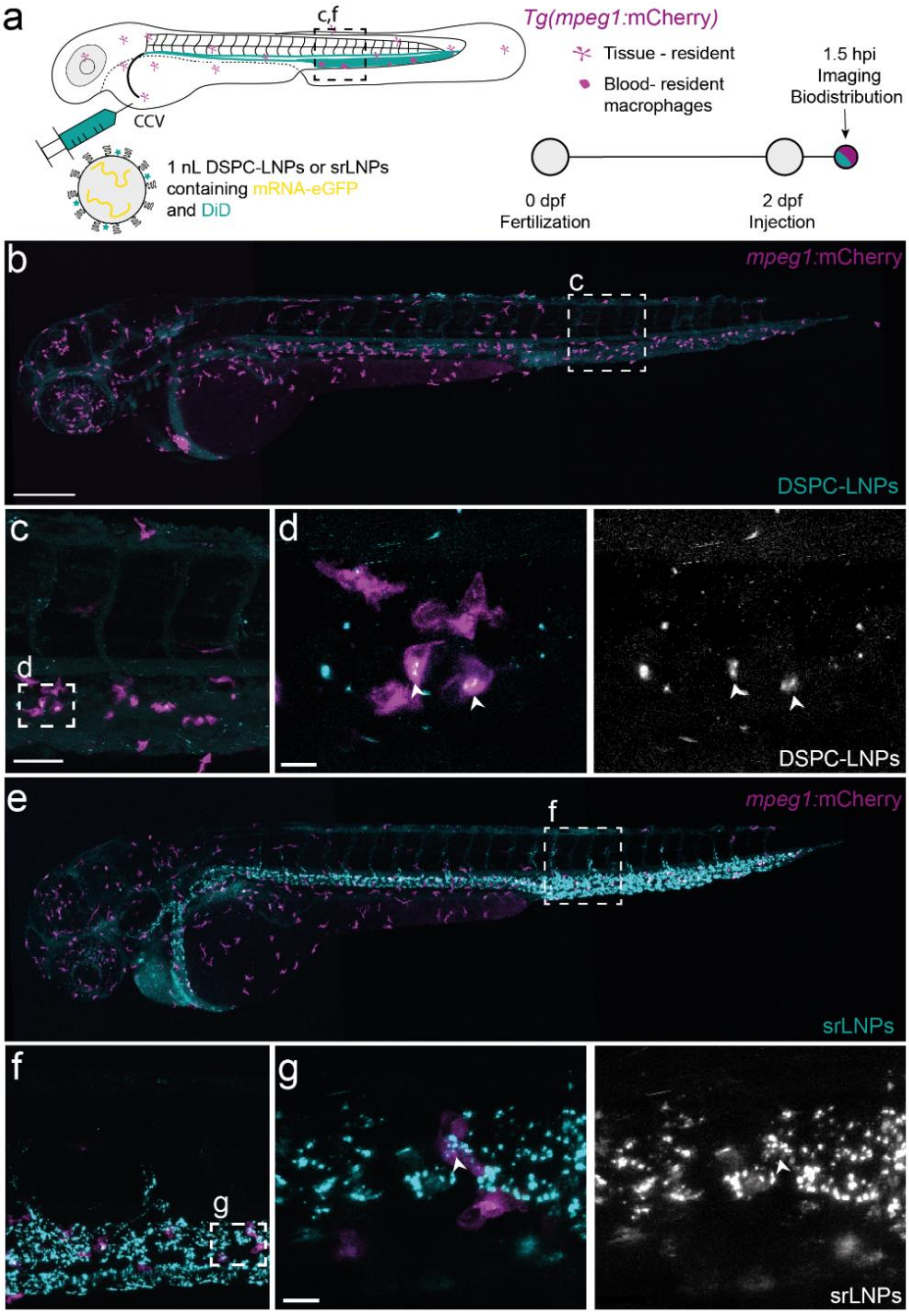


Figure S1. Biodistribution of DSPC-LNPs and srLNPs in *mpeg1:mCherry* transgenic zebrafish embryos at 1.5 hpi. (**a**) Schematic showing the site of LNP injection (*i.v*) within the embryonic zebrafish (2 dpf) and imaging timeframe. LNPs contained DiD (cy5, 0.1 mol%) as fluorescent lipid probe and unlabeled eGFP mRNA. Transgenic *mpeg1*:mCherry zebrafish embryos stably express mCherry (magenta) within all macrophages. *Injected dose*: ~10 mM lipid, ~0.2 mg/kg mRNA. *Injection volume*: 1 nL. CCV – common cardinal vein (**a**) Whole embryo view (10x magnification), (**b**) tissue level view (40x magnification), and (**c**) a zoom of a maximum projection of three confocal z-stacks, showing fluorescent co-localisation of DiD (LNP probe) and transgenic mCherry (white arrowheads), confirmed low-level DSPC-LNP uptake within blood resident macrophages. (**d**) Whole embryo view (10x magnification), (**e**) tissue level view (40x magnification) and (**f**) a zoom of a maximum projection of three confocal z-stacks, showing fluorescent co-localisation of DiD (LNP probe) and transgenic mCherry (white arrowheads), confirmed simultaneous uptake of srLNPs within both SECs and blood resident macrophages. Scale bars: 200 µm (whole body), 50 µm (tissue level), 10 µm (zoom).

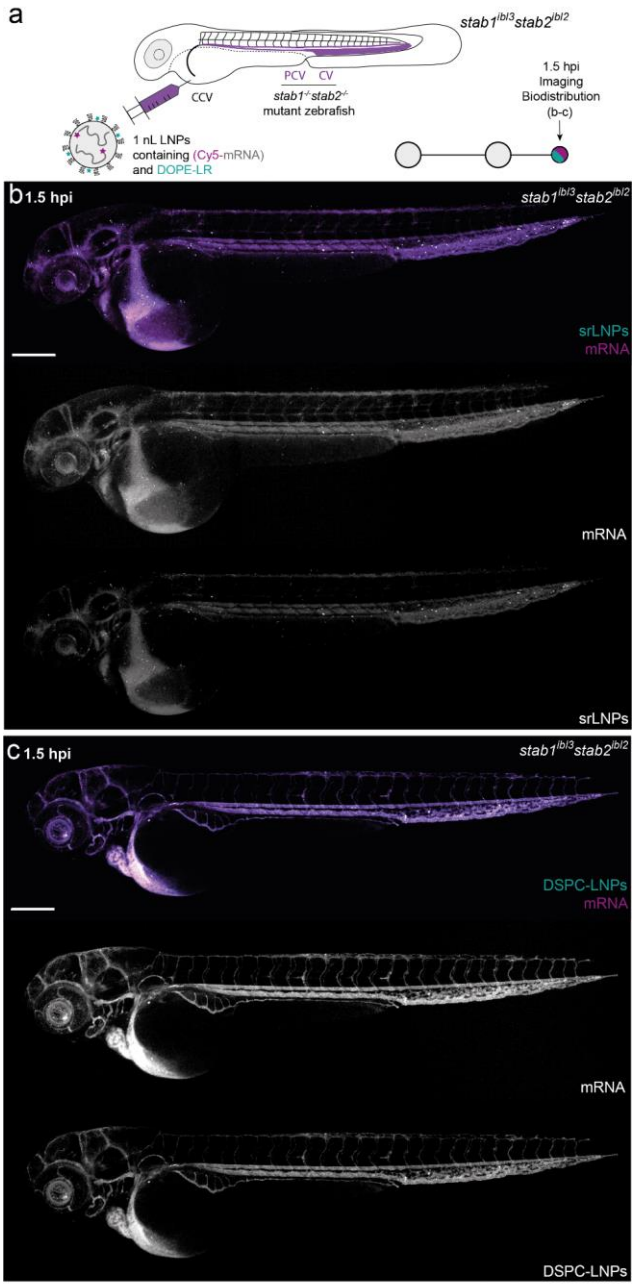


Figure S2. Biodistribution of srLNPs and DSPC-LNPs in double knock-out (*stab1*$^{-/-}$/*stab2*$^{-/-}$) mutant embryos at 1.5 hpi. (**a**) Schematic showing the site of LNP injection (*i.v.*) within double

knockout (*stab1*^{ibl3}/*stab2*^{ibl2})[1] zebrafish embryos (2 dpf) and imaging timeframe. LNPs contained DOPE-LR (cyan, 0.2 mol%) as fluorescent lipid probe and Cy5-labelled eGFP mRNA (magenta) as fluorescent mRNA probe. *Injected dose*: ~10 mM lipid, ~0.2 mg/kg mRNA. *Injection volume*: ~1 nL. CV – cardinal vein; PCV – posterior cardinal vein; CCV – common cardinal vein. (**b,c**) Whole embryo (10x magnification) views of srLNP and DSPC-LNP biodistribution within *stab1*$^{-/-}$/*stab2*$^{-/-}$ mutant embryos (2 dpf) at 1.5 hpi. In both cases, LNPs were mostly freely circulating throughout the vasculature of the embryo at 1.5 hpi. Scale bar: 200 µm.

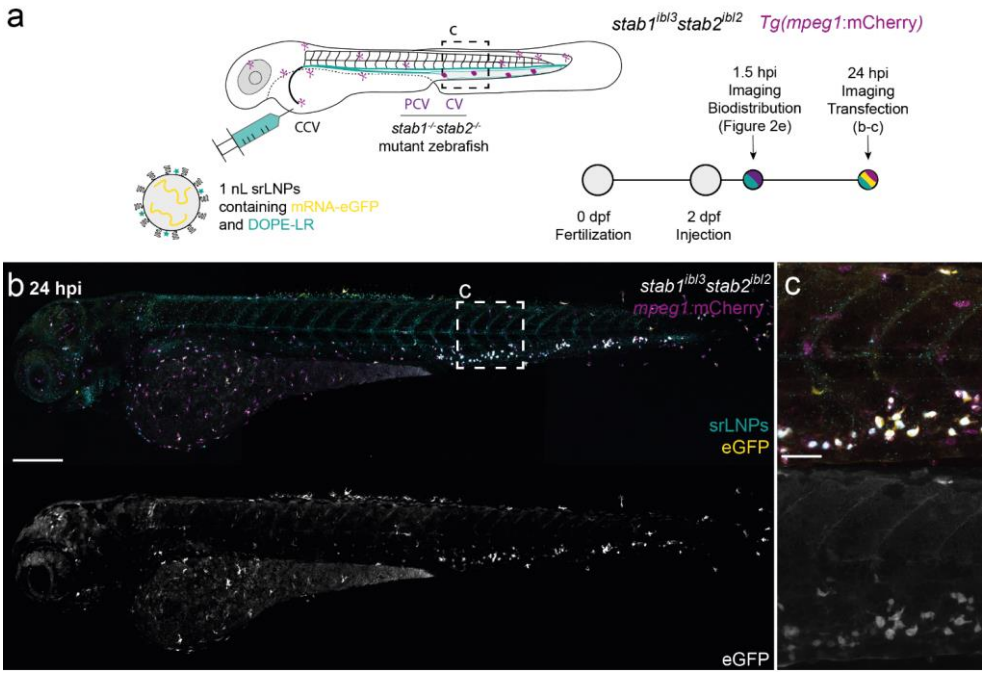


Figure S3. srLNP biodistribution and eGFP expression in double knock-out (*stab1*$^{-/-}$/*stab2*$^{-/-}$) mutant embryos at 24 hpi. (**a**) Schematic showing the site of LNP injection (*i.v.*) within transgenic *mpeg1*:mCherry, double knockout (*stab1*^{ibl3}/*stab2*^{ibl2})[1] zebrafish embryos (2 dpf) and imaging timeframe. LNPs contained DiD (cy5, 0.1 mol%, cyan) as fluorescent lipid probe and unlabeled eGFP mRNA. *Injected dose*: ~10 mM lipid, ~0.2 mg/kg mRNA. *Injection volume*: ~1 nL. CCV – common cardinal vein, CV – cardinal vein; PCV – posterior cardinal vein. (**b,c**) Whole embryo (10x magnification) and tissue level (40x magnification) views of srLNP biodistribution and eGFP expression within *stab1*$^{-/-}$/*stab2*$^{-/-}$ mutant embryos at 24 hpi. Within these embryos, srLNP localisation and eGFP expression is observed within blood resident macrophages (magenta) but not SECs at 24 hpi. Scale bars: 200 µm (whole embryo) and 50 µm (tissue level).

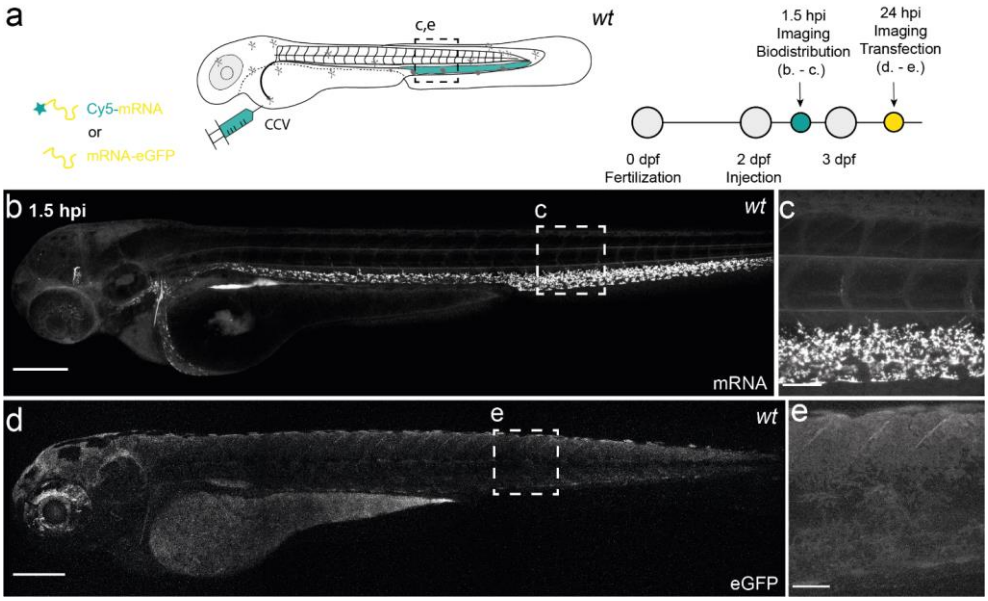


Figure S4. Biodistribution and expression of free eGFP mRNA in wildtype (AB/TL) embryonic zebrafish. (**a**) Schematic showing the site of free mRNA injection (*i.v.*; 0.2 mg/kg, 1 nL) within embryonic zebrafish (2 dpf) and imaging timeframe. CCV – common cardinal vein. (**b,c**) Whole embryo (10x magnification) and tissue level (40x magnification) views of free mRNA (Cy5-labelled) biodistribution at 1.5 hpi. Free mRNA primarily accumulated within SECs of the embryonic zebrafish at 1.5 hpi, likely mediated by Stabilin receptors.[2] Any phagocytotic uptake of free mRNA within blood resident macrophages cannot be clearly defined within the CHT of the wild-type embryo given the high fluorescence signal (Cy5) within overlapping SECs. (**d,e**) Whole embryo (10x magnification) and tissue level (40x magnification) views of eGFP expression (unlabeled mRNA) at 24 hpi. No significant eGFP expression is observed within SECs or blood resident macrophages of the embryonic fish. Scale bars: 200 µm (whole embryo) and 50 µm (tissue level).

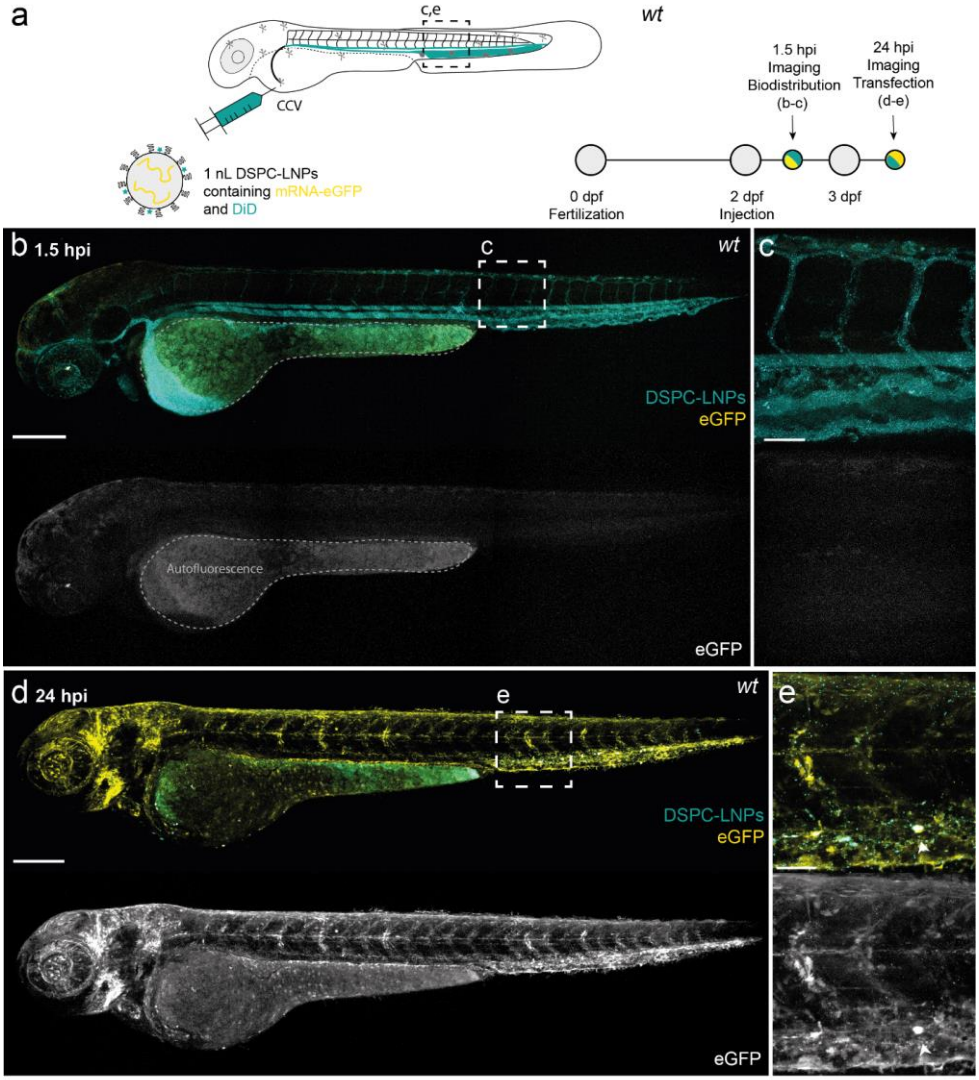


Figure S5. DSPC-LNP biodistribution and eGFP expression within wild-type (AB/TL) zebrafish embryos at 1.5 and 24 hpi. (**a**) Schematic showing the site of DSPC-LNP (*i.v.*) injection within embryonic zebrafish (2 dpf) and imaging timeframe. DSPC-LNPs contained DiD (Cy5, 0.1 mol%) as fluorescent lipid probe and unlabeled eGFP mRNA (capped) payload. *Injected dose*: ~10 mM lipid, ~0.2 mg/kg mRNA. *Injection volume*: ~1 nL. CCV – common cardinal vein. (**b,c**) Whole embryo (10x magnification) and tissue level (40x magnification) views of DSPC-LNP biodistribution and eGFP expression within the embryonic zebrafish at 1.5 hpi. DSPC-LNPs were mostly freely circulating, confined to and homogenously distributed throughout the vasculature of the embryo at 1.5 hpi. Low

level embryo autofluorescence (GFP channel) within the yolk sac and pigment cells of the embryo is highlighted. (**d,e**) Whole embryo and tissue level views of DSPC-LNP biodistribution and eGFP expression within the embryonic zebrafish at 24 hpi. Widespread eGFP expression throughout the embryo indicates non-specific uptake of DSPC-LNPs in many different cell types. eGFP expression within macrophages (based on location and morphology) highlighted with white arrowheads. Scale bars: 200 µm (whole embryo) and 50 µm (tissue level).

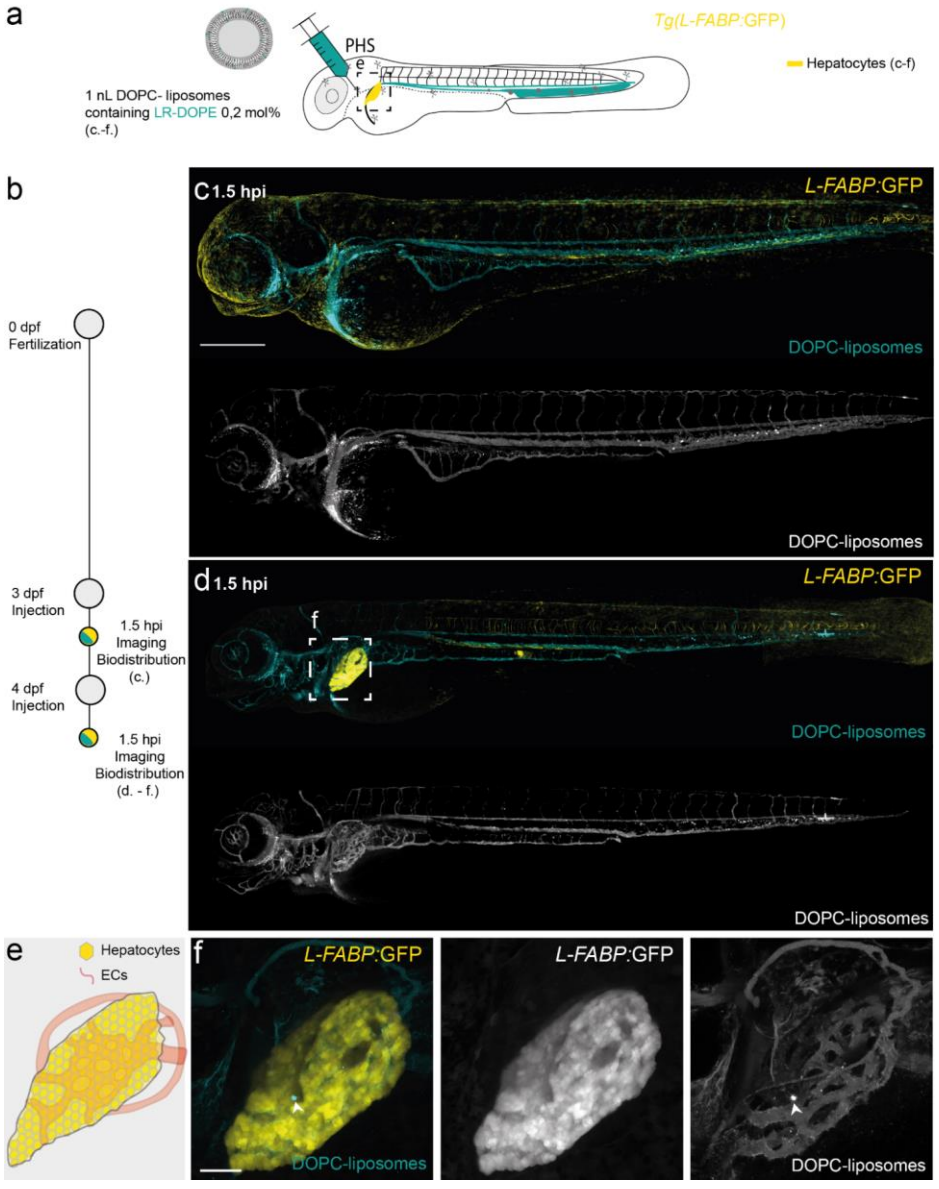


Figure S6. DOPC liposome biodistribution in *L-FABP:eGFP* transgenic zebrafish embryos (3 and 4 dpf) at 1.5 hpi. (**a**) Schematic showing the site of liposome injection (*i.v.*) within embryonic zebrafish (3 or 4 dpf). Liposomes contained 0.2 mol% DOPE-lissamine rhodamine as fluorescent lipid probe (cyan). *Injected dose*: ~5 mM lipid. *Injection volume*: 1 nL. Transgenic *L-FABP*:eGFP zebrafish embryos stably express eGFP (yellow) in hepatocytes. PHS – primary head sinus. (**b**) Injection and imaging timeframe. (**c,d**) Whole embryo (10x magnification) views of DOPC liposome biodistribution within the embryonic zebrafish (3 or 4 dpf) at 1.5 hpi. (**e**) Tissue level schematic of the embryonic liver at 4 dpf. (**f**) Tissue level (40x magnification) views of DOPC liposome biodistribution within the liver of a four-day old embryo. Liposomes freely circulate throughout the liver vasculature and do not associate with either ECs or hepatocytes of the embryonic liver. The single, intense fluorescent (DOPE-LR) punctum (white arrowhead) observed within the liver of the four-day old embryo is most likely due to macrophage uptake. Scale bars: 200 μm (whole embryo) and 50 μm (tissue level).

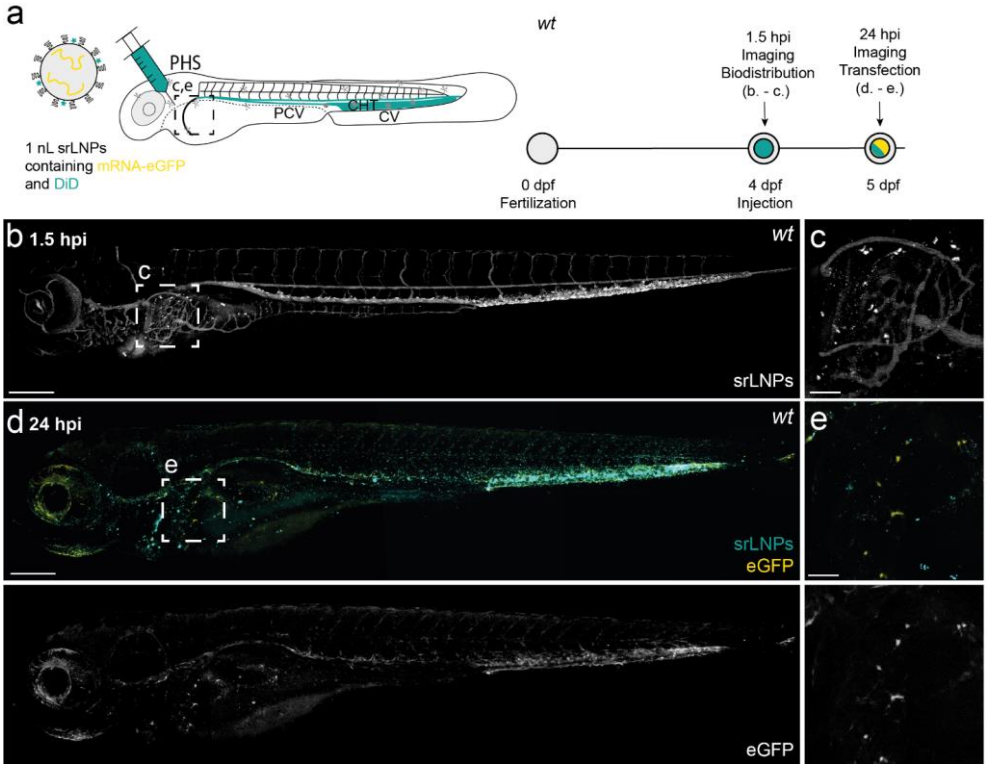
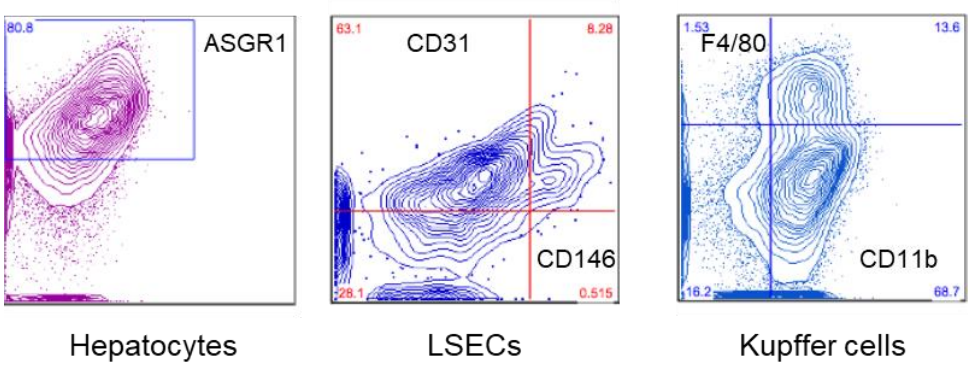


Figure S7. srLNP (30 mM) biodistribution and mRNA expression within wildtype (AB/TL) embryonic zebrafish. (**a**) Schematic showing the site of srLNP injection (*i.v.*) within embryonic zebrafish (4 dpf). srLNPs contained DiD (approx. 0.1 mol%) as fluorescent lipid probe and unlabeled, eGFP mRNA (capped) payload. Injection and imaging timeframe. *Injected dose*: ~10 mM lipid, ~0.2

mg/kg mRNA. *Injection volume*: 1 nL. PHS – primary head sinus. (**b,c**) Whole embryo (10x magnification) and tissue level (40x magnification, liver region) views of srLNP biodistribution (DiD, cyan) at 1.5 hpi. srLNPs were mainly associated with SECs within the PCV, CV and CHT of the four-day old embryo at 1.5 hpi. Due to the higher injected dosage, a significant fraction of srLNPs are also observed in circulation, possibly due to saturation of Stabilin receptors. Within the liver region, individual fluorescent punctae associated with srLNP accumulation are most likely due to macrophage uptake. (**d,e**) Whole embryo (10x magnification) and tissue level (40x magnification, liver region) views of srLNP biodistribution and eGFP expression within the embryonic zebrafish at 24 hpi. srLNPs remain predominantly localized within the PCV, CV and CHT at 24 hpi, with exogenous eGFP expression mainly restricted to this region of the five day-old embryo. Within the liver region, eGFP fluorescence is restricted to a handful of individual cells and does not evidently colocalize with srLNP-associated fluorescence (DiD). From these images, it is not clear whether eGFP fluorescence within the liver is due to macrophage uptake (possibly distal from the liver, and following macrophage migration), embryo autofluorescence or uptake within an alternative cell type. Scale bars: 200 µm (whole embryo) and 50 µm (tissue level).



Figures S8. Detection of major cell types in the liver microenvironment. Representative flow cytometry density plots illustrate the detection of specific hepatic cell types following liver perfusion and cell harvesting.

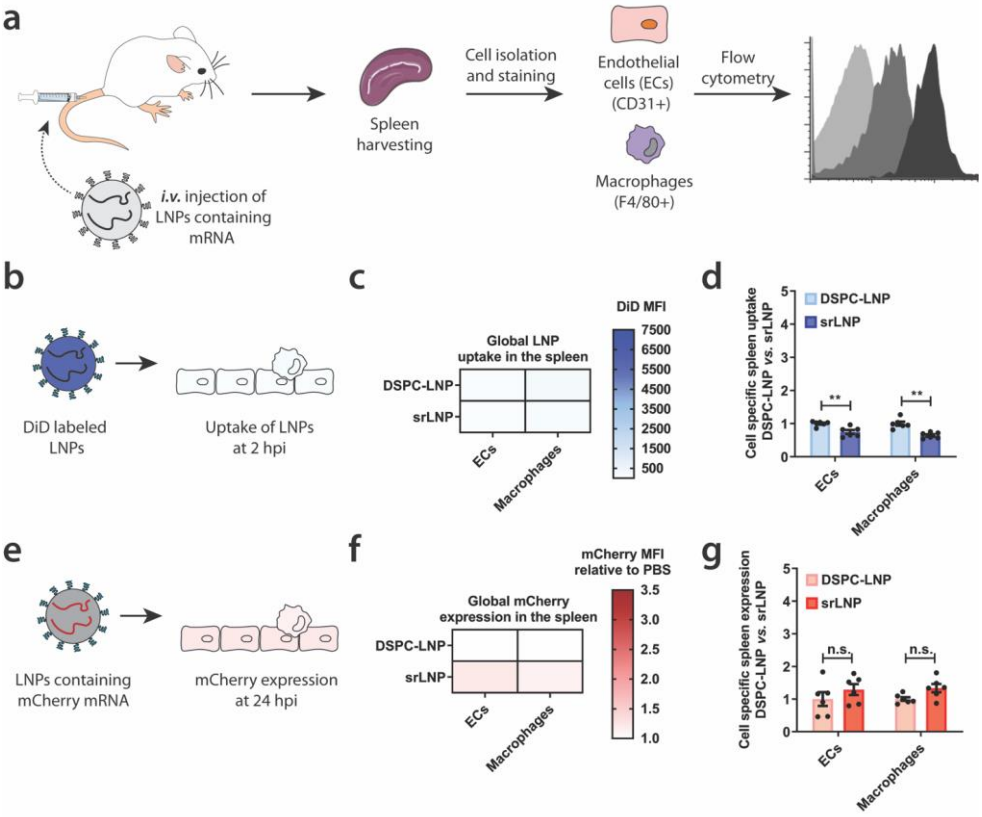


Figure S9. LNP uptake and functional mRNA delivery within different splenic cell types. (**a**) Schematic illustrating the procedure to isolate different splenic cell types and determine LNP-mRNA targeting and functional mRNA delivery. Following intravenous LNP injection (*i.v.*), splenic cells were isolated and stained with specific antibodies (in parentheses), and flow cytometry used to analyze LNP uptake or gene expression. (**b**) For biodistribution studies, LNPs contained DiD (0.5 mol%) as fluorescent probe. Cellular uptake of DSPC-LNP and srLNP was assessed 2 hpi. *Injected dose*: 42.75 mg/kg total lipid. (**c**) Heatmap of global LNP uptake in the spleen determined by absolute DiD fluorescence. (**d**) Cell specific spleen uptake normalized to DSPC-LNP for each cell type. (**e**) For gene expression experiments, LNPs contained mCherry-mRNA. Functional mRNA delivery was assessed based on mCherry reporter gene expression levels at 24 hpi. (**f**) Heatmap of mCherry expression in different spleen cell types using DSPC-LNP or srLNP. *Injected dose:* 0.25 mg/kg mRNA. srLNP show no significant mCherry expression compared to DSPC-LNP in splenic RES cells. (**g**) Cell specific mCherry expression normalized to DSPC-LNP for each cell type. In all cases, n = 6 represents 3 separate spleen tissue samples from 2 mice sorted into individual cell types. Bars and error bars in c represent mean ± s.e.m. The data was normalized to the average expression of DSPC-LNPs within each cell type. Statistical significance was evaluated using a two-tailed unpaired Student's t-test. n.s.=

not significant, ** p < 0.01, *** p < 0.001. Exact P values for d: ECs P= 0.0039, Macrophages P= 0.0011. Exact P values for g: ECs P= 0.308, Macrophages P= 0.074.

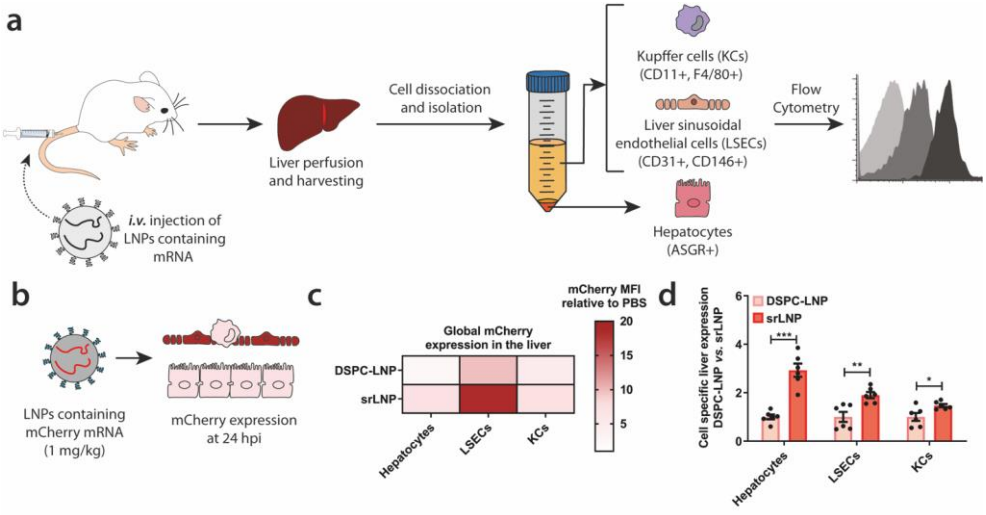


Figure S10. Functional mCherry mRNA delivery to hepatic RES cell types at an injected mRNA dose of 1 mg/kg. (**a**) Schematic illustrating the procedure to isolate different hepatic cell types and determine LNP-mRNA targeting and functional mRNA delivery. Following intravenous LNP injection (*i.v.*) the liver was perfused with collagenase IV, hepatic cells were isolated and stained with specific antibodies, and flow cytometry was used to analyze LNP uptake and gene expression. Specific antibody markers used to uniquely identify hepatocytes, LSECs and KCs, respectively, are defined in parentheses. (**b**) LNPs contained mCherry-mRNA. Functional mRNA delivery was assessed based on mCherry reporter gene expression levels at 24 hpi. (**c**) Heatmap of mCherry expression in different liver cell types enabled by mRNA delivery using DSPC-LNP and srLNP. *Injected dose:* 1 mg/kg mRNA. srLNPs led to enhanced gene expression in hepatic RES cells, predominantly in LSECs. (**d**) Cell specific mCherry expression normalized to DSPC-LNP for each cell type. In all cases, n = 6 represents 3 separate liver tissue samples from 2 mice sorted into individual cell types. Bars and error bars in c and e represent mean ± s.e.m. Statistical significance was evaluated using a two-tailed unpaired Student's t-test. * p < 0.05, ** p < 0.01, *** p < 0.001. Exact P values for d: Hepatocytes P= 0.00018, LSECs P= 0.0083, KCs P= 0.025

Formulation	mRNA	Fluorescent lipid	% of Fluorescent Lipid	Avg. Size (nm)	PDI	Zeta Potential (mV)	EE (%)	n
DSPC-LNP	eGFP	DOPE-LR	0.2	82.5 ± 2.0	0.085 ± 0.027	-5.5 ± 1.2	95 ± 2	3
srLNP	eGFP	DOPE-LR	0.2	89.2 ± 5.7	0.094 ± 0.023	-21.9 ± 2.5	88 ± 3	3
DSPC-LNP	eGFP	DiD	0.1	82.5 ± 3.4	0.081 ± 0.026	-4.1 ± 1.6	95 ± 1	3
srLNP	eGFP	DiD	0.1	94.7 ± 4.0	0.102 ± 0.016	-17.5 ± 2.4	91 ± 2	3
DSPC-LNP	eGFP	-	-	82.5 ± 4.0	0.103 ± 0.037	-4.0 ± 0.9	93 ± 1	2
srLNP	eGFP	-	-	86.6 ± 6.7	0.108 ± 0.006	-19.0 ± 1.1	91 ± 4	2
DSPC-LNP	mCherry	DiD	0.1	79.9 ± 5.2	0.072 ± 0.038	-3.7 ± 1.8	94 ± 3	2
srLNP	mCherry	DiD	0.1	92.7 ± 3.5	0.102 ± 0.012	-18.8 ± 2.1	89 ± 4	2
DSPC-LNP	Cy5-mRNA	DOPE-LR	0.2	87.0 ± 3.5	0.090 ± 0.016	-3.9 ± 0.9	95 ± 3	2
srLNP	Cy5-mRNA	DOPE-LR	0.2	94.1 ± 2.3	0.096 ± 0.01	-16.2 ± 1.2	91 ± 2	2
DOPC	-	DOPE-LR	0.2	96.3 ± 4.0	0.095 ± 0.011	-6.1 ± 1.1	-	2
DOPC+ApoE-peptide	-	DOPE-LR	0.2	104.7 ± 3.8	0.075 ± 0.012	14.7 ± 1.6	-	2

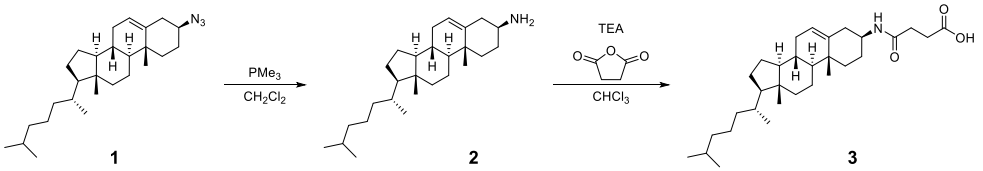
Table S1. Composition, size (as measured by DLS), polydispersity (PDI), surface charge (as measured by zeta potential), RNA encapsulation efficiency (as measured by RiboGreen assay) and reproducibility of all LNP and liposome formulations used in this study.

2. Materials and Methods

Reagents

Dimethylformamide (DMF), piperidine, acetic anhydride, pyridine, trifluoroacetic acid (TFA) and acetonitrile (MeCN) were purchased from Biosolve (Valkenswaard, The Netherlands). N,N-diisopropylethylamine (DIPEA), and Oxyma were obtained from Carl Roth GmbH & Co (Karlsruhe, Germany). Dichloromethane (DCM) and diethyl ether were supplied by Honeywell (Amsterdam, The Netherlands). Fmoc-Rink Amide AM resin was obtained from IRIS Biotech GmbH (Marktredwitz, Germany). All amino acids were supplied by NovaBioChem, (Zwijndrecht, The Netherlands), a subsidiary of Merck. 1,2-distearoyl-*sn*-glycerol-3-phosphocholine (DSPC), 1,2-distearoyl-*sn*-glycero-3-phospho-(1′-rac-glycerol) (DSPG), 1,2-dioleyl-*sn*-glycerol-3-phosphocholine (DOPC) and 1,2-dimyristoyl-rac-glycero-3-methoxypolyethylene glycol-2000 (DMG-PEG2k) were purchased from Avanti Polar Lipids (Alabaster, USA) or Lipoid GmbH (Ludwigshafen, Germany). All other chemicals were purchased from Merck (Zwijndrecht, The Netherlands). (6Z,9Z,28Z,31Z)-heptatriaconta-6,9,28,31-tetraen-19-yl-4-(dimethylamino) butanoate (DLin-MC3-DMA) was synthesized as described.[3] 3-azido-5-cholestene (1) was synthesized as described.[4] CleanCap eGFP (5moU) mRNA, CleanCap mCherry (5moU) mRNA and CleanCap Cyanine 5 eGFP (5moU) mRNA were purchased from TriLink Biotechnologies (San Diego, USA) or Tebu-bio (Heerhugowaard, The Netherlands).

Synthesis of N-succinyl-3-amino-5-cholestene (3)[5]



3-azido-5-cholestene (**1**, 1240 mg, 3 mmol) was dissolved in 30 mL dry DCM and the flask placed under a nitrogen atmosphere. A 1M solution of trimethylphosphine (12 mL, 12 mmol, 4 eq.) in toluene was added and the mixture was stirred for 21 hours. The reaction was quenched by the addition of 25 mL 1M sodium hydroxide solution, followed by vigorous stirring for 30 minutes. The mixture was transferred to a separating funnel, organic phase collected and the aqueous phase further extracted with 25 mL dichloromethane. The organic phases were combined and washed with 100 mL water (2x), 100 mL brine, and the organic phase dried over anhydrous magnesium sulfate. After concentration *in vacuo,* the resulting white powder was dried under high vacuum overnight to yield cholesteryl-amine (**2**) in quantitative yield.

Cholesteryl-amine **2** (440 mg, 1.14 mmol) was combined with succinic anhydride (342 mg, 3.4 mmol, 2.98 eq.) in 30 mL $CHCl_3$ and warmed to dissolve the mixture. Triethylamine (315 µL, 2,3 mmol, 2 eq.) was then added and the solution stirred for 16 hours. The reaction mixture was then washed with 50 mL 5% acetic acid solution in water (2x), 50 mL water (2x), 50 mL brine, and the organic phase dried over anhydrous magnesium sulfate. The mixture was concentrated *in vacuo* and filtered through a silica gel plug (eluent; 1:1 dichloromethane/ethyl acetate + 1% acetic acid). Concentration *in vacuo* yielded cholesteryl-4-amino-4-oxobutanoic acid (**3**) as a white powder (408 mg, 0.84 mmol, 74%).

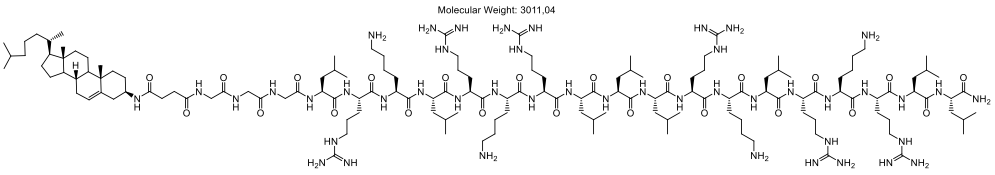
^{1}H NMR (400 MHz, DMSO): δ 12.05 (s, 1H), 7.76 (d, *J* = 7.8 Hz, 1H), 5.34 – 5.20 (m, 1H), 3.45 – 3.38 (m, 1H), 2.39 (t, *J* = 6.9 Hz, 2H), 2.26 (t, *J* = 6.9 Hz, 2H), 2.09 (d, *J* = 8.2 Hz, 2H), 2.00 – 1.86 (m, 2H), 1.80 (d, *J* = 12.3 Hz, 2H), 1.65 – 1.27 (m, 13H), 1.16 – 0.78 (m, 24H), 0.65 (s, 3H).

Peptide synthesis

Solid-phase peptide synthesis was performed at a 0.1 mmol scale with Fmoc-Rink Amide AM resin (0.64 mmol/g) on a Liberty Blue™ Automated Microwave Peptide Synthesizer. Fmoc-deprotection was achieved using 20% piperidine in DMF, and coupling reactions using DIC as activator and Oxyma as base. The final Fmoc-group was deprotected and the

resin was washed with DMF (3x) and DCM (3x) respectively and stored at 4 °C prior to further use.

Chol-NH-ApoE_peptide synthesis and purification



4
Chol-NH-GGG-LRKLRKRLLLRKLRKRLL
Chol-NH-apoE-peptide

To the synthesized peptide on solid support (0.025 mmol) in a fritted syringe was added cholesteryl-4-amino-4-oxobutanoic acid (**3**, 0.1 mmol, 4 eq.), HATU (0.1 mmol, 4 eq.), DIPEA (0.5 mmol, 20 eq.) and dimethylformamide (5 mL) and the mixture agitated overnight at room temperature. The liquids were filtered from the resin and the resin was washed with dimethylformamide (3 x 5 mL) and dichloromethane (3 x 5 mL). Cleavage from the resin was performed by the addition of a mixture of TFA : TIPS : water (95 : 2.5 : 2.5 vol%, 5 mL) and agitation at room temperature for 2 hours. The reaction was precipitated using ice-cold diethyl ether (45 mL) and the precipitate was collected by centrifugation (3000 *g*, 30 min), suspended in water and lyophilized. Purification was performed by reversed-phase HPLC on a Kinetic® Evo C18 column (5 µm, 100 Å, 150 mm x 21.2 mm) with a Shimadzu system comprising two LC-8A pumps and an SPD-10AVP UV-vis detector (operating at 220 nm). The cholesterol peptide-conjugate was purified using a gradient of 30–90% B, (where B is MeCN containing 0.1% TFA, and A is water with 0.1% TFA) over 20 minutes with a flow rate of 10 ml min^{-1}, eluting at 11.3-12.0 minutes. The collected fractions were analyzed using LC-MS, pooled and freeze-dried. LC-MS was performed on a Kinetic® Biphenyl column (2.6 µm, 100 Å, 100 mm x 4.6 mm) using a Thermo Scientific™ Dionex™ Ultimate 3000 UHPLC (with a UV-VIS detector operating at 220 nm) coupled to a TSQ Quantum access MAX electron spray ionization (ESI) mass spectrometer operating with a ionization range of 140-2000 Da. Identification was performed using a gradient of 30–90% B, (where B is MeCN containing 0.1% TFA, and A is water with 0.1% TFA) over 13 minutes with a flow rate of 1 ml min^{-1}. Calculated mass: $[M+H]^+$ = 1506.0 Da ; $[M+2H]^{2+}$ = 1004.3 Da, Detected mass: $[M+H]^+$ = 1505.44 Da $[M+2H]^{2+}$ = 1003.1 Da.

Liposome Formulation

DOPC liposomes (with and without incorporated Chol-NH-ApoE-peptide, 5 mol%) were formulated in 20 mM HEPES buffer (pH = 7.3) at a total lipid concentration of 5 mM. DOPC and Chol-NH-ApoE-peptide, as stock solutions in chloroform (10 mM), were combined to the desired molar ratios and dried to a film, first under a stream of N_2 followed by the removal of trace solvents *in vacuo* for >1 h. Lipid films were hydrated and large unilamellar vesicles formed through extrusion at room temperature (Mini-extruder, Avanti Polar Lipids, Alabaster, US). Hydrated lipids were passed 11 times through a 100 nm polycarbonate (PC) membrane (Nucleopore Track-Etch membranes, Whatman). All liposome formulations were stored at 4°C and used within 2 days.

Lipid Nanoparticle (LNP) Formulation

Lipid nanoparticles entrapping mRNA were formulated as previously described.[6] In brief, lipid components (MC3, cholesterol, DSPC or DSPG, and PEG-lipid) were dissolved in ethanol. For biodistribution studies, the non-exchangeable tracer DiD or DOPE-LR was added to lipid mixtures at a concentration of 0.1 mol% or 0.2 mol% respectively. The mRNA was dissolved in 25 mM sodium acetate or sodium citrate buffer (pH 4). The two solution were rapidly mixed (N/P ratio of 6) using a T-junction mixer (total flow rate of 20 mL/min, flow rate ratio of 3:1 v/v). The resulting LNP formulation was dialyzed overnight against PBS (pH 7.4), sterile filtered, and concentrated using 10K MWCO centrifugal filters (Amicon® Ultra, Merck). Entrapment efficiency and mRNA concentration were analyzed using the Quant-iT Ribogreen RNA assay (Life Technologies, Burlington, ON). Total lipid concentrations were measured using the Cholesterol E Total-Cholesterol assay (Wako Diagnostics, Richmond, VA). mRNA doses within embryonic zebrafish were calculated using an estimated average weight of 1 mg per embryo, independent of developmental stage, and an injection volume of 1 nL.

LNP and liposome biophysical characterization

LNP and liposome sizes and zeta potentials were measured using a Malvern Zetasizer Nano ZS (software version 7.13, Malvern Panalytical). For DLS (operating wavelength = 633 nm), measurements were carried out at room temperature in 20 mM HEPES buffer (pH = 7.3) for liposomes, and in 1x PBS (pH = 7.4) for LNPs, at a total lipid concentration of approx. 100 µM. Zeta potentials were measured at 500 µM total lipid concentration, using a dip-cell electrode (ZEN1002, Malvern) for liposomes and in a folded capillary cell (DTS1070,

Malvern) for LNPs, at room temperature. All reported DLS measurements and zeta potentials are the average of three measurements.

Cryo-electron Microscopy Imaging and Quantification

Vitrification of concentrated (~10 mM) LNPs was performed using a Leica EM GP operating at 21°C and 95% humidity. Sample suspensions were placed on glow discharged 100 µm lacey carbon films supported by 200 mesh copper grids (Electron Microscopy Sciences). Optimal results were achieved using a 60 second pre-blot and a 1 second blot time. After vitrification, sample grids were maintained below –170 °C and imaging was performed on a Tecnai T12 (ThermoFisher) with a biotwin lens and LaB6 filament operating at 120 keV equipped with an Eagle 4K x 4K CCD camera (ThermoFisher). Images were acquired at a nominal underfocus of -2 to -3 µm (49,000× magnification) with an electron dose of ~2000 e^{-}·nm^{-2}. Images were processed and particle size was quantified using the Fiji distribution of ImageJ.[7] For quantification, particle sizes were determined on particles present in amorphous vitrified water and obtained from a triplicate of assemblies (~150-200 particles per assembly per formulation). Generation of frequency distribution graphs was performed using GraphPad Prism (v 6.0).

Zebrafish Husbandry and Injections

Zebrafish (*Danio rerio*, strain AB/TL) were maintained and handled according to the guidelines from the Zebrafish Model Organism Database (http://zfin.org) and in compliance with the directives of the local animal welfare committee of Leiden University. Fertilization was performed by natural spawning at the beginning of the light period, and eggs were raised at 28.5 °C in egg water (60 µg/ mL Instant Ocean sea salts). In addition to wild-type (AB/TL) embryos, previously established *Tg*(*mpeg1:mCherry*)^{gl23} [8] and *stab2*^{ibl2}*stab1*^{ibl3} [1] zebrafish lines were also used in this study. Fluorescently labelled LNPs or liposomes were injected into 54-96 hours post fertilization (hpf) zebrafish embryos using a modified microangraphy protocol.[9] Embryos were anesthetized in 0.01% tricaine and embedded in 0.4% agarose containing tricaine before injection. To improve reproducibility of microangiography experiments, 1 nL volume were calibrated and injected into the common cardinal vein (2-3 dpf) or primary head sinus (4 dpf). A small injection space was created by penetrating the skin with the injection needle and gently pulling the needle back, thereby creating a small pyramidal space in which the liposomes or LNPs were injected. Successfully injected embryos were identified through the backward translocation of venous erythrocytes and the absence of damage to the yolk ball. Selected zebrafish embryos

successfully injected were kept in egg water at 28.5 degrees until later imaging (1.5 or 24 hours post injection, hpi).

Zebrafish confocal imaging acquisition and processing

Zebrafish embryos were randomly picked from a dish of 10-30 successfully injected embryos to be imaged after 1.5 or 24 hpi. Confocal z-stacks were captured on a Leica TCS SPE or SP8 confocal microscope, using a 10x air objective (HCX PL FLUOTAR), a 40x water-immersion objective (HCX APO L) or 63x water-immersion objective (HC PL APO CS). For whole-embryo views, 3 or 4 overlapping z-stacks were captured to cover the complete embryo. Laser intensity, gain and offset settings were identical between stacks and when comparing samples per experiment. Images were processed using the Fiji distribution of ImageJ.[7] Confocal image stacks (raw data) are available upon reasonable request.

Mouse husbandry, injection protocol and cell isolation

All mouse protocols were approved by the Canadian Animal Care Committee and conducted in accordance with relevant guidelines and regulations. Mice were maintained on a regular 12-hour light/12- hour dark cycle in a specific pathogen-free animal facility at UBC. C57Bl6 male mice aged between 8 to 10 weeks were used throughout. These mice were divided into groups of 2 and either received intravenous (*i.v*) injection of LNP-mRNAs (either DSPC-LNPs or srLNPs) or PBS as a negative control. For biodistribution studies, LNPs entrapping luciferase mRNA were labelled with 0.5 mol% DiD as fluorescent lipid marker. Injections were performed at 42.75 mg/kg total lipid and mice were sacrificed at 2 hpi. For gene expression studies, LNPs encapsulating mRNA coding for the fluorescent reporter gene mCherry were used, injections were performed at 0.25 mg/kg mRNA dose, and mice were sacrificed at 24 hpi. Mice were anesthetized using a high dose of isofluorane followed by CO_2. Trans-cardiac perfusion was performed as follows: once the animals were unresponsive, a 5 cm medial incision was made through the abdominal wall, exposing the liver and heart. While the heart was still beating, a butterfly needle connected to a 30 mL syringe loaded with pre-warmed Hank's Balanced Salt Solution (HBSS, Gibco) was inserted into the left ventricle. Next, the liver was perfused with perfusion medium (HBSS, supplemented with 0.5 mM EDTA, Glucose 10mM and HEPES 10mM) at a rate of 3 mL/min for 10 min. Once liver swelling was observed, a cut was performed on the right atrium and perfusion was switched to digestion medium (DMEM, Gibco supplemented with 10% fetal bovine serum (FBS, Gibco) and 1% penicillin streptomycin (Gibco) and 0.8 mg/mL Collagenase Type IV, Worthington) at 3 mL/min for another 10 min. At the end of the

perfusion of the entire system, as determined by organ blanching, the whole liver and spleen were dissected and transferred to 50 mL Falcon tubes containing 10 mL ice cold (4°C) perfusion media and placed on ice. Next, isolation of hepatic cell types (*i.e.* hepatocytes, Kupffer cells (KCs) and liver sinusoid endothelial cells (LSECs)) was performed following density gradient-based separation. Briefly, the liver was transferred to a Petri dish containing digestion medium, minced under sterile conditions, and incubated for 20 min at 37°C with occasional shaking of the plate. Cell suspensions were then filtered through a 40 µm mesh cell strainer to eliminate any undigested tissue remnants. Primary hepatocytes were separated from other liver residing cells (LRCs) by low-speed centrifugation at 500 rpm with no brake. The supernatant containing mainly LRCs was pelleted using low speed (3000 rpm) centrifugation at 4°C, aliquoted and washed twice with ice cold PBS containing 2% FBS. The pellet containing mainly hepatocytes was collected, washed at low speed and placed on ice. Phenotypic detection using monoclonal antibodies, assessment of LNP delivery and mRNA expression on cells liver cells was performed immediately after isolation to avoid changes in gene regulation, polarization and dedifferentiation.[10] LNP biodistribution across individual RES cell types of the spleen (*i.e.* endothelial cells and macrophages) were also characterized. Here, the spleen was also dissected and placed into a 40 µm mesh cell and mashed through the cell strainer into the petri dish using the plunger end of the syringe. The suspended cells were transferred to a 15 mL Falcon tube and centrifuged at 1000 rpm for 5 minutes. The pellet was resuspended in 1 mL ACK lysis buffer (Invitrogen) to lyse the red blood cells, aliquoted in FACS buffer and stained with antibodies as described below to identify splenic endothelial cells and macrophages.

FACS analysis

Cell aliquots were resuspended in 300 µL FACS staining buffer (FBS 2%, sodium azide 0.1% and ethylenediaminetetraacetic acid (EDTA 1mM)) followed by staining with fluorescence tagged antibodies. Prior to staining, cells were first labeled with anti-mouse CD16/CD32 (mouse Fc blocker, Clone 2.4G2) (AntibodyLab, Vancouver, Canada) to reduce background. Hepatocytes were identified following staining with primary mouse antibody detecting ASGR1 (8D7, Novus Biologicals) followed by goat polyclonal secondary antibody to mouse IgG2a labeled to PE-Cy7 (BioLegend). Kupffer cells were identified with CD11b – FITC or PE (Invitrogen) and F4/80high labeled to APC. LSECs were identified with CD146-VioBlue (Miltenyi Biotec) and CD31-PE-Cy7 (Abcam). Spleen macrophages and endothelial cells were detected using appropriate antibodies and identified as CD11bhigh and CD31+ve cells following antibody labeling as described. The data were acquired using a LSRII flow cytometer and the FACSDiva software and analyzed by FlowJo following acquisition of at

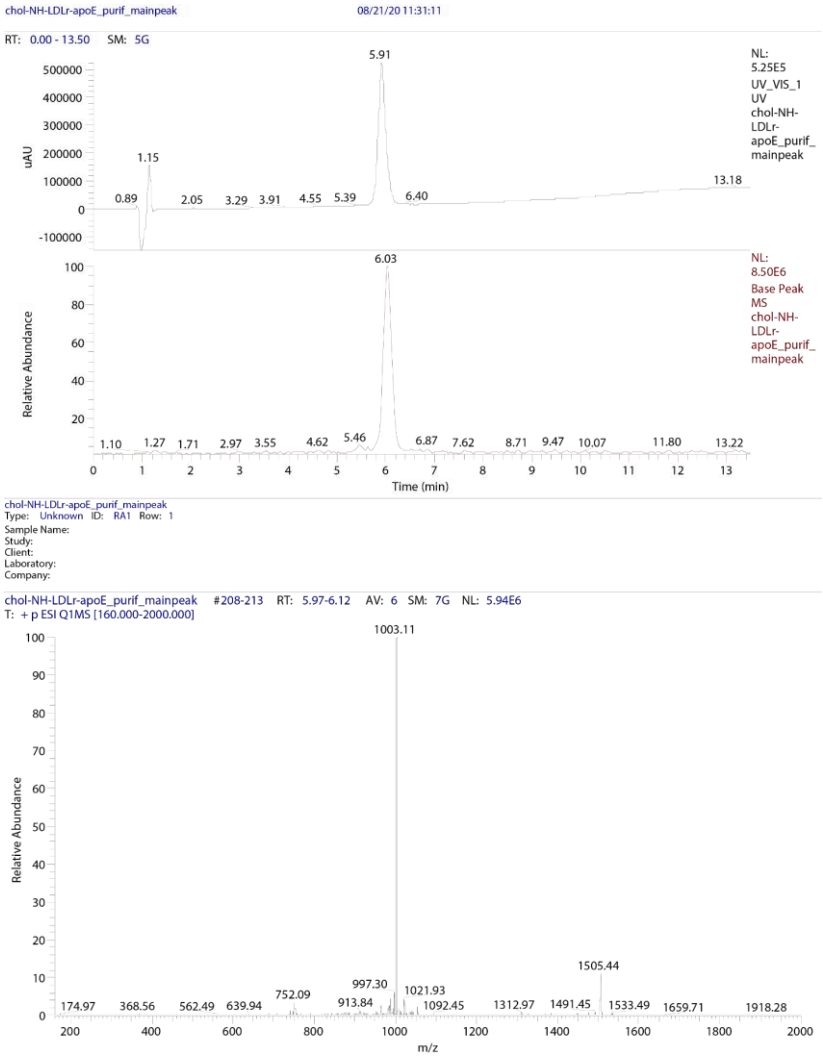
least 10,000 events after gating on viable cell populations. LNP-mRNA delivery or transfection efficacy were assessed based on the relative mean fluorescence intensity of DiD or mCherry positive cells, respectively, measured on histograms obtained from gated cell populations.

Statistics and Reproducibility

Frequency distributions for LNP size, derived from cryo-EM micrographs, and mean ± standard deviation was obtained using Prism (v8.1.1, GraphPad Software, Inc.). All zebrafish experiments were repeated at least twice, with the exception of Supporting Figure 3 (performed once). All replicate experiments were performed using freshly prepared LNPs or liposomes. All replicate experiments were successful and confirmed the presented data. For all experiments performed in embryonic zebrafish, at least four embryos were randomly selected (from a pool of 10-30 successfully injected embryos) and analyzed (low resolution microscopy). All selected embryos showed consistent results and confirmed the presented data. From these embryos, at least one embryo was selected for high resolution, confocal microscopy. No statistical analysis was performed on acquired zebrafish data. Statistical analysis for mouse studies was performed by a Student's t-test with a correction for multiple comparisons using the Holm-Sidak method using Prism (v8.1.1, GraphPad Software, Inc.). All data represent at $n \geq 2$ independent measurements. Comparisons were considered significant at $P < 0.01$.

3. LC-MS spectra

LC-MS spectrum of Chol-NH-ApoE_peptide



4. References

1. Arias-Alpizar, G. *et al.* Stabilin-1 is required for the endothelial clearance of small anionic nanoparticles. *Nanomedicine Nanotechnology, Biol. Med.* **34**, 102395 (2021).
2. Miller, C. M. *et al.* Stabilin-1 and Stabilin-2 are specific receptors for the cellular internalization of phosphorothioate-modified antisense oligonucleotides (ASOs) in the liver. *Nucleic Acids Res.* **44**, 2782–2794 (2016).
3. Jayaraman, M. *et al.* Maximizing the potency of siRNA lipid nanoparticles for hepatic gene silencing in vivo. *Angew. Chemie - Int. Ed.* **51**, 8529–8533 (2012).
4. Sun, Q., Cai, S. & Peterson, B. R. Practical Synthesis of 3β-Amino-5-cholestene and Related 3β-Halides Involving i-Steroid and Retro-i-Steroid Rearrangements. *Org. Lett.* **11**, 567–570 (2009).
5. Daudey, G. A., Zope, H. R., Voskuhl, J., Kros, A. & Boyle, A. L. Membrane-Fusogen Distance Is Critical for Efficient Coiled-Coil-Peptide-Mediated Liposome Fusion. *Langmuir* **33**, 12443–12452 (2017).
6. Kulkarni, J. A. *et al.* Fusion-dependent formation of lipid nanoparticles containing macromolecular payloads. *Nanoscale* **11**, 9023–9031 (2019).
7. Schindelin, J. *et al.* Fiji: an open-source platform for biological-image analysis. *Nat. Methods* **9**, 676–682 (2012).
8. Ellett, F., Pase, L., Hayman, J. W., Andrianopoulos, A. & Lieschke, G. J. mpeg1 promoter transgenes direct macrophage-lineage expression in zebrafish. *Blood* **117**, e49-56 (2011).
9. Weinstein, B. M., Stemple, D. L., Driever, W. & Fishman, M. C. Gridlock, a localized heritable vascular patterning defect in the zebrafish. *Nat. Med.* **1**, 1143–1147 (1995).
10. Severgnini, M. *et al.* A rapid two-step method for isolation of functional primary mouse hepatocytes: cell characterization and asialoglycoprotein receptor based assay development. *Cytotechnology* **64**, 187–195 (2012).

Appendix 3

Supplementary Information to Chapter 4

1. Supplementary Figures and Tables

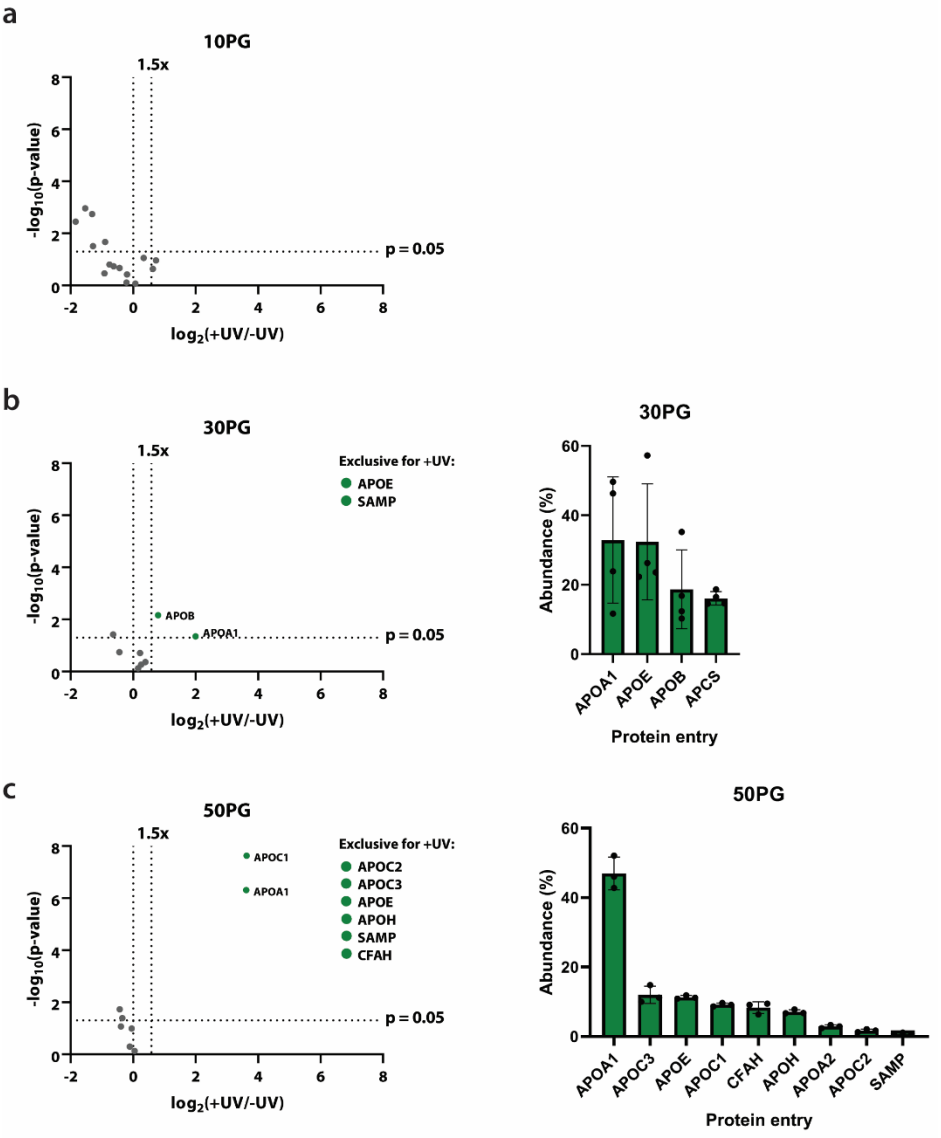


Figure S1. Volcano plots showing the enrichment of proteins in "+UV" over "-UV" samples as $\log_2$(+UV/-UV) against the statistical significance between the two groups ($n \geq 3$) as $-\log_{10}$(p-value). Selection threshold is set at 1.5-fold enrichment and a p-value < 0.05. Abundance plots only show proteins that meet selection criteria. (**a**) 10PG (**b**) 30PG (**c**) 50PG.

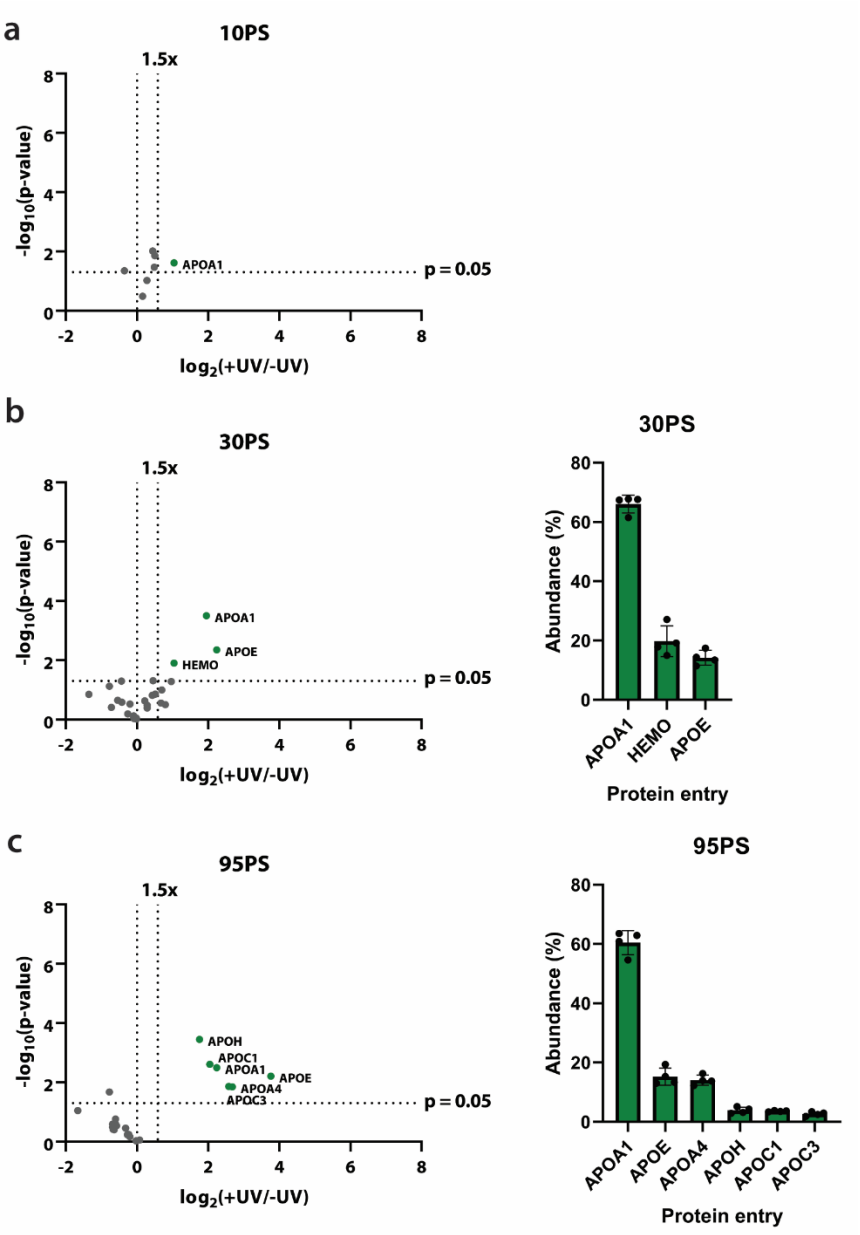


Figure S2. Volcano plots showing the enrichment of proteins in "+UV" over "-UV" samples as $\log_2$(+UV/-UV) against the statistical significance between the two groups ($n \geq 3$) as $-\log_{10}$(p-value). Selection threshold is set at 1.5fold enrichment and a p-value < 0.05. Abundance plots only show proteins that meet selection criteria. (**a**) 10PS (**b**) 30PS (**c**) 95PS.

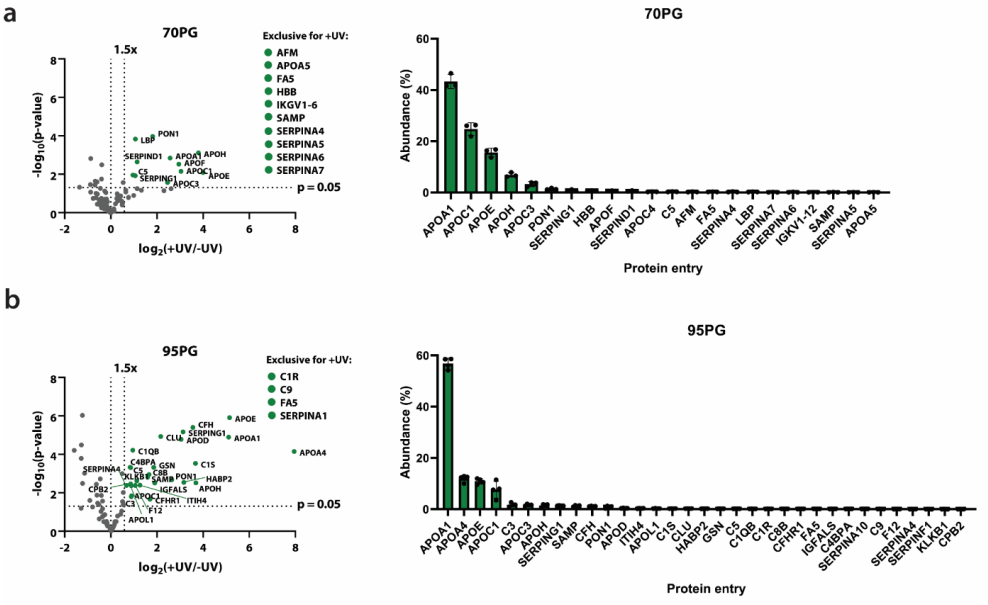
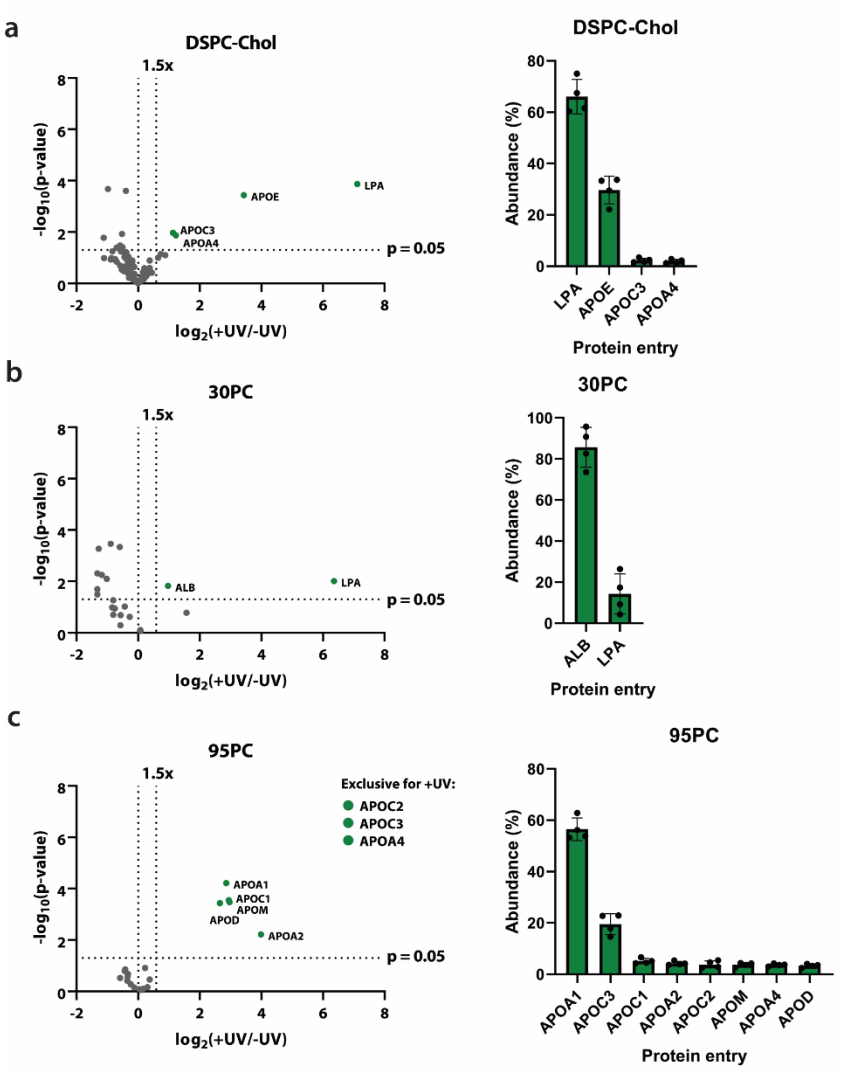
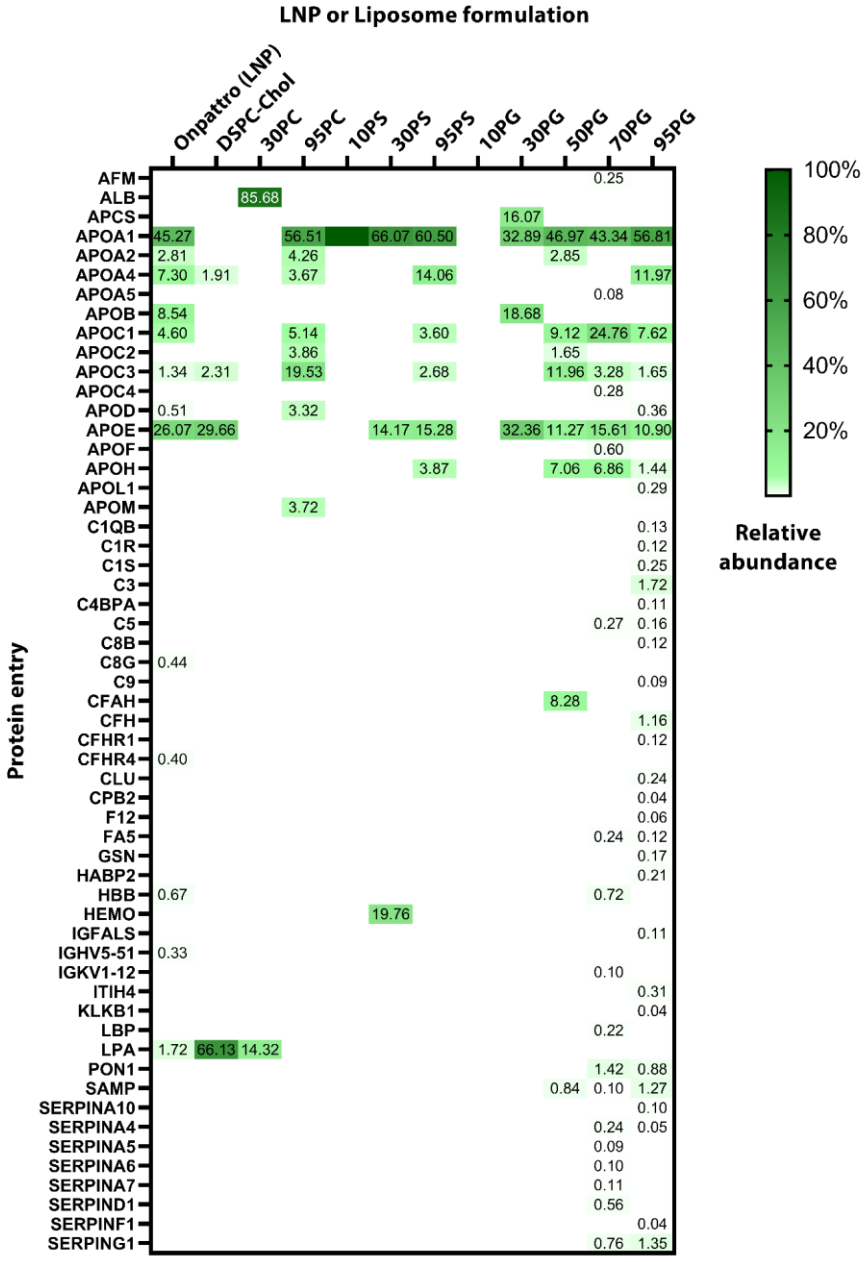


Figure S3. Volcano plots showing the enrichment of proteins in "+UV" over "-UV" samples as $\log_2$(+UV/-UV) against the statistical significance between the two groups (n ≥ 3) as -$\log_{10}$(p-value). Selection threshold is set at 1.5-fold enrichment and a p-value < 0.05. Abundance plots only show proteins that meet selection criteria. (**a**) 70PG (**b**) 95PG.



Supplementary Figure 4. Volcano plots showing the enrichment of proteins in "+UV" over "-UV" samples as $\log_2$(+UV/-UV) against the statistical significance between the two groups (n ≥ 3) as -$\log_{10}$(p-value). Selection threshold is set at 1.5-fold enrichment and a p-value < 0.05. Abundance plots only show proteins that meet selection criteria. (**a**) DSPC-Chol (**b**) 30PC (**c**) 95PC.



Supplementary Figure 5. Complete heatmap containing the proteins identified across all protein coronas and their average relative abundance in % (denoted by values).



Supplementary Figure 6. The structure of APOA1 (PDB entry 1AV1)[1] in which cationic residues (Lysine, Arginine and Histidine) are colorded in blue and anionic residues (Glutamic acid and Aspartic acid) in red.

Formulation (+IKS02)	Avg. Size (nm)	PDI	ζ-potential (mV)
Onpattro	78	0.098	-3.9
DSPC-Chol	115	0.109	-2.5
30PC	105	0.074	-3.4
95PC	110	0.099	-1.3
10PS	99	0.085	-12.5
30PS	104	0.079	-25.4
95PS	101	0.113	-48.6
10PG	111	0.109	-13.9
30PG	96	0.100	-21.4
50PG	105	0.088	-33.8
70PG	109	0.079	-45.0
95PG	101	0.071	-50.3
Formulation (-IKS02)	**Avg. Size (nm)**	**PDI**	**ζ-potential (mV)**
Onpattro	75	0.111	-2.5
DSPC-Chol	109	0.106	-1.2
30PC	106	0.108	-4.7
30PG	108	0.092	-23.5

Supplementary Table 1. Size and surface charge measurements of all formulations used in this study. PDI = Polydispersity Index.

siRNA name	Sequence
Patisiran®	Sense: 5' $GU_mAAC_mC_mAAGAGU_mAU_mU_mC_mC_mAU_mT_dT_d$ 3'
	Antisense: 3' $T_dT_dCAU_mUGGU_mU_mCUCAU_mAAGGU_mA$ 5'

Supplementary Table 2. siRNA sequence of Patisiran® used in this study. U_m and C_m are ribonucleotides with a 2'-OMe functionalization on the ribose ring. T_d, G_d and A_d are DNA ribonucleotides.

2. Materials and methods

General

All solvents and reagents were obtained from general commercial sources (Sigma Aldrich, Acros Organics, Alfa Aesar, Fluka, Merck) and used as received without further purification, unless stated otherwise. Dynamic light scattering and zeta potential measurements were performed on a Malvern Zetasizer Nano ZS. For light irradiation, a CaproBox™ (Caprotec Bioanalytics GmbH) was used with a wavelength of 350 nm and applying a 300 nm light filter. Cholesterol (C8667), Heparin (H3149), Cy5-alkyne (777358) and Biotin-PEG4-alkyne (764213) were purchased from Merck (Zwijndrecht, The Netherlands). IKS02 was synthesized as described before.[2] DLin-MC3-DMA was synthesized as described before.[3] 1,2-dioleoyl-*sn*-glycero-3-phosphocholine (DOPC), 1,2-dioleoyl-*sn*-glycero-3-phospho-L-serine (DOPS, sodium salt), 1-palmitoyl-2-oleoyl-glycero-3-phosphocholine (POPC), 1,2-distearoyl-*sn*-glycero-3-phosphocholine (DSPC), 1,2-dioleoyl-*sn*-glycero-3-phospho-(1'-*rac*-glycerol) (DOPG, sodium salt) and 1,2-dimyristoyl-*rac*-glycero-3-methoxypolyethylene glycol-2000 (DMG-PEG2000) were purchased from Avanti Polar Lipids through Merck. Patisiran siRNA was purchased from Integrated DNA Technologies (Leuven, Belgium) through custom synthesis, exact sequence can be found in Supplementary Table 2. Human Plasma (citrated) was purchased from Merck (P9523). Albumin from human serum (SRP6182), Human transferrin (T3309) and recombinant human apolipoprotein E3 (SRP4696) were purchased from Sigma-Aldrich. Human prothrombin (RP-43087) was purchased from Thermo-Fisher Scientific. Recombinant human Apolipoprotein A1 (ab50239) was purchased from Abcam B.V. (Amsterdam, The Netherlands). Evaporation of solvents with a vacuum centrifuge was performed using an Eppendorf speedvac (Eppendorf Concentrator Plus 5301). Sequencing grade modified trypsin was purchased from Promega (product code = V5111). Acetonitrile (LC-MS grade) and methanol (LC-MS grade) were purchased from Biosolve. Formic acid (LC-MS grade) was purchased from

Actu-All Chemicals. BioSpin columns were purchased from Bo-Rad. The Empore C18 47-mm extraction disks (model 2215) were purchased from 3M™ Purification. Enolase digest standard was purchased from Waters MassPREP™.

Liposome assembly

Liposome assembly was done as described before.[2] Briefly, lipids were combined from stocks in chloroform, dried under a nitrogen flow and trace solvents were removed *in vacuo* for at least 1 hour. The lipid films were hydrated with phosphate buffered saline (PBS, pH = 7.4) and extruded through double stacked 100 nm polycarbonate membrane filters (Nucleopore Track-Etch, Whatman) at 60 °C (Mini-extruder, Avanti Polar Lipids, Alabaster, US).

Lipid Nanoparticle assembly

Lipid Nanoparticles (LNPs) were assembled as described previously.[4] Briefly, lipid films were generated similarly as for liposome assembly and dissolved in absolute ethanol. A solution of siRNA in 50 mM citrate buffer (pH = 4, RNase free) was prepared to resemble a nitrogen:phosphate ratio of 3 of siRNA to DLin-MC3-DMA. The solutions were mixed in a T-junction mixer at a 3:1 flow ratio of siRNA:lipids and afterwards directly loaded in 20k MWCO dialysis cassettes (Slide-A-Lyzer™, Thermo Scientific) and dialyzed against PBS (1x). LNPs were concentrated to the appropriate lipid concentration using 100k MWCO centrifugal filters (Amicon® Ultra, Merck).

Photoaffinity based chemoproteomic workflow

The photoaffinity based chemoproteomic workflow was performed as described before with minor modifications,[2] which are described in the following paragraphs.

Incubation, photo crosslinking and click chemistry

Liposomes or LNPs containing the photoaffinity probe IKS02 (50 µL, 5 mM for liposomes, 10 mM for LNPs) were added to pre-warmed human plasma (37 °C, 50 µL) and incubated in the dark at 37 °C for 1 hour. Half of the replicates were irradiated with 350 nm light for 15 minutes, while cooling. The other replicates were kept at room temperature in the dark for 15 minutes. Afterwards, the liposomes or LNPs were solubilized by addition of 20 µL 0.1% Triton X-100 in ultrapure water and incubated for 10 minutes. The proteins were precipitated according to Wessel and Flügge,[5] by addition of water (up to 400 µL), methanol (650 µL), chloroform (200 µL) and ultrapure water (150 µL) sequentially with

vigorous vortexing in between. The mixture was centrifuged (3000 *g*, 15 min, 4 °C) and the liquid layers were removed, followed by resuspension of the pellet in methanol (600 µL) and centrifugation (14,000 *g*, 5 min, 4 °C). The supernatant was discarded and the pellet was dissolved in HEPES buffer with 0.5% SDS (200 µL, 100 mM, pH 8.0). For each protein sample, click reagent mixture (50 µL) was added from a 10x concentrated stock to obtain a final concentration of 100 µM $CuSO_4$, 1000 µM sodium ascorbate, 500 µM THPTA, 5000 µM aminoguanidine and 25 µM Biotin-PEG4-alkyne, followed by incubation at room temperature for 1 hour at room temperature. After the reaction, the protein precipitation protocol described above was repeated. The pellet dissolved in freshly prepared denaturing buffer (250 µL, 6 M urea, 25 mM NH_4HCO_3) and used for enrichment. Alternatively, samples were snap-frozen with liquid nitrogen and stored for no longer than 2 weeks at -80 °C.

Reduction-alkylation, enrichment and on-bead digestion

To lipid-protein samples conjugated to biotin was added 5 µL 1 M DTT (20 mM final concentration). Samples were vortexed, centrifuged and incubated at 56 °C while shaking (600 rpm) for 30 minutes. The samples were allowed to cool down to room temperature, after which 40 µl 0.5 M iodoacetamide (80 mM final concentration) was added and the samples incubated at room temperature in the dark for 30 minutes. Afterwards, 20 µL 1 M DTT (100 mM final concentration) was added and the samples were vortexed and incubated at 56 °C for 5 minutes. Reduced and alkylated proteins were used directly for avidin bead enrichment. Avidin agarose beads (50% slurry, 100 µL per sample, Thermo Fisher Scientific) were washed three times with PBS (10 mL PBS per 400 µL slurry), centrifuging at 2500 g for 3 minutes. The beads were resuspended in PBS (1 mL PBS per 100 µL slurry) and divided over 15 mL tubes in 1 mL fractions. An additional 2 mL PBS and 5 µL of SDS (10% in water) was added to each tube, after which the denatured and alkylated protein samples were added and the samples were shaken gently in an overhead shaker at RT for at least 3 hours. Beads were pelleted (2,500 g, 5 min) and the supernatants were discarded. The beads were washed twice with SDS in PBS (0.5% w/v, 10 mL), three times with PBS (10 mL) and twice with ultrapure water (10 mL). In between each washing step, the samples were vortexed, centrifuged (2,500 g, 5 min) and the supernatants were discarded. The washed beads were resuspended in 250 µL on-bead digestion buffer (100 mM TRIS pH 8.0, 100 mM NaCl, 1 mM $CaCl_2$ and 2% v/v acetonitrile (LC-MS grade)) and transferred to 1.5 mL low-binding Eppendorf tubes. Next, 10 µL 0.1 µg/µL trypsin was added and the samples were incubated at 37 °C while shaking (950 rpm) overnight. To the samples was added 12.5 µL formic acid and loaded onto Bio-Spin columns (Bio-Rad), the flow-

through was collected by centrifugation (2,500 g, 2 min) in low-binding Eppendorf tubes. The samples were desalted using the StageTips procedure described below.

Protein validation and competition assay

Incubation, photo crosslinking and click chemistry

Proteins from concentrated stock solutions were mixed and pre-warmed (37 °C) to generate a composition of Albumin (ALBU, 50 µg), Transferrin (TRFE, 16 µg), apolipoprotein A1 (APOA1, 3 µg), apolipoprotein E3 (APOE, 3 µg) and prothrombin (THRB, 3 µg) in a total volume of 25 µL (1x PBS) for each replicate. To each replicate was added liposomes or LNPs containing IKS02 (25 µL, 1 mM for liposomes, 2 mM for LNPs). For competition experiments, liposomes without IKS02 or heparin was added according to the competitive ratio. The mixture was incubated at 37 °C for 1 hour followed by UV irradiation (15 min, 350 nm) lysis with 1% Triton X-100 (5 µL). Proteins were precipitated by addition of water up to a volume of 400 µL, methanol (400 µL) and chloroform (100 µL), followed by vigorous vortexing and centrifugation (3000 *g*, 10 min, 4 °C). The liquid layers were removed, the pellet resuspended with methanol (200 µL) and centrifuged (14,000 *g*, 5 min, 4 °C). The supernatant was discarded and the pellet was dissolved in HEPES buffer (90 µL, 100 mM, pH 8.0). For each protein sample, click reagent mixture (10 µL) was added from a 10x concentrated stock to give a final concentration of 100 µM $CuSO_4$, 1000 µM sodium ascorbate, 500 µM THPTA, 5000 µM aminoguanidine and 25 µM Cy5-alkyne, followed by incubation at room temperature for 1 hour. Protein precipitation was repeated as prior to the click reaction and the pellet was dissolved in 0.1% SDS in PBS (100 µL).

SDS-PAGE, In-gel fluorescence and Coomassie blue imaging

Protein concentration was determined by BCA assay prior to loading samples for in-gel fluorescence. To a volume corresponding to 7.5 µg of protein was added Laemmli buffer (4x stock) and the proteins were heated at 70 °C for 10 minutes followed by resolving on 4–15% Mini-PROTEAN® TGX™ Precast Protein Gel (Bio-Rad) at 180 V. The subset of fluorescent proteins was imaged on a Typhoon FLA 9500 (GE Healthcare), followed by staining of all the proteins with Coomassie Brilliant Blue R-250 staining solution (Bio-Rad) and imaging on a ChemiDoc MP system (Bio-Rad). Images were processed using the Fiji package of ImageJ.[6]

StageTips desalting

The protein digest desalting procedure was conducted as previously described.[7] Briefly, C_{18} extraction disks (47 mm) were placed in 200 µL pipette tips. These StageTips were conditioned, loaded, washed and eluted, following the scheme below. The eluted fractions were collected into low-binding Eppendorf tubes, dried using a vacuum centrifuge and stored at -20 °C or immediately prepared for UPLC-MS/MS measurements.

STAGE	BUFFER
Conditioning 1	50 µL MeOH (LC-MS grade)
Conditioning 2	50 µL StageTip solution B: 0.5% (v/v) formic acid, 80% (v/v) acetonitrile and 19.5% ultrapure water
Conditioning 3	50 µL StageTip solution A: 0.5% (v/v) formic acid in ultrapure water
Loading	Sample
Washing	100 µL StageTip solution A
Elution	100 µL StageTip solution B

NanoUPLC-MS/MS analysis

Peptide samples were dissolved in 50 µL LC-MS sample solution (ultrapure water:acetonitrile:formic acid 97:3:0.1) containing 10 fmol/µL enolase digest as an internal standard for label-free quantification. LC-MS/MS measurements were performed on a Synapt G2Si mass spectrometer (Waters) operating with Masslynx as described before without any modification,[2,8] or on an UltiMate 3000 RSLCnano system with a HQExactive mass spectrometer. The latter was set in a trap-elute configuration with a nanoEase M/Z Symmetry C18 100Å, 5µm, 180µm x 20 mm (Waters) trap column for peptide loading/retention and nanoEase M/Z HSS C18 T3 100Å, 1.8µm, 75 µm x 250 mm (Waters) analytical column for peptide separation. The column was kept at 40°C in a column oven. Flow gradient used for analysis was a steep (45 min) gradient of mobile phase A (0.1% formic acid (FA) in ULC-MS grade water (Biosolve)) and mobile phase B (0.1% FA in ULC-MS grade acetonitrile (ACN, Biosolve)) controlled by a flow sensor at 0.3µl/min with average pressure of 400-500 bar (5500-7000 psi). Samples were injected (5 µL) on the trap column at a flow rate of 15 µl/min for 9 min with 99%A, 1%B eluent. The gradient was programmed with linear increment to 1% B from t0 to t2 min, 10%B to t5 min, 30%B at t25, 90%B at t26 to t33 and 1%B at t34 to t45 min. The eluent was introduced by electro-spray

ionization (ESI) via the nanoESI source (Thermo) using stainless steel Nano-bore emitters (40 mm, OD 1/32", ES542, Thermo Scientific). The QExactive HF was operated in positive mode with data dependent acquisition without the use of lock mass, default charge of 2+ and external calibration with LTQ Velos ESI positive ion calibration solution (88323, Pierce, Thermo) every 3-5 days to less than 2 ppm. The tune file for the survey scan was set to scan range of 350 – 1400 m/z, 60.000 resolution, 1 microscan, automatic gain control (AGC) of 1e6, max injection time of 50 ms, no sheath, aux or sweep gas, spray voltage ranging from 1.7 to 3.0 kV, capillary temp of 250°C and a S-lens value of 80. The sensitive MS method settings were: the survey scan was taken at 120,000 resolution, AGC target of 3e6, maximum IT time of 100 ms, and scan range of 350 to 1400 m/z. For the 10 data dependent MS/MS events the loop count was set to 10 and the general settings were resolution to 15,000, AGC target 1e5, max IT time 50 ms, isolation window of 1.6 m/z, fixed first mass of 120 m/z and normalized collision energy (NCE) of 28 eV. For individual peaks the data dependent settings were 1.00e3 for the minimum AGC target yielding an intensity threshold of 2.0e4 that needs to be reached prior of triggering an MS/MS event. No apex trigger was used, unassigned, +1 and charges >+8 were excluded with peptide match mode preferred, isotope exclusion on and dynamic exclusion of 10 sec. In between experiment samples routine wash and control runs were done by injecting 5 µl 97.3.0.1 solution, 5 µl of 10 fmol/µl BSA or enolase digest and 1 µl of 10 fmol/µl angiotensin III (Fluka, Thermo)/oxytocin (Merck) to check the performance of the platform on each component (nano-LC, the mass spectrometer (mass calibration/quality of ion selection and fragmentation) and the search engine).

Proteomic analysis

The resulting proteomics data from the Synapt and HQExactive Mass spectrometers were processed using ISOQuant or MaxQuant software respectively.[9,10] In both cases, label-free quantification (LFQ) was applied using a TOP3 approach. Limitations for peptides was set a minimum length of 6 amino acids and positive identification of at least 2 different peptides. Protein identification was done using the reviewed proteins from the PLGS or Uniprot databases (Human, reviewed, downloaded on 1st of June, 2020) to which Trypsin, Enolase, Avidin, Strepatividin and Bovine Serum Albumin were added manually. Processing of proteins into volcano plots and the selection of "hits" were subject to certain criteria and statistical processing. First, proteins had to be present in all replicates of "+UV" samples. Second, self-introduced proteins were excluded for volcano plots and further analysis. Third, sufficient enrichment over background was set at 1.5-fold. Fourth, the maximum p-value for a hit was set at p = 0.05. P-values were determined by multiple t-tests comparing the replicates of each group with a Benjamini-Hochberg approach using the

GraphPad Prism software (v8.0). If proteins did not have any background signal or not enough replicates in the background in order to perform a t-test, the proteins were labeled as "exclusive" and were directly selected as hits. Abundance plots were generated by plotting the average LFQ intensity values, substracted by the background, for each protein and calculating their relative abundance.

Cryogenic transmission electron microscopy

CryoTEM was performed as described previously.[4] Briefly, LNPs (~10-15 mM) were vitrified using a Leica EM GP operating at 22°C or 37°C and 95% relative humidity. Sample suspensions were placed on glow discharged 150 µm lacey carbon films supported by 200 mesh copper grids (Electron Microscopy Sciences). Sample grids were maintained below –170 °C and imaging was performed on a Tecnai T12 (ThermoFisher) with a biotwin lens and LaB6 filament operating at 120 keV equipped with an Eagle 4K x 4K CCD camera (ThermoFisher). Images were acquired at a nominal underfocus of -2 to -3 µm (49,000× magnification) with an electron dose of ~2000 $e^{-} \cdot nm^{-2}$. Image processing was performed using the Fiji distribution of ImageJ.[6]

3. References

1. Borhani, D. W., Rogers, D. P., Engler, J. A. & Brouillette, C. G. Crystal structure of truncated human apolipoprotein A-I suggests a lipid-bound conformation. *Proc. Natl. Acad. Sci.* **94**, 12291–12296 (1997).
2. Pattipeiluhu, R. *et al.* Unbiased Identification of the Liposome Protein Corona using Photoaffinity-based Chemoproteomics. *ACS Cent. Sci.* **6**, 535–545 (2020).
3. Jayaraman, M. *et al.* Maximizing the potency of siRNA lipid nanoparticles for hepatic gene silencing in vivo. *Angew. Chemie - Int. Ed.* **51**, 8529–8533 (2012).
4. Pattipeiluhu, R. *et al.* Paracrystalline Inverted Lipid Phases Encapsulating siRNA Enhance Lipid Nanoparticle Mediated Transfection. *Chapter 5, This Thesis* (2021).
5. Wessel, D. & Flügge, U. I. A method for the quantitative recovery of protein in dilute solution in the presence of detergents and lipids. *Anal. Biochem.* **138**, 141–143 (1984).
6. Schindelin, J. *et al.* Fiji: an open-source platform for biological-image analysis. *Nat. Methods* **9**, 676–682 (2012).
7. Rappsilber, J., Mann, M. & Ishihama, Y. Protocol for micro-purification, enrichment, pre-fractionation and storage of peptides for proteomics using StageTips. *Nat. Protoc.* **2**, 1896–1906 (2007).
8. van Rooden, E. J. *et al.* Mapping in vivo target interaction profiles of covalent inhibitors using chemical proteomics with label-free quantification. *Nat. Protoc.* **13**, 752–767 (2018).
9. Distler, U. *et al.* Drift time-specific collision energies enable deep-coverage data-independent acquisition proteomics. *Nat. Methods* **11**, 167–170 (2014).
10. Tyanova, S., Temu, T. & Cox, J. The MaxQuant computational platform for mass spectrometry-based shotgun proteomics. *Nat. Protoc.* **11**, 2301–2319 (2016).

Appendix 4

Supplementary Information to Chapter 5

1. Supplementary Figures and Tables

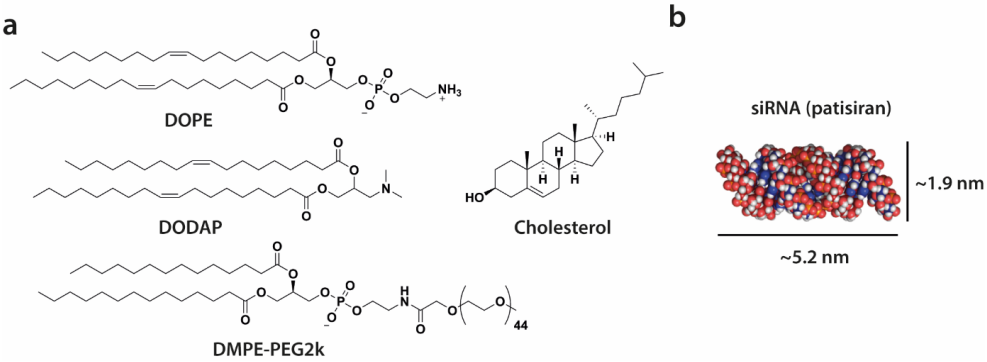


Figure S1. LNP components used in this study. (**a**) Chemical structures of lipid components used in LNP assembly. (**b**) RNA A-form structure of Patisiran®, model was created using UCSF Chimera. Width and length were determined in PyMol.

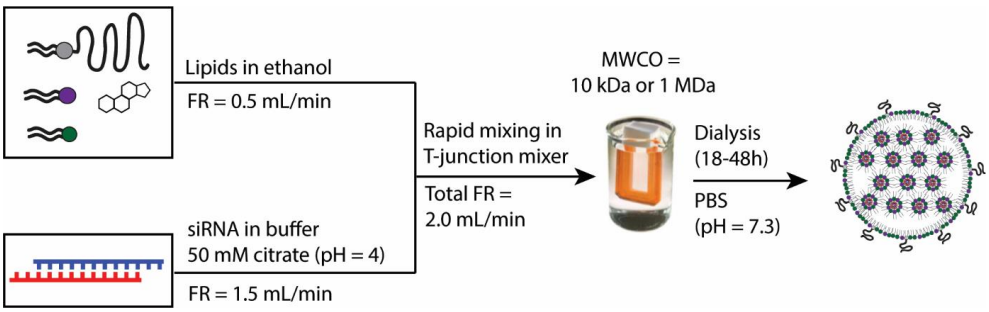


Figure S2. Schematic of LNP assembly. Lipids in ethanol were mixed through a T-junction mixture with siRNA in 50 mM citrate buffer (pH = 4.0) at respective flow rates (FRs) of 0.5 mL/min and 1.5 mL/min. The acquired suspension was dialyzed against PBS to obtain the fully assembled LNPs.

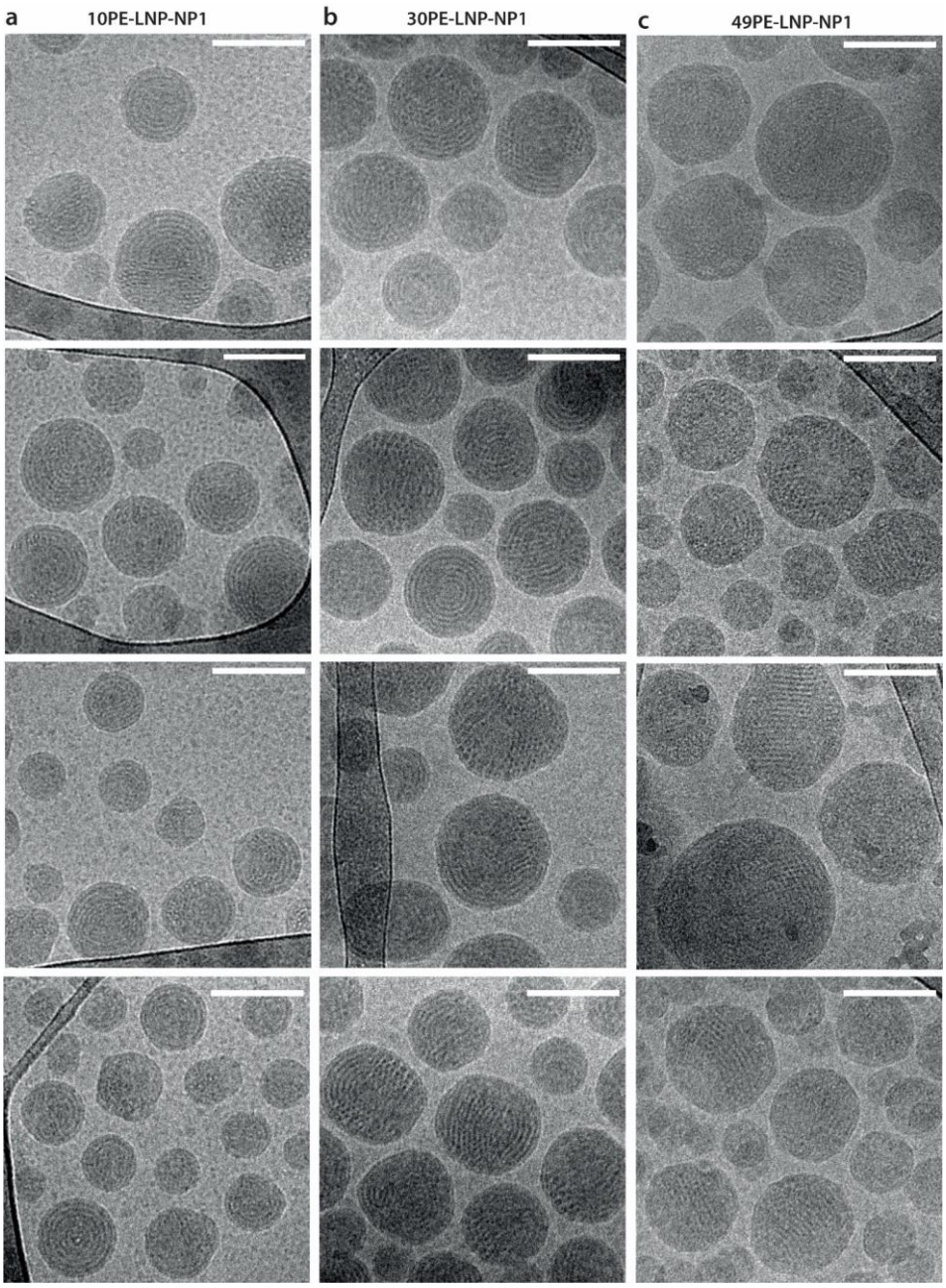


Figure S3. Additional cryoTEM images of 10PE-LNP-NP1, 30-PE-LNP-NP1 and 49PE-LNP-NP1. (**a**-**c**) Imaging was performed on a 120 kV Tecnai T12 as described in the Materials and Methods section. All scale bars are 100 nm.

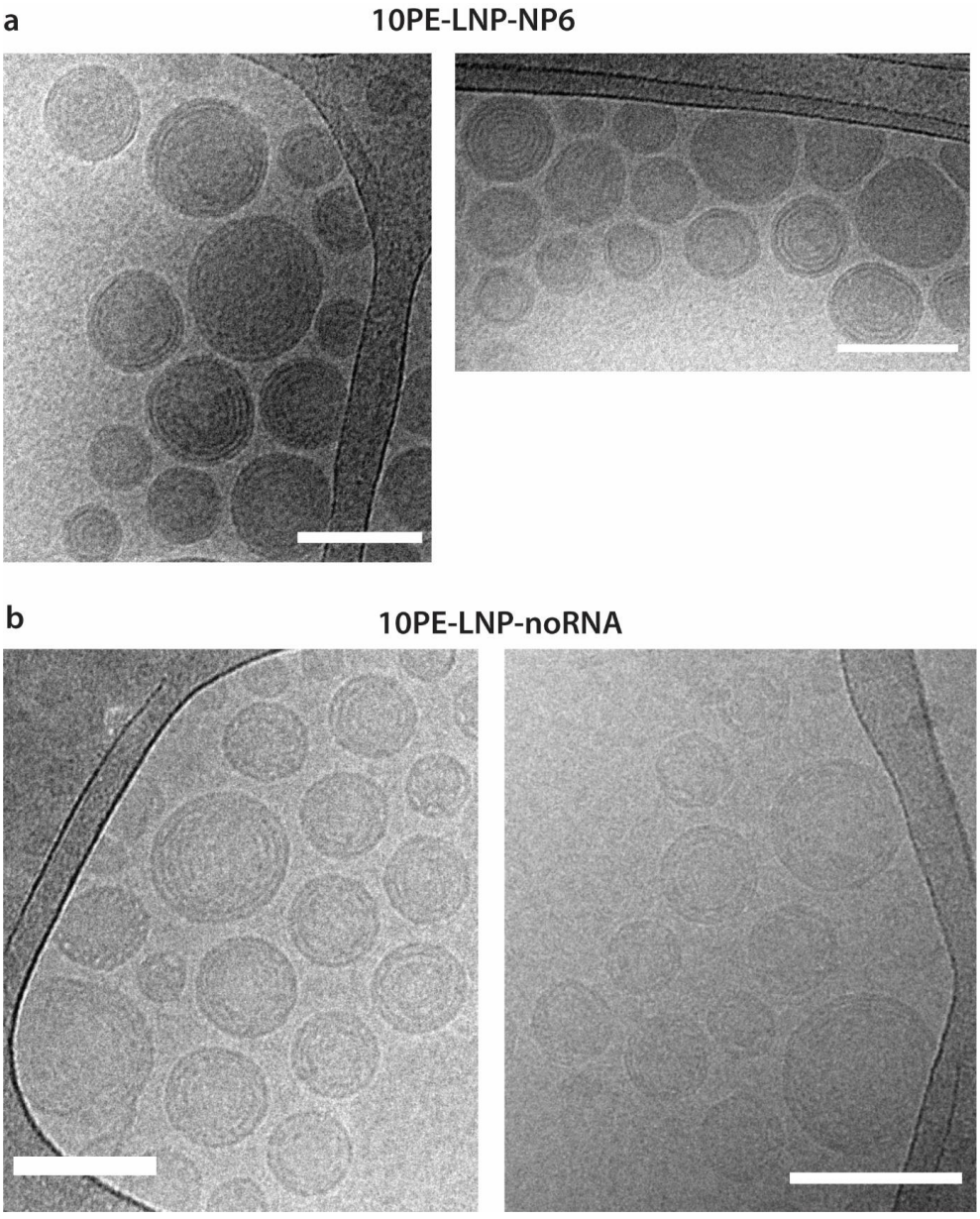


Figure S4. CryoTEM images of 10PE-LNP-NP6 and 10PE-LNP-noRNA. (**a**-**b**) Imaging was performed on a 120 kV Tecnai T12 as described in the Materials and Methods section. All scale bars are 100 nm.

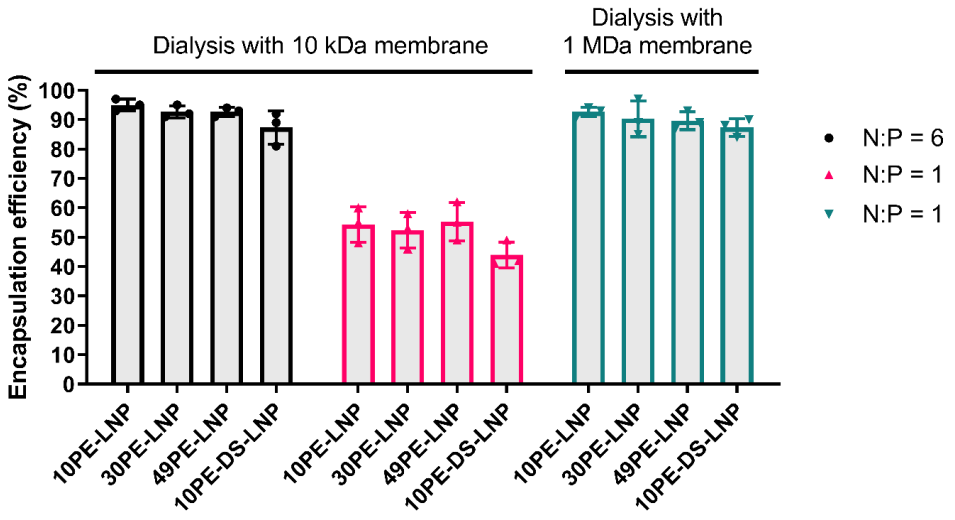


Figure S5. Encapsulation efficiency (%) of all formulations formulated at NP ratios of 6 and 1. For the NP ratio of 1, dialysis performed with 1 MDa membranes (Spectra-Por® Float-A-Lyzer® G2, Thermo Scientific) shows the efficient removal of non-encapsulated siRNA over dialysis with 10 kDa membranes (Slide-A-Lyzer™, Thermo Scientific). Dialysis time was 48 hours in all cases. Bar plots and error bars represent the average and standard deviation from a triplicate of independent assemblies.

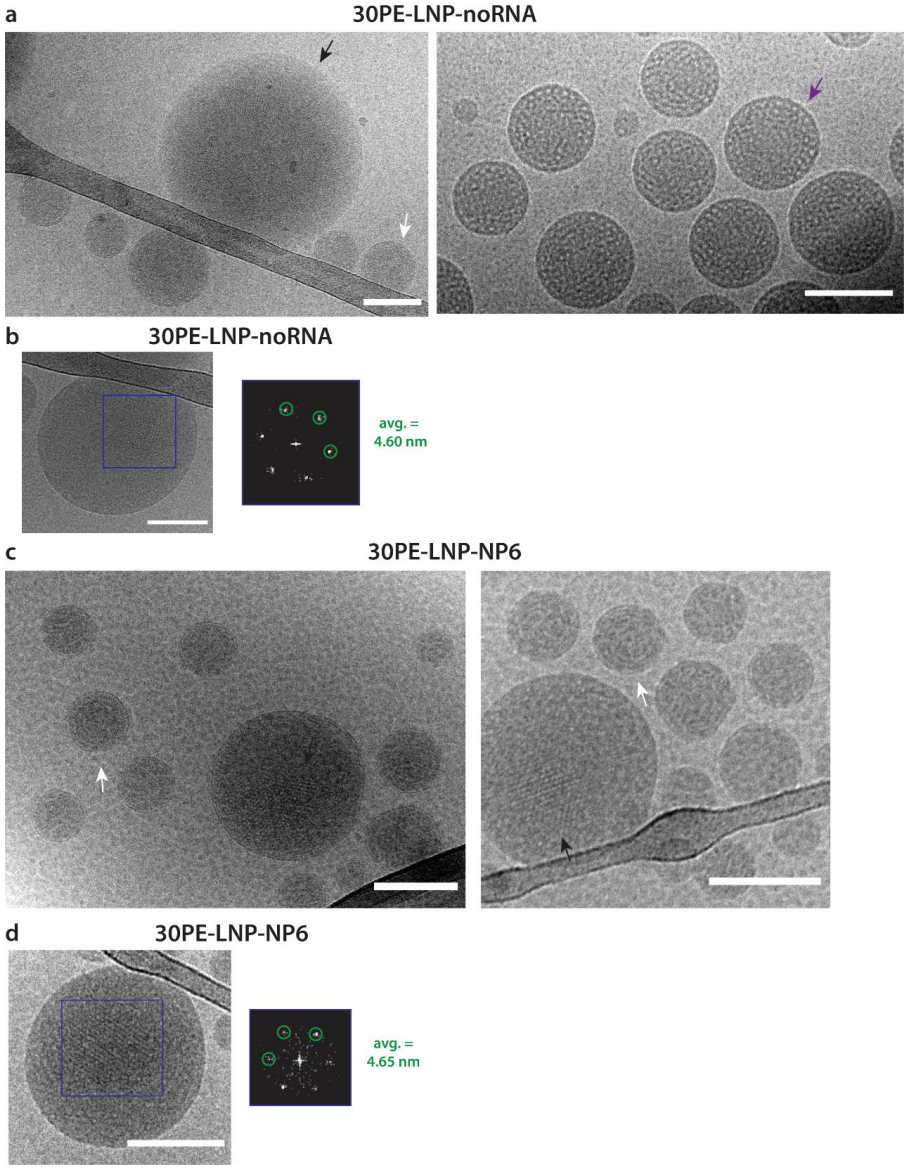


Figure S6. CryoTEM images of 30PE-LNP-NP6 and 30PE-LNP-noRNA. (**a**-**d**) Imaging was performed on a 120 kV Tecnai T12 as described in the Materials and Methods section. All scale bars are 100 nm. Black arrows indicate the presence of tubular inverse hexagonal structures. White arrows indicate the presence of concentric lamellar structures. Purple arrows indicate the presence of undefined lipid structures. FFT values represent the average of the [001] structure of the selected areas in individual particles.

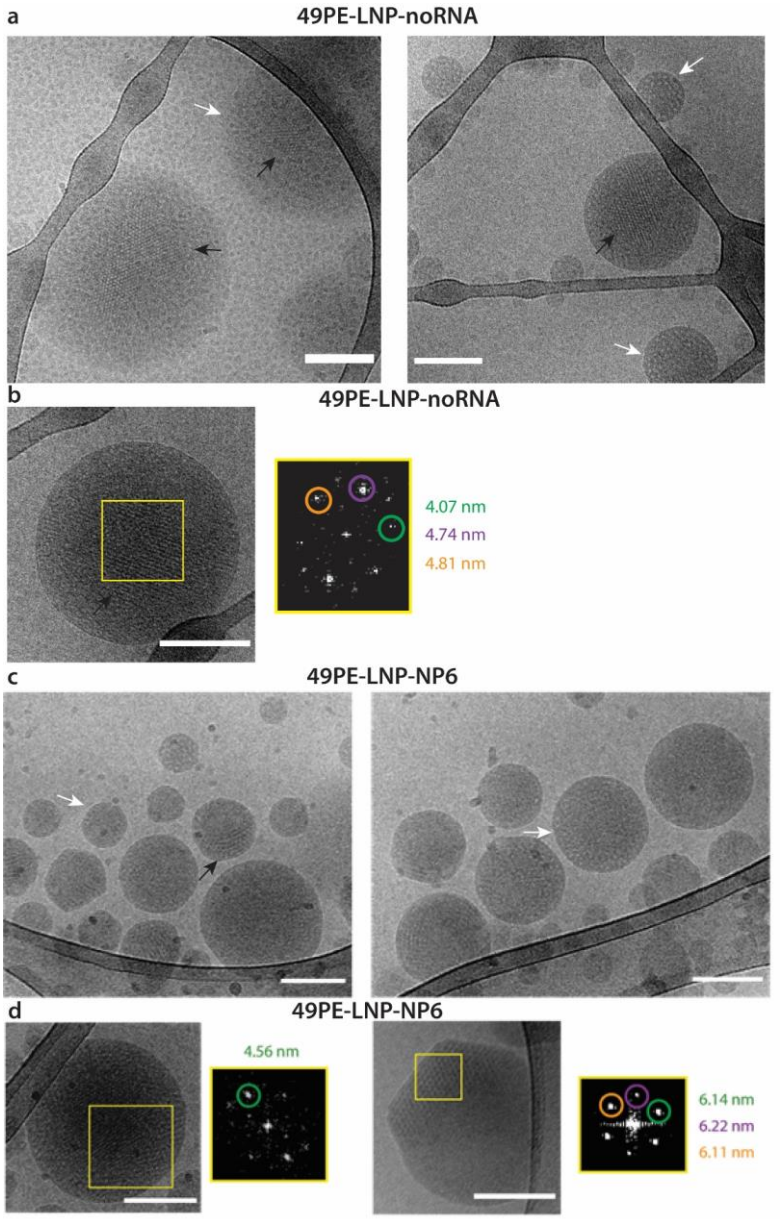


Figure S7. CryoTEM images of 49PE-LNP-NP6 and 49PE-LNP-noRNA. (**a-d**) Imaging was performed on a 120 kV Tecnai T12 as described in the Materials and Methods section. All scale bars are 100 nm. FFT values are matched by color in the selected areas in individual particles. Black arrows indicate the presence inverse hexagonal structures throughout the LNP core. White arrows indicate the presence of spherical structures described in Supplementary Figure 10.

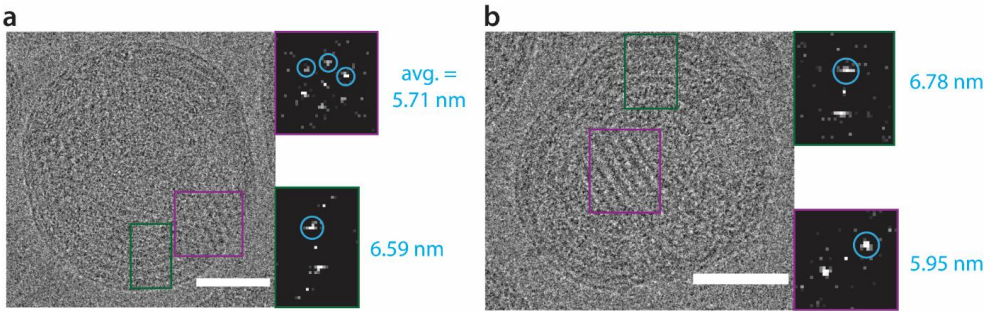


Figure S8. Co-existence of lamellar, straight line and hexagonal structures in 30PE-LNP-NP1. (**a,b**) cryoTEM images of 30PE-LNP-NP1 particles, showing the co-existence of structures within the same particle, along with FFT analysis of the color coded selections. Purple selections represent hexagonal or straight line structures of inverse hexagonal structures, green selections represent lamellar structures. Imaging was performed on a 300 kV Titan Krios 2 as described in the Materials and Methods section. All scale bars are 50 nm.

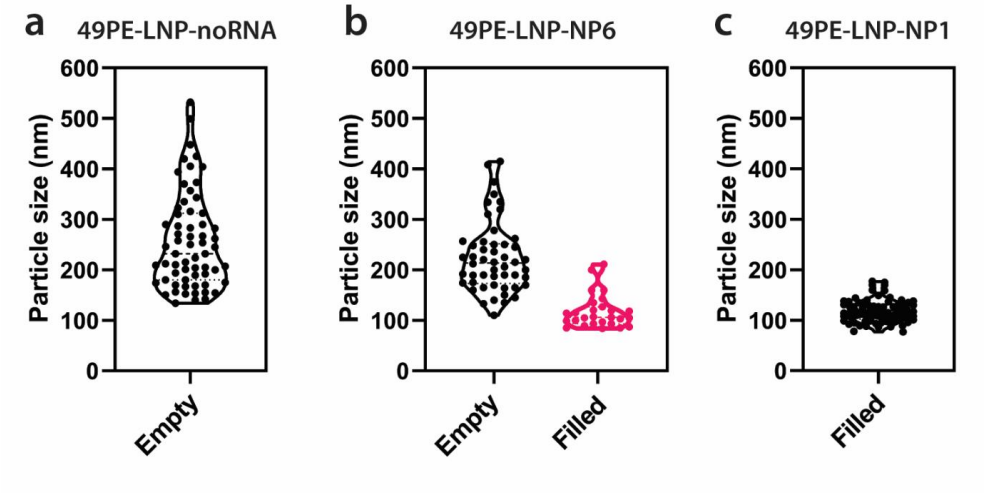


Figure S9. Correlation of filled paracrystalline inverse hexagonal phases with LNP particle size. Relation between lattice spacings show in **Figure 3b** to particle size for 49-LNP variants at different siRNA amounts. (**a**) 49PE-LNP-noRNA (n = 63, 257 nm ± 95 nm), (**b**) 49PE-LNP-NP6, empty (n = 50, 224 nm ± 70 nm) NP = 6 filled (n = 27, 117 nm ± 33 nm) and (**c**) 49PE-LNP-NP1 (n = 81, 118 nm ± 22 nm).

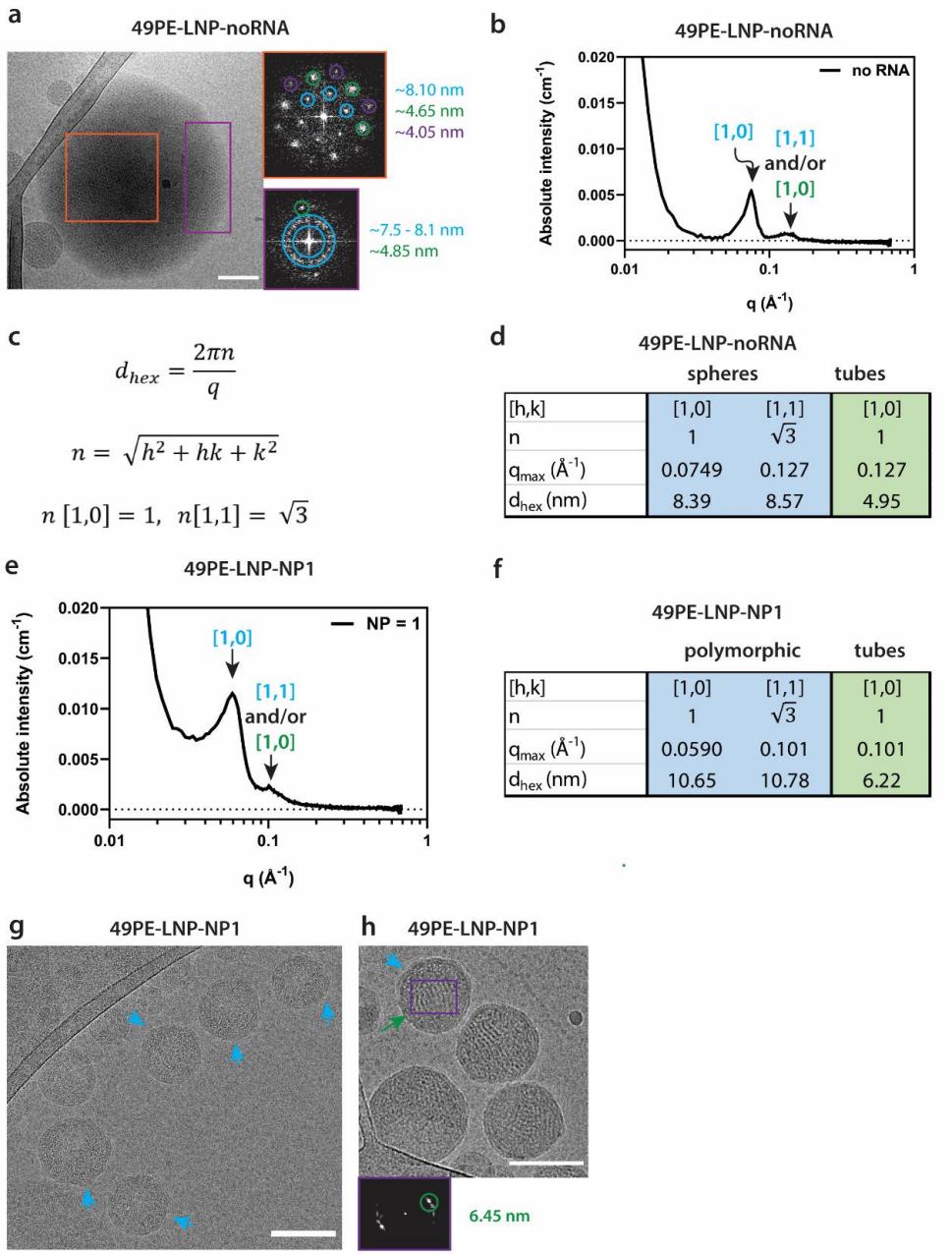


Figure S10. Comparison of identified structures in cryoTEM of 49PE-LNP to SAXS profiles. (**a**) CryoTEM image of large 49PE-LNP-noRNA particle showing both hexagonally packed spheres and inverse hexagonal tubular structures. (**b**) SAXS profile of 49PE-LNP-noRNA derived from **Figure 1f**,

with indications of Bragg peaks with Miller indices. (**c**) Formulas used for the calculation of the d-spacing assuming a hexagonally packed structure. (**d**) d-spacing calculations for 49PE-LNP-noRNA (**e**) SAXS profile of 49PE-LNP-NP1 derived from **Figure 1f**, with indications of Bragg peaks with Miller indices. (**f**) Formulas used for the calculation of the d-spacing assuming a hexagonally packed structure. (**g**-**h**) cryoTEM images of 49PE-LNP-NP1 showing polymorphic (blue arrows) and inverse hexagonal tubular structures (green arrow).

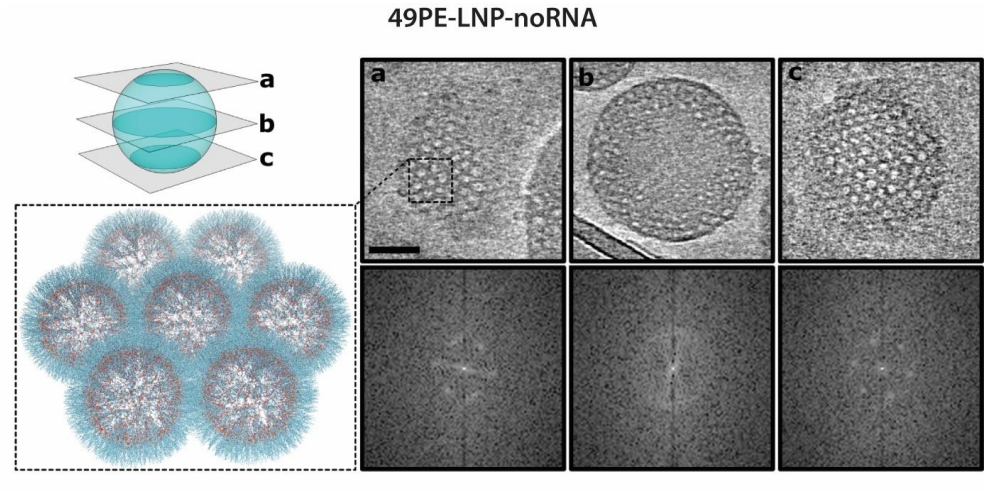


Figure S11. CryoET slices of an individual 49PE-LNP-noRNA particle. Tomographic slices through an individual 49PE-LNP-noRNA particle (cyan) at the heights indicated with (**a,b,c**), revealing the hexagonally packed spheres through the LNP, with an amorphous core. Model displays spheres with lipid tails pointed outwards and an average size of ~8 nm. Scale bar = 50 nm.

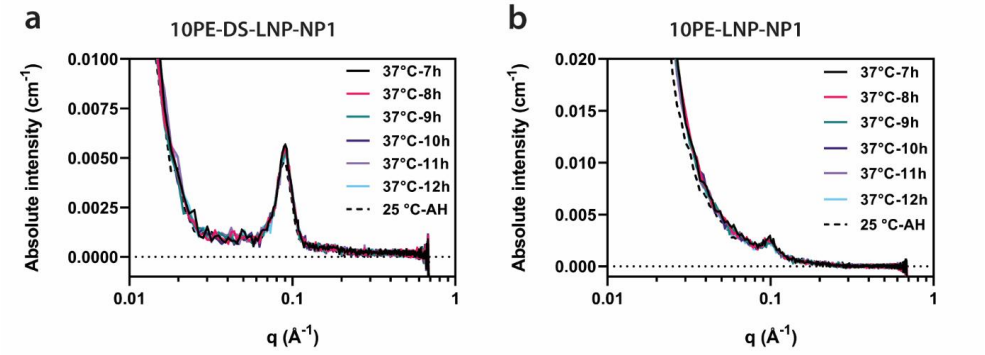


Figure S12. SAXS profiles after incubation at 37 °C for 7-12 hours. SAXS profiles at additional points of incubation at 37 °C and 25 °C after heating (AH) for (**a**) 10PE-DS-LNP-NP1 and (**b**) 10PE-LNP-NP1.

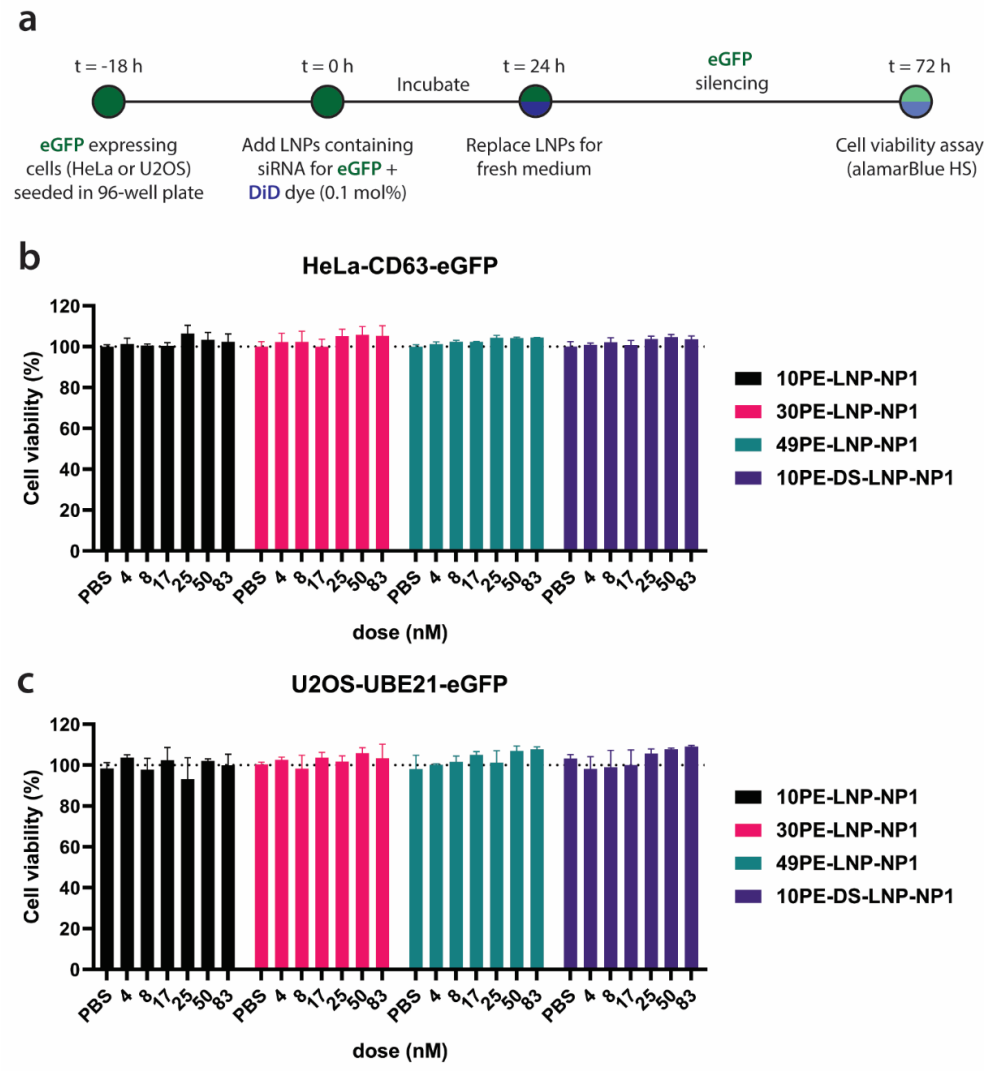


Figure S13. Cell viability study of cell lines treated with LNPs. (**a**) Schematic showing the timeline of the cell viability study conducted. (**b**-**c**) Results of the cell-viability assay (alamarBlue HS) of the HeLa and U2OS cell lines.

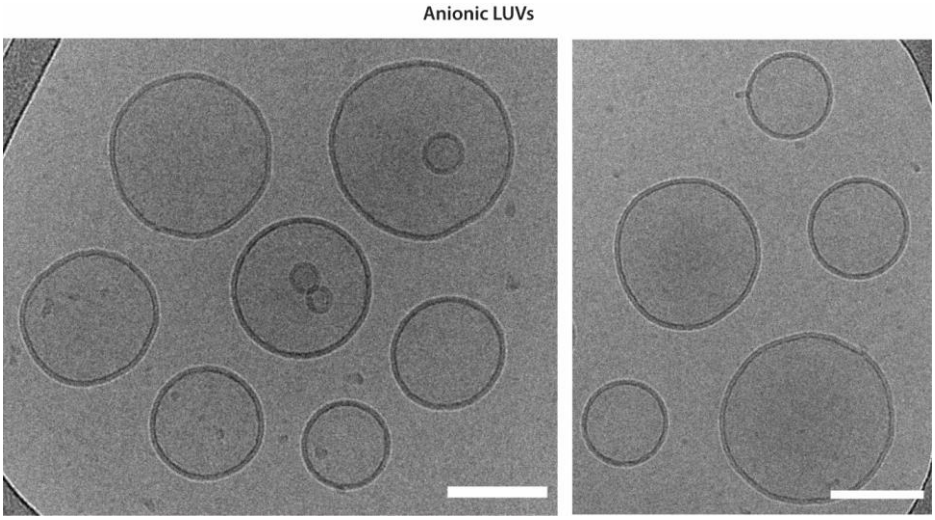


Figure S14. CryoTEM images of anionic LUVs. LUVs are composed of PC:PE:PS:Chol:PI at a ratio of 50:27:10:10:3 mol%. Sample vitrification in the mixture of 100 mM citrate buffer and PBS (1:2 vol:vol) at 37 °C as described in the Materials and Methods section. All scale bars are 100 nm.

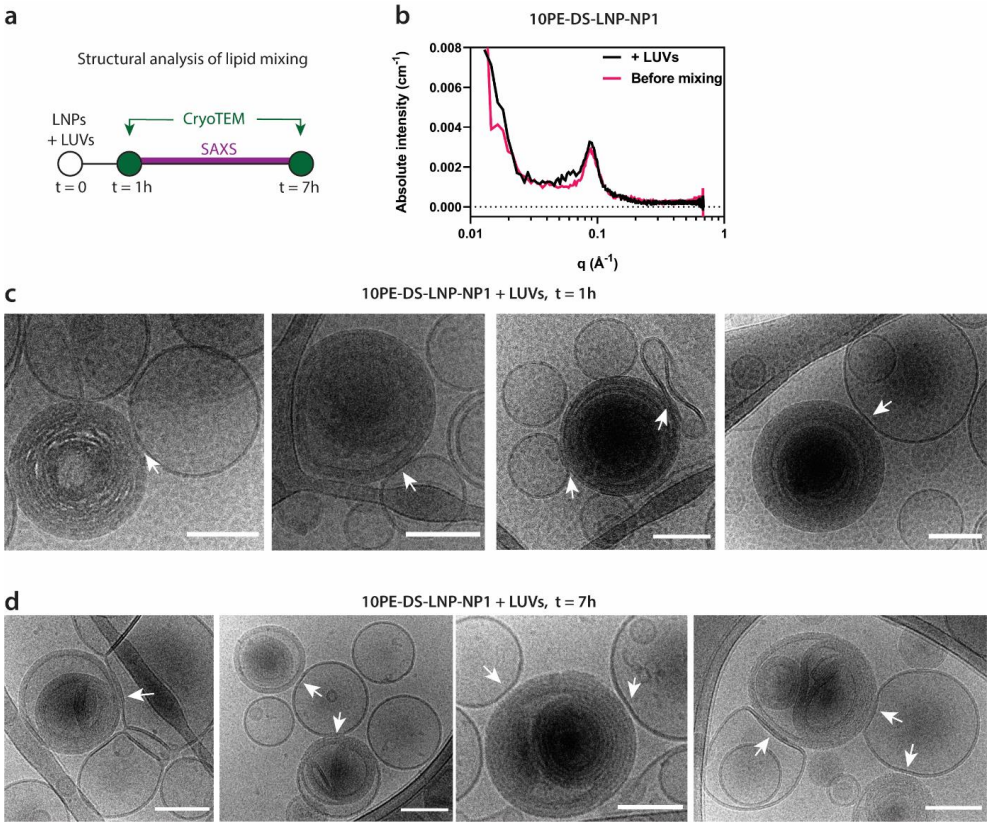


Figure S15. Interaction of 10PE-DS-LNP-NP1 with anionic LUVs. (**a**) Schematic representation depicting the experiments for the structural analysis of the LNP-LUV interaction. (**b**) SAXS profile of 10PE-DS-LNP-NP1 incubated with anionic LUVs. (**c,d**) CryoTEM images of 10PE-DS-LNP-NP1 incubated with anionic LUVs at pH 6 after 1 hour (t = 1h) and after 7 hours (t = 7h). White arrows indicate positions where docking between LNPs and LUVs is observed. All scale bars are 100 nm.

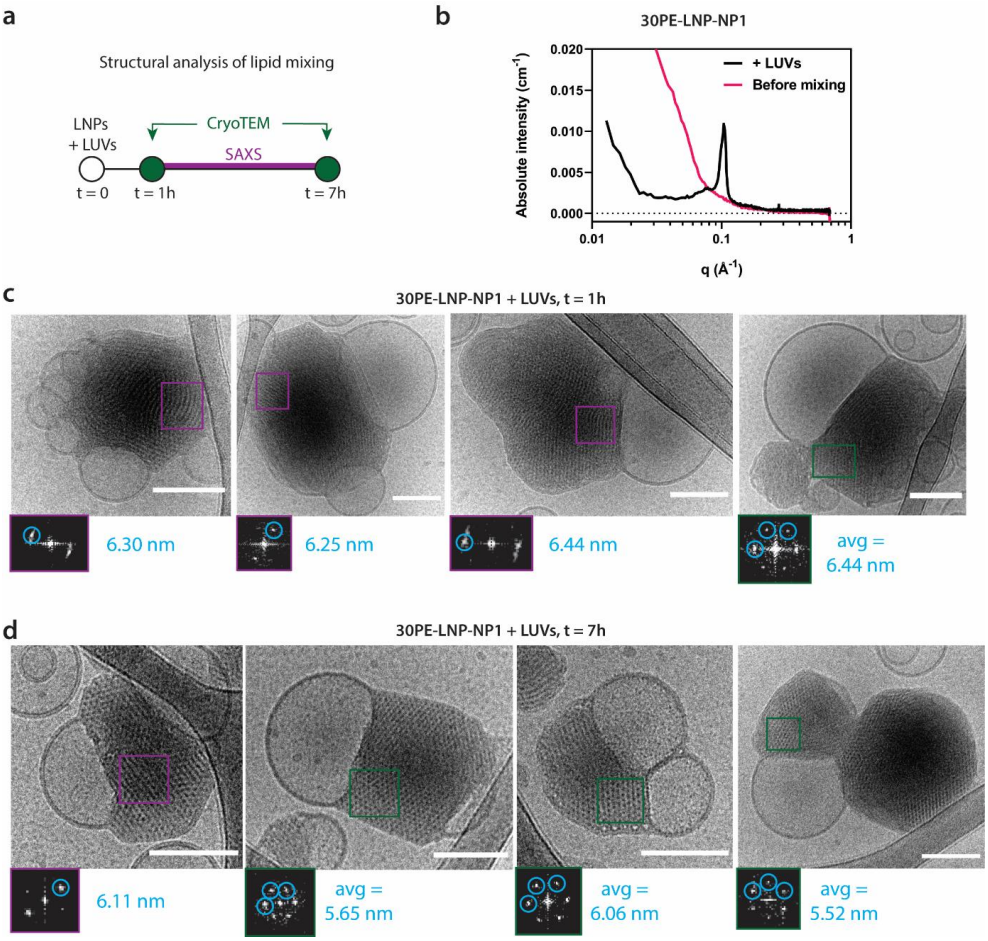


Figure S16. Interaction of 30PE-LNP-NP1 with anionic LUVs. (**a**) Schematic representation depicting the experiments for the structural analysis of the LNP-LUV interaction. (**b**) SAXS profile of 30PE-LNP-NP1 incubated with anionic LUVs. (**c,d**) CryoTEM images and FFTs of selected areas of 30PE-LNP-NP1 incubated with anionic LUVs after 1 hour (t = 1h) and after 7 hours (t = 7h). All scale bars are 100 nm.

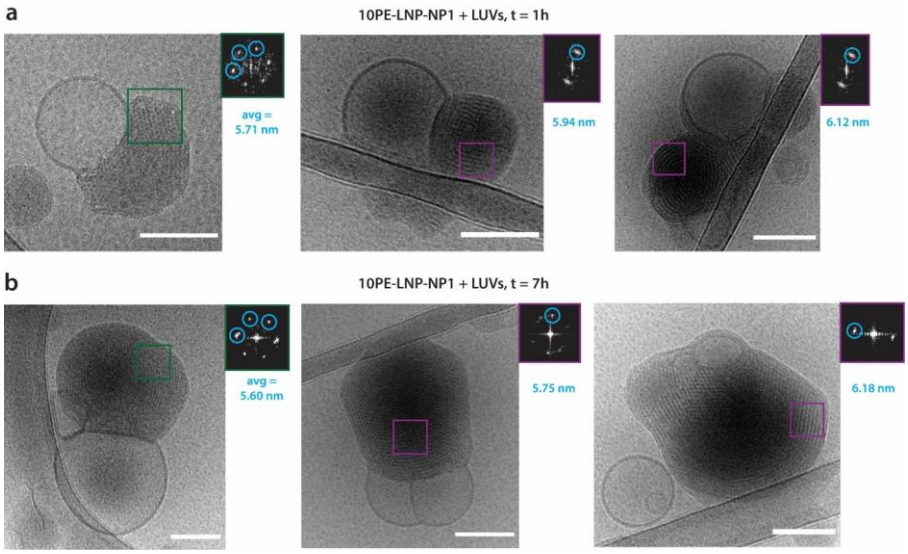


Figure S17. Additional cryoTEM images of 10PE-LNP-NP1 interaction with anionic LUVs. (**a**,**b**) Additional CryoTEM images and FFTs of selected areas of 10PE-LNP-NP1 incubated with anionic LUVs after 1 hour (t = 1h) and after 7 hours (t = 7h). All scale bars are 100 nm.

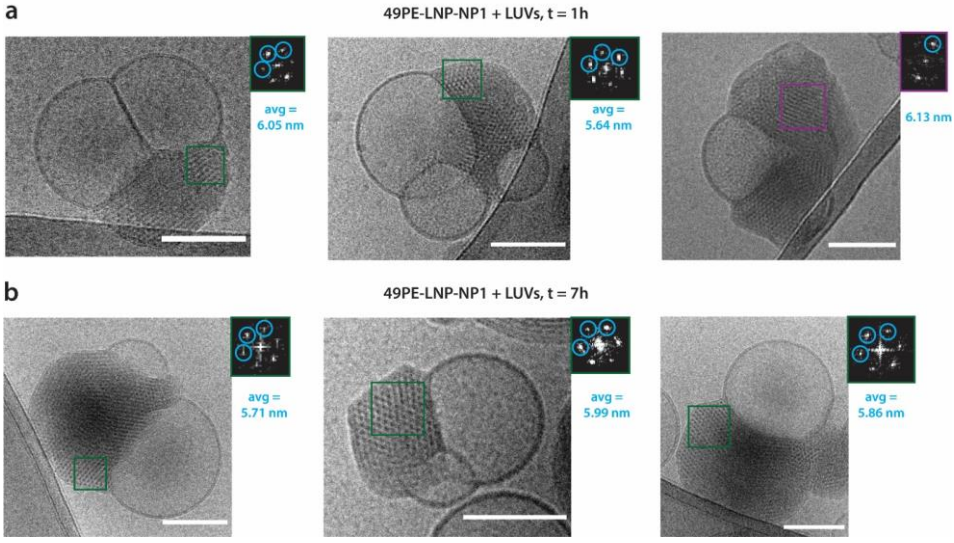


Figure S18. Additional cryoTEM images of 49PE-LNP-NP1 interaction with anionic LUVs. (**a**,**b**) Additional CryoTEM images and FFTs of selected areas of 49PE-LNP-NP1 incubated with anionic LUVs after 1 hour (t = 1h) and after 7 hours (t = 7h). All scale bars are 100 nm.

2. Materials and methods

Reagents

Cholesterol was purchased from Sigma-Aldrich (Zwijndrecht, The Netherlands). 1,1′-Dioctadecyl-3,3,3′,3′-Tetramethylindodicarbocyanine (DiD) was purchased from Thermo Fisher Scientific (Landsmeer, The Netherlands). L-α-phosphatidylserine (Brain, Porcine, PS), L-α-phosphatidylcholine (Brain, Porcine, PC), L-α-phosphatidylethanolamine (Brain, Porcine, PE), L-α-phosphatidylinositol (Brain, Porcine, PI), 1,2-dioleoyl-*sn*-glycero-3-phosphoethanolamine-N-(7-nitro-2-1,3-benzoxadiazol-4-yl) (PE-NBD), 1,2-dioleoyl-*sn*-glycero-3-phosphoethanolamine-N-(lissamine rhodamine B sulfonyl) (PE-LR), 1,2-dioleoyl-*sn*-glycero-3-phosphoethanolamine(DOPE),1,2-dimyristoyl-*sn*-glycero-3-phosphoethanolamine-N-methoxypolyethylene glycol-2000 (DMPE-PEG2k), 1,2-dioleoyl-3-dimethylammonium-propane (DODAP) and 1,2-distearoyl-3-dimethylammonium-propane (DSDAP) were purchased from Avanti Polar Lipids through Merck. All siRNA molecules were purchased from Integrated DNA Technologies (Leuven, Belgium) either through custom synthesis or from the catalog, exact sequences can be found in Supplementary Table 1. HeLa-CD63-eGFP, U2OS-UBE21-eGFP cell line were cultured in DMEM growth medium (Sigma Aldrich) containing sodium bicarbonate, without sodium pyruvate and HEPES, was supplemented with 10% fetal bovine serum (Sigma), 1% of L-glutamine (Thermo Fisher Scientific) and 1% penicillin/streptomycin (Thermo Fisher Scientific), at 37 °C in the presence of 5% CO2. Opti-MEM reduced serum medium (Thermo Fisher Scientific) was applied among transfection experiments.

Self-assembly of Lipid Nanoparticles (LNPs)

Lipids were combined at the desired molar ratios and concentrations from stock solutions (1-10 mM) in chloroform:methanol (1:1). Solvents were evaporated under a nitrogen flow and residual solvent was removed *in vacuo* for at least 30 minutes. The lipid film was dissolved in absolute ethanol and used for the assembly. A solution of siRNA was made by dissolving siRNA in 50 mM citrate buffer (pH = 4, RNase free). The solutions were loaded into two separate syringes and connected to a T-junction microfluidic mixer. The solutions were mixed in a 3:1 flow ratio of siRNA against lipids (1.5 mL/min for siRNA solution, 0.5 mL/min for lipids solution). After mixing, the solution was directly loaded in a 10k MWCO dialysis cassette (Slide-A-Lyzer™, Thermo Scientific) or a 1 MDa MWCO dialysis cassette (Spectra-Por® Float-A-Lyzer® G2, Thermo Scientific) and dialyzed against Phosphate Buffered Saline (PBS, 137 mM NaCl, 2.7 mM KCl, 8 mM Na_2HPO_4, and 2 mM KH_2PO_4) overnight. After overnight dialysis, siRNA encapsulation efficiency was determined by

Quant-iT™ RiboGreen™ RNA Assay Kit as described below. If necessary, LNPs were concentrated using 100k MWCO centrifugal filters (Amicon® Ultra, Merck). Adjustment and dilution of LNPs was done with Dulbecco's PBS (Merck).

RNA encapsulation and dose determination assay

Encapsulation efficiency (EE%) defined as the amount of siRNA encapsulated versus the free siRNA in solution after dialysis was determined using a Quant-iT™ RiboGreen™ RNA Assay Kit (Invitrogen). For the determination of non-encapsulated siRNA, LNPs after dialysis were diluted with the supplied 1 x TE buffer (RNase free) and treated with the RiboGreen™ reagent. For the determination of the complete amount of siRNA in the sample, LNPs after dialysis were treated with 1% Triton X-100 in TE buffer (RNase free) and incubated for 15 minutes followed by dilution with TE buffer and treatment with the RiboGreen™ reagent. Both conditions were performed in triplicate to ensure proper lysis of the LNPs. Change in fluorescence was measured in 96-well plates using a TECAN Infinite M1000 Pro microplate reader and the percentage of siRNA encapsulation (EE%) was determined using the fraction of $(F_{\text{total RNA}} - F_{\text{free RNA}})/F_{\text{total RNA}} \times 100\%$. Quantification of the dose was determined using a similar protocol, in which the RiboGreen™ fluorescence was determined of concentrated LNPs. The supplied RNA standards were used to generate a standard curve and the concentration of encapsulated mRNA was determined by inserting $(F_{\text{total RNA}} - F_{\text{free RNA}})$ in the standard curve.

Cryogenic Transmission Electron Microscopy (cryoTEM)

Vitrification of concentrated LNPs (~10-15 mM) was performed using a Leica EM GP operating at 22°C or 37°C and 95% relative humidity. Sample suspensions were placed on glow discharged 150 µm lacey carbon films supported by 200 mesh copper grids (Electron Microscopy Sciences). In general, optimal results were achieved using a 30-60 second pre-blot and a 1 second blot time. After vitrification, sample grids were maintained below –170 °C and imaging was performed on a Tecnai T12 (ThermoFisher) with a biotwin lens and LaB6 filament operating at 120 keV equipped with an Eagle 4K x 4K CCD camera (ThermoFisher). Images were acquired at a nominal underfocus of -2 to -3 µm (49,000× magnification) with an electron dose of ~2000 $e^{-} \cdot nm^{-2}$.

For higher resolution cryoEM, grids were loaded into a Titan Krios transmission electron microscope (FEI Company) equipped with a field emission gun operating at 300 kV and were imaged using a Falcon 3 direct electron detector (FEI). Images were acquired a

calibrated magnification of 75,000× with a nominal underfocus of -1 to -2 µm and an electron dose of ~2000 $e^{-} \cdot nm^{-2}$.

Single particle analysis of cryoTEM data

Single particles were chosen based on the presence of structure formation from a collection of 2D cryoTEM images, divided over three independent assemblies of the same LNP formulation. Only particles present in vitreous ice were considered for analysis. Regions of interest from individual particles and the fast Fourier transform (FFT), as well as the determination of particle size was performed using the Fiji distribution of ImageJ.[1]

Cryogenic Electron Tomography (cryoET)

Samples for cryoET were prepared as described for 2D cryoTEM, but with the addition of BSA coated 10 nm gold beads immediately prior to vitrification to act as fiducial markers for tomogram reconstruction. Tilt series were collected using Tomo 4.0 (FEI) on a Titan Krios at a magnification of 75,000×, for a final pixel size 1.87 Å/pixel, using a continuous tilt series from -60° to +60° with increments of 2° and an electron dose of ~200-250 e^{-}/nm^{2} per tilt image. Focusing to −4 to −5 µm was performed every second image acquisition using a low-dose routine. Tomograms were processed using IMOD software,[2] using fiducial tracking and reconstructed with both weighted back-projection and 5 iterations of a SIRT-like filter within IMOD to enhance contrast. Tomograms were visualised and analysed using a combination of IMOD and UCSF Chimera.[3]

Model building

DOPE and DODAP lipids were built using PyMOL,[4] before parametrization in eLBOW within Phenix.[5,6] Lipids were relaxed into varied appropriate geometries using ISOLDE within UCSF ChimeraX.[7,8] UCSF Chimera was used to build models of siRNA and lipid-siRNA structures.

Small Angle X-Ray Scattering (SAXS)

SAXS measurements were performed in transmission mode on a SAXSLAB GANESHA system with a Pilatus 300K solid-state photon-counting 2D detector using a high brilliance Microfocus Cu Source, Xenocs Genix3D, wavelength 1.54184 Å. The LNPs (~12 mM) were loaded into 2mm lockable thin wall capillaries and measured at a q-range of 0.0129 – 0.6870 $Å^{-1}$ with an exposure time of 6 hours. Prior to each measurement series, a silver behenate standard was used to correct for deviations in the sample to detector distance. For

temperature dependent experiments, the temperature was equilibrated to 25 °C or 37 °C for 30 minutes prior to measurement. The measured SAXS profiles are displayed as the average intensity I(q) vs. the q-range. For kinetic temperature experiments, the measurement time was divided into the average intensity of 1-hour sections.

Assembly of large unilamellar vesicles (LUVs)

LUVs were assembled using a combination of freeze-thaw cycles and extrusion. Lipids were combined from stock solutions (2-10 mM) in chloroform to a achieve a lipid composition of PC:PE:PS:Chol:PI of 50:27:10:10:3 mol% or PC:PE:PS:Chol:PI:PE-NBD:PE-LR of 50:24:10:10:3:1.5:1.5 mol%. The solvent was evaporated from the mixture under a nitrogen flow, followed by removal of trace solvents *in vacuo* for at least 1 hour. The resulting lipid film was hydrated with either 100 mM citrate buffer (pH = 5.5) or phosphate buffered saline (PBS, pH = 7.3), to achieve the desired total lipid concentration (10-20 mM) and vortexed until the entire lipid film was fully suspended in solution. The suspension was subjected to seven freeze-thaw cycles. In each cycle, the mixture was frozen completely with liquid nitrogen and left to thaw at room temperature, followed by vigorous mixing to ensure complete thawing. After these cycles, the mixture was extruded at 40 °C (Mini-extruder, Avanti Polar Lipids, Alabaster, US). The mixture was passed 11 times through a 200 nm polycarbonate (PC) membrane (Nucleopore Track-Etch membranes, Whatman). All liposome formulations were stored at 4 °C and used within 2 days.

Lipid mixing determined by Fluorescence Resonance Energy Transfer (FRET)

For the determination of lipid mixing efficiency by FRET, LUVs with a composition of PC:PE:PS:Chol:PI:PE-NBD:PE-LR of 50:24:10:10:3:1.5:1.5 mol% were prepared in 100 mM citrate buffer (pH = 5.5) or PBS (pH = 7.4) as described above. The LUVs were diluted with their respective buffers to 250 µM and 100 µL was transferred to black F-bottom chimney 96-well plates (Greiner®). The LUVs were heated to 37 °C prior to further use. For the control serving as 100% lipid mixing, 20 µL of 1% Triton X-100 in H_2O was added followed by the addition of 80 µL PBS. For the control serving as 0% lipid mixing, 100 µL PBS was added to the LUVs. LNPs were assembled and diluted in PBS (pH = 7.4) to 500 µM and 100 µL was added to the acceptor LUVs, yielding a final concentration 125 µM LUVs and 250 µM LNPs. In the case where 100 mM citrate buffer was used for the LUVs, the final pH was ~6.0. All of the conditions were performed in triplicate. After addition of the LNPs, the dequenching of the PE-NBD signal was measured every 15 seconds for 25 minutes using a TECAN Infinite M1000 Pro microplate reader (λ: excitation = 460 nm ± 10 nm, emission = 535 nm ± 10 nm).

CryoTEM and SAXS analysis of lipid mixing

For the assessment of lipid mixing with cryoTEM and SAXS analysis, LUVs with a composition of PC:PE:PS:Chol:PI of 50:27:10:10:3 mol% were prepared in 100 mM citrate buffer (pH = 5.5) at a concentration of 20 mM as described above. LNPs were prepared as described before and concentrated to ~20 mM. The LUVs and LNPs were mixed at a volumetric ratio of 1:2 respectively, and incubated at 37 °C. For cryoTEM, samples were vitrified after 1 hour of incubation as described above. In the case of SAXS measurements, the mixture of LUVs and LNPs were loaded into capillaries and equilibrated at 37 °C for 1 hour prior to the start of the measurement, as described above. The presented data is of the mixed samples minus the background of LUVs in citrate buffer mixed with PBS (without LNPs) at the same final concentration.

Cell transfection and FACS experiments

HeLa-CD63-eGFP, U2OS-UBE21-eGFP were seeded in 96-well plate at the density of $1*10^4$ cells/well on the day before, different concentrations of siRNA-GFP encapsulated LNPs (0 – 83 nM) in 100 µL Opti-MEM medium were added to the cells and incubated for 24 h, then the medium was removed and refreshed with new Opti-MEM for continuous 48 h culturing. After 72h incubation, cells were digested, collected and resuspended in PBS for FACS measurements (Guava easyCyte Flow Cytometers). DiD mean fluorescence intensities (Red-R channel) was quantified as the uptake of LNPs into cells. The eGFP expression (GFP MFI, Green-B channel) of all LNP treated cells are relative to PBS treated cells, for which the values are set as 100%.

Cell viability assay

HeLa-CD63-eGFP, U2OS-UBE21-eGFP cells were seeded 96-well plate at a density of $1*10^4$ cells per well the day before, then followed with the same procedure as the transfection with different concentrations of LNPs determined by the Ribogreen RNA assay. After 72 h incubation, cell viabilitity reagent alarmaBlue HS solution (10 µL, ThermoFisher) was added to the medium (100 µL) and incubated for another 4 h at 37°C. After 4 h, the absorbance at 570 nm (using 600 nm as a reference wavelength) was measured at room temperature using a Tecan infinite M1000, which was shaken for 60 s before measurement (2 mm linearly, 654 rpm). The cell viability was normalized with control (blank HeLa-CD63-eGFP, U2OS-UBE21-eGFP cells), which was set at 100% cell survival. All conditions were performed in triplicate.

3. References

1. Schindelin, J. *et al.* Fiji: an open-source platform for biological-image analysis. *Nat. Methods* **9**, 676–682 (2012).
2. Mastronarde, D. N. & Held, S. R. Automated tilt series alignment and tomographic reconstruction in IMOD. *J. Struct. Biol.* **197**, 102–113 (2017).
3. Pettersen, E. F. *et al.* UCSF Chimera--a visualization system for exploratory research and analysis. *J. Comput. Chem.* **25**, 1605–1612 (2004).
4. Schrodinger LLC. The PyMOL Molecular Graphics System, Version 1.8. (2015).
5. Afonine, P. V *et al.* Real-space refinement in PHENIX for cryo-EM and crystallography. *Acta Crystallogr. Sect. D, Struct. Biol.* **74**, 531–544 (2018).
6. Moriarty, N. W., Grosse-Kunstleve, R. W. & Adams, P. D. electronic Ligand Builder and Optimization Workbench (eLBOW): a tool for ligand coordinate and restraint generation. *Acta Crystallogr. D. Biol. Crystallogr.* **65**, 1074–1080 (2009).
7. Croll, T. I. ISOLDE: a physically realistic environment for model building into low-resolution electron-density maps. *Acta Crystallogr. Sect. D, Struct. Biol.* **74**, 519–530 (2018).
8. Pettersen, E. F. *et al.* UCSF ChimeraX: Structure visualization for researchers, educators, and developers. *Protein Sci.* **30**, 70–82 (2021).

Nederlandse samenvatting

In het jaar 1900 beschreef Paul Ehrlich het concept van de "*magic bullet*", waar wordt verwezen naar een medicijn dat zich met hele hoge precisie richt op ziekmakende cellen, zonder schade te brengen aan gezonde cellen. Hiermee kunnen bijwerkingen van medicatie tot het verleden worden gerekend. Traditioneel worden antibiotica gezien als medicatie die het meest in de buurt komen van *magic bullets*, aangezien zij in staat zijn om selectief bacteriële cellen te doden en menselijke cellen met rust te laten. Echter, in de moderne geneeskunde, worden deze algemene medicijnen niet langer beschouwd als de ideale strategie. In plaats daarvan wordt juist gekeken naar gepersonaliseerde medicijnen die met precisie van een *magic bullet* de moleculaire defecten van individuele patiënten kunnen repareren, bijvoorbeeld in de vorm van gentherapie.

Het toepassen van nanotechnologie wordt gezien als een van de meest veelbelovende manieren om deze strategie te realiseren. Nanotechnologie is een veld binnen de wetenschap dat zich richt op de het maken van functionele systemen kleiner dan 100 nm, in grootte vergelijkbaar met een virus. Het is hierbij aan de wetenschapper om de juiste zuivere moleculaire componenten en fabricatiemethode te kiezen, zodat de verschillende componenten door hun chemische eigenschappen een nanosyteem vormen, bijvoorbeeld in de vorm van een bolvormig nanodeeltje. Als een van deze componenten dan ook nog het actieve medicijn is dan kan er worden gesproken over zogeheten **nanomedicatie**. Het grootste voordeel van nanomedicatie is dat fragiele, zeer toxische, of slecht te transporteren medicatie, alsnog selectief zijn doel kan bereiken in het menselijk lichaam. Een vaak toegepaste strategie is bijvoorbeeld een anti-kanker medicijn beschermen door andere componenten in een nanodeeltje en selectief naar een celtype in het lichaam transporteren. Hiermee is het niet direct beschikbaar voor opname in alle cellen dat het tegenkomt en kunnen ernstige bijwerkingen worden voorkomen.

Deze toepassingen van nanomedicatie heeft wetenschappers al tientallen jaren gefascineerd en heeft een grote hoeveelheid aan verschillende nanodeeltjes opgeleverd. Hierin kan worden gevarieerd met verschillende moleculaire componenten, zoals bijvoorbeeld lipiden, suikers, synthetische polymeren of eiwitten. Daarnaast wordt ook gekeken naar de actieve medicatie, bijvoorbeeld tegen kanker, ontstekingen en infecties. Het gaat hierbij voornamelijk om de juiste selectie van de verschillende componenten die leiden tot een goede assemblage, en de juiste therapeutische respons in een biologisch systeem.

Een recente doorbraak in dit onderzoeksveld zijn zogenaamde lipide nanodeeltjes (LNPs) voor het afleveren van ribonucleïnezuren (RNA-moleculen). Lipiden zijn vetten, of vetachtige moleculen, die bijvoorbeeld een cruciale rol spelen in het maken van celmembranen. De lipiden die worden gebruikt in deze nanosystemen kunnen zowel een biologische oorsprong hebben, of synthetisch zijn. Aangezien het vaak gaat om zeer vergelijkbare moleculen als die we in ons lichaam tegenkomen, is de afbraak van deze componenten makkelijk en worden de nanodeeltjes goed getolereerd. Ook de RNA-moleculen hebben vaak een endogene biologische functie, zo zorgen bijvoorbeeld zogenaamde *messenger* RNA-moleculen (mRNA) voor de productie van eiwitten in menselijk cellen. De lipide nanodeeltjes worden gemaakt uit individuele lipiden die samen met RNA-moleculen een nanosysteem vormen met een diameter van ~30-80 nm. Decennia van onderzoek naar verschillende lipiden hebben ertoe geleid dat RNA-afgifte in een voorspelbare en selectieve manier kan plaatsvinden. Dit zorgde in 2018 voor de goedkeuring van Onpattro® voor de behandeling van erfelijke transthyretine-gemedieerde amyloïdose (hATTR-amyloïdose) bij volwassenen met polyneuropathie. Recent zijn LNPs goedgekeurd voor het gebruik in de aflevering van mRNA in de coronavaccins van Pfizer/BioNTech en Moderna voor de bescherming tegen Covid-19.

Deze enorme therapeutische translatie voor nanodeeltjes is een bevestiging van tientallen jaren aan fundamenteel en klinisch onderzoek in deze richting. Door de goede tolerantie van het lichaam voor LNPs en de wijde toepasbaarheid van verschillende RNA-moleculen voor een grote variëteit aan ziektes, wordt de potentie van deze nanosystemen als mogelijke *magic bullets* nog groter.

In veel gevallen wordt het onderzoek naar nieuwe variaties van LNPs en hun toepassingen vaak empirisch uitgevoerd. Hier worden grote hoeveelheden aan verschillende lipide en RNA-moleculen gescreend en worden degenen met het beste effect gekozen voor een volgende ronde aan testen. Echter zijn hier vaak enorme faciliteiten, budget en tijd voor nodig. Daarnaast wordt er met deze strategie vaak belangrijke fundamentele kennis van de nanodeeltjes in biologische systemen genegeerd. Deze kennis geeft echter de mogelijkheid om verbeterde nanodeeltjes en nieuwe strategieën rationaal te ontwikkelen. In het onderzoek beschreven in deze dissertatie wordt juist fundamenteel gekeken naar het **gedrag van lipide nanosystemen in biologische systemen**, de zogeheten **nano-bio interface**.

Om deze kleine nanosystemen in een heel complex systeem te bestuderen, wordt gebruik gemaakt van een combinatie van chemische, biochemische en biofysische methoden, zoals chemische synthese, eiwit massaspectroscopie en elektronenmicroscopie. Daarnaast wordt

informatie verzameld over de interactie van nanodeeltjes met verschillende biologische systemen, zoals menselijk serum en plasma, in het lab gekweekte cellen, maak ook diermodellen zoals levende transparante zebravis embryo's en muizen. De onderwerpen waarnaar werd gekeken zijn de effecten van LNP-structuur op de biologische toepassing, de adsorptie van menselijke eiwitten aan lipide nanosystemen en de interactie van LNPs met receptoren in de bloedbaan. De resultaten zijn uiteengezet in vier experimentele hoofdstukken die ieder een ander onderwerp bestuderen:

In **hoofdstuk 2** wordt een nieuwe methode beschreven om eiwitadsorptie aan lipide nanosystemen, in dit geval liposomen, in menselijk serum te identificeren. Waar bestaande methodes gebaseerd waren op fysieke scheiding van de nanodeeltjes met eiwitten uit het serum, wordt hier een chemische methode gepresenteerd. Door middel van organische synthese werd een nieuw lipide molecuul gesynthetiseerd dat kan worden toegevoegd aan lipide nanosystemen. Dit lipide heeft twee belangrijke eigenschappen: ten eerste is het in staat om een binding te vormen met eiwitten aan de buitenkant van het nanodeeltje als het met specifiek Uv-licht bestraald wordt. Ten tweede kan dit lipide, gebonden aan het eiwit, selectief uit het menselijk plasma worden gezuiverd. Gekoppeld aan *eiwit massaspectroscopie* kunnen vervolgens de eiwitten die adsorberen aan het nanosysteem worden geïdentificeerd. Waar in vorige methoden veel interferentie was van grote en veel voorkomende eiwitten, zorgt deze nieuwe zuiveringstechniek voor een veel preciezere identificatie van de correcte geadsorbeerde eiwitten. Daarnaast kan de methode ook worden toegepast om de binding van specifieke eiwitten te valideren en zo vals-positieve eiwitidentificaties te vermijden.

In **hoofdstuk 4** gaat het onderzoek met de methode uit hoofdstuk 2 verder, en wordt de eiwit adsorptie geïdentificeerd van een specifieke selectie aan liposomen en uitgebreid naar LNPs die RNA-moleculen bevatten. In dit geval werden de belangrijkste eiwitten wederom gevalideerd en was er een duidelijk patroon zichtbaar van specifieke eiwitten die gebaseerd is op de oppervlakte lading van de verschillende nanodeeltjes. Daarnaast wordt door middel van inhibitie experimenten de *exacte positie van adsorptie van het eiwit apolipoproteine E* aan negatief geladen liposomen bepaald. Dit gebeurt via een deel van het eiwit dat positief geladen is en daarmee een elektrostatische interactie kan aangaan. Echter, hetzelfde eiwit bindt neutraal geladen liposomen en LNPs niet op deze manier, maar namelijk via een ander domein. Dit verschil in binding kan het mogelijke verschil in uiteindelijke opname door verschillende levercellen verklaren. Deze informatie wordt daarmee gebruikt door collega's om te bestuderen op welke manier het ontbreken van dit eiwit een effect gaat hebben op de aflevering van deze lipide nanodeeltjes. Met de informatie die hieruit komt kunnen vervolgens nieuwe strategieën worden bedacht voor selectieve medicijnafgifte

door het manipuleren van de binding van dit specifieke eiwit. Bovendien laat dit werk ook voor de eerste keer de selectieve binding zien van specifieke eiwitten aan lipide nanodeeltjes met een moleculair detail, en kan de methode in de toekomst verder worden gebruikt voor soortgelijke ontdekkingen.

In **hoofdstuk 3** wordt het selectief afleveren van mRNA moleculen met LNPs in verschillende biologische systemen beschreven. Door gebruik te maken van fundamentale kennis van voorheen beschreven lipide nanosystemen, was het mogelijk om rationeel, en met minimale verandering tot het klinisch toegepaste Onpattro®, een LNP te produceren dat selectief mRNA aflevert aan de cellen van het *reticulo-endotheliaal systeem* in de lever. In dit geval werden *transparante zebravis embryo's* gebruikt als veelzijdig diermodel om de nanodeeltjes in een levend systeem te kunnen bestuderen met behulp van fluorescentie microscopie. In dit geval kon worden herkend in welke cellen de nanodeeltjes terechtkomen en waar het mRNA dat codeerde voor fluorescente eiwitten goed tot werking kwam. Daarnaast zijn er meerdere genetische manipulaties mogelijk binnen zebravissen die het mogelijk maken om het effect van individuele receptoren te bestuderen. Hiermee wordt bewezen dat de opname van de negatief geladen LNPs selectief gebeurt door de receptoren stabiline-1 en 2, die voornamelijk voorkomen op specifieke bloedvatcellen en macrofagen in de zebravis. Aangezien het bekend is dat de geobserveerde cellen in de zebravis overeenkomen met bloedvatcellen en macrofagen in de lever van zoogdieren, was er slechts een beperkt en gericht experiment nodig met muizen om deze strategie te bevestigen. Door het rationele ontwerp van de LNPs op basis van fundamentele kennis zijn veel tijd, geld en proefdieren gespaard gebleven. Het selectief afgeven van mRNA aan bijvoorbeeld de endotheelcellen in de lever zal door andere wetenschappers verder als strategie worden gebruikt om de juiste eiwitten to expressie te brengen die kunnen helpen bij leverziektes, zoals leverfibrose en kanker, maar ook voor het manipuleren van nodige immuunrespons die via deze celtypen werken.

In **hoofdstuk 5** wordt het effect op de efficiëntie van specifieke lipide structuren met RNA-moleculen in de kern van LNPs beschreven. De positie en interactie van RNA-moleculen in lipide nanosystemen is lastig te bestuderen en kan vrij willekeurig en zonder kenmerkende structuur voorkomen. Toch is het in sommige gevallen toch waargenomen dat bepaalde specifieke structuren kunnen vormen. Het is van grote interesse of deze geordende structuren een specifieke werking hebben op de efficiëntie van LNPs. In dit hoofdstuk wordt door het zorgvuldig selecteren van de lipide componenten en de verhoudingen ten opzichte van de RNA-moleculen voor de fabricatie, het mogelijk om LNPs te maken met gedefinieerde lipide-RNA structuren. Deze gedefinieerde structuren zijn lamellen (gelaagd), inverse hexagonaal of een mengsel van de twee. Aangezien de orde van grootte

van deze structuren tussen de 4 en 10 nm ligt, werd er gebruikt gemaakt van een combinatie van geavanceerde technieken om ze te bestuderen. Met behulp van *small-angle X-ray scattering* (SAXS) kon in het monster de hoeveelheid verschillende structuren kwalitatief in kaart worden gebracht. Uiteindelijk werd met *cryogene elektronenmicroscopie* (cryoEM) tot hele hoge vergroting (49.000x) ingezoomd op individuele LNPs en konden de structuren in de kern van het lipide nanosysteem worden gevisualiseerd en geanalyseerd. Met de gedetailleerde beschrijving van deze structuren kon een correct vergelijkend onderzoek worden uitgevoerd naar het verschil in efficiëntie. Er werd aangetoond dat LNPs met een *inverse hexagonale structuur* efficiënter RNA-moleculen afleveren in levende cellen. Verdere elektronmicroscopie studies tussen LNPs en kunstmatig gemaakte celmembranen laten zien dat het mechanisme van RNA vanuit een invers hexagonale structuur efficiënter verloopt via een 1-staps mechanisme, t.o.v. een 2-staps mechanisme in het geval van gelaagde structuren. Deze kennis kan worden gebruikt om de efficiëntie van LNPs met andere composities te verhogen, door het rationeel selecteren van de juiste componenten die het vormen van een invers hexagonale structuur bevorderen.

Samenvattend beschrijft dit proefschrift een collectie aan alternatieve strategieën voor het begrijpen, ontwerpen en toepassen van lipide nanosystemen, waarin de rol van de bio-nano interacties centraal staan. Het onderzoeksgebied van de nanomedicatie kan gebruik maken van de specifieke voorbeelden die worden beschreven, maar er kan ook inspiratie worden opgedaan om de aanpak van onderzoek doen te verschuiven van een kostbare empirische aanpak naar rationeel gedreven ontwerpstrategie.

Curriculum Vitae

Roy Pattipeiluhu was born on the October 3, 1991 in Rotterdam, the Netherlands. In 2009, he graduated from csg. Calvijn in Rotterdam. In 2011, he obtained a propaedeutic certificate in Chemistry from the Hogeschool Rotterdam. In 2014, he obtained his Bachelor's degree in Molecular Science & Technology from Delft University and Technology and Leiden University, with a major in Chemistry and a minor in Education.

In 2017, he received a cum laude Master's degree in Chemistry from Leiden University, with a specialization in Chemical Biology. In addition, he participated in the 2015 honors program of the Netherlands Research School of Chemical Biology. During his Master's program, he performed several internships and projects. As a part of his master's thesis in 2015, he developed light-activated angiogenic peptides for the use in embryonic zebrafish in the Supramolecular and Biomaterials Chemistry group at Leiden University, under the supervision of Dr. Jeroen Bussmann and Prof. dr. Alexander Kros. In addition, he was funded a NWO Top Sector Chemistry Student grant and spend several months working on dual directed liposomes for tumor treatment. In 2016, he worked on an enzymatic fluorescent labelling method in the bacterium *C. Crescentus* under the supervision of Dr. Samuel Ho in the lab of Prof. dr. David A. Tirrell at the California Institute of Technology.

In 2017, Roy started his PhD in the Supramolecular and Biomaterials Chemistry group at Leiden University, under the supervision of promotor Prof. dr. Alexander Kros (Leiden University) and co-promotor Dr. Thomas H. Sharp (Leiden University Medical Centre). During this period, he focused on understanding the behavior of lipid-based nanomedicine at the nano-bio interface, as described in this dissertation. To this end, he collaborated with scientists from the groups of Prof. dr. Pieter R. Cullis (University of British Columbia, Vancouver, Canada) and Prof. dr. Ilja K. Voets (Eindhoven University of Technology, the Netherlands). In addition, he supervised multiple Bachelor and Master students during their internships and presented the work described in this dissertation at several (inter)national conferences.

Since September 2021, Roy is working as a Scientist in the Early-Stage Formulation Process Development group at BioNTech SE in Mainz, Germany.

The research described in this dissertation was presented at the following meetings and conferences:

- CHAINS editions 2017, 2018 and 2019, Veldhoven, the Netherlands (poster presentations)
- Activity Based Protein Profiling Symposium, Leuven, Belgium, 2019 (poster presentation)
- TIDES, Amsterdam, the Netherlands, 2019 (poster presentation)
- Nanomedicine Journal Club, *digital*, 2020 (oral presentation)
- Annual Meeting of the Biophysical Society, San Diego, United States of America, 2020 (oral presentation)

List of publications

1. **R. Pattipeiluhu**, S. Crielaard, I. Klein-Schiphorst, B. I. Florea, A. Kros, F. Campbell, ACS Cent. Sci. **2020**, 6, 535. "Unbiased Identification of the Liposome Protein Corona Using Photoaffinity Based Chemoproteomics"

2. **R. Pattipeiluhu***, G. Arias-Alpizar*, G. Basha, J. Bussmann, T.H. Sharp, M.A. Moradi, N. Sommerdijk, P.R. Cullis, A. Kros, D. Witzigmann, F. Campbell. "Anionic Lipid Nanoparticles Preferentially Deliver mRNA to the Hepatic Reticuloendothelial System", **submitted**.

3. **R. Pattipeiluhu**, Y. Zeng, M.R.M. Hendrix, I.K. Voets, A. Kros, T.H. Sharp. "Paracrystalline Inverted Lipid Phases Encapsulating siRNA Enhance Lipid Nanoparticle Mediated Transfection", **submitted**.

4. **R. Pattipeiluhu**, B.I. Florea, K. Dickie, T.H. Sharp, F. Campbell, A. Kros. "Site Selective Binding of Apolipoprotein E in the Protein Corona of Anionic Liposomes", *in preparation*.

*These authors contributed equally